

1-1-2012

Multi-fuel operation of modern engines; on board fuel identification

Florin Mocanu
Wayne State University,

Follow this and additional works at: http://digitalcommons.wayne.edu/oa_dissertations



Part of the [Other Mechanical Engineering Commons](#)

Recommended Citation

Mocanu, Florin, "Multi-fuel operation of modern engines; on board fuel identification" (2012). *Wayne State University Dissertations*. Paper 493.

© COPYRIGHT BY

FLORIN MOCANU

2012

All Rights Reserved

DEDICATION

To my wife Petronela, my future daughter Victoria, my mother Viorica and my father Matei, who recently passed away, for their continuous and ceaseless support throughout this research work.

ACKNOWLEDGMENTS

The research work described in this Doctor of Philosophy dissertation was conducted at the Center for Automotive Research (CAR) at Wayne State University, Detroit-Michigan, USA. This work would not have been possible without the guidance and patience of my professor and advisor Dr. Dinu Taraza who helped me numerous times in finding the best solutions to challenges encountered throughout the period of my graduate study. I would like to thank my committee members, Dr. Dinu Taraza, Dr. Naeim Henein, Dr. Marcis Jansons, Dr. Harpreet Singh and to Dr. Trilochan Singh and Dr. Walter Bryzik for their help and support throughout my dissertation work and for their valuable opinions. I would also like to thank Ms Lidia Nedeltcheva in Mechanical Engineering Department Lab and to Mr. Eugene Snowden, Mr. Dave Griffin and Mr. Marvin Santure in the machine shop, for their generous, valuable, and on-time help in my work. I also appreciate the sincere efforts of my colleagues and friends Radu and Elena Florea, Radu Ceausu, Bunpreet Singh, Amrinder Singh, Rafik Rofail, Tamer Badawy, Fadi Estefanopulos, Kan Zha, Ashish Gupta, Nilesh Rai and other members for their help and support.

PREFACE

Present trend to use alternative fuels on modern engines requires the possibility of on-board identification of the fuel and, accordingly, the adaptation of the injection strategy.

For commercial vehicles, the multi-fuel engine operation is supported by the necessity to eliminate the dependency on foreign oil. For military vehicles this flexibility is a big advantage, allowing them to run properly on any fuel accessible on the battlefield.

Because the use of an inexpensive, nonintrusive sensor is highly desirable, the development of techniques based on the measurement of the instantaneous crankshaft speed and engine dynamics could be a convenient solution.

TABLE OF CONTENTS

Dedication	ii
Acknowledgments.....	iii
Preface.....	iv
List of Tables.....	viii
List of Figures.....	x
List of Abbreviations.....	xxii
Chapter 1 - The effects of alternative fuels on engine operation. Fuel identification methods - Literature review	1
1.1 Introduction.....	1
1.2 The effects of alternative fuels on engine operation.....	2
1.3 Fuel identification methods.....	37
1.4 Conclusions.....	75
Chapter 2 - Experimental investigation.....	76
2.1 Experimental setup	76
2.1.1. Single-cylinder engine.....	76
2.1.2. Four-cylinder engine	77
2.1.3. Six-cylinder engine	80
2.2 Fuel tested and their combustion characteristics.....	93

2.2.1. Adaptation of injection strategy to the type of fuel.....	93
2.2.2. Physical and chemical properties of tested fuels	94
2.3 Experimental results	103
2.3.1. Single cylinder engine	103
2.3.2. Four-cylinder engine	108
2.3.3. Six-cylinder engine	108
2.4 Conclusions	121
Chapter 3 - Fuel Identification Methods	123
3.1 Methodology	123
3.2 Dynamic model of the crankshaft	126
3.3 Direct simulation method. Computation of motion for the 1 st mass using transfer matrices	127
3.4 Single cylinder engine model validation	130
3.5 Model-based recognition (transfer matrices reversed) method on a single cylinder engine.....	138
3.6 Direct Recognition Method on a single-cylinder engine.....	148
3.7 Direct Recognition Method on a four-cylinder engine	153
3.8 Estimation of Start of Combustion (Ignition Delay).....	162
3.8.1. Introduction	162
3.8.2. Representation of measured signal as a Fourier series.	166

3.8.3. Estimation of Start of Combustion (Ignition Delay) on a single-cylinder engine	170
3.8.4. Estimation of Start of Combustion (Ignition Delay) on a multi-cylinder engine	176
3.9 Fuel identification method on a six-cylinder engine.....	189
3.9.1. Motivation	189
3.9.2. Artificial neural network functionality and neuron structure.....	190
3.9.3. Layer of neurons and multiple layers of neurons.....	194
3.9.4. Back-propagation algorithm	197
3.9.5. Design of the Artificial Neural Network.....	200
3.9.6. ANN fuel identification on a single-cylinder engine.....	202
3.9.7. ANN fuel identification on a six-cylinder engine.....	212
Chapter 4 - Conclusions and future work.....	222
4.1 Conclusions	222
4.2 Future work	224
APPENDIX – Computation Codes.....	225
References.....	258
Abstract.....	263
Autobiographical Statement.....	264

LIST OF TABLES

Table 1.1 - Percentage of biodiesel blends approved by manufacturers in accordance with B.McCormick	10
Table 1.2 - USPS study vehicle information by Richard Fraer et. al.	17
Table 1.3 - Fuel properties by A.Tsolakisa et.al.	19
Table 1.4 - ULSD and RME volume and mass percentages of the tested fuel mixtures by A.Tsolakisa et.al.....	20
Table 1.5 - Engine conditions and fuel mixtures tested by A.Tsolakisa et.al.	20
Table 1.6 - Durability test cycle specifications according to Yang Hsi-Hsien et.al.	24
Table 1.7 - B20 and diesel specifications in accordance with Yang Hsi-Hsien et.al.....	25
Table 1.8 - Tailpipe emissions from road vehicles using biodiesel and conventional diesel for the UK, G.S Hitchcock et al. 1998	29
Table 1.9 - Tailpipe emissions from road vehicles using biodiesel and conventional diesel for Germany, M. Kaltschmitt et al. 1997.....	29
Table 1.10 - Sample of tailpipe emissions from road vehicles using Biodiesel and ULSD for Australia, T. Beer et al. 2002.....	30
Table 1.11 - Sample of variability of tailpipe emissions in road vehicle tests, T. Beer et al. 2002.....	30

Table 1.12 - Sample of emissions from austrian bus trials relative to low sulphur fossil diesel, T. Sams et al. 1996.....	31
Table 1.13 - Emission factors of regulated air pollutants determined by engine durability test according to U.S. Environmental Protection Agency.....	32
Table 2.1 – Deutz engine characteristics	76
Table 2.2 – VM Motori engine characteristics	77
Table 2.3 – Physical and chemical properties of the tested fuels.	94
Table 3.1 - Deutz single cylinder engine parts and their mass Characteristics.....	132
Table 3.2 - VM Motori 2.5 L four cylinder engine and their masses characteristics	15
	6

LIST OF FIGURES

Figure 1.1 - Biodiesel emission reductions by B.McCormick.....	6
Figure 1.2 - Change in regulated emissions with increase of Biodiesel percentage as presented by B.McCormick	11
Figure 1.3 - Change in NO _x emissions with increase of biodiesel percentage as said by B.McCormick.....	12
Figure 1.4 - Plugged B20 fuel filter in accordance with Kennteh Proc et.al.....	14
Figure 1.5 - B20 valve deck sludge accumulation according to Richard Fraer et.al.	18
Figure 1.6 - Effects of fuel blend composition and EGR on engine exhaust emissions IMEP 4.5 bar reproduced from A.Tsolakisa.....	21
Figure 1.7 - Cylinder pressure and net heat release rate at 4.5 bar IMEP reproduced from A. Tsolakisa, A.Megaritisb et.al.	23
Figure 1.8 - Emission factors of regulated air pollutants determined by engine durability test as stated by Yang Hsi-Hsien et.al.	27
Figure 2.1 - 0.7 l Deutz engine.....	76
Figure 2.2 - Engine Dynamics Laboratory at Wayne State University: 2.5 L common-rail direct injection diesel engine VM Motori.....	77
Figure 2.3 - Engine Dynamics Laboratory at Wayne State University: 2.5 L common-rail direct injection engine VM Motori.....	78

Figure 2.4 - VM Motori 2.5 L engine home-made adaptor and extended (brazed) EGR intake pipe..... 78

Figure 2.5 - Home-made adaptors for pressure transducers mounted before and after the EGR cooler (VM Motori 2.5 L engine)..... 79

Figure 2.6 - Mercedes 6-cyl engine upon arrival at Wayne State University..... 81

Figure 2.7 - Mercedes 6-cyl engine mounted on a cart: 3D design and manufacturing of steel supports..... 82

Figure 2.8 - Installation of shaft encoder: adaptor 3D design and manufacturing (Mercedes 6-cyl engine)..... 83

Figure 2.9 - Succession of operations to replace the cylinder head with one customized for pressure transducers on the Mercedes 6-cyl engine..... 84

Figure 2.10 - Reassembling the 7.2 I Mercedes 6-cyl engine..... 85

Figure 2.11 - Mercedes 6-cyl engine: Mounting of the after-treatment device (oxidation catalyst and particulate filter) and the muffler..... 86

Figure 2.12 - Attaching the cooling system for pressure transducers and connecting the thermocouples of the after-treatment to the PUMA data acquisition system (7.2 I Mercedes 6-cyl engine)..... 87

Figure 2.13 - The 7.2 I Mercedes 6-cyl engine, attached to the dynamometer, before the final instrumentation (Wayne State University)..... 88

Figure 2.14 - The 7.2 I Mercedes 6-cyl engine instrumentation (Wayne State University)..... 89

Figure 2.15 - AVL 16-channel high speed data acquisition system.....	90
Figure 2.16 - AVL 48-channel low speed data acquisition system.....	91
Figure 2.17 - Complete setup of 7.2 l Mercedes 6-cyl engine (Wayne State University).....	92
Figure 2.18 - Density curves - ULSD vs S8 vs JP8 vs B100 as stated by C.Jayakumar et.al.	97
Figure 2.19 - Distillation curves - ULSD vs S8 vs JP8 vs B100 .as demonstrated by C. Jayakumar et.al.	98
Figure 2.20 - Definition of bulk modulus	99
Figure 2.21 - Schematic representation of octane and cetone number	100
Figure 2.22 - Spatial representation of ethane.....	101
Figure 2.23 - Spatial representation of hexadecane.....	102
Figure 2.24 - Spatial representation of aromatic hydrocarbons.....	102
Figure 2.25 - Single-cylinder 0.7 L Deutz engine on ULSD at 1500 rpm and 4 Nm torque: Measured cylinder pressure.....	104
Figure 2.26 - Single-cylinder 0.7 L Deutz engine on ULSD at 1500 rpm and 4 Nm torque: Measured speed.....	105
Figure 2.27 - Single-cylinder 0.7 L Deutz engine on S-25 at 1500 rpm and 4 Nm torque: Measured cylinder pressure.....	106
Figure 2.28 - Single-cylinder 0.7 L Deutz engine on S-25 at 1500 rpm and 4 Nm torque: Measured	

speed.....	107
Figure 2.29 - VM Motori 2.5 L four-cylinder engine idling at 1000 rpm on ULSD: Measured cylinder pressures	109
Figure 2.30 - VM Motori 2.5 L four-cylinder engine idling at 1000 rpm on ULSD: Measured engine speed.....	110
Figure 2.31 - VM Motori 2.5 L four-cylinder engine idling at 1500 rpm on ULSD: Measured cylinder pressures	111
Figure 2.32 - VM Motori 2.5 L four-cylinder engine idling at 1500 rpm on ULSD: Measured engine speed.....	112
Figure 2.33 - Mercedes engine: sample of the testing conditions at 1500 rpm / 360 Nm (7.5 bar IMEP) on the dynamometer controller and data acquisition system PUMA OPEN 1.2	113
Figure 2.34 - Mercedes 6-cylinder engine diagram ULSD vs S-8: pressure trace (green), rate of heat release (red), fuel rail pressure (pink) and injector current probe of cylinder #6 (blue) at 1500 rpm, 360 Nm / 7.5 bar IMEP.....	114
Figure 2.35 - Various types of flames: on the left, a rich fuel mixture with no premixed oxygen produces a yellow sooty diffusion flame; on the right, a lean oxygen premixed flame yields no soot and the flame color is produced by molecular radical band emission	115
Figure 2.36 - 7.2 l Mercedes 6-cylinder engine at 1300 rpm / 360Nm torque: Measured crankshaft speed for S-8, ULSD and biodiesel	118
Figure 2.37 - 7.2 l Mercedes 6-cylinder engine at 1300 rpm / 360Nm torque: Pressure traces for S-8, ULSD and biodiesel - average of 100 cycles.....	119

Figure 2.38 - 7.2 l Mercedes 6-cylinder engine at 1300 rpm / 360Nm torque: Rates of pressure rise for S-8, ULSD and biodiesel - average of 100 cycles	120
Figure 3.1 - Typical in-cylinder pressure trace.....	123
Figure 3.2 - Pressure sensors: regular and cooled, for high temperatures operating conditions.....	124
Figure 3.3 - Customized cylinder head with sleeves for pressure transducers (7.2 l Mercedes engine).....	124
Figure 3.4 - Mercedes engine: 1. flywheel, 2. housing, 3. crankshaft speed sensor.....	125
Figure 3.5 - Dynamic model of the crankshaft	126
Figure 3.6 - Lumped mass dynamic model of the single cylinder engine.....	130
Figure 3.7 - 3D drawing of the single cylinder engine (Catia V5).....	136
Figure 3.8 - FEM computation of the shaft stiffness (Catia V5).....	136
Figure 3.9 - Single-cylinder engine model validation: left (ULSD), right (S-8); measured speed (blue), simulated speed (red); the operating point is 1500 rpm and 4 Nm torque / 2.9 bar IMEP.....	137
Figure 3.10 - Gas pressure torque reconstruction by reverse calculation at 1500 rpm, 4 Nm torque: left (ULSD), right (S-8) engine torque (red), reconstructed engine torque (blue).....	145
Figure 3.11 - Cylinder pressure reconstruction by reverse calculation at 1500 rpm, 4 Nm torque: left (ULSD), right (S-25); measured cylinder pressure (Blue), reconstructed pressure from measured speed (Red).....	147

Figure 3.12 - Gas pressure torque reconstruction by direct recognition method: left (ULSD), right (S-25); engine torque (red), reconstructed engine torque (blue)..... 149

Figure 3.13 - Cylinder pressure reconstruction by direct recognition method: left (ULSD), right (S-25) reconstructed cylinder pressure (red), measured pressure (blue)..... 149

Figure 3.14a - Lumped mass dynamic model of a four-cylinder engine..... 150

Figure 3.14b - VM Motori 2.5 L engine dismantled in order to draw its moving parts..... 153

Figure 3.15 - VM Motori 2.5 L engine: drawing of the moving parts..... 154

Figure 3.16 - VM Motori engine: drawings of the moving parts..... 155

Figure 3.17 - VM Motori 2.5 L engine in motion..... 158

Figure 3.18 - Four cylinder pressures and average cylinder pressure variation (black curve) when idling at 1000 rpm (left) and 1500 rpm (right) on ULSD..... 158

Figure 3.19 - Engine speed variation idling 1000 rpm (left) and 1500 rpm (right): measured speed (blue), average speed (red), smoothed average speed (black) on ULSD 158

Figure 3.20 - Crankshaft angular acceleration at idling 1000 rpm (left) and 1500 rpm (right)..... 159

Figure 3.21 - Torques acting on the crankshaft when idling 1000 rpm (left) and 1500 rpm (right): gas pressure torque (red), inertia torque (magenta), resultant torque (cyan), reconstructed torque (blue)..... 159

Figure 3.22 - Reconstructed cylinder pressure (blue) and measured cylinder pressure (red) when idling 1000 rpm (left) and 1500 rpm..... 160

Figure 3.23 - Rates of heat release at cylinder #6 for ULSD, S-8, JP-8 and B-20 at 1500 rpm, 360 Nm / 7.5 bar IMEP (Mercedes 6-cylinder engine)..... 165

Figure 3.24 - Example of an even function: $f(x) = x^2$ 167

Figure 3.25 - Example of an odd function: $f(x) = x^3$ 167

Figure 3.26 - 0.7 L Deutz engine running on ULSD: Cylinder pressures at 1500 rpm and 4 Nm torque / 2.9 bar IMEP - motoring (green), combustion (red), total (blue) 170

Figure 3.27 - 0.7 L Deutz engine running on ULSD: Tangential gas pressures at 1500 rpm and 4 Nm torque/2.9 bar IMEP: motoring (green), combustion (blue), inertia (red), total (black)..... 171

Figure 3.28 - 0.7 L Deutz engine on ULSD: Tangential gas pressure at 1500 rpm and 4 Nm torque / 2.9 bar IMEP: total (red), simulated (blue), combustion (green), combustion simulated (magenta)..... 172

Figure 3.29 - 0.7 L Deutz engine on ULSD: Tangential combustion pressure at 1500 rpm and 4 Nm torque / 2.9 bar IMEP: total (green), simulated (magenta); SOC is at TDC..... 173

Figure 3.30 – 0.7 L Deutz engine on S-8: Tangential gas pressure at 1500 rpm and 4 Nm torque / 2.9 bar IMEP: total (red), simulated (blue), combustion (green), combustion simulated (magenta).....	174
Figure 3.31 – 0.7 L Deutz engine on S-8: Tangential combustion pressure for S-8 at 1500 rpm and 4 Nm torque / 2.9 bar IMEP: total (green), simulated (magenta); Start Of Combustion is at 7 CAD after TDC.....	175
Figure 3.32 – 2.5 L VM Motori multi-cylinder engine	176
Figure 3.33 – 2.5 L VM Motori 4-cylinder engine on ULSD at 2750rpm / 30 Nm torque: Cylinder pressures and individual contributions - compression (blue), combustion (cyan), total (red).....	177
Figure 3.34 – Detail for cylinder #1 of 2.5 L VM Motori engine on ULSD at 2750rpm / 30 Nm torque: Tangential gas pressures - compression (red), combustion (blue), total (cyan); SOC is at 10 CAD after TDC.....	178
Figure 3.35 – 2.5 L VM Motori 4-cylinder engine on ULSD at 2750rpm / 30 Nm torque: Inertia tangential pressures for each cylinder group: 1-4 (cyan), 2-3 (blue), resultant value (red).....	179
Figure 3.36 – The components of the engine torque for 2.5 L VM Motori 4-cylinder engine on ULSD at 2750rpm / 30 Nm torque: Inertia (red), motoring (blue), combustion (cyan), total (black).....	179

Figure 3.37 – 2.5 L VM Motori 4-cylinder engine on ULSD at 2750rpm / 30 Nm torque: Engine torque from measured cylinder pressure (black) and Engine torque estimated from measured crankshaft speed (red)..... 180

Figure 3.38 – 2.5 L VM Motori 4-cylinder engine on ULSD at 2750rpm / 30 Nm torque: Measured crankshaft speed (blue), averaged crankshaft speed (cyan), smoothed average speed: red 181

Figure 3.39 – 2.5 L VM Motori 4-cylinder engine on ULSD at 2750rpm / 30 Nm torque - Combustion pressure torque: calculated from pressure (cyan), estimated from speed (red)..... 182

Figure 3.40 – 2.5 L VM Motori 4-cylinder engine on ULSD at 2750rpm / 30 Nm torque - Combustion pressure torque: calculated from pressure (cyan), estimated from speed (red); Start of combustion estimation: 10 CAD after TDC..... 182

Figure 3.41 - 2.5 L VM Motori 4-cylinder engine on JP-8 at 1300rpm / 150 Nm torque: cylinder pressures and individual contributions - compression (blue), combustion (cyan), total (red)..... 183

Figure 3.42 - Detail for cylinder #1 of 2.5 L VM Motori engine on JP-8 at 1300rpm / 150 Nm torque: tangential gas pressures - compression (red), combustion (blue), total (cyan); SOC = 3 CAD after TDC..... 184

Figure 3.43 - 2.5 L VM Motori 4-cylinder engine on JP-8 at 1300rpm / 150 Nm torque: measured crankshaft speed (blue), averaged crankshaft speed (cyan), smoothed average speed (red)..... 185

Figure 3.44 - 2.5 L VM Motori 4-cylinder engine on JP-8 at 1300rpm / 150 Nm torque - Combustion pressure torque: calculated from pressure (cyan), estimated from speed (red) 186

Figure 3.45 - 2.5 L VM Motori 4-cylinder engine on JP-8 at 1300rpm / 150 Nm torque - Combustion pressure torque: calculated from pressure (cyan), estimated from speed (red); Start of combustion estimation: 3 CAD after TDC..... 186

Figure 3.46– Cummins 6-cylinder engine on ULSD at 1360rpm / 200 Nm torque - Cylinder pressures and individual contributions: compression (blue), combustion (green), total (red). The disturbance (red) of a firing cylinder (green) is higher here than in a four-cylinder engine..... 187

Figure 3.47 – Schematic representation of fuel identification from engine speed using artificial neural..... 189

Figure 3.48 – Neural network functional process..... 190

Figure 3.49 – Neural network structure: weights w , biases b , transfer functions f 191

Figure 3.50 – Neuron without bias..... 191

Figure 3.51 – Neuron with bias..... 191

Figure 3.52 – Examples of transfer functions 193

Figure 3.53 – Layer of neurons..... 194

Figure 3.54– Multiple layers of neurons..... 195

Figure 3.55– Neural networks types and complexity 196

Figure 3.56 – Network training back-propagation algorithm: Function signals propagates forward while error propagates backwards.....	197
Figure 3.57 – Network training algorithms; preferred is Levenberg – Marquardt	199
Figure 3.58 – Network input: the instantaneous measured crankshaft speed; Network output: not set yet.....	203
Figure 3.59 – Network output selection: in-cylinder pressure.....	204
Figure 3.60 – Measured pressure cyclic variations for all fuels: peak values.....	205
Figure 3.61 – Network training: an iterative adjustment of biases and weights to achieve a desired performance; in our case the goal was met in 7 steps (epochs).....	207
Figure 3.62 – Network over-fitting (overtraining) phenomenon: Properly fitted data – good generalization (left); overtrained data – poor generalization (right) according to S.Haykin.....	208
Figure 3.63 – Simulated pressure cyclic variations: peak values...	210
Figure 3.64 – Network testing: validation of simulation and fuel identification; blue decision lines between simulated peak pressures determine the fuel type; red decision lines between measured peak pressures decide whether it is True / False.....	211
Figure 3.65 – Network input: the instantaneous measured crankshaft speed; Network output: not set yet.....	213
Figure 3.66 – In-cylinder pressures cannot be selected as network output because their peaks are very close to each other.....	214

Figure 3.67 – Network output selection: rates of pressure rise..... 215

Figure 3.68 – Rate of measured pressure rise: cyclic peak values..... 217

Figure 3.69 – Network training: an iterative adjustment of biases and weights to achieve a desired performance; the goal was met in 2 steps (epochs)..... 218

Figure 3.70 – Simulated rate of pressure rise: cyclic peak values..... 219

Figure 3.71 – Network testing: validation of simulation and fuel identification. Blue decision lines between peaks of simulated rate of pressure rise determine the fuel type. Red decision lines between peaks of rate of measured pressure rise decide whether it is True / False..... 220

LIST OF ABBREVIATIONS

ANN = Artificial Neural Network

B-100 = 100% biodiesel

B-20 = blend of 20% biodiesel and 80% ULSD

BHP = Brake Horse Power

BSFC = Brake Specific Fuel Consumption

CAD = Crank Angle Degree

CSHVC = City-Suburban Heavy-Vehicle Cycle

DFT = Discrete Fourier Transform

ECU = Electronic Control Unit

EGR = Exhaust Gas Recirculation

EPA = Environment Protection Agency

FEA = Finite Element Analysis

FRF = Frequency Response Function

GC-MS = Gas chromatography mass spectrometry

Gas Pressure Torque = indicated engine torque (see Chapters 1 and 5)

IMEP = Indicated Mean Effective Pressure

JP-8 = Jet Propellant 8 kerosene-based fuel JP-8 fuel (see Chapter 2)

MBRC = Miles Between Road Calls

MFB50 = the moment at which 50% of the mass fraction has burned during combustion

MLP = Multi Layer Perceptron

PAH = Polycyclic Aromatic Hydrocarbons

PFI = Ported Fuel Injection

PPM = Parts Per Million

RHR = rate of heat release

RME = Rapeseed Methyl Ester

RMSE = Root Mean Square Error

RPM = Revolutions Per Minute (average engine speed)

S-8 = Synthetic fuel 8 or synthetic jet A fuel (see Chapter 2)

S-25 = Synthetic fuel having cetane number 25

TC = Turbo-Charger

TDC = Top Dead Center

ULSD = Ultra Low Sulfur Diesel

VOC = Volatile Organic Compound

ZDDP = Zinc-Dialkyl-Dithio-Phosphate

CHAPTER 1

THE EFFECTS OF ALTERNATIVE FUELS ON ENGINE OPERATION.

FUEL IDENTIFICATION METHODS

- Literature Review -

1.1 Introduction

The flexibility of running safely multiple fuels on an engine is a desirable but also a challenging task. For commercial vehicles, this task is supported in the first place by the necessity to eliminate the dependency on foreign oil. For military vehicles this flexibility is a big advantage, allowing them to run properly on any fuel accessible on the battlefield. Furthermore, the use of alternative and renewable fuels has great potential to increase energy sustainability.

On the other hand, various fuels have various physical and chemical properties that affect the combustion process. Examples of such characteristics are density, heating value, viscosity, octane / cetane number, volatility, bulk modulus. As a consequence, when a vehicle is being supplied with a different fuel, its properties should be automatically identified and the injection control strategy modified so that the engine operation is optimally adjusted to that particular fuel without affecting power, fuel consumption and emissions. In these conditions on-board fuel

identification and adaptation of engine controls to the type of fuel becomes extremely important.

1.2 The effects of alternative fuels on engine operation

The fuels studied in this work are ULSD (Ultra-Low-Sulfur-Diesel), synthetic fuel S-8, jet propellant fuel JP-8 and bio-diesel. Their physical and chemical properties are presented in Chapter 2 of this work.

One of these fuels, JP-8, is an aviation grade fuel derived from petroleum, while other aviation grade fuels, such as S-8, are derived from Fischer-Tropsch gas-to-liquid process. JP-8 has been preferred by the US Army because its Single Fuel Forward (SFF) policy requires the use of a single fuel for both air and ground tactical vehicles.

Papers such as C.Jayakumar et.al. [1] and [3], J.Nargunde et.al. [2] analyze in detail how the engine performance, fuel economy and emissions levels change with the change in the type of fuel.

A combustion parameter that is specific to a certain fuel is its ignition delay. Tests have demonstrated that even though JP-8 is more volatile than biodiesel, the latter ignites faster because of its higher cetane number (CN). CN variability of JP-8 is explained by the presence of the heavier chains of 18 carbon atoms in its molecule which are more than the average

chains length of S-8, B-100 and ULSD. The heavier molecules of biodiesel break-up faster than the lighter carbon molecules of the other three combustible mixtures. Unlike them, biodiesel has no aromatic content hence no strong bonds in its composition that would require much energy to split-up. Not only the cetane number, but also the fuel volatility plays an important role in the auto-ignition process according to C.Jayakumar et.al. [1]. For example, despite the fact that JP-8 has a smaller cetane number than ULSD, the ignition delay of JP-8 is shorter due to its faster rate of evaporation and faster mixture formation as said by J.Nargunde et.al. [2].

Regarding the combustion process, by comparing the rates of heat release RHR curves, biodiesel has the lowest peak mainly because of its lowest heating value as presented by C.Jayakumar et.al. [1]. On the other hand, ULSD, with longer ignition delay, which means more time for mixture formation, and with higher density, has the highest RHR peak.

Biodiesel produces the largest diffusion controlled combustion fraction at all injection pressures compared to ULSD, JP-8 and S-8. That can be explained by the presence of heavier compounds in its molecules, up to C18, which start to burn later as compared to the lighter fractions in the premixed phase.

Fuel consumption is generally inversely correlated to the heating value of each fuel: the greater the heating value, the lower the fuel consumption. From this point of view the best fuel economy is achieved by S-8, followed by JP-8, ULSD and finally by biodiesel. A good indicator for fuel economy is the temperature in the exhaust too: the lower, the better meaning complete combustion. Per comparison with JP-8, the lower volatility and the less atomized sprays of ULSD contribute in reducing its combustion efficiency. Thus more heat (useful energy) is rejected in the exhaust and its fuel consumption increases in accordance with J.Nargunde et.al. [2].

In contradiction to the general observations in literature, NO_x emissions for biodiesel can be lower than for other fuels if the combustion phasing (the location of the peak of premixed combustion of the rate of heat release) is kept constant for all tested fuels in compliance with C.Jayakumar et.al. [1]. This condition means in fact that, for a certain operating point, the engine run is optimized for that particular type of fuel. The results in literature about the increase of NO_x with biodiesel use are valid if biodiesel is simply poured into the tank and the engine, usually optimized for ULSD, runs with its stock ECU. If the engine controls are optimized for biodiesel, then the NO_x emissions would decrease. For the

tests performed by C.Jayakumar et.al. [1], on average, biodiesel produced 37% less NO_x emissions compared to other fuels. However, ULSD produces more NO_x than JP-8 because of its higher aromatic content that generates higher flame temperatures, responsible for the formation of nitrogen oxides as stated by J.Nargunde et.al. [2].

HC and CO emissions are usually the products of an incomplete combustion. They are lower for biodiesel because its later combustion leads to higher temperatures in the expansion stroke, causing additional burning of such species. Also, due to the presence of oxygen atom in its molecules, the oxidation reactions are enhanced according to C.Jayakumar et.al. [1]. HC and CO are also lower for S-8 and JP-8 than for ULSD because of their higher volatility and ability to form enhanced combustible mixtures as demonstrated by J.Nargunde et.al. [2].

Concerning the particulate matter PM, bio-diesel produces the highest number of NMPs (Nucleation-Mode-Particles) among all fuels. Its enhanced soot oxidation minimizes the adsorption of SOFs (Soluble-Organic-Fractions), responsible for nano-particle formation. ULSD produces the highest AMPs (Accumulation-Mode-Particles) because of its highest aromatic content, widely known as a soot precursor according to J.Nargunde et.al. [2].

Of the four fuels considered in this work, biodiesel has a minimal impact on the environment. A thorough analysis has been performed on how it affects engine performance, emissions levels and last, but not least, engine wear and operating costs.

The first question regards whether nitrogen oxides NO_x , an aggressive factors against the Earth's protective layer of ozone, will always be higher ; the second question is whether carbon monoxide CO , a poisonous gas, and hydrocarbons HC , a contributing factor in the formation of smog, and particulate matter PM , a human health hazard when inhaled, will be lower; finally, it is not sure how PAH (Polycyclic Aromatic Hydrocarbons), widely recognized as potential cancer causing

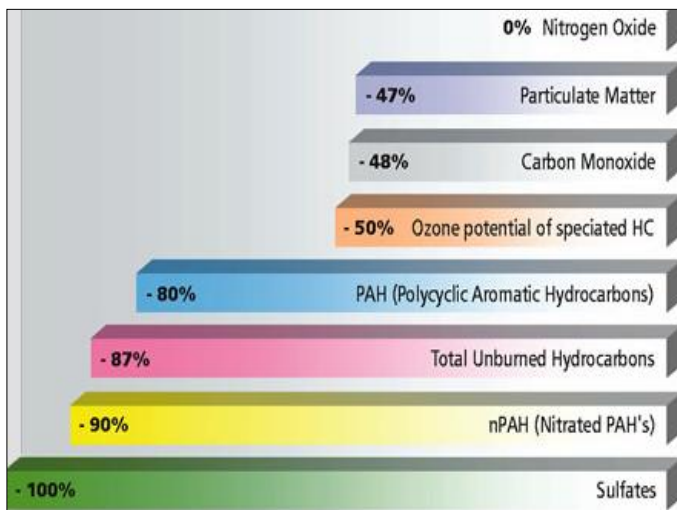


Figure 1.1 - Biodiesel emission reductions by B. McCormick [4]

compounds, will develop. Several papers on this topic have been published, and interesting conclusions have been drawn: when switching from regular diesel to biodiesel, all regulated exhaust gas emissions such as CO , HC , PM

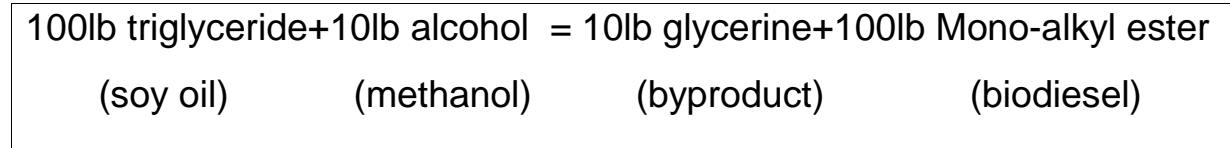
decrease, with the exception of NO_x which slightly increase. Moreover, all can be reduced if the maps of the ECU (Electronic Control Unit), an on-board computer by which an engine operates, are adjusted by the manufacturer to the new fuel characteristics.

Biodiesel is the first and only alternative fuel to have a complete evaluation of emission results and potential health effects submitted to the EPA (Environmental Protection Agency) under the Clean Air Act Section 211 (b). These programs include the most stringent emissions testing protocols ever required by the EPA for the certification of fuels or fuel additives in the U.S.

It is still unclear whether conventional pollutants increase or decrease with biodiesel use. This lack of information is a major barrier to its market penetration and acceptance. Papers such as B. McCormick et.al. [4-12] provide a thorough analysis and bring more light on this issue.

In order to understand what comes out of an engine tailpipe must be known the composition and physical properties of the fuel used. Biodiesel represents mono-alkyl esters of fatty acids like methyl or ethyl esters. It is not vegetable or used cooking oil and must meet the quality requirements of standard ASTM D6751.

One of biodiesel's formation reactions, e.g. from soybean, is as follows in compliance with B.McCormick [4]:



Compared to ULSD (Ultra Low Sulfur Diesel), used since 2007, biodiesel has a higher molecular weight. It is less volatile meaning that it evaporates more slowly and it ignites faster due to its higher cetane number. Its chemical composition includes molecules varying from C7 to C18, unlike ULSD with a more compact range between C7 to C12.

Biodiesel's higher cetane number and molecular weight impact the combustion process significantly, which starts earlier but cannot develop as consistently as in the case of ULSD because lighter fractions of biodiesel that sustain combustion burn quickly. The combustion extends more into the expansion stroke where heavier components come into play. This late burning has another positive aspect such as the extended burning of HC. Also, the oxygen atom in its molecule favors the formation of the NO_x species. These two examples show us how important the fuel properties are. Regarding the use of biodiesel on series vehicles, most manufacturers, such as General Motors, Ford, Cummins, John Deere are generally comfortable with biodiesel blends up to 5% and 95 % regular diesel, due to

environmental and engine warranty issues - Table 1.1.

Other manufacturers, such as Daimler (former Detroit Diesel) or Caterpillar, who adjusted their electronically-controlled injection strategies specifically to biodiesel, are able to withstand percentages such as 20 % and higher.

Engine emissions have been controlled in various ways as stated by B. McCormick [4] such as fuel injection timing retard to reduce NO_x , higher injection pressure, for a better fuel atomization and mixing, to reduce PM and EGR (Exhaust Gas Recirculation) to further decrease NO_x . Particle filters and catalyst systems have come into play later, to drastically reduce PM emissions, CO, HC and NO_x respectively. All these systems require ULSD as fuel with 15 ppm (parts per million) sulfur only.

According to EPA the emissions levels by 2012 are required to be:

}	NO_x	= 0.2 g / BHP * hr
	PM	= 0.01 g / BHP * hr
	NMHC (non-methane HC)	= 0.14 g / BHP * hr
	THC (total hydrocarbon)	= 1.3 g / BHP * hr
	CO	= 15.5 g / BHP * hr,

which, according to specialists, are very tight.

Manufacturer	Biodiesel percentage approved to run on engines	Operational criteria
Caterpillar	Many engines approved for B100, others limited to B5	Must meet ASTM D6751
Cummins	All engines approved for up to 5% biodiesel	Must meet ASTM D6751
Daimler (former Detroit Diesel)	Approved up to 20% biodiesel	Must meet DDC specific diesel fuel specifications
Ford	Up to 5% biodiesel	Must meet both ASTM D6751 and EN 14214
General Motors	All engines approved for up to 5% biodiesel	Must meet ASTM D6751
John Deere	All engines approved for 5% biodiesel	Must meet ASTM D6751
Fuel Injection Equipment		
Bosch	Up to 5% biodiesel	Must meet EN 14214
Delphi	Up to 5% biodiesel	Must meet ASTM D6751

Table 1.1 - Percentage of biodiesel blends approved by manufacturers in accordance with B. McCormick [4]

At the same time, the EPA issued a technical report regarding biodiesel impact on exhaust gas emissions, according to which NO_x increase and PM, HC and CO decrease, as presented in Figure 1.2.

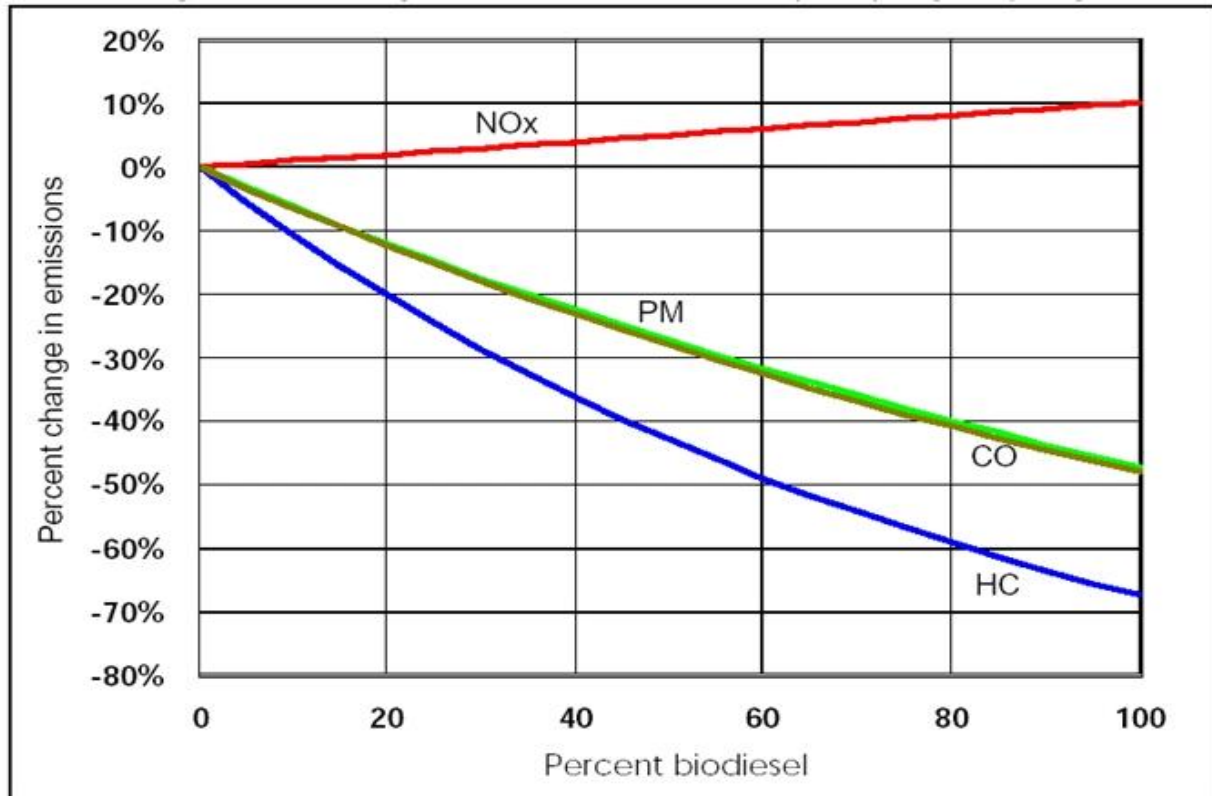


Figure 1.2 - Change in regulated emissions with increase of biodiesel percentage as presented by B. McCormick [4]

The average values for B0...B100 that the EPA obtained as a percent change in emissions were as follows [4]:

NO_x = + 2.0 %

PM = - 10.1 %

HC = - 21.1 %

CO = -11.0 %.

For soybean-based B-20 the emission impact was as follows:

- NO_x: no change for B5 ; 2% up for B-20 ; 10% up for B100
- PM : 5% down for B5 ; 12% down for B-20 ; 48% down for B100.

The effects of biodiesel on NO_x emissions are presented in Figure 1.3 and are divided into two engine categories:

- typical Older Engines (thru 1997): B-20 = +2%, B100 = +10%
- newer Engines (2004 compliant): B-20 = +4%, B100 = +30%

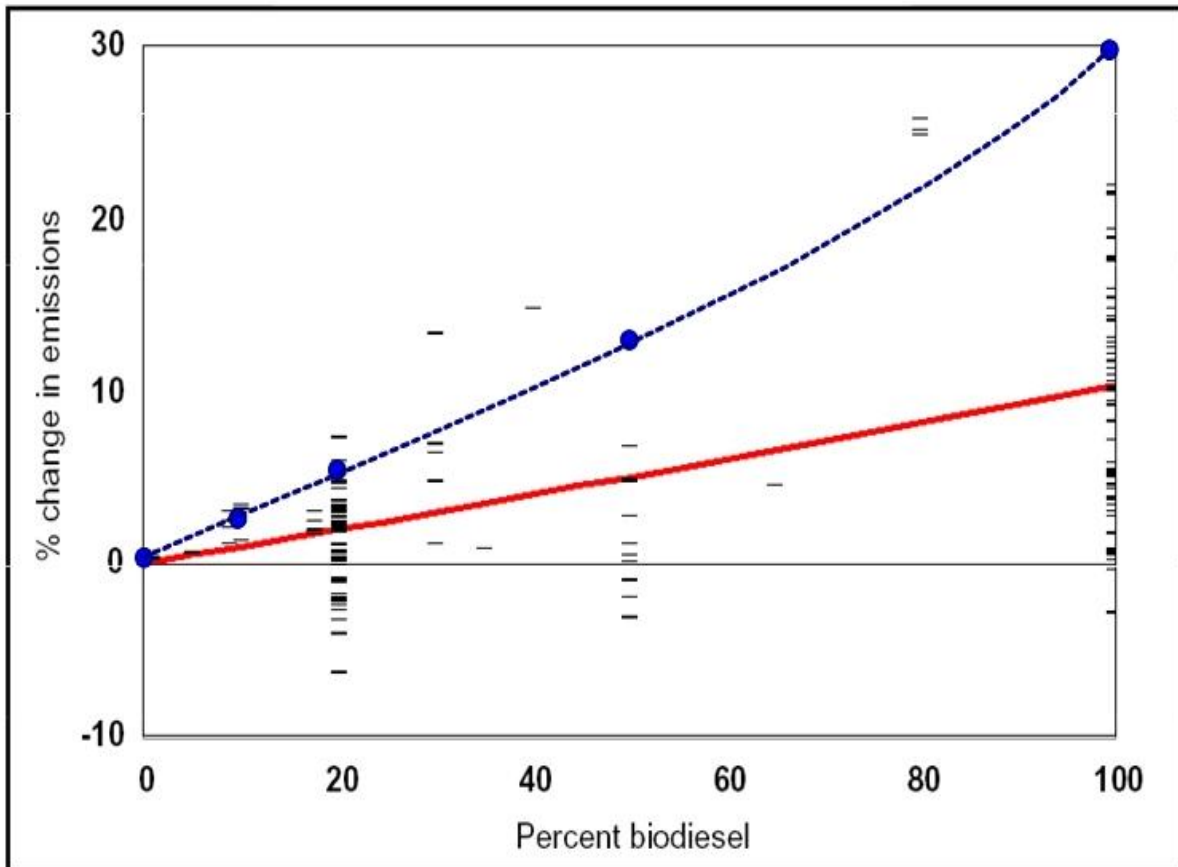


Figure 1.3 - Change in NO_x emissions with increase of biodiesel percentage according to [4]: red = older engines; blue = newer engines

As a first conclusion the use of biodiesel blends can significantly reduce PM and toxic compound emissions, but may slightly increase NO_x , both partially explained by the content of oxygen by weight, 10 %. It should not be forgotten though that these values were obtained on engines with an optimized, but closed, on-board computer for diesel fuel. NO_x levels can decrease if the computer maps are adjusted to biodiesel.

Experimental data and detailed conclusions are given by Kennteh Proc et.al. [5]: nine transit buses have used B-20 and diesel fuel for two years. Five of them operated on B-20 (20% biodiesel blend) and the other four on regular diesel. The buses were model year 2000 Orion V equipped with Cummins ISM engines, and all operated on the same bus route. Each bus accumulated about 100,000 miles over a 24-month period of study.

The data show that for these vehicles on this test cycle, operation on B-20 reduced all regulated pollutants, including NO_x . This may not be so surprising since, according to N.Eyre et.al. [9], an increase in the cetane number from 40 (diesel) to 47 (biodiesel), may lead to a reduction of NO_x by 3%. Even though a slightly lower energy per gallon was noticed between regular diesel and B-20, the thermal efficiency and the maintenance cost of fuel pump and injectors remained unchanged. Chassis dynamometer emissions testing selected cycle was the CSHVC (City-Suburban Heavy-

Vehicle Cycle) because the parameters of this cycle are a close match to the actual bus route. The B-20 buses were compared to the petroleum diesel buses in terms of:

- 1) Mileage accumulation: it was similar for both groups of 4 diesel buses and 5 B-20 buses, averaging 4,000 miles/month
- 2) Fuel economy: there was no difference among the diesel group (4.41 mpg) and the B-20 group (4.41 mpg)
- 3) Vehicle maintenance. The cost per mile was calculated as follows:

$$\text{Cost per mile} = ((\text{labor hours} * \$50) + \text{parts cost}) / \text{mileage}$$

The results were 5.2% lower for B-20: \$0.51 vs. \$0.54 for Diesel group. It was interesting that the money spent for the replacement of the fuel system parts was much higher for the B-20 group, \$6293, than for the Diesel group, \$1763. Further analysis is necessary to determine if B-20 use is related to that.



Figure 1.4 - Plugged B20 fuel filter in accordance with Kennteh Proc et.al. [5]

4) Road calls and average MBRC (Miles Between Road Calls) are an

important reliability indicator for the transit industry. Average MBRC-s over

24 months were 14% higher for the B-20 buses: 3,197 for diesel and 3,632 for B-20 groups, respectively. This was considered a beginning settlement period because after 24 months of evaluation there was no negative impact on MBRC from the use of B-20. Three buses though reported road calls for engine misfiring and stalling caused by plugged fuel filters. Gas chromatography mass spectrometry (GC-MS) suggested that high levels of plant sterols, with much higher molecular weight, might be responsible for the filter plugging.

5) Fuel analysis made by FTIR (Fourier Transfer Infrared spectroscopy) showed that the fuel from each delivery truck offloaded into the storage tank appeared to have been completely blended, resulting in B-20 and showing reductions in fuel sulfur content as well as in energy content by 2.4%. The B-20 blends exhibited significantly higher cetane number, having a shorter ignition delay and more time for the combustion to complete.

6) Oil analysis for the two fuels was made in terms of:

- ZDDP (ZinC-Dialkyl-Dithio-Phosphate), the dominant anti-wear agent which decays but with no significant difference involving the two fuels;
- TBN (Total Base Number) related to the lubricant's reserve capacity of neutralizing acids; it decays more slowly for the B-20 blends;
- Oxidation, which grows exponentially with mileage; no difference was

observed between the two fuels;

- Fuel dilution in oil: low in all cases, lower for the B-20 blends;
- Viscosity: did not decay significantly during the oil drain interval for either group of vehicles;
- Soot loading: about 50% lower on average in the B-20 lubricant samples;
- Wear metals: calcium, zinc, and phosphorus do not exhibit any trend with mileage
- Sodium levels: they were low in all cases indicating no coolant leak or contamination with high soap content, therefore no discernable difference was found.

7) Pollutant emissions – the tests conducted showed that the operation on B-20 reduced all regulated pollutants, including NO_x. Fuel consumption, on a mpg basis, has increased by roughly 2% in agreement with the lower energy content of B-20.

Because little information is available on the impact of biodiesel on engine operating costs and durability, some authors focused their research mostly on engine wear and operability. This lack of information is a major barrier to B-20 market penetration and acceptance.

Eight engines, four Mack E7-300 and four Ford 7.8 L, and fuel systems as stated by Richard Fraer et.al. [6] were removed from trucks that had

operated on B-20 or diesel to compare wear characteristics after four years of operation and more than 600,000 miles accumulated -Table 1.2.

USPS Truck Number	VIN	Vehicle Mileage at Teardown	Engine Make/Model	Engine Number in Teardown
6610170	1M1K194Y0VM009162	364,514	Mack E7-300	Mack #1
6610131	1M1K194Y1VM009123	395,584	Mack E7-300	Mack #2
6610209	1M1K194Y6VM009201	384,464	Mack E7-300	Mack #3
6610191	1M1K194Y8VM009183	339,916*	Mack E7-300	Mack #4
1891990	1FDXH81A4DVA17292	343,185	Ford 7.8L	Ford #1
1892111	1FDXH81A8PVA21037	377,272	Ford 7.8L	Ford #2
1892158	1FDXH81A6PVA23644	351,967	Ford 7.8L	Ford #3
1892193	1FDXH81AXPVA25350	347,803	Ford 7.8L	Ford #4

* Engine was rebuilt at 144,687 miles (mileage since overhaul is 195,229).

Table 1.2 - USPS study vehicle information according to [6]

The results indicate there was little difference that could be attributed to fuel in operational and maintenance costs. At any rate, vehicles operated on B-20 exhibited higher frequency of fuel filter and injector nozzle replacement accompanied by a sludge build-up around the rocker assemblies. The vehicle mileage at teardown ranged from 343,185 to 395,584. The results of the evaluation are summarized in four general areas, which represent the overall condition of the engines:

- Cylinder heads and combustion chambers
- Cylinder block and crankcase
- Lubrication system
- Fuel system

Regarding the Mack tractors, after examining the cylinder block, the crankcase and the lubrication system, no significant differences were found between the B-20 and diesel engines. The cylinder heads of the B-20 engines contained a heavy amount of sludge thick and gel-like



Figure 1.5 - B20 valve deck sludge accumulation according to Richard Fraer et.al. [6]

on the valve deck around the rocker assemblies - Figure 1.5. The sludge contained 1.3% - 2.4% bio-derived carbon, an order of magnitude above the level observed in the motor oil. The presence of a measurable renewable component in the sludge supports the idea that the biodiesel fuel is involved in the sludge formation. As it concerns the fuel system, the fuel pumps did not show any difference but the injectors, however, did. The injector nozzles from B-20 were not within the specified leak-down limits and the required replacement; the fuel filter-plugging was another problem.

No significant differences were noted in the teardown of the Ford vehicles: cylinder heads, combustion chambers and fuel systems. No issues were found with the lubrication systems and the oil pumps. In addition,

both B-20 Ford and Mack tractors had essentially the same maintenance costs as the petroleum diesel tractors. Further research and analysis is necessary to determine the susceptibility of different engine and vehicle types to B-20-related operating issues.

Other researchers such as A.Tsolakisa, A.Megaritisb et.al. [7] used biodiesel obtained from RME (Rapeseed Methyl Ester) and different diesel / RME blends on a single-cylinder diesel engine to further explore the effects on NO_x emissions, smoke, fuel consumption, engine efficiency, cylinder pressure and net rate of heat release.

Various blends such as B-20, B-50, pure ULSD and pure RME biodiesel with various properties have been tested under different loads, speeds and EGR rates – Tables 1.3,1.4 and 1.5.

Fuel analysis	Method	Ultra-low sulphur diesel (ULSD)	Rapeseed methyl ester (RME)
Cetane number	ASTM D613	53.9	54.7
Density at 15 °C (kg/m ³)	ASTM D4052	827.1	883.7
Viscosity at 40 °C (cSt)	ASTM D445	2.467	4.478
50% distillation (°C)	ASTM D86	264	335
90% distillation (°C)	ASTM D86	329	342
LCV (MJ/kg)		42.7	39
Sulphur (mg/kg)	ASTM D2622	46	5

Table 1.3 - Fuel properties according to A.Tsolakisa, et.al. [7]

Fuel	ULSD vol. (%)	ULSD mass (%)	RME vol. (%)	RME mass (%)
ULSD	100	100	0	0
B20	80	78.9	20	21.1
B50	50	48.3	50	51.7
RME	0	0	100	100

Table 1.4 - ULSD and RME volume and mass percentages of the tested fuel mixtures according to A.Tsolakisa, et.al. [7]

Engine condition	Speed (rpm)	IMEP (bar)	Torque (Nm)	Fuel
1	1500	4.5	20	ULSD B20 B50 RME
2	1500	6.1	30	ULSD B20 B50 RME

Table 1.5 - Engine conditions and fuel mixtures tested according to A.Tsolakisa, et.al. [7]

The results were similar to those published by the Environment Protection Agency - Figure 1.6. NO_x increase and CO, HC and soot decrease. When oxygen is available, soot precursor species react with molecular oxygen or oxygen-containing radicals, such as OH, O, and eventually produce CO rather than aromatics and soot. The reduction of smoke can also be attributed to the significantly lower sulfur content of RME, 5 mg/kg, compared to that of ULSD, 46 mg/kg as demonstrated by A.Tsolakisa, A.Megaritis et.al. [7]. CO decreases due to advanced injection timing with the use of biodiesel and oxygen availability.

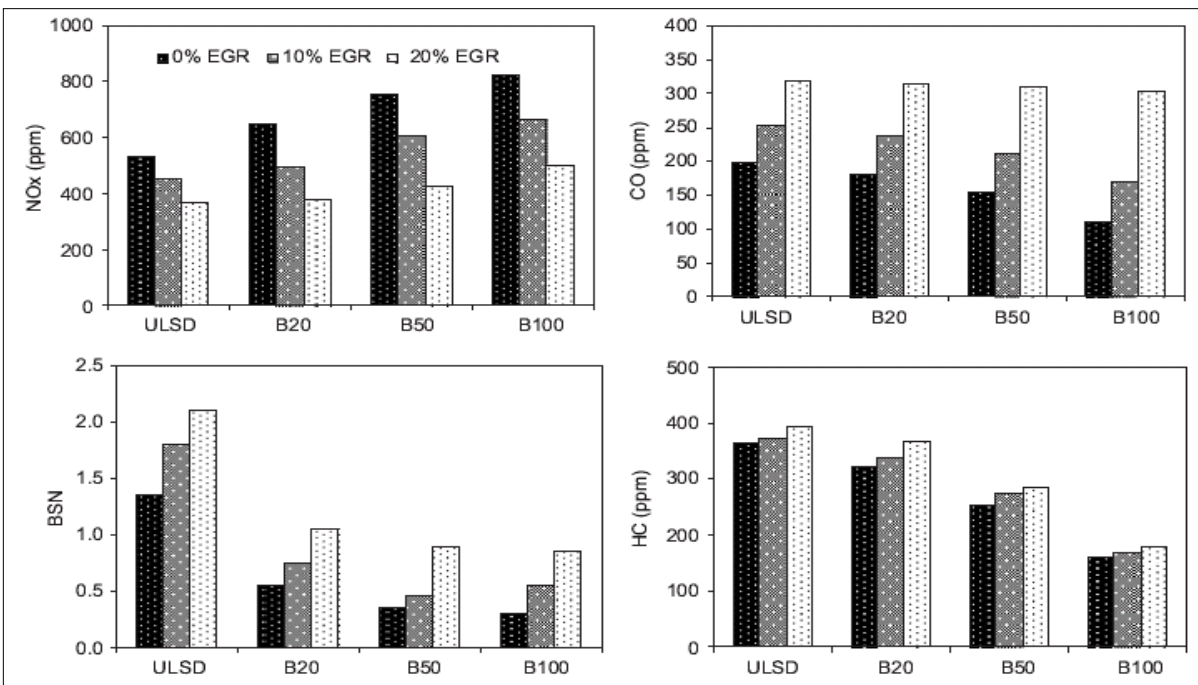


Figure 1.6 - Effects of fuel blend composition and EGR on engine exhaust emissions IMEP 4.5 bar reproduced from A.Tsolakisa, A.Megaritis et.al. [7]

The BSFC (Brake Specific Fuel Consumption) increased due to lower

calorific value of RME bio-diesel, 39 MJ/Kg, compared to 42.7 MJ/Kg of ULSD. That leads to higher flow rates, higher mass rates because of higher RME bio-diesel density, 883.7 kg/m³, as compared to ULSD, 827.1 kg/m³ as demonstrated by A.Tsolakisa, A.Megaritisb et.al. [7]. Thus, even though thermal efficiency was mostly unchanged, the BSFC was higher for RME bio-diesel.

The EGR was more effective when using RME bio-diesel than when using ULSD due to a higher reduction of NO_x with a lower increase in smoke, HC, and CO. The biodiesel NO_x emissions dropped to values similar to ULSD with the same EGR percentage while the smoke levels were kept at considerably lower values as presented by A.Tsolakisa, A.Megaritisb et.al. [7]. The use of EGR in the case of the bio-diesel fuelled engine resulted in the increase of the ignition delay and shifted the start and the end of combustion to later stages in the compression stroke and in the expansion stroke, respectively.

The RME biodiesel injection pressure increased because of the higher bulk modulus, which means less fuel compressibility than for the ULSD and faster fuel pressure build-up. Faster pressure waves are also due to the higher biodiesel density. All these factors result in higher injection pressures. Because the viscosity of biodiesel is almost

double than that of ULSD, meaning less fuel losses, then higher rates of fuel pressure rise for the same CAD interval are achieved and an earlier start of injection is obtained. Moreover, biodiesel has a higher cetane number, hence the rate of fuel burnt in the premixed phase increases, leading to higher in-cylinder pressures and temperatures as compared to ULSD. The overall biodiesel combustion duration is smaller due to its lower calorific value that cannot sustain the burning process like ULSD does – Figure 1.7. The retardation of the injection timing resulted in reduced NO_x emissions and in increased smoke, CO and HC emissions, due to an incomplete combustion, but did not affect

significantly the fuel consumption and the engine efficiency.

An 80,000-km durability test has been performed according to Yang Hsi-Hsien et.al. [8] on two new Mitsubishi 4 cylinders 2.8 l engines,

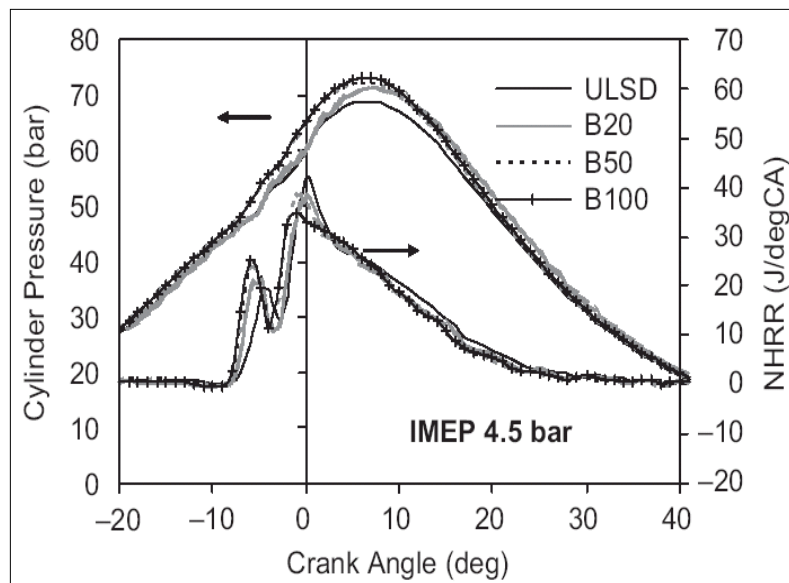


Figure 1.7 - Cylinder pressure and net heat release rate at 4.5 bar IMEP according to A.Tsolakisa, A.Megaritisb et.al. [7]

turbocharged, with indirect injection, using diesel and biodiesel, in order to examine the following exhaust gas emissions in both cases: CO, HC, NO_x, PM, and PAHs (Polycyclic Aromatic Hydrocarbons). HC was analyzed continuously using a HORIBA FIA-125 heated flame ionization detector. CO and CO₂ were analyzed by a non dispersive infrared instrument (HORIBA AIA-120) and NO_x by chemiluminescence using a HORIBA CLA-155.

Steps	Rotational speed (rpm)	Throttle width (%)	Duration (min)
Start	800	0	4.0
Warm-up	1500	25	6.0
	2000	50	3.0
Accumulation	3700	100	780
Shutdown	2000	50	3.0
	1500	25	6.0
	800	0	4.0

Table 1.6 - Durability test cycle specifications according to [8]

The test procedure consisted of four steps – Table 1.6: start, warm-up, accumulation and shutdown. After warm up, the engine was run at maximum speed of 3700 rpm for 13h every day until the durability test equivalent of 500h had accumulated. The accumulation duration can be converted to the actual mileage accumulation based on the fuel consumption rate. For example, the accumulation durations of

0, 125, 250, 375 and 500 h are nearly equivalent to 0, 20,000, 40,000, 60,000 and 80,000 km, respectively. The specifications of both fuels are listed in Table 1.7.

Fuel parameters	B20	Diesel	Analytical method
Density (g ml ⁻¹ at 15 °C)	0.84	0.83	ASTM D4052
Flash point (°C)	97	78	ASTM D93
Viscosity (CST at 40 °C)	3.53	3.15	ASTM D445
Carbon residue (mg g ⁻¹)	<0.01	<0.01	ASTM D4530
Cetane index	55.7	53.1	ASTM D613
Ash (wt%)	<0.001	<0.001	ASTM D482
Lubricity (µm)	196	332	HFRR-diesel lubricity test
Corrosiveness	1A	1A	ASTM D130
Water and residue (vol%)	<0.0005	<0.0005	ASTM D2709
Sulfur (ppmw)	20.5	21.8	ASTM D5453
Heat value (kcal kg ⁻¹)	9978	10234	ASTM D240

Table 1.7 - B20 and diesel specifications in accordance with Yang Hsi-Hsien et.al. [8]

The viscosity of B-20, 3.53 CST, is higher than that of diesel, 3.15 CST as presented by Yang Hsi-Hsien et.al. [8]. An important finding was

that “the higher viscosity of biodiesel can reduce atomization and cause higher air-pollutant emission after long-term operation”, as M.Pugazhivadivu and K. Jeyachandran claimed in [10]. Emission levels of HC, CO and PM at the beginning of the durability test were lower for B-20 (blend of 20% biodiesel and 80% diesel) than those for diesel. But after running for 20,000 km and longer, the emission levels became higher for B-20 as said by Yang Hsi-Hsien et.al. [8].

Fuel with higher viscosity tends to cause deposits in injectors, pump parts and chambers of the engine, which may result in the incomplete combustion of fuel as compliance with M.A.Kalam and H.H.Masjuki [11]. The higher viscosity of B-20 is one cause for higher air-pollutant emissions for long-term driving compared to diesel. The emissions of HC and CO for B-20 were, therefore, higher than those for diesel after long-term driving.

The deterioration coefficient is the value of the emission factor at 80,000 km divided by the emission factor at 20,000 km:

- for diesel, the deterioration coefficients of HC, CO, NO_x and PM were 0.81, 0.94, 0.93 and 1.04, respectively – Figure 1.8;

- for B-20, the deterioration coefficients were 1.01, 0.98, 0.96 and

1.3 for HC, CO, NO_x and PM, respectively.

A deterioration coefficient higher than 1.0 implies that air-pollutant emissions after 80,000 km of driving would be of higher values than those at 20,000 km. The above results indicate that after 80,000 km of driving, PM emission for diesel, HC and PM emission for B-20 increased.

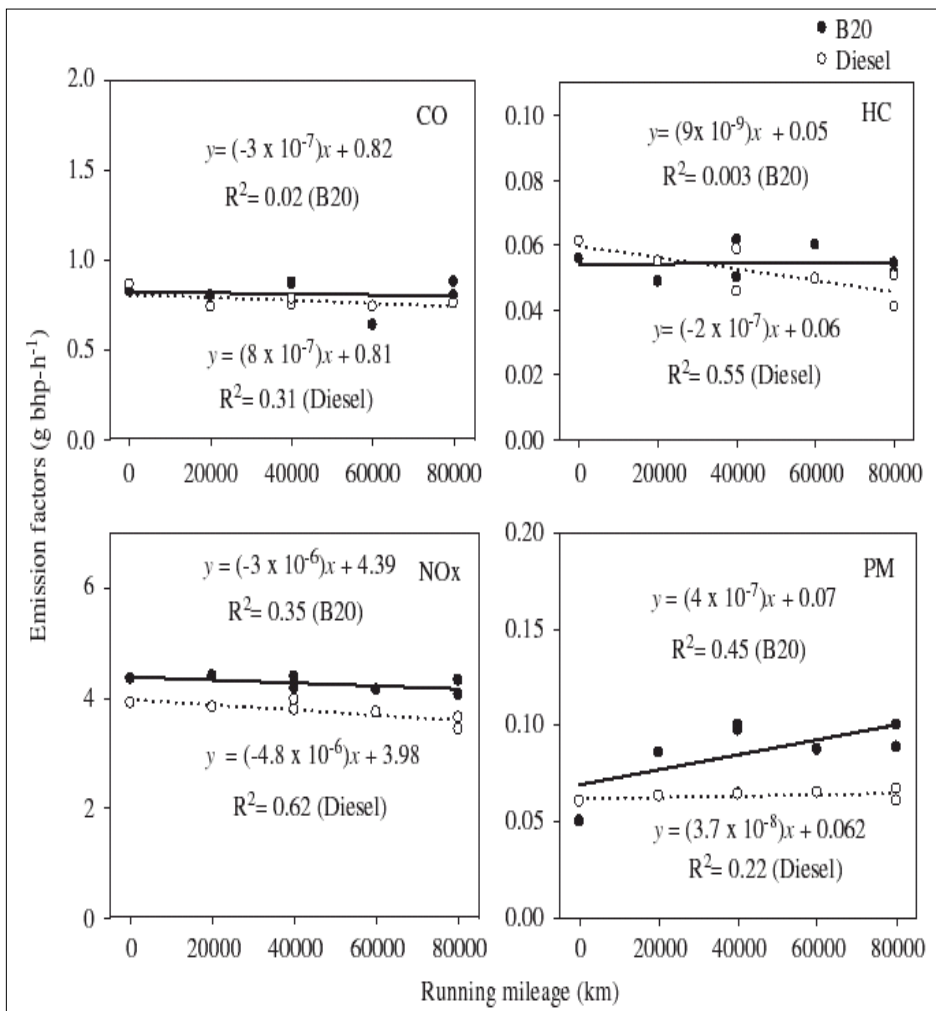


Figure 1.8 - Emission factors of regulated air pollutants determined by engine durability test according to Yang Hsi-Hsien et.al. [8]

Regarding the PAHs air-pollutant emissions, B-20 has lower PAH emission levels than for diesel fuel as demonstrated by Yang Hsi-Hsien et.al. [8]. However, particulate PAH emissions increased for B-20 as the mileage increased. Statistical analysis results show that B-20 would cause higher particulate PAH emissions with long term driving.

As for its suspected toxicity, 68.7% reduction was achieved in total BaP_{eq}, equivalent Benzo(a)Pyrene emissions when B-20 was used as a fuel. These results show that B-20 can reduce not only PAH emission factors, but also their corresponding carcinogenic potential.

A number of studies investigating the comparison of tailpipe emissions have been conducted by N.Eyre et.al. [9]. Biodiesel marginally reduces carbon monoxide (CO), hydrocarbon (HC) and particulate matter (PM) emissions. Other species, like carbon dioxide (CO₂), are effectively reduced to zero, as are sulfur dioxide (SO₂). Nonetheless, when using biodiesel, nitrogen oxide (NO_x) emissions are slightly higher. The test results shown in Table 1.8 are from a study conducted by G.S Hitchcock et al. in 1998 in the UK.

<i>Vehicle</i>	<i>Fuel</i>	<i>CO₂</i> <i>(g/km)</i>	<i>CO</i> <i>(g/km)</i>	<i>HC</i> <i>(g/km)</i>	<i>NO_x</i> <i>(g/km)</i>	<i>SO₂</i> <i>(g/km)</i>	<i>PM</i> <i>(g/km)</i>
<i>Car</i>	Conventional Diesel	139	0.42	0.08	0.64	0.05	0.15
<i>Car</i>	Biodiesel	0	0.37	0.07	0.77	0	0.13
<i>Light Goods Vehicle</i>	Conventional Diesel	267	1.33	0.33	1.39	0.09	0.24
<i>Light Goods Vehicle</i>	Biodiesel	0	1.16	0.24	1.67	0	0.24
<i>Heavy Goods Vehicle</i>	Conventional Diesel	853	3.92	0.45	13.06	0.28	1.07
<i>Heavy Goods Vehicle</i>	Biodiesel	0	2.63	0.36	15.02	0	0.72
<i>Bus (old)</i>	Conventional Diesel	1119	16.04	5.03	15.86	0.38	1.55
<i>Bus (old)</i>	Biodiesel	0	10.75	4.03	18.24	0	1.04
<i>Bus (new)</i>	Conventional Diesel	885	4.26	0.44	14.09	0.29	1.06
<i>Bus (new)</i>	Biodiesel	0	2.86	0.35	16.21	0	0.71

Table 1.8 - Tailpipe emissions from road vehicles using biodiesel and conventional diesel for the UK, G.S Hitchcock et al. 1998 [9]

M. Kaltschmitt et al. in Germany in 1997 [9], obtained similar levels of CO, HC, NO_x, and PM, using biodiesel and conventional diesel. The net CO₂ was reduced to zero.

It is known that PM emissions have a link with respiratory diseases in humans. Biodiesel is biodegradable and non-toxic and can be used in populated areas to maintain a healthy environment. Many countries have adopted it for public transportation.

<i>Vehicle</i>	<i>Fuel</i>	<i>CO₂</i> <i>(g/km)</i>	<i>CO</i> <i>(g/km)</i>	<i>HC</i> <i>(g/km)</i>	<i>NO_x</i> <i>(g/km)</i>	<i>SO₂</i> <i>(g/km)</i>	<i>PM</i> <i>(g/km)</i>	<i>N₂O</i> <i>(g/km)</i>
<i>Car</i>	Conventional Diesel	146	0.5	0.08	0.52	0.041	0.06	0.032
<i>Car</i>	Biodiesel	0	0.5	0.08	0.52	0.005	0.04	0.032

Table 1.9 - Tailpipe emissions from road vehicles using biodiesel and conventional diesel for Germany, M. Kaltschmitt et al. 1997 [9]

At the same time, another study conducted in Australia by Beer et al. shows that for buses using biodiesel CO, HC, NO_x and PM are higher

compared with ULSD and the net CO₂ is zero.

<i>Vehicle</i>	<i>Fuel</i>	<i>CO₂</i> <i>(g/km)</i>	<i>CO</i> <i>(g/km)</i>	<i>HC</i> <i>(g/km)</i>	<i>NO_x</i> <i>(g/km)</i>	<i>PM</i> <i>(g/km)</i>
<i>Bus</i>	Ultra Low Sulphur Diesel	1406	1.41	0.53	14.32	0.16
<i>Bus</i>	Biodiesel	0	7.68	0.86	17.2	0.6

Table 1.10 - Sample of tailpipe emissions from road vehicles using Biodiesel and ULSD for Australia, T. Beer et al. 2002 [9]

Substantial variations were experienced in the tailpipe emissions of the same type of vehicle under the same test conditions. An explanation of this variation is that apart from CO₂, there are only trace amounts of pollutants being measured.

<i>Vehicle</i>	<i>Fuel</i>	<i>Variation</i>	<i>CO₂</i> <i>(g/km)</i>	<i>CO</i> <i>(g/km)</i>	<i>VOC</i> <i>(g/km)</i>	<i>NO_x</i> <i>(g/km)</i>	<i>PM</i> <i>(g/km)</i>
<i>Bus</i>	Conventional Diesel	Minimum	-17%	-68%	-38%	-46%	-92%
		Maximum	+33%	+275%	+35%	+73%	+124%
<i>Bus</i>	Biodiesel	Minimum		-43%	-22%	-62%	-50%
		Maximum		+55%	+19%	+39%	+114%

Table 1.11 - Sample of variability of tailpipe emissions in road vehicle tests, T. Beer et al. 2002 [9]

Other bus trials were conducted at Graz University, Austria, by T. Sams et al [9]. ULSD was used on two city buses over a three year period. The emissions of CO were 20% lower than conventional diesel. Tailpipe emissions of SO_x were reduced completely while particulate matter has been reduced by almost 40%. The authors concluded that, by advancing injection timing, NO_x emissions could be reduced by 23% compared with

fossil derivatives.

In the United States the Southwest Research Institute carried out different tests, using B-20 on a 5.9L Cummins pick-up truck. They found out that VOC (Volatile Organic Compound) emissions dropped by 30%, benzene by 78%, PAHs by 35% and butadiene by 85% according to N.Eyre et.al. [9].

<i>Emission</i>	<i>SO_x</i>	<i>CO</i>	<i>NO_x</i>	<i>NO_x *</i>	<i>PM</i>	<i>VOC</i>
<i>Reduction with biodiesel</i>	-99%	-20%	+1%	-23%	-39%	-32%

Table 1.12 - Sample of emissions from austrian bus trials relative to low sulphur fossil diesel, T. Sams et al. 1996 [9]

Biodiesel's lack of sulfur allows the use of NO_x control technologies such as after treatment devices or "lean traps" in the exhaust pipe that cannot be used with conventional diesel. Additionally, some companies have successfully developed additives to reduce NO_x emissions in biodiesel blends.

A detailed and costly analysis has been developed so far regarding the use of biodiesel. Its benefits are worldwide recognized by the U.S. Environmental Protection Agency under the Clean Air Act Section 211(b) [12] - Table 1.13.

AVERAGE BIODIESEL EMISSIONS COMPARED TO CONVENTIONAL DIESEL, ACCORDING TO EPA		
Emission Type	B100	B20
<u>Regulated</u>		
Total Unburned Hydrocarbons	-67%	-20%
Carbon Monoxide	-48%	-12%
Particulate Matter	-47%	-12%
Nox	+10%	+2% to -2%
<u>Non-Regulated</u>		
Sulfates	-100%	-20%*
PAH (Polycyclic Aromatic Hydrocarbons)**	-80%	-13%
nPAH (nitrated PAH's)**	-90%	-50%***
Ozone potential of speciated HC	-50%	-10%

Table 1.13 - Emission factors of regulated air pollutants determined by engine durability test according to U.S. Environmental Protection Agency [12]

In conclusion, most regulated and unregulated pollutants are reduced with biodiesel use: carbon monoxide emissions are lower than those from diesel; particulate matter decrease too; hydrocarbons are consistently reduced; nitrogen oxides increase or decrease depending on the engine family and testing procedures. Biodiesel's lack of sulfur allows the use of NO_x control technologies that cannot be used with conventional diesel. Some companies have successfully developed additives to reduce NO_x emissions in biodiesel blends. For B-100, they increase on average by

10 percent. According to the latest studies though, NO_x can always decrease if the injection control strategies are modified in the ECU (Electronic Control Unit) by the manufacturer. Polycyclic aromatic hydrocarbons exhibit smaller levels. In health effects testing, their compounds were dramatically reduced. The fuel consumption was mostly unchanged, sometimes higher by roughly 2%, in agreement with the lower energy content of biodiesel. The long-term maintenance of vehicles using biodiesel does not differ significantly from vehicles using diesel fuel. On the other hand, plugged fuel filters were found after biodiesel use due to high levels of plant sterols, with high molecular weight. After a teardown analysis of engines running on both fuels, the cylinder heads of the B-20 engines contained a heavy amount of sludge thick and gel-like on the valve deck around the rocker assemblies but out-of-specification fuel is the suspected cause, since this was not found on Ford engines. Beside the fuel filter-plugging problem, the injector nozzles from B-20 were not within specified leak-down limits and they required replacement.

On the long-term durability test of more than 80,000 km the regulated emission levels became higher for B-20 due to the higher viscosity of biodiesel that reduces atomization, leading to a poorer combustion.

So far biodiesel is the first and only alternative fuel to have a complete evaluation of emission results and potential health effects.

Here are the conclusions regarding advantages of biodiesel use:

- The high cetane number of biodiesel when compared to petro-diesel indicates potential for higher engine performance
- The superior lubricating properties of biodiesel increases functional engine efficiency
- Their higher flash point makes them safer to store
- Generally, particulate matter decreases with the use of biodiesel fuels. This effect is attributed to higher oxygen content in the biodiesel fuels, which enables more complete oxidation in the engine cylinder
- They contain higher amount oxygen (up to 10%) that ensures more complete combustion of hydrocarbons
- The application of biodiesel fuel is examined from the point of view of prevention of global warming, since biodiesel is CO₂ neutral in principle. However, the effect of CO₂ reduction becomes higher in proportion to the concentration of biodiesel in the blended fuel.

The literature also specifies several shortcomings resulting from biodiesel use:

- Vehicles running on biodiesel blends may exhibit more drivability problems at severe winter temperatures than do vehicles running on petroleum diesel
- Biodiesel is biodegradable; microbes forms films that can plug filters
- Biodiesel has a possibility of poor fuel atomization and vaporization, because of higher density, kinematic viscosity and vaporization
- Biodiesel may be incompatible with the seals used in the fuel systems of older vehicles and machinery, necessitating the replacement of those parts if biodiesel blends are used
- Oxidation stability of the biodiesel fuels decreases, sunlight having the strongest influence on the fuel.

Despite economical issues related to production costs, distribution, and infrastructure improve, biodiesel may become a reliable alternative source of energy when all other fossil derivatives reserves have depleted.

As a consequence a new idea is to be explored: instantaneous, on-board fuel identification. In other words, when an alternative fuel, such as biodiesel, is poured into the tank, the ECU must automatically switch the injection strategy to maintain satisfactory emissions concentrations at similar power and fuel consumption. Some of these issues such as fuel recognizing procedure, number of alternative fuels strategies or maps that can be stored in

the ECU memory and the actual engine efficiency when running on different fuels must be further investigated.

1.3 Fuel identification methods

One way to identify the fuel type is first to determine the in-cylinder pressure trace based on the crankshaft speed measurement. The evaluation of pressure trace is very useful since it provides a fair estimation of the in-cylinder combustion parameters such as peak pressure, rate of pressure rise, start of combustion and ignition delay. Because ignition delay is strongly correlated to the cetane number associated to a certain type of fuel, it means that, if the pressure trace can be evaluated, that fuel can be eventually identified.

Many papers have analyzed this aspect, in detail, providing more or less accurate results. Fair approximations of the pressure trace were obtained, particularly in the area of interest, the combustion process itself: the points of minimum and maximum of the pressure trace, including the peak pressure, their position with respect to TDC (Top Dead Center), and the corresponding values at those locations.

Some authors evaluate the pressure trace from the measured speed in order to determine the MFB50, which is the moment at which 50% of the mass fraction is burned during combustion as stated by Fabrizio Ponti et.al [14]. It is suggested that two steps are required.

First is to develop a torsional dynamic model of the crank-slider mechanism, in order to determine the relationship between the harmonic components of the speed and the corresponding harmonic components of the torque. If this dynamic model can be accurately estimated, e.g. the stiffness of the shaft, the moment of inertia of masses in rotation, the damping coefficients and other structural driveline parameters, then a transfer function can easily describe the strong relationship involving the speed and torque fluctuations, especially at an order specific to the engine, where the amplitude of the waveform speed is the highest. This order is mainly related to the number of strokes per cycle, 2 or 4, the number of cylinders, and the firing order.

Second, a relationship between the phase of the engine torque component and the MFB50 is established.

An explanation of how the frequency range needs to be investigated is provided for a four-stroke four-cylinder engine. The order to be considered is that of the first major harmonic component, equal to half the number of cylinders: $4 / 2 = 2$. Therefore running the engine from 800 rpm to 4500 rpm gives us the frequency of interest ranging from 27 Hz to 150 Hz, e.g. $(800/60)*2=27$. It is assumed that the crankshaft natural frequencies are out of the range of interest and one or more driveline

natural frequencies within this range have been verified. Otherwise additional restrictions must be imposed.

Using a two lumped-mass system, the engine and the driveline, the authors develop an expression of the engine speed as a function of the engine torque, related by a Frequency Response Function (FRF) and obtained from a CAD representation of the system or experimentally. Graphs show that the amplitude of the gas pressure (or indicated) torque depends on the engine speed and load, while the amplitude of the reciprocating inertia torque, normalized here, is a function of the speed only. Its amplitude increases with angular velocity, but both torques show similar phases.

By measuring the speed and the pressure, from which the engine torque is computed, the FRF can then be experimentally determined. The engine torque represents the summation between the indicated torque and the reciprocating inertia torque. A test covering the entire range of engine speeds, up to 4500 rpm, is conducted, with the 1st gear coupled, and the 2nd order amplitudes and phases of the engine torque and speed are graphically displayed. The 2nd order amplitude of the engine torque first decreases, because the gas pressure component is still larger than the inertia one. As the engine speed increases, the inertia component becomes

equal and higher than the gas pressure one. The 2nd order amplitude of the total torque reaches a minimum of 0 (zero), then increases continuously up to the highest testing point, 4500 rpm. For the same reason, the phase changes too after that point of minimum, from -90° , corresponding to the initial dominating component of the gas pressure torque, to $+90^{\circ}$, correlated to the final controlling component of the reciprocating inertia torque.

When deceleration starts, the gas pressure torque component quickly decreases, so the reciprocating component prevails even more. Consequently, the engine torque component, even though is decreasing, is higher now as compared to the one corresponding to the acceleration process. The new balancing point is now at a lower speed than the previous one. After that point, the indicated torque component prevails, so the engine torque component increases again until idling state is attained.

In conclusion, the indicated torque depends not on only the speed and load, but also on the acceleration / deceleration regime.

A similar behavior is noticed for the harmonic component of order 2 of the engine speed. As a consequence, the relationship to the engine torque is strong. The amplitude and phase of the FRF can now be determined experimentally for the frequency range of interest, 27 to 150 Hz, so the torsional model is determined. The FRF can also be calculated from CAD

drawings, if they are available, by computing the corresponding mass moments of inertia, stiffnesses and dampings, and both representations should match.

In any case, once the transfer function FRF is known, along with the measured speed, the indicated torque components can be easily estimated.

The diagrams displaying the amplitude and phase of the components of the torque show an approximately linear distribution, at 45°, between the measured and estimated data, with acceptable small errors. Similarly, different FRF-s have been computed for each gear, up to the 6th. Small differences are noted in the frequency range of 95 to 135 Hz, where probably a resonance with a node in the gear box occurs.

The subsequent study of the relationship involving the engine torque and the MFB50 according to Fabrizio Ponti et.al.[14] is beyond the scope of our topic. Nevertheless, an example of how the engine torque can be estimated from the measured crankshaft speed has been illustrated here.

Engine torque or in-cylinder pressure can be evaluated from crankshaft speed measurement in various ways.

A four-stroke engine running at 6000 rpm has a cycle duration of $1 / [(6000 \text{ rev} / 2 \text{ rev} / \text{cycle}) / 60 \text{ sec}] = 2 \text{ sec} / 100 \text{ cycles} = 20 \text{ millisecond} /$

cycle. Consequently, in order to implement on-board engine performance control, the simulation computing time should be much lower than this value.

Some authors such as D.Brand et.al. [15] claim to have reduced it to 6 milliseconds. However, since the full speed curve is required for computation, the in-cylinder pressure trace is evaluated with a delay of one engine cycle duration.

The model has 2 parts. The 1st consists of pressure estimation path from the engine speed, the air-fuel ratio, the inlet manifold pressure and the spark advance. In the 2nd part, the crankshaft angular velocity is measured and also computed from the in-cylinder pressure estimated before. Furthermore, the corresponding phases at firing frequency and their difference, representing a correction factor of the flame speed, are used to update the combustion model, and therefore the estimated in-cylinder pressure.

In the combustion model, the mass fraction burned x_b is calculated using a Vibe function formula, which includes: measured values of the air-fuel ratio and the spark discharge angle θ_{sa} ; mapped values of the flame development angle θ_d^0 , the rapid burning angle θ_b^0 , the air-fuel ratio Φ^0 , and the spark discharge angle θ_{sa}^0 . From the spark discharge angle θ_{sa}^0 the

combustion start angle θ_{cs} and the combustion end angle θ_{ce} can be further estimated. The graphs show good correlation with such measured angles, therefore the mass fraction burned x_b is correctly estimated.

Because the mass fraction burned x_b , an interpolation coefficient, is now known, the in-cylinder pressure may be calculated using an interpolation formula involving two polytropic pressure envelopes, in the shape of motoring-traces, as lower and upper bounds of the actual firing pressure curve. The pressure value at 80 CAD after TDC is formulated by utilizing the pressure value at 80 CAD before TDC and the assumption that the pressure rise linking the two points is proportional to the energy released during combustion within that interval. Good correlation exists between measured and estimated pressure data.

Having determined the in-cylinder pressure and assuming that the external load torque and friction torque components are negligible, the engine torque can be calculated, with a shift phase of 90° with respect to the angular velocity.

In order for the in-cylinder pressure and engine torque to be correctly estimated, the combustion phase φ needs to be corrected in a feedback loop to compensate for other factors that have an influence on the flame speed, beside the air-fuel ratio Φ and the spark advance θ_{sa} . Such factors

are temperature, residual gas mass, air humidity etc. An adaptation algorithm for the correction factor k_s is presented. This factor contains the ratio of the calculated flame speed to the nominal flame speed, which is known from the mapped values. Using the state space formulation, the stability, robustness and performance of the system are analyzed. The system shows good tracking response, being able to reject different disturbances, such as modified spark advance values, EGR rate, camshaft phasing etc.

The results obtained by using this correction look promising. The measured and estimated values of the pressure show a linear dependency, at an approximately 45° angle. They are also compared to the values obtained by a different computational method, using a sliding mode observer (SMO), at steady-state and transient operation. The conclusion is that, even though the response of the proposed method is slower, the accuracy at steady state is higher. If the rigid crankshaft assumption was adopted here, good results would be obtained, including at lower resolutions, for example, at 6 CAD sampling rate, instead of 1 CAD sampling rate. That would make it suitable for standards measurements with a regular magnetic pick-up sensor.

A method for IMEP estimation on a multiple cylinder engine using one in-cylinder compression pressure trace and the engine speed was proposed as stated by C. Kallenberger et.al. [16]. A white-box model contains purely physical information. A black-box model is entirely data-based. The authors use here a gray-box model of the crankshaft torsional effects because the input and structural information comes from physical observation, while the identification is sustained by measured data.

A detailed but stiff four-cylinder crankshaft physical model is adopted. The torque balance equation is fully described in all its terms, and then developed into a second order differential equation. This equation is transformed subsequently into a first order differential equation by a state space representation. Non-linear state space equations, state variables (crank angle and speed vectors), inputs and outputs are clearly presented. The order of the system is high, 16, for each of the eight degrees of freedom, two states being introduced. Parameters like stiffness or dampness matrices are difficult to predict and solving a non-linear system requires intense computation. As a result, authors propose a gray-box model of the crankshaft, using a SIM subspace identification method. The idea is that the system matrices can be determined by linear optimization method if the states of the LTI (Linear Time Invariant) system are known.

Assuming equal inertia (mass) torques for all four cylinders, they linearize the first state space equation.

According to the Matlab Identification Toolbox, the “System Identification” enables you to build mathematical models of a dynamic system based on measured data. You adjust the parameters of a given model until its output coincides as well as possible with the measured output.” The specific `n4sid` function is also used.

The measurement for system identification is the angular acceleration, which is known. The authors select an inversion strategy of the LTI MISO (Linear Time Invariant Multiple Input Single Output) system in order to estimate the indicated cylinder torque, by separating it into two: a compression torque, computed from a corresponding compression pressure, and a combustion torque, computed from a corresponding combustion pressure. By measuring the pressure in one cylinder and assuming identity for all four cylinders, all four compression torques can be evaluated. Mass (inertia) torques are also known, so the combustion torques are to be determined.

The identified MISO subspace model, now split into 4 SISO (Single Input Single Output) systems, each corresponding to one cylinder, is presented, together with an example of an iteration of the combustion

torque estimation for cylinder number four. That includes: a forward simulation resulting in an estimated value of the engine angular acceleration, as an effect of compression and inertia torques only; a comparison of the engine angular acceleration to the corresponding measured data; a SISO inversion of the residual angular acceleration and its multiplication to the inverse system response, to estimate the corresponding combustion torque. All three steps are repeated sequentially for the other cylinders.

Once the compression and combustion components are known, the actual engine torque and IMEP can be evaluated.

The subspace model is compared to the benchmark model of the rigid crankshaft and to the measured data. Net superior performance is achieved in the case of the subspace model. In spite of that, at higher speeds, due to noise accumulation, the model suffers from accuracy and further investigation of this technique is recommended.

A different approach to model the dependence between crankshaft speed and in-cylinder pressure is to use a MLP (multi-layer perceptron) neural network. Authors such as F.Taglialatela, N.Cesario et.al. [17] assert that none of the previous methods in literature rendered a pressure trace

highly comparable to the measured one because they had used simplifying assumptions that literally lead to errors.

Nonetheless, the goal here is to estimate the in-cylinder pressure peak value and its location only, representing the outputs of a neural network. Its inputs are the engine angular velocity and its derivative, the angular acceleration. A PFI (Ported Fuel Injection) engine was used to train and validate the neural network model.

The measurements were performed at full load (wide open throttle) by varying the speed from 1000rpm to 2000 rpm in steps of 200 rpm, and then, for each engine speed, by modifying the absolute intake pressure from 1 bar to 1.6 bar, in increments of 200 mbar. Some of these tests were utilized to train the network; the remaining ones were used to validate it.

A feed forward MLP (Multi Layer Perceptron) neural network, having one hidden layer with thirty neurons and the tanh function, as an activation function, was chosen. Out of the eighteen training available functions in the Matlab toolbox, the trainbr function was selected, because, according to the Matlab toolbox, this function “minimizes a combination of squared errors and weights and determines the correct combination so as to produce a network that generalizes well” in a process called “Bayesian regularization”.

The results at different speeds, 1500 rpm and 2000 rpm, indicate a good correspondence between the measured values of the peak pressure and their location, and the simulated corresponding ones. A RMSE (Root Mean Square Error) and a Relative Error analysis show acceptable results. In addition, the model seems to be capable of predicting instantaneous variations of the peak pressure and its location due to combustion anomalies, such as misfiring or partial burning.

Pressure trace can be rapidly computed using stochastic estimation techniques which are “computationally inexpensive”, leading to an estimation error of peak pressure of only 1-2 % because “all complexities of the physical system, such as combustion phenomena, engine dynamics, are self-extracted from the data” in compliance with Yann G.Guezennec et.al.[18].

The theoretical concept is briefly presented: in order to approximate as best as possible a set of variables (y^1, \dots, y^p) as a function of basis functions f_j^l in the form of $a_j^l f_j^l(x_1, \dots, x_n)$, the error must be minimal. Hence the “l” sets of coefficients representing the solutions of the linear system: $L^l a^l = D^l$ or $\langle f_k^l f_j^l \rangle a_k^l = \langle y^l f_j^l \rangle$. The basis functions can be measured or derived mathematically, so they are known. Once L and D have been built, the

coefficients a_j^l can be solved and the variables y^l can be approximated by the terms $a_j^l f_j^l(x_1, \dots, x_n)$.

In IC engines, the basis functions are built to correlate a quantity to be estimated, the in-cylinder pressure, and a quantity to be measured, the velocity of the crankshaft. The tests were conducted on a single cylinder engine, a four cylinder engine and a six cylinder engine, at different operating conditions.

A detailed explanation of how to choose the proper basis functions is provided. These functions should include the crankshaft position, the speed, the acceleration but also a function f_θ , proportional to V^{-k} , representing the actual motoring pressure variation. This motoring pressure variation is derived from the $pV^k = C$ polytropic behavior, where V is the in-cylinder volume, during compression and expansion. Using five basis functions: $1, f_\theta, f_\theta \theta', f_\theta \theta'', \theta' \theta''$, they expressed the in-cylinder pressure as follows:

$$p_{est} = a_{00} + a_{10} f_\theta + a_{12} f_\theta \theta' + a_{13} f_\theta \theta'' + a_{23} \theta' \theta''$$

From here, a system of five equations was developed, and the five coefficients $a_{00}, a_{10}, a_{12}, a_{13}, a_{23}$ were found. Then the in-cylinder pressure p_{est} was computed. Graphics show good coincidence between measured and estimated pressure traces.

Many other modeling expressions were used. An estimation error was defined to quantitatively assess the performance of each expression. The optimal should have had the lowest estimation error but also the smallest number of terms. Since this was not actually possible, they chose a compromising solution, considering both aspects.

Moving further into analysis, the authors tried to estimate how the coefficients a_{ij} change from one operating point to another, in order to avoid the entire re-calculation process of the functions at each operating condition. The coefficients were expressed then differently: first, as a 1st order function of the spark timing: $a_{ij} = b_{ij} \cdot \theta_s + c_{ij}$, where b_{ij} and c_{ij} were linear functions of the engine speed, load, and EGR percentage; then, as a 0th order and a 2nd order fitting functions. After analyzing the results, the authors concluded that the basis functions and the coefficients do not have to be evaluated for each operating point, but “only at sparse mapping conditions”. Moreover, for those particular cases, a 1st order curve fit is suitable enough.

Additional comparison among signals without noise, with noise, and with noise but filtered, proves that the method is robust in all three conditions. A block diagram indicating the inputs and the outputs of the ECU, demonstrates that the procedure can be implemented, according to

its authors, in real-time engine control, by adding an induction pick-up or an optical sensor to provide the position of the crankshaft.

The gas pressure torque, or the indicated torque, is directly related to the in-cylinder pressure and can also be determined from the crankshaft speed measurement as said by D.Taraza, Naeim A. Henein et.al. [19]. The harmonic components of the crankshaft speed can be obtained by a DFT (Discrete Fourier Transform) and then correlated to the harmonic components of the gas pressure torque, using a dynamic model of the crankshaft.

The engine speed varies during a cycle because of the gas pressure variation in the cylinder. The torsional deformations or oscillations of the crankshaft superimpose over the initial variation of the speed, therefore the relationship connecting the torque and the speed becomes more complicated.

Nevertheless, because torsional vibrations had been investigated, the authors present a dynamic model of the crankshaft. They consider: mass moments of inertia of the rotating parts (J_i), torsional stiffnesses (C_i), absolute (r_i) and relative dampings (c_i). For each harmonic component k , there is a point matrix P_{ik} that corresponds to each mass J_i , and a field (elastic) matrix E_{ik} that corresponds to each elastic shaft C_i . A state vector,

$Z_{ik}^{R,L}$, whose elements are the real and imaginary parts of the angular deflection θ_{ik}^{Re} , θ_{ik}^{Im} and the real and imaginary parts of the torque M_{ik}^{Re} , M_{ik}^{Im} , defines the state of each lumped mass, connected to the left and to the right to elastic elements.

By multiplication of all corresponding points and field matrices, one global matrix H_k is obtained, which now directly relates the state at one end of the crankshaft to the state at the other end of the crankshaft:

$$Z_{Nk}^R = H_k * Z_{ik}^L$$

The torque corresponding to cylinder “i” is the sum of the harmonic components of the gas pressure torque (sine and cosine terms) and the harmonic components of the inertia torque (sine terms only). By rearranging terms, both real and imaginary parts of the torque at cylinder “i”, $(M_k^{Re})_i$, $(M_k^{Im})_i$ are identified. Then they are introduced in the corresponding point matrices P_{ik} and finally, in the submatrix Y_k of the global matrix H_k .

In order to validate the dynamic model, a direct calculation is performed: by knowing the gas pressure torque in each cylinder and the average engine speed (rpm) the speed variation at each end of the crankshaft is estimated.

The engine load, acting on the flywheel J_N , is almost constant or has little fluctuations, therefore its harmonic components (amplitudes of oscillations) M_{Nk}^{Re} , M_{Nk}^{Im} can be approximated to 0 (zero). The system of equations given by $Z_{Nk}^R = H_k * Z_{ik}^L$ is solved by determining the deflections and the speed variations at each end of the crankshaft. These values follow very close the experimental data, which means that the dynamic model is valid and can now be used in a reversed calculation. Once the harmonic components of the speed variation at one end of the crankshaft and the average engine speed (rpm) are known, the individual engine torque components can be determined.

If the speed at the pulley is known (measured), then the two equations that describe the individual torque components, real and imaginary have $2*q$ unknowns, representing individual torque components, where q stands for the number of cylinders. However, the speed signal measured at the flywheel is of better quality, because the flywheel has a greater mass moment of inertia than the other moving parts so the torsional vibrations are smaller here. Thus the corresponding node of their first mode is situated close to this location. If the speed at the flywheel is known (measured), then there are four equations and $2q+2$ unknowns: $2q$

excitations and two deflections at the pulley, one real and one imaginary part.

In both cases, the number of unknowns is higher than the number of equations. An approach, which includes “basic solutions”, by assuming 2q-2 unknown equal to zero, is proposed. A desired solution is a linear combination of these “basic solutions”. According to theory, the major harmonic orders that have a significant influence on a four-stroke cylinder engine are multiple of the half-number of cylinders, that is 2, 4, 6, 8, 10..., a fact which is also supported by the gas pressure torque calculation from the experimental data.

Therefore, taking into consideration only the major harmonic orders $k = 2, 4, 6, 8$ and 10, the gas pressure torque is reconstructed with good precision, as long as the differences between cylinders contributions are not too large.

In the direct method, small inaccuracies of the parameters in the dynamic model, such as stiffnesses, mass moments of inertia, lead to small differences in the reconstructed speed variation. Oppositely, during the reverse calculation, they lead to large distortions, increasing with speed and load, therefore the dynamic model parameters must be determined as accurately as possible.

If the interest is to estimate the average gas pressure torque and correspondingly, the IMEP, a more convenient method is presented. Based on the proven observation that the amplitudes of the major harmonic components preserve a fairly constant value at constant speed and load, a linear correlation involving the major harmonic components and the IMEP is established.

From the graphics it can be easily inferred that, for a four cylinder engine, the 6th harmonic component, one of the major ones: 2, 4, 6, 8..., expresses in the best way a linear correlation to the IMEP. For a six cylinder engine, the 3rd harmonic component, again, one of the major ones: 3, 6..., expresses a linear correlation to the IMEP. This direct dependence is robust, remaining true even in the case of misfiring.

In conclusion, the instantaneous gas-pressure torque and the IMEP of a multi-cylinder engine can be estimated from the crankshaft speed measurement, given the following conditions: good estimation of the parameters of the dynamic model, uniform cylinder's contribution to the total engine torque, and last but not least, preferably low speeds, to avoid increased torsional vibrations. The linear correlation between the IMEP and major harmonic components can be stored as a map in the PROM of the engine controls and used to determine the IMEP "on-the-fly".

A quantitative insight into the correlation linking the engine speed variation and the gas pressure torque is also brought into discussion as presented by Dinu Taraza [20]. The lowest harmonic orders of the engine torque do not contribute to torsional vibrations, thus they are in good correspondence with the lower harmonics of the engine speed, a fact which is also proved by a statistical analysis. The lowest harmonic orders of the engine torque also determine the IMEP of the engine and the corresponding half-orders may detect a faulty cylinder.

Because the lowest harmonic orders of the engine torque T_k are lower than the first natural frequency of the crankshaft, the engine can be considered as a rigid rotor, having the total mass moment of inertia J_{tot} . This total mass moment of inertia is equal to the mass moment of inertia of the crankshaft assembly, including the flywheel, plus that of the reciprocating masses. The equation of motion is: $J_{tot} \theta_k'' = |T_k| \sin(k\omega t)$, where θ_k'' is the angular acceleration. By derivation, the solution gives us the angular speed: $\omega_k = |T_k| / k\omega J_{tot} \sin(k\omega t - \pi/2)$, whose k^{th} harmonic component is delayed with respect to the corresponding harmonic term of the engine torque by 90° . Thus, a fairly simple correlation is established among the two parameters, considering, again, their lower harmonic constituents.

To validate this correspondence, a four-stroke, six-cylinder, direct injection diesel engine was used. Both speed and gas-pressure torque were applied a DFT (Discrete Fourier Transform) to find the amplitudes and phases of the first 24 harmonic components. An expression of the harmonic order “k” of the engine torque is provided, reflecting the contribution of both gas pressure torque and inertia torque. Being a four-stroke engine, there are half-order harmonics only, determined by the gas pressure torque components. The integer-order harmonics of the engine torque derive from the gas pressure torque components and, for the harmonic orders from 1 to 6, they also derive from the inertia torque components.

The author considers in this study two harmonics: the half-order ($k = \frac{1}{2}$) and the first major order for a four-stroke, six-cylinder engine, which is the third ($k=3$). The experimental results show that the phase angle (lag) connecting the speed and the torque components is, indeed, constant and almost equal to 90° , even with one cylinder disconnected, so the rigid body model is valid for these low harmonic orders.

Good correlations are obtained between the cylinder IMEP and the amplitudes of the harmonic components $k = \frac{1}{2}$ and $k=3$ of the tangential

gas pressure, and between the cylinder IMEP and the corresponding phases of the same harmonic components.

A vector interpretation of the k -th order harmonic component of the cylinder torque is graphically provided: a vector that rotates “ k ” times faster than the crankshaft and whose phase angle with respect to TDC (Top Dead Center) is φ_k . However, because of the non-uniform character of these vectors representing the harmonic components, a normal distribution is assumed. Mean values, standard deviations, covariance formulas, the angle ζ linking the vector and the axes of coordinates and the ellipse of dispersion are displayed.

Fortunately, for non-major harmonic orders, the corresponding vectors in the phase angle diagrams are symmetric and cancel each other, even though the standard deviations have a finite value and the center of the ellipse of dispersion is located at the origin of the coordinate system. For $2k$ non-major harmonic orders, the situation is identical and, moreover, the ellipse reduces to a circle. The formulas for the non-uniform contribution of a cylinder are also provided.

The experimental results and simulation intervals are also in good match in the matter of the average value of the 3rd order component of the engine torque, its phase angle and the amplitude of the 3rd order

component of the crankshaft speed. The robustness of the model is confirmed by further experiments, having one cylinder disconnected. A linear correlation has been established between the IMEP and the amplitude of the 3rd order constituent of the crankshaft speed.

According to the phase angle diagram, the half-order components should cancel each other if all cylinders perform uniformly. This arrangement is interrupted though, if a cylinder becomes faulty, producing a non-zero torque on crankshaft. This half-order component increases in the spectrum of engine speed. Its magnitude is related to the degree of non-uniformity and its phase will tell which cylinder is faulty.

By analyzing the table with the average value of the half-order harmonic of the engine torque and the table with its corresponding phase angle, it can be inferred that the statistical model is robust even in the case of non-uniform functionality.

A graphic representation is provided showing the statistical position and magnitude of the half-order component of the gas pressure torque and its related component of the speed. This component lags, as it was found before, by 90°, when a cylinder is disconnected.

By disconnecting all cylinders successively, an image of six domains is obtained where the half-order harmonics of the engine speed are statistically located.

If a cylinder contributes less and less to the engine torque, the amplitude of the half-order harmonic of the speed starts to increase, becoming very large and also the phase domain reduces, reaching eventually a certain direction that indicates the faulty cylinder.

By disconnecting again, all cylinders successively, another image of six domains is obtained where the half-order harmonics of the engine speed are now, experimentally located.

For less non-uniformities, e.g. 10% only at cylinder number 6, the amplitude of the half-order harmonic of the speed is smaller and its phase domain larger. Nonetheless, the phase domains and amplitudes of the half-order component show fairly good correlation between statistical model and experiments.

In conclusion, for a four-stroke six cylinder engine, the amplitude of the half-order harmonic of the speed can be used as a tool to diagnose the degree of non-uniformity in the contribution of a cylinder to the total engine torque, while its corresponding phase can detect which cylinder is malfunctioning.

At the low frequencies (Hz) of the low non-major harmonic orders of the engine torque, e.g. the $\frac{1}{2}$ order harmonic for a four-stroke six-cylinder engine whose first major harmonic component is the 3rd, the crankshaft acts like a rigid body [21]. Hence a direct correspondence between the numerically identical harmonic components of the engine torque and the components of the measured engine speed can be achieved, with the final purpose of identifying faulty cylinders.

In this case, the vector of a harmonic order of the crankshaft speed lags the corresponding vector of the same harmonic order of the gas pressure torque by 90°. By applying a DFT (Direct Fourier Transform) the engine torque is expressed as a summation of its mean value and the sum of the harmonic components from order $\frac{1}{2}$ to M. Each such harmonic component, of order j ranging from $\frac{1}{2}$ to M, has an amplitude T_j and a phase φ_j , which can be calculated.

Because the half-orders components $\frac{1}{2}$, $1\frac{1}{2}$... are the result of the gas-pressure torque only and not of the inertia torque, in addition, as in the case of the integer harmonic orders 1, 2 ..., they represent a better option for the detection procedure, being less computationally intensive.

In order to give a general character to this method, the author divides the expression of the instantaneous gas pressure torque by the piston area

and by the crank radius to obtain an expression more suitable for different engines, called tangential gas-pressure. Furthermore, regarding the average values, the IMEP (Indicated Mean Effective Pressure) concept instead of the mean engine torque is used.

As previously explained, the amplitudes T_j and the phases ϕ_j of each harmonic component j of the gas pressure torque are known. The IMEP is also known, being directly related to the gas pressure torque. Consequently, a correlation connecting the IMEP and the harmonic components of the gas pressure torque can be established. A four stroke six cylinder was used to determine and validate such correspondence.

Both measured speed and pressure were applied a DFT (Direct Fourier Transform) to find their harmonic components. The graphics show good correlation between the corresponding amplitudes and the IMEP-s and also between the corresponding phases and the IMEP-s, especially for the $\frac{1}{2}$ order component.

Nonetheless, because there is random cycle-by-cycle variation of the cylinder IMEP, a statistical approach is required to calculate the amplitude and the phase of the vector representing the harmonic component of the gas pressure torque. A detailed such model is provided.

In the case of uniform contribution of all cylinders, the six random vectors, corresponding to the six cylinders, will have identical mean values and standard deviations, being symmetrically distributed with respect to the system of axes of coordinates, similar to the phase angle diagram, but rotated by the phase angle specific to that harmonic order. For instance, by reading a previous graph, for order $k= \frac{1}{2}$ this angle is 226° . The resultant vector is of zero mean value and its ellipse of dispersion is a circle centered in the origin of the coordinates system.

When one cylinder starts contributing less, this symmetry is disturbed. The resultant of the remaining five vectors corresponding to the five properly working cylinders is directed in opposition to the mean random vector of the malfunctioning cylinder. The IMEP of the deficient cylinder changes, therefore its vector phase and amplitude change too. However, all of them are known, including the ones of the unaffected cylinders. By summing all vectors, the resultant vector of the gas pressure torque component is then calculated. Using the rigid body approach and rotating it by 90° , the direction of the resultant vector of the crankshaft speed with the same harmonic order, $\frac{1}{2}$, is now determined and its phase angle, -27° , is therefore uniquely correlated to the faulty cylinder number, #1. Its amplitude and dispersion angle, $\pm 10^\circ$, are also uniquely correlated to the

cylinder degree of non-uniformity. An accentuated malfunction that leads eventually to a complete misfire means larger amplitude and smaller dispersion angle. Repeating the sequence of misfiring for the other cylinders, a diagram of six unique corresponding vectors of the half-order harmonic of the speed is developed.

In order to validate the model, a series of tests are conducted. First, cylinders #1, #3 and #4 are brought to misfiring conditions successively. The vectors of the half-order component have distinct directions (phases) and magnitudes, with very little dispersion around the average values. As any cylinder is progressively brought back to running conditions, for instance, cyl #2 providing at least 65% of its maximum power, the amplitude of the corresponding vectors decreases, the scatter around the phase angle increases, so the identification of the faulty cylinder becomes a little more difficult.

Nevertheless, there are two options: one is to examine, in addition, the $1 \frac{1}{2}$ order harmonic component of the speed, which proves effective. For example, if there is doubt regarding which of the cylinders, #2 or #6, is a lesser contributor after analyzing the half-order harmonic component, the investigation of the $1 \frac{1}{2}$ order harmonic component clearly separates the

culprit, which can be now either to the right, cyl #6, either to the left, cyl #2, of the measured diagram.

Another option is to avoid the $1 \frac{1}{2}$ order harmonic component verification and simply determine the mean value of the half-order component of the crankshaft speed along a number of successive cycles. In both examples of 19% and 7% power loss at cyl #6, the mean value of the speed vector after 10 cycles points, undeniably, in the direction of cyl #6.

As a conclusion, the half –order harmonic component of the speed not only identifies a misfiring cylinder but it also detects any small non-uniformity in the functionality of any cylinder.

The model can serve, therefore, as a good tool for On-Board Diagnostics.

The question is how accurately the IMEP can be determined from engine speed measurement. The answer to that depends on the statistical nature of the cyclical variation while the engine is operating according to Dinu Taraza [22]. The lumped-mass model of the crankshaft works fairly well in predicting the crankshaft speed from the measured pressure trace. However, in the reverse calculation, when the crankshaft speed is measured, this model is not so recommended anymore, since small

inaccuracies in the assessment of its physical parameters lead to large errors in the estimation of the pressure trace.

Because at steady state, the torque that drives the auxiliaries and the load torque can be considered constant, then the equation of motion includes only the sum of the harmonic components of the gas pressure torque, the inertia torque, the valve train and the friction torque on one side, and the product between the total mass moment of inertia and the sum of the harmonic components of the crankshaft acceleration on the other side. Moreover, the equation is expressed as vectors because its terms have different phase angles.

Considering the lowest harmonic only, which is not affected by torsional vibrations, the summations of the terms now become the terms themselves only. By integration, the expression of the amplitude of the speed is obtained, but, in order to calculate it, the amplitude and phase correspondence involving the three types of torque must first be known.

Then the author develops a general expression of the gas pressure torque of one cylinder, which also includes the more general concept of the tangential gas pressure, an equivalent pressure that would act directly on the crank pin instead of the top of the piston. From here, the formula for the k^{th} harmonic component of the gas pressure torque is derived.

By extrapolation of this expression to the multi-cylinder case, the phase angle diagram corresponding to all cranks can now be a figure of either symmetrically placed vectors, with small resultants given the cylinders work uniformly, or a figure of vectors adding up in one direction, in which case, the k^{th} harmonic component becomes a major one.

The major components of the gas pressure torque, acting in the same direction, do not produce deformations on the crankshaft. In addition, they will yield large harmonics in the speed frequency spectra as well.

For a six-cylinder engine an example of major harmonic components of the speed 3, 6, 9 and 12 at three different speeds is presented. Beside these clearly distinct constituents, there are significant components of other orders too, that excite torsional vibrations this time, because the crankshaft is an elastic element, e.g. harmonics of order 8 at 1200 rpm or 6.5 at 1500 rpm. Therefore, in order to prevent this interference, only the lowest order, in this case 3 will be considered to correlate the measured speed and the gas pressure torque and, eventually, the IMEP.

A correspondence formula based on graphic representation is established linking the amplitude of the 3rd order component of the tangential gas pressure, directly related to the gas pressure torque, to the IMEP. That is in good agreement to the literature data. The formula is

extrapolated for different engine speeds. A linear dependence between the phase angle of the 3rd order harmonic of the tangential gas pressure and the IMEP is also formulated.

A DFT is applied to the gas pressure torque and speed to determine the amplitudes and phases for the harmonic order $k=3$. Then their corresponding vectors are graphically represented. The formula for the harmonic component $k=3$ of the inertia torque, containing a sine term only, can be evaluated too: it is a vector parallel to the vertical axis.

As previously discussed the k^{th} harmonic order of the crankshaft speed lags the total engine torque by 90° so the total engine torque vector direction or phase for $k = 3$ is also known. Its amplitude is simply the product of the average angular speed, total mass moment of inertia, number $k = 3$, and the amplitude of the harmonic order 3 of the angular speed. Therefore the total engine torque vector can also be represented.

Yet, when the phase angle between the 3rd order harmonic of the speed and the resultant of the gas pressure and inertia torque is measured along 10 cycles, the values are close to, but not exactly 90° . It means that the total engine torque, beside the gas pressure and inertia torques, includes, in addition, a small, but non-zero component: the valve train and friction torque. Hence, this constituent can be represented as a vector in

the initial diagram, expressing the difference between the total engine torque and the summation of the gas pressure and inertia torques.

Even though the correspondence between the values of the friction torque and of the speed is not uniform as expected, a linear correlation is graphically presented, relating the total engine torque, and the summation of the gas pressure and inertia torques, while the speed varies. Based on that, a formula that estimates the gas pressure torque as a function of parameters depending on engine speed only is developed.

The steps to calculate the IMEP directly from the measured speed are described in a tabular form. In the final step, the IMEP is calculated using a more complex formula, as a function of both speed and tangential gas pressure, also previously estimated from speed, resulting in an acceptable error of 1.9%.

A statistical analysis is performed on the same parameters at medium and high loads. The errors are acceptable, because in those cases, the friction torque is low with respect to the total engine torque, an assumption that was used in the previous tabular calculation. At lower loads though, less than 4 bar IMEP, the friction torque becomes comparable to the total engine torque and the error in the IMEP estimation increases.

As a result, if the frequency of the lowest major harmonic component order is small as compared to the first natural frequency of the crankshaft, for all operating engine speeds, then the crankshaft operates like a rigid-body and the lowest major order harmonic component of the measured speed, such as the 3rd for a four-stroke 6-cyl engine, can be used to evaluate the overall engine IMEP.

Multi-cylinder engines have been analyzed so far but it is still unclear if the situation is similar for single-cylinder engines. The variation of angular velocity is a function of cylinder pressure variation, friction torque and engine dynamics as presented by Dinu Taraza, Naeim A.Henein et.al. [23]. Using a lumped mass model of the crankshaft, similar correlations between harmonic components of the gas pressure torque and harmonic components of the speed are established.

Unlike the case of a multi-cylinder engine, where the number of equations is less than the number of unknowns, for a single cylinder engine, the system is determined, so it is possible to reconstruct the cylinder pressure.

Theoretical background includes a dynamic model of the crankshaft coupled to a dynamometer, point matrices corresponding to the masses in rotation and field matrices corresponding to the elastic elements (shafts),

and a system of equations expressing the state vectors at one end as a function of the state vector at the other end, using a global transformation matrix. This system reduces eventually to four equations, with two solving options.

First, in a direct calculation, if the cylinder pressure is measured, meaning that the real and imaginary part of the excitation (torque) are known, then the system can be solved for the four remaining unknowns, which are the real and imaginary parts of the deflection at the front end and at the flywheel. By derivation, the two corresponding speeds at both ends are obtained.

Second, in a reverse calculation, if the speed is measured at one end, then, by integration, the real and imaginary parts of the deflection are found. The system is now solved for the real and imaginary part of the excitation and, optionally, for the real and imaginary parts of the deflection at the other end. The real and imaginary parts of the excitation help us calculate the engine torque. The inertia torque is a function of the physical engine parameters, which are known, and of the speed, which is measured, so is also known. By subtracting the inertia torque from the engine torque, the gas pressure torque and the cylinder pressure are evaluated.

A block diagram in Matlab / Simulink, including functions representing the four equations of the dynamic model (pulley, cylinder, flywheel and dynamometer) is also presented.

To validate the model, a single-cylinder diesel engine with bore 80 mm and stroke 82 mm is used. By using the transfer matrix method in a direct approach, starting from the pressure measurement, the engine speed is estimated. Since this estimation coincides fairly well with the measured data, it means the dynamic model is valid and can now be used in a reverse calculation too. First, the gas pressure torque is reconstructed. Its corresponding curve has additional small vibrations that are not present in the torque curve computed from the cylinder pressure. These vibrations represent the resonance frequencies of the crank-slider mechanism, which is excited immediately after the combustion starts. The phenomenon continues further into the exhaust and the intake stroke.

When an attempt is made to finally estimate the cylinder pressure from the gas pressure torque, the denominator of the conversion formula becomes 0 (zero) at the TDC. To accommodate this, another formula, based on the ratio of the differences between the parameters this time, is now used, for a small interval around this point.

The reconstructed cylinder pressure approximates the measured data but the coincidence is not the best one because the gas pressure torque curve does not pass exactly through the origin at TDC, as it should. That is because of the crankshaft vibrations mentioned before. Moreover, if the speed increases, these vibrations amplify too and the differences between the measured and the estimated pressure curves become larger.

By comparing the results from the Matlab code with the ones from the Simulink model, it can be inferred that both techniques lead to similar results. However, transient condition estimations can be performed only by using the Simulink model. If the dynamics of the crankshaft would be further extended into the crank-slider mechanism, and the mass of the piston-assembly and the stiffness of the connecting rod would also be included, then the distortions of the gas pressure curve may be eliminated.

1.4 Conclusions

Most of the references in literature consider a dynamic model of the crankshaft in their computations. Once the model has been validated it can be used to determine the harmonic components of the gas pressure torque because crankshaft movement and functional cylinders characteristics are correlated. Some models are simpler, some are more complex. Based on these models, combustion parameters such as peak pressure, start of combustion, rate of pressure rise are identified. These parameters can be further used in the fuel recognition process.

Before elaborating this aspect, the experimental set-up and the procedure of how fuel chemical and physical properties influence the combustion process are first presented.

CHAPTER 3

FUEL IDENTIFICATION METHODS

3.1 Methodology

The purpose is to develop a method to estimate at least one of the main combustion characteristics: peak cylinder pressure, rate of pressure rise or ignition delay. That is easily achieved when in-cylinder pressure sensors are used and the pressure trace is readily obtained.

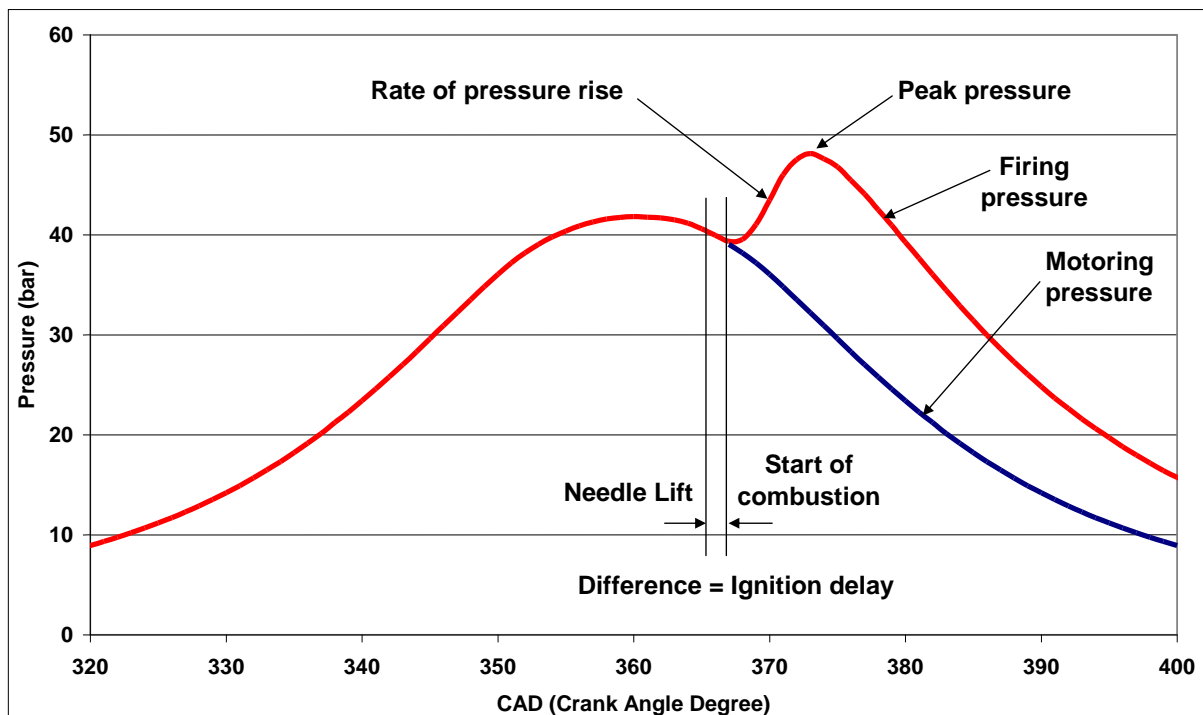


Figure 3.1 - Typical in-cylinder pressure trace

The start of combustion is defined as the point where the firing pressure curve separates from the motoring (cranking) pressure curve – Figure 3.1. The needle lift is measured separately with a position sensor.

The difference between the two signals represents the ignition delay. Estimation of ignition delay means, in fact, estimation of start of combustion. Thus, ideally, the measurement of the pressures in each cylinder will provide the required information for electronic controls.

For that purpose engineers usually use a pressure transducer whose price ranges from 1,800 to 2,500 US dollars, including cables and signal amplifier, and that happens for each cylinder under study. If an engine has four cylinders for example, then four such transducers are required – Figure 3.2. This is a very expensive solution.

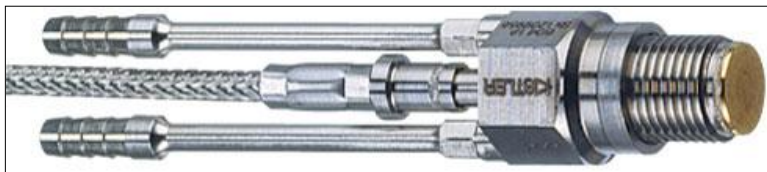
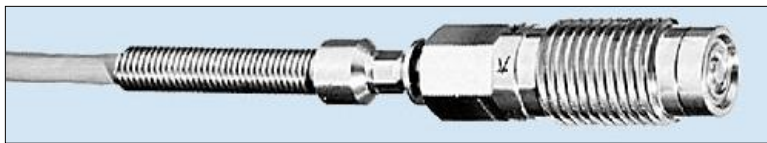


Figure 3.2 - Pressure sensors: regular and cooled, for high temperatures operating conditions

Moreover, special sleeves must be machined into the cylinder head in order to install these pressure sensors – Figure 3.3.

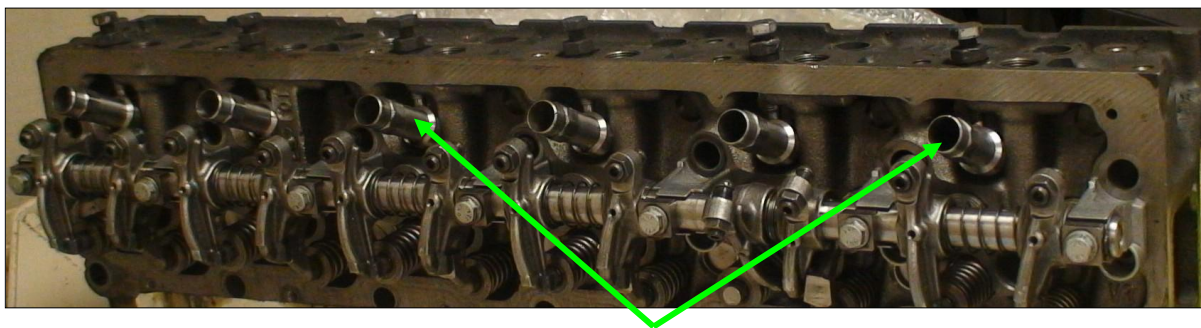


Figure 3.3 - Customized cylinder head with sleeves for pressure transducers (7.2 l Mercedes engine)

Proper handling and maintenance are among other issues. Obviously the solution offered by the use of pressure transducers is not feasible for series engines as far as it concerns price and reliability.

Fortunately there are other estimating methods of the pressure trace that do not require a pressure sensor. One of them is to use the engine speed signal which is measured by a speed sensor present on any vehicle. This methodology is robust since the instantaneous crankshaft speed (not the average rpm) fluctuates due to the in-cylinder pressure variations transmitted through the crank-slider mechanism and is directly expressed by the flywheel gear tooth spacing variations.

If the estimated pressure trace is satisfactory, then the cost of its evaluation is reduced drastically by eliminating the need of pressure sensors. The measurement of speed variation of the crankshaft is simple, inexpensive and is already available on modern engines – Figure 3.4. That is why the possibility of using crankshaft speed measurement to estimate engine torque and cylinder

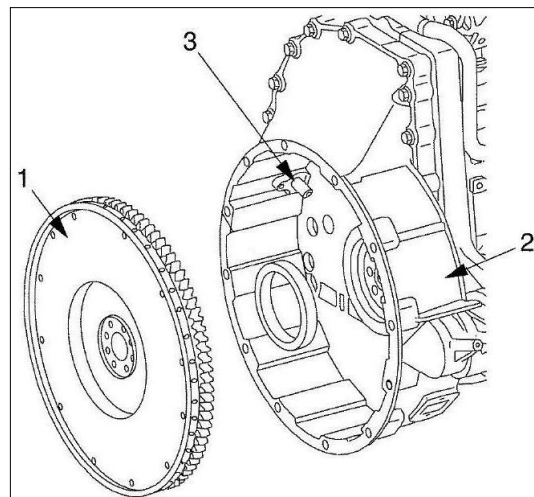


Figure 3.4 - Mercedes engine:

- 1. flywheel, 2. housing
- 3. crankshaft speed sensor

pressure variation, mainly peak cylinder pressure and its location with respect to TDC, looks very attractive. In order to achieve that, reliable correlations must be established between cylinder pressure variation and crankshaft speed variation. The estimated parameter (peak pressure, start of combustion, rate of pressure rise or its derivative) is then correlated to the cetane number to recognize the fuel type and finally, the engine controls are switched so that the engine operates safely and optimally on the identified fuel.

3.2 Dynamic model of the crankshaft

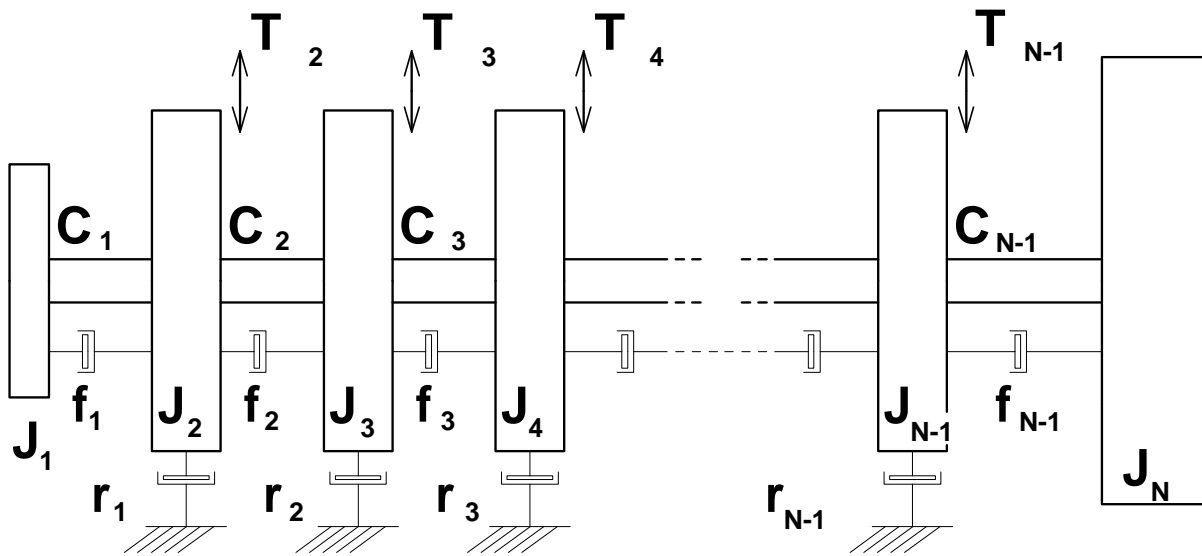


Figure 3.5 - Dynamic model of the crankshaft

In figure 3.5 a lumped mass dynamic model of the crankshaft has been represented using the following notations [24]:

J_1 = Mass moment of inertia of the pulley and auxiliaries at the front end

$J_2, J_3 \dots J_{N-1}$ = Mass moment of inertia the crank-slider mechanism

J_N = Mass moment of inertia of the flywheel

$C_1, C_2 \dots C_{N-1}$ = Crankshaft stiffness coefficients for each elastic element

$r_1, r_2 \dots r_{N-1}$ = Absolute damping coefficients

$f_1, f_2 \dots f_{N-1}$ = Relative damping coefficients

Excitation torques $T_2, T_3 \dots T_{N-1}$ represent the individual cylinder torques acting on the crankshaft.

3.3 Direct simulation method. Computation of motion for the 1st mass using transfer matrices

One way to determine the angular motion of the crankshaft is to use the transfer matrices of the lumped masses and mass-less elastic elements of the dynamic model of the crankshaft.

According to D.Taraza [24] the transfer matrices of masses and mass-less elastic elements are multiplied according to the crankshaft dynamic model to obtain:

$$Z_{N_k}^R = P_{N_k} \times E_{(N-1)_k} \times P_{(N-1)_k} \times \dots \times E_{1_k} \times P_{1_k} \times Z_{1_k}^L = H_k \times Z_{1_k}^L \quad (1)$$

The boundary conditions reveal that at both ends of the crankshaft the excitation torques are 0 (zero). The state vectors become:

$$Z_{1_k} = \begin{bmatrix} \theta^{\text{Re}} \\ 0 \\ \theta^{\text{Im}} \\ 0 \\ 1 \end{bmatrix}_{1k} \quad \text{and} \quad Z_{N_k} = \begin{bmatrix} \theta^{\text{Re}} \\ 0 \\ \theta^{\text{Im}} \\ 0 \\ 1 \end{bmatrix}_{Nk} \quad (2)$$

therefore only columns one, three and five will subsist in the H_k matrix:

$$H_k = \begin{bmatrix} h_{11_k} & 0 & h_{13_k} & 0 & h_{15_k} \\ h_{21_k} & 0 & h_{23_k} & 0 & h_{25_k} \\ h_{31_k} & 0 & h_{33_k} & 0 & h_{35_k} \\ h_{41_k} & 0 & h_{43_k} & 0 & h_{45_k} \\ 0 & 0 & 0 & 0 & 1 \end{bmatrix} \quad (3)$$

Cylinder excitations are in accordance with D. Taraza [24]:

$$M_i = M_{0_i} + \sum_{k=1}^N [A_{k_{p_i}} \cos k(\omega t + \varphi_i) + (B_{k_{p_i}} + B_{k_r}) \sin k(\omega t + \varphi_i)] \quad (4)$$

For an arbitrary harmonic component “k” the following relation is true:

$$M_{k_i} = (M_k^{\text{Re}})_i \cos k\omega t + j(M_k^{\text{Im}})_i \sin k\omega t \quad (5)$$

thus real and imaginary parts to be introduced in the point matrices are:

$$(M_k^{\text{Re}})_i = A_{k_{p_i}} \cos k\varphi_i - (B_{k_{p_i}} + B_{k_r}) \sin k\varphi_i \quad (6)$$

$$(M_k^{\text{Im}})_i = -A_{k_{p_i}} \sin k\varphi_i - (B_{k_{p_i}} + B_{k_r}) \cos k\varphi_i \quad (7)$$

The system has four equations with four unknowns: θ_{1k}^{Re} , θ_{1k}^{Im} , θ_{Nk}^{Re} , θ_{Nk}^{Im} .

The situation is similar for any intermediary mass i : θ_{1k}^{Re} , θ_{1k}^{Im} , θ_{ik}^{Re} , θ_{ik}^{Im} , therefore all four unknowns can be determined. For example, the components of the first mass deflections are:

$$\theta_{1k}^{\text{Re}} = \frac{-h_{25}h_{43}+h_{45}h_{23}}{h_{21}h_{43}-h_{23}h_{41}} \quad \text{and} \quad \theta_{1k}^{\text{Im}} = \frac{-h_{45}h_{21}+h_{25}h_{41}}{h_{21}h_{43}-h_{23}h_{41}} \quad (8)$$

By superposition the variation in time of the first mass angular deflection is obtained:

$$\theta_1 = \sum_{k=1}^M (\theta_{1k}^{\text{Re}} \cos k\omega t - \theta_{1k}^{\text{Im}} \sin k\omega t) \quad (9)$$

and furthermore the variation in time of the first mass angular speed according to D. Taraza [24]:

$$\dot{\theta}_1 = \omega_1 = k\omega \sum_{k=1}^M [-\theta_{1k}^{\text{Im}} \cos(k\omega t) - \theta_{1k}^{\text{Re}} \sin(k\omega t)] \quad (10)$$

The motion of each mass i is determined if the excitations (engine torques) are known for each cylinder i . In other words, if the in-cylinder pressure is known, the angular speed can be determined.

This direct calculation is used to validate the parameters of the dynamic model to assure the required accuracy when the calculation is reversed to determine the gas pressure torque from the measured crankshaft speed.

3.4 Single cylinder engine model validation

The direct simulation method used to determine the crankshaft speed from the cylinder pressure can be applied to single and multi-cylinder engines. Due to the complexity of the problem, the development of the technique has been implemented first on a single cylinder engine, the 0.7 L Deutz engine. The notations for the connecting elements, used in subchapters 3.2 and 3.3 are utilized to build the dynamic model of the crankshaft – Figure 3.6.

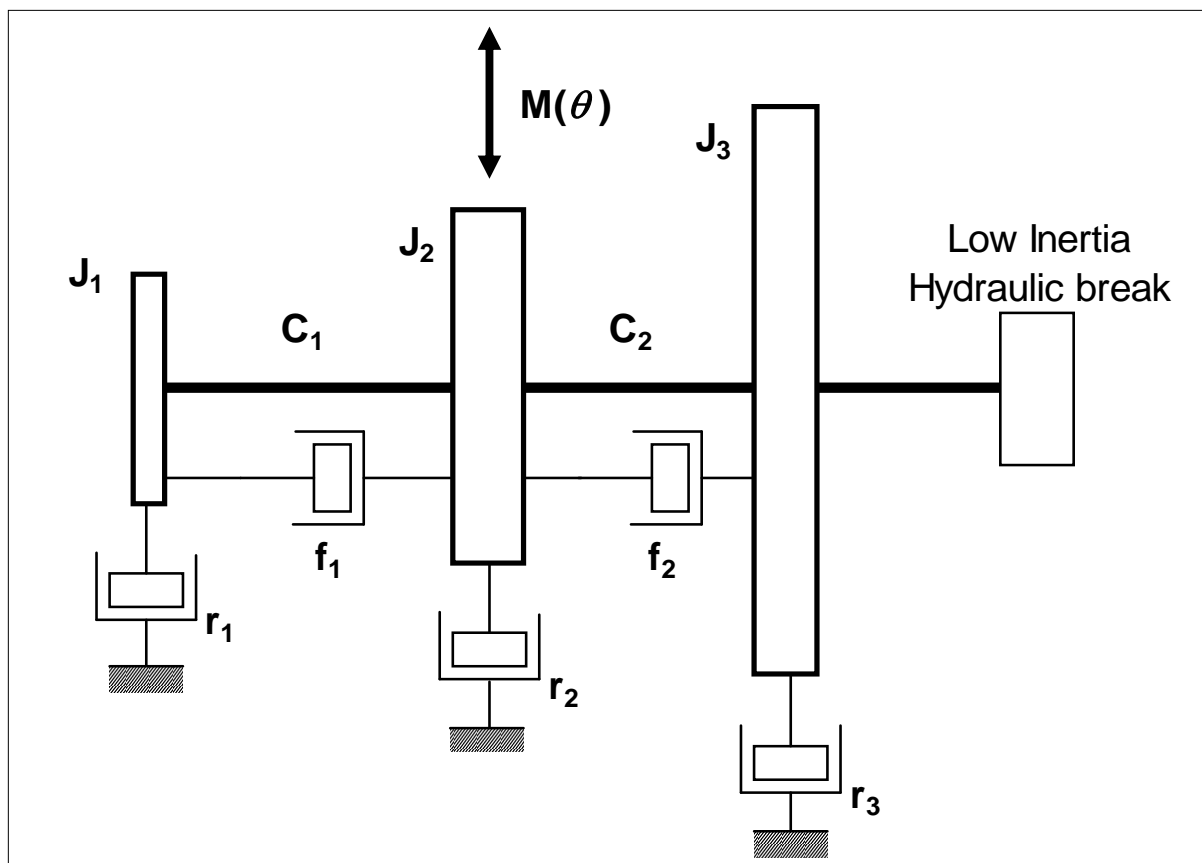


Figure 3.6 - Lumped mass dynamic model of the single cylinder engine

The point and field transfer matrices are determined by the mass moments of inertia, by the absolute damping coefficients as a consequence of the friction between the piston and the liner, by the stiffness coefficients of the elastic elements of the crankshaft and by the relative damping coefficients as a result of the oil film being squeeze in the main bearings as stated by D. Taraza [24].

The question is how to determine these parameters. The absolute and relative damping coefficients can be adopted. The mass moments of inertia and the stiffness coefficients must be precisely determined though. To achieve that a spare 0.7 l Deutz engine was dismantled and the separate rotating parts such as crankshaft, camshaft, flywheel, balancing shaft, oil pump gear, connecting rods were drawn using CAD software, as represented in Table 3.1.

By individually weighing the parts, their masses were determined. After drawing the parts, their volumes could be computed using the software. An alternate method would be to submerge the parts in liquid in a tank and measure the difference in liquid heights. Having the mass and the volume for each part, the individual densities were then calculated. Finally, after inserting the density as a value, the mass moment of inertia of each rotating part was automatically computed using the software.

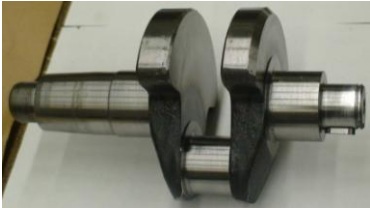
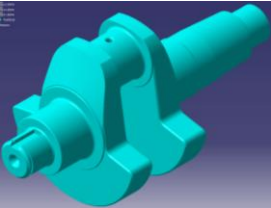





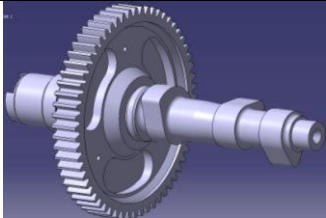
Part name	Actual part	Designed part	Mass (kg)	Mass moment of inertia (kg*m ²)
Crankshaft			5.415	0.006740
Flywheel			23.45	0.227400
				
Camshaft			1.91	0.001874

Table 3.1 - Deutz single cylinder engine parts and their mass characteristics


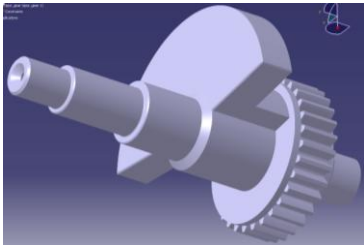

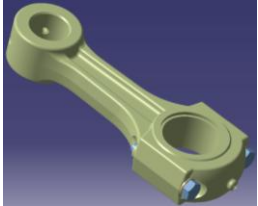

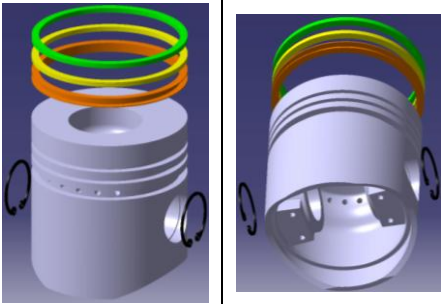
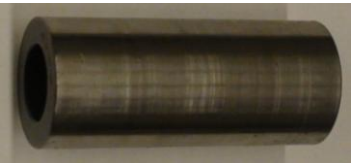

Part name	Actual part	Designed part	Mass (kg)	Mass moment of inertia (kg*m ²)
Balancing shaft			1.705	0.000904
Connecting rod			0.5	-
Piston assembly			0.52	-
Piston bolt			0.21	-

Table 3.1 (continued) - Deutz single cylinder engine parts and their mass characteristics







Part name	Actual part	Designed part	Mass (kg)	Mass moment of inertia (kg*m ²)
Pulley			0.445	0.000898
Crankshaft gear			0.285	0.000162
Oil pump gear			0.14	0.000172
Total moving engine parts			34.58	0.24481

Table 3.1 (continued) - Deutz single cylinder engine parts and their mass characteristics

The mass in translation is:

$$m_{tr} = m_{group_piston} + 0.275 * m_{connecting_rod} = 0.73 + 0.275 * 0.5 = 0.8675 \text{ kg}$$

The individual mass of the connecting rod in rotation is:

$$m_{cr} = 0.725 * m_{connecting_rod} = 0.725 * 0.5 \text{ kg} = 0.3625 \text{ kg}$$

The corresponding summation is:

$$m_{tr}/2 + m_{cr} = 0.8675 \text{ kg} / 2 + 0.3625 \text{ kg} = 0.79625 \text{ kg}$$

The crankshaft radius is:

$$r = \text{stroke} / 2 = 0.082 \text{ m} / 2 = 0.041 \text{ m}$$

The total mass moment of inertia is:

$$J_{total} = J_{crankshaft} + 4 * (m_{tr} / 2 + m_{cr}) * r^2 + J_{flywheel} + J_{camshaft} * (1/2)^2 + \\ + 2^2 * J_{balancing_shaft} + J_{pulley} + J_{gear1} + J_{gear_oil}$$

$$J_{total} = 0.006740 + 4 * 0.79625 * 0.041^2 + 0.227400 + 0.001874 / 4 + \\ + 4 * 0.000904 + 0.000898 + 0.000162 + 0.000172$$

$$J_{total} = 0.006740 + 0.005353985 + 0.227400 + 0.0004685 + \\ + 0.003616 + 0.000898 + 0.000162 + 0.000172$$

$$J_{total} = 0.244810485 \text{ kg} * \text{m}^2$$

Using the same software, the stiffness coefficients were evaluated by FEA (Finite Element Analysis) while applying a known torque and reading the corresponding angular deformation - Figure 3.8. The torque divided by the deformation yielded the stiffness of each elastic element.

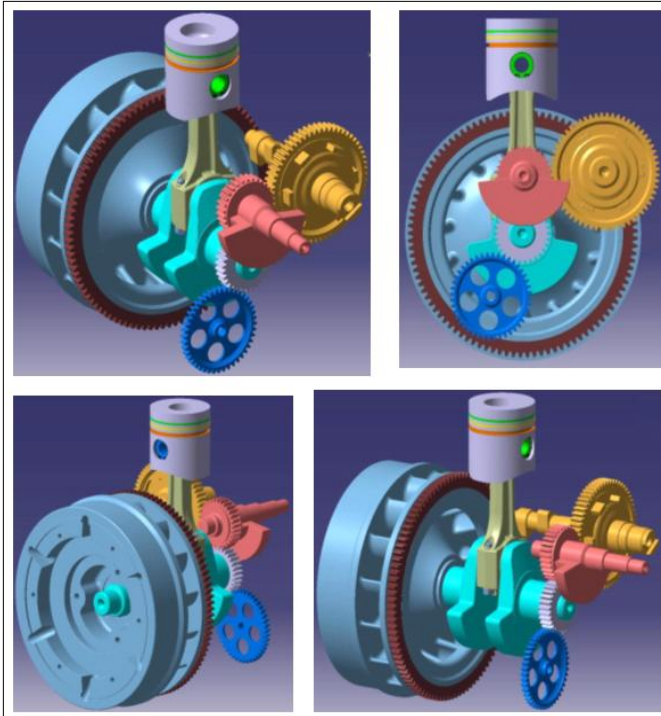


Figure 3.7 - 3D drawing of the single cylinder engine (Catia V5)

Once the field and point matrices were determined, the computational procedure presented in subchapter 3.3 was followed and the angular speed variation was estimated from the in-cylinder pressure.

ULSD and S-25 (Synthetic fuel S-8 having cetane number 25) were tested at 1500 rpm

and 4 Nm torque (2.9 bar IMEP). Both cases show good coincidence between simulation and measured data – Figure 3.9.

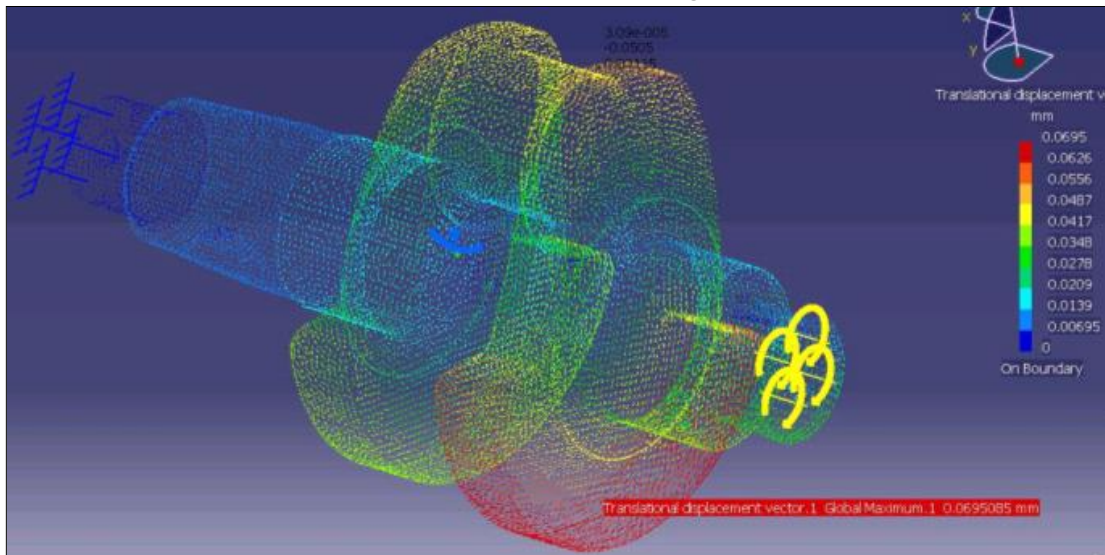


Figure 3.8 - FEM computation of the shaft stiffness (Catia V5)

The Matlab code for the computation of the crankshaft speed from the in-cylinder pressure is presented in the Appendix.

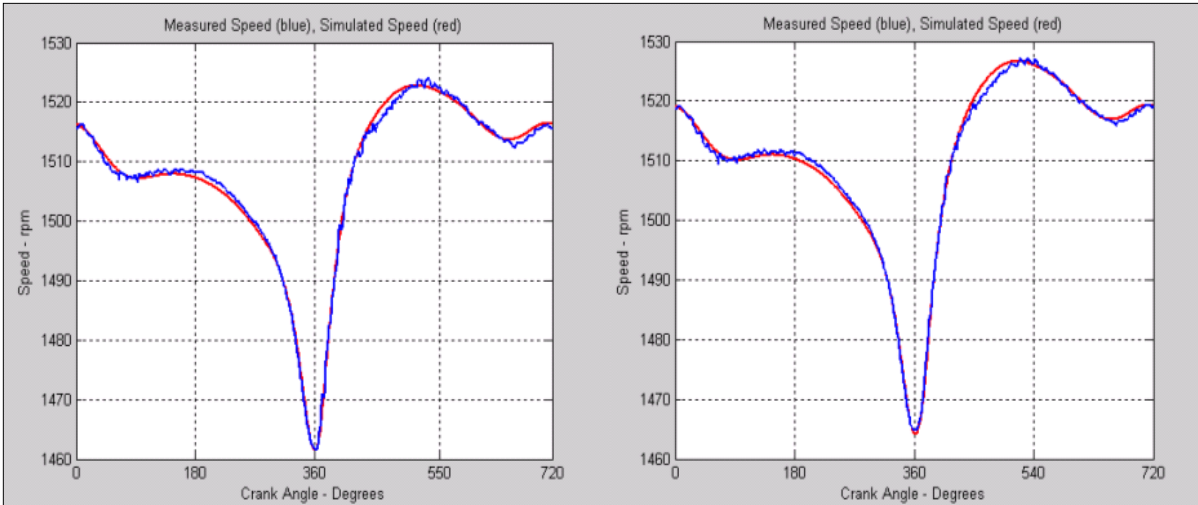


Figure 3.9 - Single-cylinder engine model validation: left (ULSD), right (S-8); measured speed (blue), simulated speed (red); the operating point is 1500 rpm and 4 Nm torque / 2.9 bar IMEP

The direct method of calculation of the crankshaft speed from the in-cylinder pressure has been used to validate the parameters of the dynamic model in order to ensure the required accuracy for a reversed computation of the in-cylinder pressure from the crankshaft speed.

This reversed estimation, as the name suggests, uses the same transfer matrices but in a reverse order, and is called the transfer matrices reversed approach.

3.5 Model-based recognition (transfer matrices reversed) method on a single cylinder engine

This approach is accurate but it requires a very precise dynamic model of the power-train. Mass moments of inertia of the engine moving parts, shafts stiffnesses, absolute and relative damping coefficients and detailed engine construction data are necessary. Instantaneous crankshaft speed can be measured using a shaft encoder at the front of the engine (pulley side) or at the back of the engine (flywheel side). The second option is preferred in order to minimize distortions caused by torsional vibrations. From the measured crankshaft speed the gas pressure torque is calculated. The gas pressure torque is used to determine the cylinder pressure.

As compared to the transfer matrices direct approach where the crankshaft speed was computed from the in-cylinder pressure, in the transfer matrices reversed approach the input data is now the instantaneous engine speed, preferably at the flywheel where the measured signal is less affected by noise and vibrations. The output is the engine torque from which the in-cylinder pressure is computed.

In this case the terms of the matrix $H_k (h_{ij_k})$ are functions of the unknown values of the harmonic components of the engine torque.

Using the notations in Figure 3.5 and the dynamic model in Figure 3.6 the transfer matrices of masses and mass-less elastic elements according to the crankshaft are multiplied to obtain:

$$Z_{1_k} = P_{1_k} \times F_{1_k} \times P_{2_k} \times F_{2_k} \times P_{3_k} \times Z_{3_k} , \quad (14) \quad \text{where:}$$

$$P_{3_k} = \begin{bmatrix} 1 & 0 & 0 & 0 & 0 \\ -J_3(k\omega)^2 & 1 & -r_3(k\omega) & 0 & 0 \\ 0 & 0 & 1 & 0 & 0 \\ r_3(k\omega) & 0 & -J_3(k\omega)^2 & 1 & 0 \\ 0 & 0 & 0 & 0 & 1 \end{bmatrix} = \begin{bmatrix} P_{3_k}^* & 0 \\ 0 & 1 \end{bmatrix} \quad (15) \quad \text{and}$$

$$F_{2_k} = \begin{bmatrix} 1 & \frac{C_2}{C_2^2 + (f_2 k\omega)^2} & 0 & \frac{f_2(k\omega)}{C_2^2 + (f_2 k\omega)^2} & 0 \\ 0 & 1 & 0 & 0 & 0 \\ 0 & \frac{-f_2(k\omega)}{C_2^2 + (f_2 k\omega)^2} & 1 & \frac{C_2}{C_2^2 + (f_2 k\omega)^2} & 0 \\ 0 & 0 & 0 & 1 & 0 \\ 0 & 0 & 0 & 0 & 1 \end{bmatrix} = \begin{bmatrix} F_{2_k}^* & 0 \\ 0 & 1 \end{bmatrix} \quad (16) \quad \text{and}$$

$$P_{2_k} = \begin{bmatrix} 1 & 0 & 0 & 0 & 0 \\ -J_2(k\omega)^2 & 1 & -r_2(k\omega) & 0 & -A_{kp} \cos k\varphi_i + (B_{kp} + B_{ktr}) \sin k\varphi_i \\ 0 & 0 & 1 & 0 & 0 \\ r_2(k\omega) & 0 & -J_2(k\omega)^2 & 1 & A_{kp} \sin k\varphi_i + (B_{kp} + B_{ktr}) \cos k\varphi_i \\ 0 & 0 & 0 & 0 & 1 \end{bmatrix} \quad (17)$$

$$\text{or } P_{2_k} = \begin{bmatrix} 0 \\ P_{2_k}^* & -T_k^{\text{Re}} \\ 0 \\ -T_k^{\text{Im}} \\ 0 & 1 \end{bmatrix}, \quad \text{with the notation } \begin{bmatrix} 0 \\ -T_k^{\text{Re}} \\ 0 \\ -T_k^{\text{Im}} \end{bmatrix} = T_{2k}$$

It is true that:

$$F_{1_k} = \begin{bmatrix} 1 & \frac{C_1}{C_1^2 + (f_1 k \omega)^2} & 0 & \frac{f_1(k\omega)}{C_1^2 + (f_1 k \omega)^2} & 0 \\ 0 & 1 & 0 & 0 & 0 \\ 0 & \frac{-f_1(k\omega)}{C_1^2 + (f_1 k \omega)^2} & 1 & \frac{C_1}{C_1^2 + (f_1 k \omega)^2} & 0 \\ 0 & 0 & 0 & 1 & 0 \\ 0 & 0 & 0 & 0 & 1 \end{bmatrix} = \begin{bmatrix} F_{1_k}^* & 0 \\ 0 & 1 \end{bmatrix} \quad (18)$$

and

$$P_{1_k} = \begin{bmatrix} 1 & 0 & 0 & 0 & 0 \\ -J_1(k\omega)^2 & 1 & -r_1(k\omega) & 0 & 0 \\ 0 & 0 & 1 & 0 & 0 \\ r_1(k\omega) & 0 & -J_1(k\omega)^2 & 1 & 0 \\ 0 & 0 & 0 & 0 & 1 \end{bmatrix} = \begin{bmatrix} P_{1_k}^* & 0 \\ 0 & 1 \end{bmatrix} \quad (19)$$

The multiplication in steps in the initial matrix equation is the following:

$$F_{2_k} \times P_{3_k} = \begin{bmatrix} F_{2_k}^* P_{3_k}^* & 0 \\ 0 & 1 \end{bmatrix}$$

$$P_{2_k} \times (F_{2_k} \times P_{3_k}) = \begin{bmatrix} P_{2_k}^* & T_{2k} \\ 0 & 1 \end{bmatrix} \times \begin{bmatrix} F_{2_k}^* P_{3_k}^* & 0 \\ 0 & 1 \end{bmatrix} = \begin{bmatrix} P_{2_k}^* F_{2_k}^* P_{3_k}^* & T_{2k} \\ 0 & 1 \end{bmatrix}$$

$$F_{1_k} \times (P_{2_k} \times F_{2_k} \times P_{3_k}) = \begin{bmatrix} F_{1_k}^* & 0 \\ 0 & 1 \end{bmatrix} \times \begin{bmatrix} P_{2_k}^* F_{2_k}^* P_{3_k}^* & T_{2k} \\ 0 & 1 \end{bmatrix} = \begin{bmatrix} F_{1_k}^* P_{2_k}^* F_{2_k}^* P_{3_k}^* & F_{1_k}^* T_{2k} \\ 0 & 1 \end{bmatrix}$$

$$P_{1_k} \times (F_{1_k} \times P_{2_k} \times F_{2_k} \times P_{3_k}) = \begin{bmatrix} P_{1_k}^* & 0 \\ 0 & 1 \end{bmatrix} \times \begin{bmatrix} F_{1_k}^* P_{2_k}^* F_{2_k}^* P_{3_k}^* & F_{1_k}^* T_{2k} \\ 0 & 1 \end{bmatrix} = \begin{bmatrix} P_{1_k}^* F_{1_k}^* P_{2_k}^* F_{2_k}^* P_{3_k}^* & P_{1_k}^* F_{1_k}^* T_{2k} \\ 0 & 1 \end{bmatrix}$$

or in a simpler form:

$$P_{1_k} \times (F_{1_k} \times P_{2_k} \times F_{2_k} \times P_{3_k}) = \begin{bmatrix} H_k & P_{1_k}^* F_{1_k}^* T_{2k} \\ 0 & 1 \end{bmatrix} \quad (20)$$

For a single cylinder engine mass # 3 represents the flywheel (F). The indices 'F' is used instead of '3' and the initial system of equations becomes:

$$\begin{bmatrix} \theta^{\text{Re}} \\ 0 \\ \theta^{\text{Im}} \\ 0 \\ 1 \end{bmatrix}_{1k} = \begin{bmatrix} H_k & P_{1_k}^* F_{1_k}^* T_{2k} \\ 0 & 1 \end{bmatrix} \times \begin{bmatrix} \theta^{\text{Re}} \\ 0 \\ \theta^{\text{Im}} \\ 0 \\ 1 \end{bmatrix}_{F_k} \quad (21)$$

where the H_k matrix is a function of engine physical parameters only. The

$P_{1_k}^* F_{1_k}^* T_{2k}$ term also includes the influence of the engine torque.

$$F_{1_k}^* \times T_{2k} = \begin{bmatrix} 1 & \frac{C_1}{C_1^2 + (f_1 k \omega)^2} & 0 & \frac{f_1(k\omega)}{C_1^2 + (f_1 k \omega)^2} \\ 0 & 1 & 0 & 0 \\ 0 & \frac{-f_1(k\omega)}{C_1^2 + (f_1 k \omega)^2} & 1 & \frac{C_1}{C_1^2 + (f_1 k \omega)^2} \\ 0 & 0 & 0 & 1 \end{bmatrix} \times \begin{bmatrix} 0 \\ -T_k^{\text{Re}} \\ 0 \\ -T_k^{\text{Im}} \end{bmatrix}$$

$$F_{1_k}^* \times T_{2k} = \begin{bmatrix} -T_k^{\text{Re}} \frac{C_1}{C_1^2 + (f_1 k \omega)^2} - T_k^{\text{Im}} \frac{f_1(k\omega)}{C_1^2 + (f_1 k \omega)^2} \\ -T_k^{\text{Re}} \\ T_k^{\text{Re}} \frac{f_1(k\omega)}{C_1^2 + (f_1 k \omega)^2} - T_k^{\text{Im}} \frac{C_1}{C_1^2 + (f_1 k \omega)^2} \\ -T_k^{\text{Im}} \end{bmatrix} \quad (22)$$

Furthermore

$$\begin{aligned}
 P_{1_k}^* F_{1_k}^* T_{2k} &= \begin{bmatrix} 1 & 0 & 0 & 0 \\ -J_1(k\omega)^2 & 1 & -r_1(k\omega) & 0 \\ 0 & 0 & 1 & 0 \\ r_1(k\omega) & 0 & -J_1(k\omega)^2 & 1 \end{bmatrix} \times \begin{bmatrix} -T_k^{\text{Re}} \frac{C_1}{C_1^2 + (f_1 k \omega)^2} - T_k^{\text{Im}} \frac{f_1(k\omega)}{C_1^2 + (f_1 k \omega)^2} \\ -T_k^{\text{Re}} \\ T_k^{\text{Re}} \frac{f_1(k\omega)}{C_1^2 + (f_1 k \omega)^2} - T_k^{\text{Im}} \frac{C_1}{C_1^2 + (f_1 k \omega)^2} \\ -T_k^{\text{Im}} \end{bmatrix} = \\
 &= \begin{bmatrix} -T_k^{\text{Re}} \frac{C_1}{C_1^2 + (f_1 k \omega)^2} - T_k^{\text{Im}} \frac{f_1(k\omega)}{C_1^2 + (f_1 k \omega)^2} \\ -J_1(k\omega)^2 \left[-T_k^{\text{Re}} \frac{C_1}{C_1^2 + (f_1 k \omega)^2} - T_k^{\text{Im}} \frac{f_1(k\omega)}{C_1^2 + (f_1 k \omega)^2} \right] - T_k^{\text{Re}} - r_1(k\omega) \left[T_k^{\text{Re}} \frac{f_1(k\omega)}{C_1^2 + (f_1 k \omega)^2} - T_k^{\text{Im}} \frac{C_1}{C_1^2 + (f_1 k \omega)^2} \right] \\ T_k^{\text{Re}} \frac{f_1(k\omega)}{C_1^2 + (f_1 k \omega)^2} - T_k^{\text{Im}} \frac{C_1}{C_1^2 + (f_1 k \omega)^2} \\ r_1(k\omega) \left[-T_k^{\text{Re}} \frac{C_1}{C_1^2 + (f_1 k \omega)^2} - T_k^{\text{Im}} \frac{f_1(k\omega)}{C_1^2 + (f_1 k \omega)^2} \right] - J_1(k\omega)^2 \left[T_k^{\text{Re}} \frac{f_1(k\omega)}{C_1^2 + (f_1 k \omega)^2} - T_k^{\text{Im}} \frac{C_1}{C_1^2 + (f_1 k \omega)^2} \right] - T_k^{\text{Im}} \end{bmatrix} \quad (23)
 \end{aligned}$$

and the system of equations (21) becomes:

$$\begin{bmatrix} \theta^{\text{Re}} \\ 0 \\ \theta^{\text{Im}} \\ 0 \\ 1 \end{bmatrix}_{1k} = \begin{bmatrix} h_{11} & h_{12} & h_{13} & h_{14} & h_{15} \\ h_{21} & h_{22} & h_{23} & h_{24} & h_{25} \\ h_{31} & h_{32} & h_{33} & h_{34} & h_{35} \\ h_{41} & h_{42} & h_{43} & h_{44} & h_{45} \\ 0 & & & & 1 \end{bmatrix} \times \begin{bmatrix} \theta^{\text{Re}} \\ 0 \\ \theta^{\text{Im}} \\ 0 \\ 1 \end{bmatrix}_{F_k} \quad (24). \text{ The coefficients } h_{15}, h_{25}, h_{35} \text{ and } h_{45} \text{ are:}$$

$$h_{15} = -T_k^{\text{Re}} \frac{C_1}{C_1^2 + (f_1 k \omega)^2} - T_k^{\text{Im}} \frac{f_1(k\omega)}{C_1^2 + (f_1 k \omega)^2}$$

$$h_{25} = -J_1(k\omega)^2 \left[-T_k^{\text{Re}} \frac{C_1}{C_1^2 + (f_1 k \omega)^2} - T_k^{\text{Im}} \frac{f_1(k\omega)}{C_1^2 + (f_1 k \omega)^2} \right] - T_k^{\text{Re}} - r_1(k\omega) \left[T_k^{\text{Re}} \frac{f_1(k\omega)}{C_1^2 + (f_1 k \omega)^2} - T_k^{\text{Im}} \frac{C_1}{C_1^2 + (f_1 k \omega)^2} \right]$$

$$h_{35} = T_k^{\text{Re}} \frac{f_1(k\omega)}{C_1^2 + (f_1 k \omega)^2} - T_k^{\text{Im}} \frac{C_1}{C_1^2 + (f_1 k \omega)^2}$$

$$h_{45} = r_1(k\omega) \left[-T_k^{\text{Re}} \frac{C_1}{C_1^2 + (f_1 k \omega)^2} - T_k^{\text{Im}} \frac{f_1(k\omega)}{C_1^2 + (f_1 k \omega)^2} \right] - J_1(k\omega)^2 \left[T_k^{\text{Re}} \frac{f_1(k\omega)}{C_1^2 + (f_1 k \omega)^2} - T_k^{\text{Im}} \frac{C_1}{C_1^2 + (f_1 k \omega)^2} \right] - T_k^{\text{Im}}$$

The terms h_{25} and h_{45} are regrouped and expressed as:

$$h_{25} = T_k^{\text{Re}} \left[\frac{J_1 C_1 (k\omega)^2}{C_1^2 + (f_1 k\omega)^2} - 1 - r_1(k\omega) \frac{f_1(k\omega)}{C_1^2 + (f_1 k\omega)^2} \right] + T_k^{\text{Im}} \left[J_1 \frac{(k\omega)^2 f_1(k\omega)}{C_1^2 + (f_1 k\omega)^2} + r_1(k\omega) \frac{C_1}{C_1^2 + (f_1 k\omega)^2} \right]$$

$$h_{45} = T_k^{\text{Re}} \left[-r_1(k\omega) \frac{C_1}{C_1^2 + (f_1 k\omega)^2} - J_1 \frac{(k\omega)^2 f_1(k\omega)}{C_1^2 + (f_1 k\omega)^2} \right] + T_k^{\text{Im}} \left[-r_1(k\omega) \frac{f_1(k\omega)}{C_1^2 + (f_1 k\omega)^2} + J_1 \frac{(k\omega)^2 C_1}{C_1^2 + (f_1 k\omega)^2} - 1 \right]$$

By using the following convenient notations:

$$\psi = \frac{J_1 C_1 (k\omega)^2}{C_1^2 + (f_1 k\omega)^2} - 1 - r_1(k\omega) \frac{f_1(k\omega)}{C_1^2 + (f_1 k\omega)^2}$$

$$\phi = J_1 \frac{(k\omega)^2 f_1(k\omega)}{C_1^2 + (f_1 k\omega)^2} - r_1(k\omega) \frac{C_1}{C_1^2 + (f_1 k\omega)^2}$$

and equations (2) and (4) of the system of equations (24):

$$0 = h_{21} \theta_{F_k}^{\text{Re}} + h_{23} \theta_{F_k}^{\text{Im}} + h_{25}$$

$$0 = h_{41} \theta_{F_k}^{\text{Re}} + h_{43} \theta_{F_k}^{\text{Im}} + h_{45}$$

the following expressions are obtained:

$$-(h_{21} \theta_{F_k}^{\text{Re}} + h_{23} \theta_{F_k}^{\text{Im}}) = h_{25} = T_k^{\text{Re}} \psi + T_k^{\text{Im}} \phi$$

$$-(h_{41} \theta_{F_k}^{\text{Re}} + h_{43} \theta_{F_k}^{\text{Im}}) = h_{45} = -T_k^{\text{Re}} \phi + T_k^{\text{Im}} \psi \quad \text{from which the expressions}$$

of the real and imaginary parts of the engine torque are derived as a function of the deflections (or the speed) at the flywheel :

$$T_k^{\text{Re}} = \frac{-(h_{21} \theta_{F_k}^{\text{Re}} + h_{23} \theta_{F_k}^{\text{Im}}) \psi + (h_{41} \theta_{F_k}^{\text{Re}} + h_{43} \theta_{F_k}^{\text{Im}}) \phi}{\psi^2 + \phi^2} \quad (25) \quad \text{and}$$

$$T_k^{\text{Im}} = \frac{-(h_{41}\theta_{F_k}^{\text{Re}} + h_{43}\theta_{F_k}^{\text{Im}})\psi - (h_{41}\theta_{F_k}^{\text{Re}} + h_{43}\theta_{F_k}^{\text{Im}})\phi}{\psi^2 + \phi^2} \quad (26)$$

The harmonic component of order “k” of the engine torque is:

$$T_k = (T_k^{\text{Re}})\cos k\omega t + j(T_k^{\text{Im}})\sin k\omega t \quad (27)$$

and the total engine torque is [24]:

$$T = T_0 + \sum_{k=1}^N [A_{k_p} \cos k(\omega t + \varphi) + (B_{k_p} + B_{k_r}) \sin k(\omega t + \varphi)] \quad (28)$$

The simulation results show that for the operating condition of 1500 rpm, 4 Nm torque / 2.9 bar IMEP the single cylinder engine Deutz 0.7 l the engine torque can be evaluated from the measured flywheel speed both when ULSD and S-8 are used - Figure 3.10.

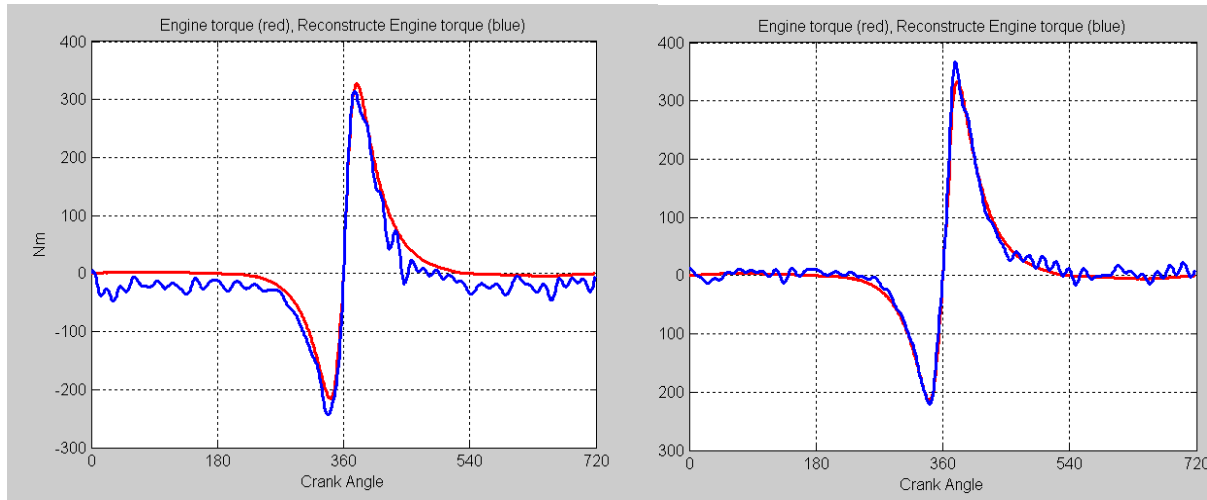


Figure 3.10 - Gas pressure torque reconstruction by reverse calculation at 1500 rpm, 4 Nm torque: left (ULSD), right (S-8), engine torque (red), reconstructed engine torque (blue)

It is to be noticed that the gas pressure torque T_p at TDC is = 0 (zero).

The in-cylinder pressure p is related to the gas pressure torque T_p by:

$$p = p_c + T_p \cos \beta / (A_p R \sin(\theta + \beta)) \quad (29)$$

where

p = in-cylinder pressure

p_c = carter pressure

T_p = gas pressure torque

A_p = piston area

R = crank radius

L = length of connecting rod

θ = crank angle

β = angle between the connecting rod and the cylinder axis,

$$\beta = \arcsin\left(\frac{R}{L} \sin \theta\right)$$

At TDC, where θ and β are 0 (zero), $\sin(\theta + \beta)$ also equals 0 (zero) hence the second term of the summation in (29) represents a division of 0 (zero) to 0 (zero) which, mathematically, is undefined.

To avoid the division by zero, the pressure around TDC is calculated

as:

$$P_{j+1} = \frac{M_{j+1} - M_j}{\text{trig}(\theta_{j+1}) - \text{trig}(\theta_j)} \frac{1}{A_p R}$$

and the results are displayed in figure 3.11.

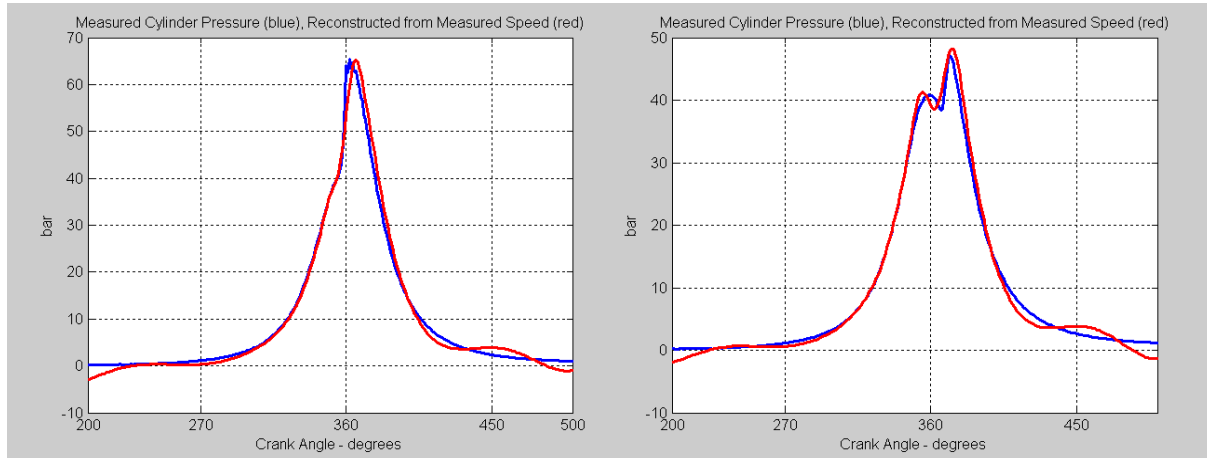


Figure 3.11 - Cylinder pressure reconstruction by reverse calculation at 1500 rpm, 4 Nm torque: left (ULSD), right (S-8); measured cylinder pressure (Blue), reconstructed pressure from measured speed (Red)

In conclusion, the model based method applied on a single-cylinder engine is fairly accurate because it reconstructs the pressure trace from which different combustion parameters can be evaluated. On the other hand, the technique is computationally intensive and it is hard to imagine that it could be used in real time (on-board) applications to identify the fuel. For this reason a more direct method has been developed and it is presented in the next chapter.

3.6 Direct Recognition Method on a single-cylinder engine

In order to find a technique less computational than the Model-Based Recognition Method, the Direct Recognition Method is considered as an alternative. The procedure assumes that the crankshaft is a rigid body and consists of the following steps:

1) the measured speed is smoothed by a Fast Fourier Transformation and expressed as a Fourier series

2) the speed is then differentiated to obtain the crankshaft angular acceleration

3) the angular acceleration is multiplied by the total mass moment of inertia to yield the engine torque

4) the reciprocating inertia torque is subtracted from the engine torque and the gas pressure torque is obtained

5) the gas pressure torque is used in the same way to obtain the cylinder pressure.

For the single cylinder engine, the 0.7 L Deutz, the engine torque is obtained from the measured flywheel speed for the same operating conditions: 1500 rpm, 4 Nm torque IMEP = 2.9 bar - Figure 3.12.

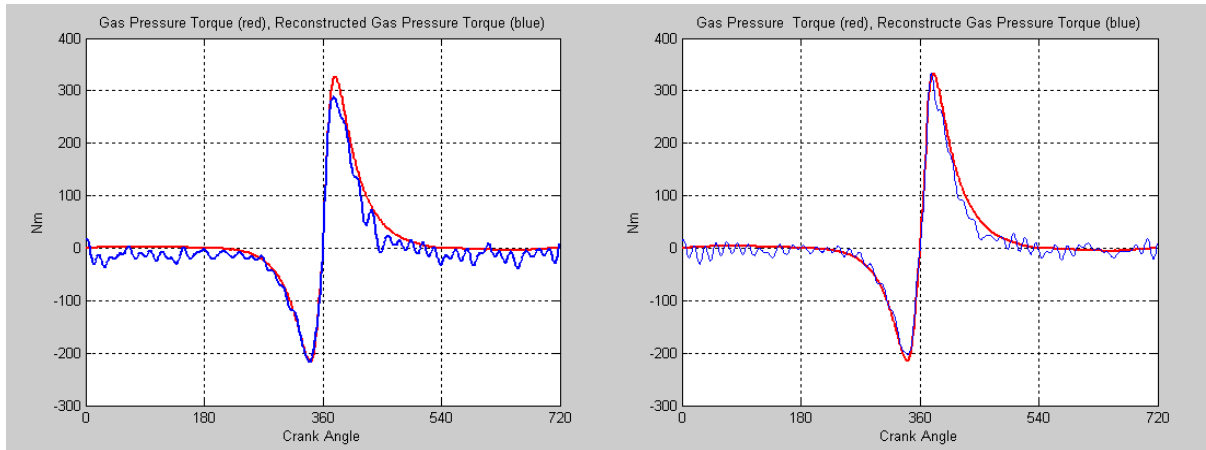


Figure 3.12 - Gas pressure torque reconstruction by direct recognition method: left (ULSD), right (S-8); engine torque (red), reconstructed engine torque (blue)

From the gas pressure torque the cylinder pressure is calculated –

Figure 3.13.

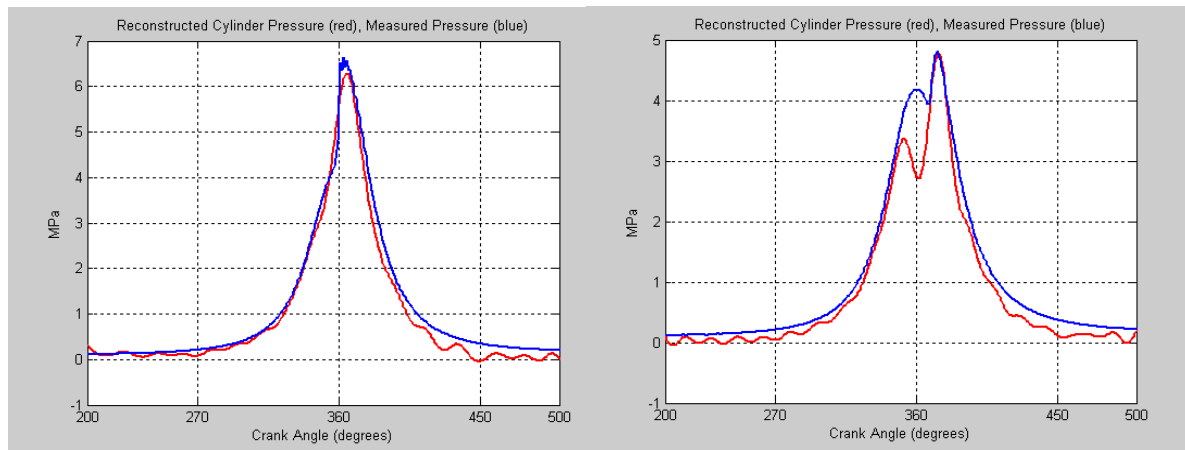


Figure 3.13 - Cylinder pressure reconstruction by direct recognition method: left (ULSD), right (S-8) reconstructed cylinder pressure (red), measured pressure (blue)

In conclusion, because of the rigid body assumption, the estimation of pressure trace using Direct Recognition Method is less accurate than the estimation of pressure trace using Model-Based Recognition Method – compare Figures 3.11 and 3.13.

Nonetheless, on a single-cylinder engine, both Direct Recognition Method and Model-Based Recognition Method determine fairly well the peak cylinder pressure and its location with respect to the TDC. The Model-Based Recognition Technique yields slightly better estimates, while the Direct Recognition Technique is less computationally intensive.

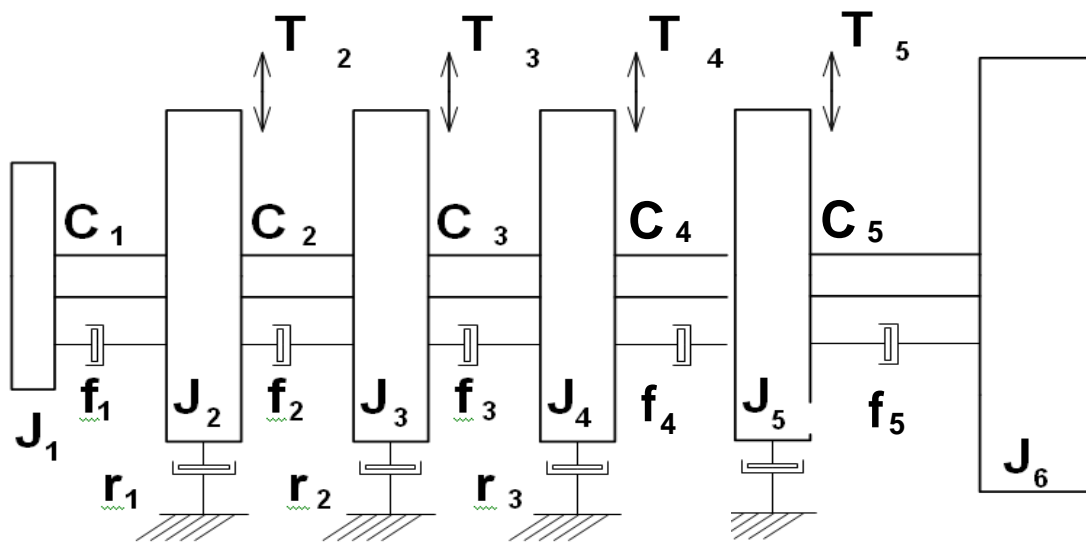


Figure 3.14a - Lumped mass dynamic model of a four-cylinder engine

If the Model-Based Recognition Technique is applied on a multi-cylinder engine, e.g. on a four-cylinder engine – Figure 3.14, then expression (14) in subchapter 3.5, representing the multiplication of

transfer matrices of masses and mass-less elastic elements according to the crankshaft model, becomes as follows:

$$Z_{1_k} = P_{1_k} \times F_{1_k} \times P_{2_k} \times F_{2_k} \times P_{3_k} \times F_{3_k} \times P_{4_k} \times F_{4_k} \times P_{5_k} \times F_{5_k} \times P_{6_k} \times Z_{6_k} \quad (30)$$

Considering that all four cylinder torques are equal $T_{2k} = T_{3k} = T_{4k} = T_{5k} = T_k$,

then the multiplication in steps – see expression (20), is the following:

$$F_{5_k} \times P_{6_k} = \begin{bmatrix} F_{5_k}^* P_{6_k}^* & 0 \\ 0 & 1 \end{bmatrix}$$

$$P_{5_k} \times (F_{5_k} \times P_{6_k}) = \begin{bmatrix} P_{5_k}^* & T_k \\ 0 & 1 \end{bmatrix} \times \begin{bmatrix} F_{5_k}^* P_{6_k}^* & 0 \\ 0 & 1 \end{bmatrix} = \begin{bmatrix} P_{5_k}^* F_{5_k}^* P_{6_k}^* & T_k \\ 0 & 1 \end{bmatrix}$$

$$F_{4_k} \times (P_{5_k} \times F_{5_k} \times P_{6_k}) = \begin{bmatrix} F_{4_k}^* & 0 \\ 0 & 1 \end{bmatrix} \times \begin{bmatrix} P_{5_k}^* F_{5_k}^* P_{6_k}^* & T_k \\ 0 & 1 \end{bmatrix} = \begin{bmatrix} F_{4_k}^* P_{5_k}^* F_{5_k}^* P_{6_k}^* & F_{4_k}^* T_k \\ 0 & 1 \end{bmatrix}$$

$$\begin{aligned} P_{4_k} \times (F_{4_k} \times P_{5_k} \times F_{5_k} \times P_{6_k}) &= \begin{bmatrix} P_{4_k}^* & T_k \\ 0 & 1 \end{bmatrix} \times \begin{bmatrix} F_{4_k}^* P_{5_k}^* F_{5_k}^* P_{6_k}^* & F_{4_k}^* T_k \\ 0 & 1 \end{bmatrix} \\ &= \begin{bmatrix} P_{4_k}^* F_{4_k}^* P_{5_k}^* F_{5_k}^* P_{6_k}^* & (P_{4_k}^* F_{4_k}^* + 1)T_k \\ 0 & 1 \end{bmatrix} \end{aligned}$$

$$\begin{aligned} F_{3_k} \times (P_{4_k} \times F_{4_k} \times P_{5_k} \times F_{5_k} \times P_{6_k}) &= \begin{bmatrix} F_{3_k}^* & 0 \\ 0 & 1 \end{bmatrix} \times \begin{bmatrix} P_{4_k}^* F_{4_k}^* P_{5_k}^* F_{5_k}^* P_{6_k}^* & (P_{4_k}^* F_{4_k}^* + 1)T_k \\ 0 & 1 \end{bmatrix} = \\ &= \begin{bmatrix} F_{3_k}^* P_{4_k}^* F_{4_k}^* P_{5_k}^* F_{5_k}^* P_{6_k}^* & F_{3_k}^* (P_{4_k}^* F_{4_k}^* + 1)T_k \\ 0 & 1 \end{bmatrix} \end{aligned}$$

⋮

The final multiplication in expression (30) becomes as follows:

$$P_{1_k} \times (F_{1_k} \times P_{2_k} \times F_{2_k} \times P_{3_k} \times F_{3_k} \times P_{4_k} \times F_{4_k} \times P_{5_k} \times F_{5_k} \times P_{6_k}) =$$

$$= \begin{bmatrix} P_{1_k}^* F_{1_k}^* P_{2_k}^* F_{2_k}^* P_{3_k}^* F_{3_k}^* P_{4_k}^* F_{4_k}^* P_{5_k}^* F_{5_k}^* P_{6_k}^* & (P_{1_k}^* F_{1_k}^* P_{2_k}^* F_{2_k}^* P_{3_k}^* F_{3_k}^* P_{4_k}^* F_{4_k}^* + P_{1_k}^* F_{1_k}^* P_{2_k}^* F_{2_k}^* P_{3_k}^* F_{3_k}^* + P_{1_k}^* F_{1_k}^* P_{2_k}^* F_{2_k}^* + P_{1_k}^* F_{1_k}^*) T_k \\ 0 & 1 \end{bmatrix}$$

or in a simpler form:

$$P_{1_k} \times (F_{1_k} \times P_{2_k} \times F_{2_k} \times P_{3_k} \times F_{3_k} \times P_{4_k} \times F_{4_k} \times P_{5_k} \times F_{5_k} \times P_{6_k}) = \quad (31)$$

$$= \begin{bmatrix} H_k & (P_{1_k}^* F_{1_k}^* P_{2_k}^* F_{2_k}^* P_{3_k}^* F_{3_k}^* P_{4_k}^* F_{4_k}^* + P_{1_k}^* F_{1_k}^* P_{2_k}^* F_{2_k}^* P_{3_k}^* F_{3_k}^* + P_{1_k}^* F_{1_k}^* P_{2_k}^* F_{2_k}^* + P_{1_k}^* F_{1_k}^*) T_k \\ 0 & 1 \end{bmatrix}$$

If we continue the computation pattern presented in subchapter 3.5 we will eventually derive an expression of the engine torque from the crankshaft speed, similar to formula (28).

However, because expression (31) already involves a very large number of computations (matrices multiplications), the final formula for the engine torque for a four cylinder engine will be even more computationally expensive therefore it is less likely that this method can be used in real time (on-board) applications.

Because of that reason, for multi-cylinder engines, it is preferred to use the direct method in the same manner as it was applied on single-cylinder engines. The procedure and the results are presented in the next subchapter.

3.7 Direct Recognition Method on a four-cylinder engine

The Direct Recognition Technique yields good results on a single-cylinder engine – see subchapter 3.6. Nonetheless, it can also be applied on multiple-cylinder engines. In a multi-cylinder engine there are small differences in the operation of the cylinders even under steady state operation conditions. Due to the increased length of the crankshaft, torsional vibrations disturb the variation of the crankshaft speed.

The less disturbed speed is that of the flywheel where the measurement has to be performed.



Figure 3.14b - VM Motori 2.5 L engine dismantled
in order to draw its moving parts

All these disturbances require that average values for the cylinder pressure and the crankshaft speed variations should be first determined.

Similarly to the single-cylinder engine case, in order to proceed with our calculations, the value of the total mass moment of inertia of the parts in rotation had to be known.

The total mass moment of inertia of the parts in rotation has been determined by dismantling a spare four-cylinder 2.8 l VM Motori engine (figure 3.14) and drawing the corresponding 3D parts - figures 3.15–3.17.

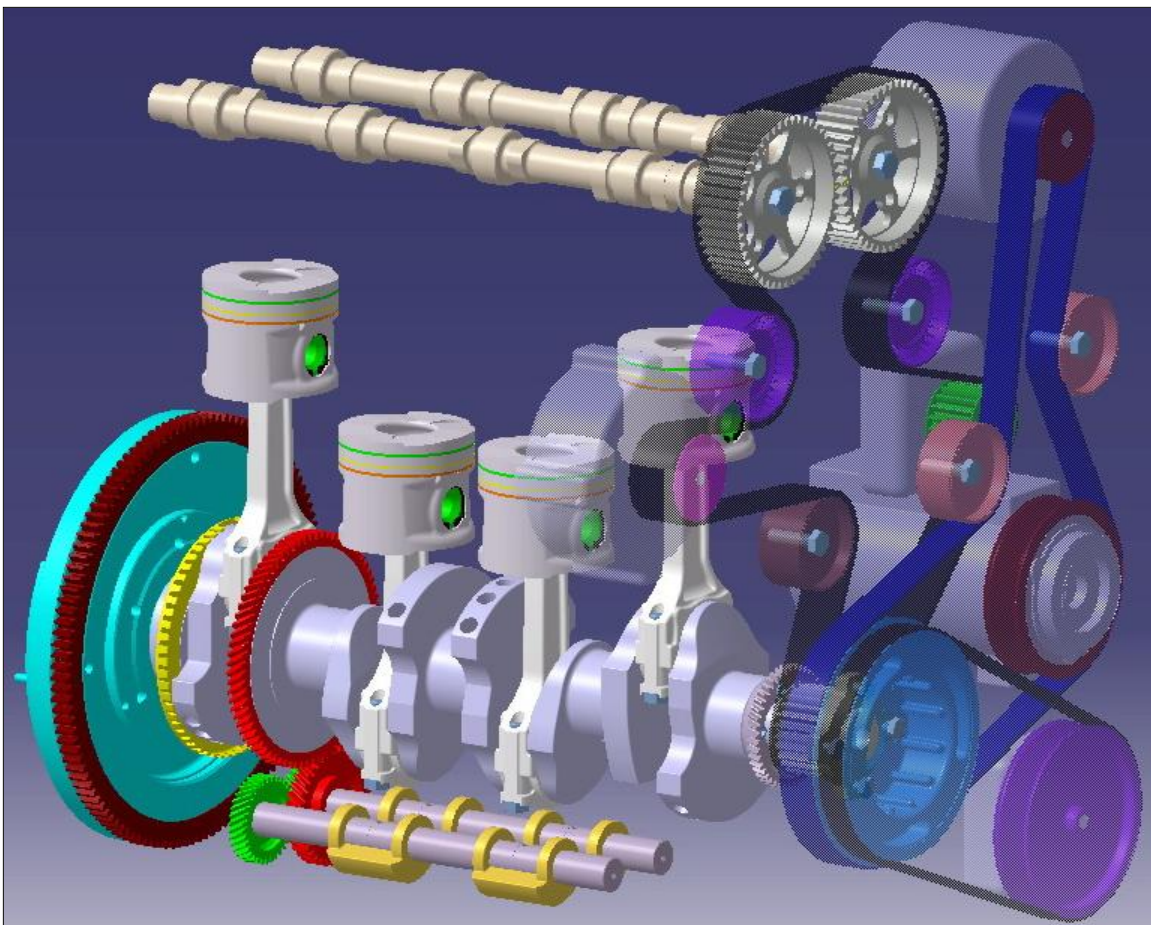


Figure 3.15 - VM Motori 2.5 L engine: drawing of the moving parts

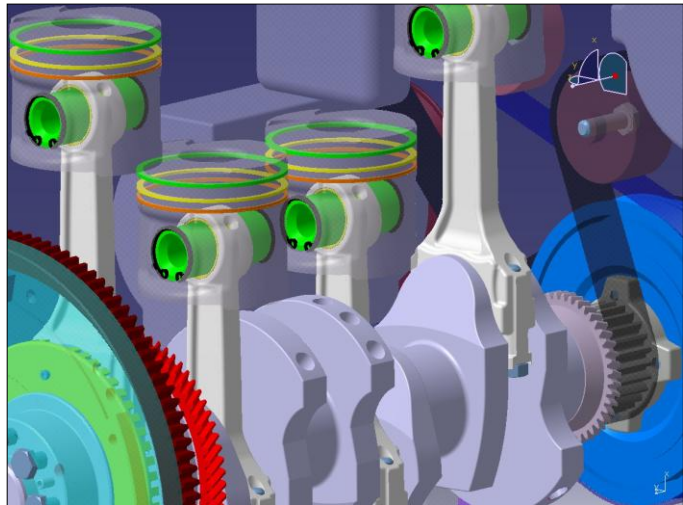
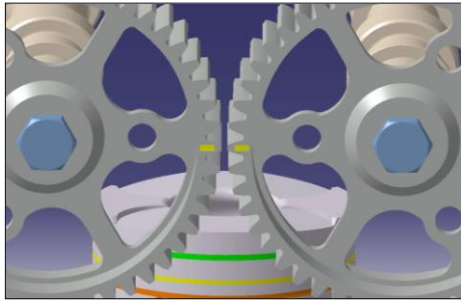
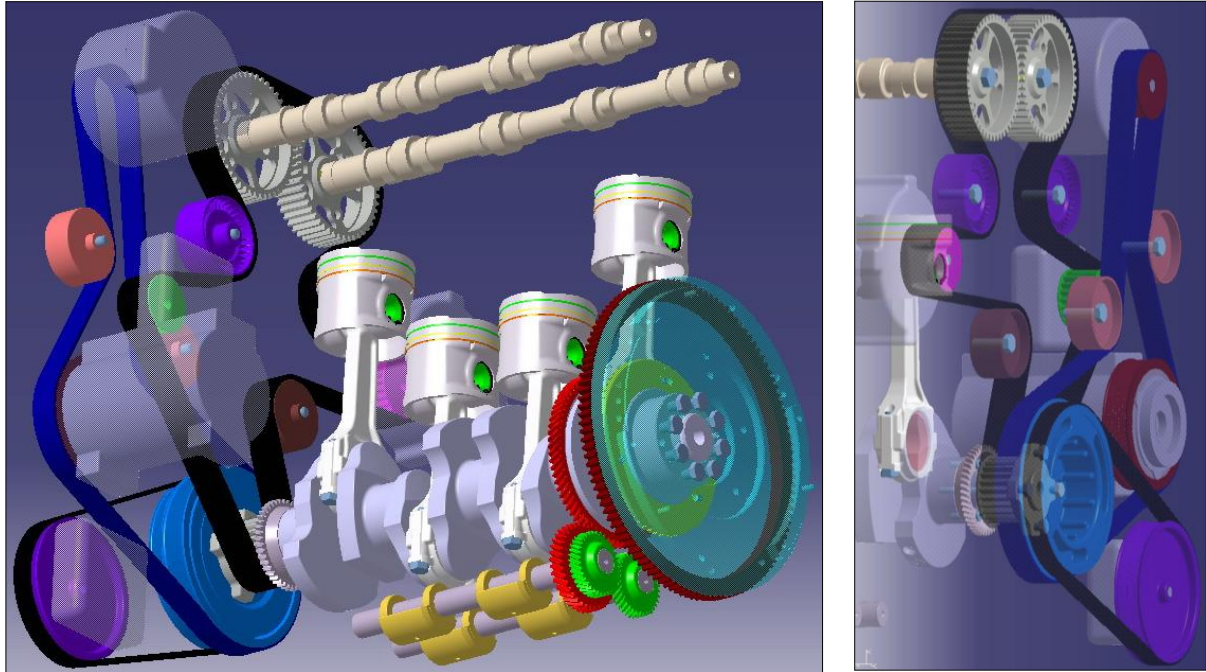
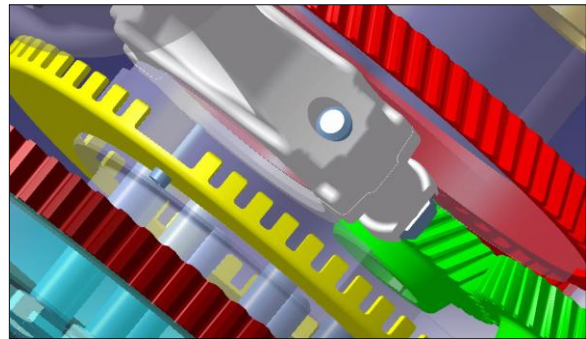
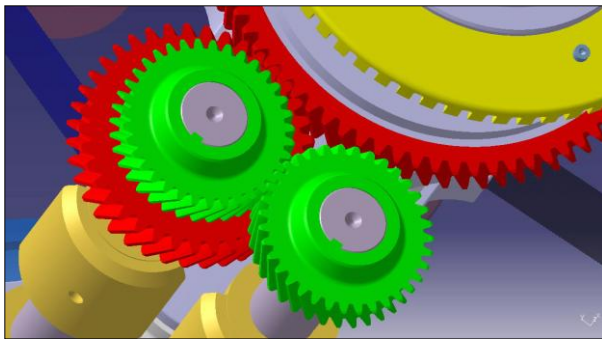


Figure 3.16 - VM Motori engine: drawings of the moving parts



By following the procedure described in chapter 3.4 the mass moment of inertia of the VM Motori engine was determined – see Table 3.2.


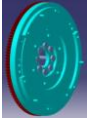


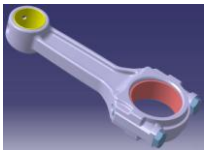
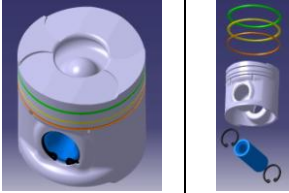


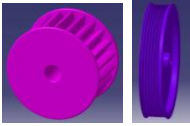
Part name	Designed part	Mass (kg)	Mass moment of inertia around the principal axis of the part (kg*m ²)
Crankshaft		21.65	0.0397
Flywheel		14.36	0.1882
Camshafts assembly		2 * 3.543 = 7.086	2 * 0.002169 = 0.004338
Balancing shafts assembly		2.464 + 2.061 = 4.4525	0.008704 + 0.005241 = 0.013945
Connecting rod assembly (4 pieces)		4 * 0.374 = 1.496	-
Piston assembly, including piston bolt (4 pieces)		4 * 0.811 = 3.244	-
Pulley		4.663	0.01984
Crankshaft gear		0.87	0.00557164
5 auxiliary components, wheels		5 * 0.081 = 0.405	5 * 0.00031181 = 0.00155905
Total moving engine parts (see calculations on the next page)		58.225	0.317372822

Table 3.2 - VM Motori 2.5 L four cylinder engine parts and their masses characteristics

The individual mass in translation is:

$$m_{tr} = m_{group_piston} + 0.275 * m_{connecting_rod} = 0.811 + 0.275 * 0.374 = 0.914 \text{ kg}$$

The individual mass of the connecting rod in rotation is:

$$m_{cr} = 0.725 * m_{connecting_rod} = 0.725 * 0.374 \text{ kg} = 0.271 \text{ kg}$$

The summation is:

$$m_{tr}/2 + m_{cr} = 0.914 \text{ kg} / 2 + 0.271 \text{ kg} = 0.457 \text{ kg} + 0.271 \text{ kg} = 0.728 \text{ kg}$$

The crankshaft radius is:

$$r = \text{stroke} / 2 = 0.088 \text{ m} / 2 = 0.044 \text{ m}$$

The total mass moment of inertia of the engine moving parts is:

$$J_{total} = J_{crankshaft} + 4 * (m_{tr} / 2 + m_{cr}) * r^2 + J_{flywheel} + J_{camshafts} * (1/2)^2 + \\ + 2^2 * J_{balancing_shafts} + J_{pulley} + J_{gear} + J_{wheels}$$

$$J_{total} = 0.0397 + 4 * 0.728 * 0.044^2 + 0.1882 + 0.004338 / 4 + \\ + 4 * 0.013945 + 0.01984 + 0.00557164 + 0.00155905$$

$$J_{total} = 0.0397 + 0.005637632 + 0.1882 + 0.0010845 + 0.05578 + 0.01984 \\ + 0.00557164 + 0.00155905$$

$$J_{total} = 0.317372822 \text{ kg} * \text{m}^2$$

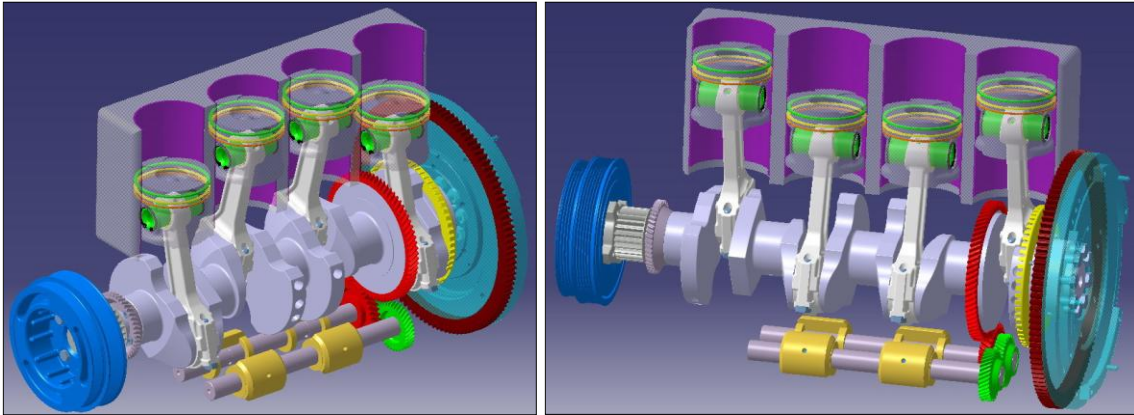


Figure 3.17 - VM Motori 2.5 L engine in motion

Then the average values of the cylinder pressure and of the crankshaft speed variations were calculated – figures 3.18 and 3.19.

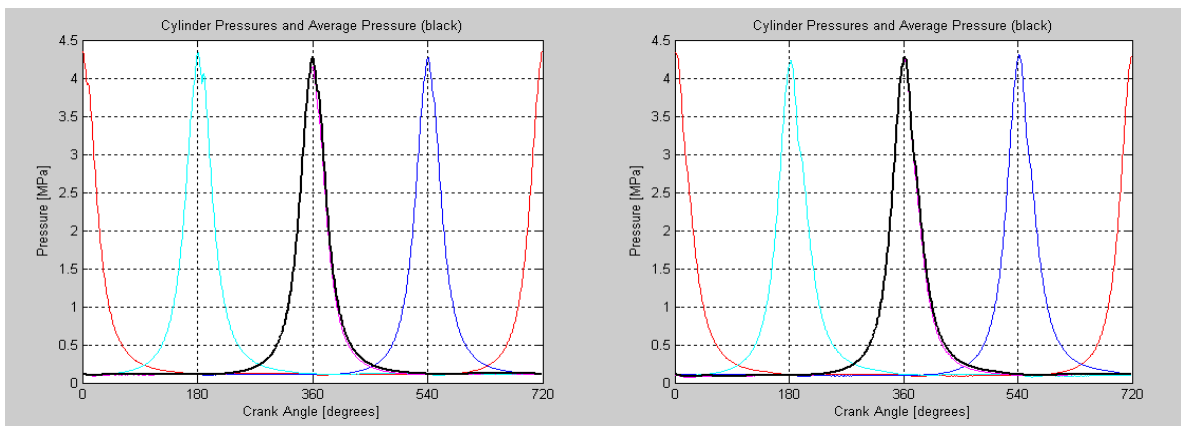


Figure 3.18 - Four cylinder pressures and average cylinder pressure variation (black curve) when idling at 1000 rpm (left) and 1500 rpm (right) on ULSD

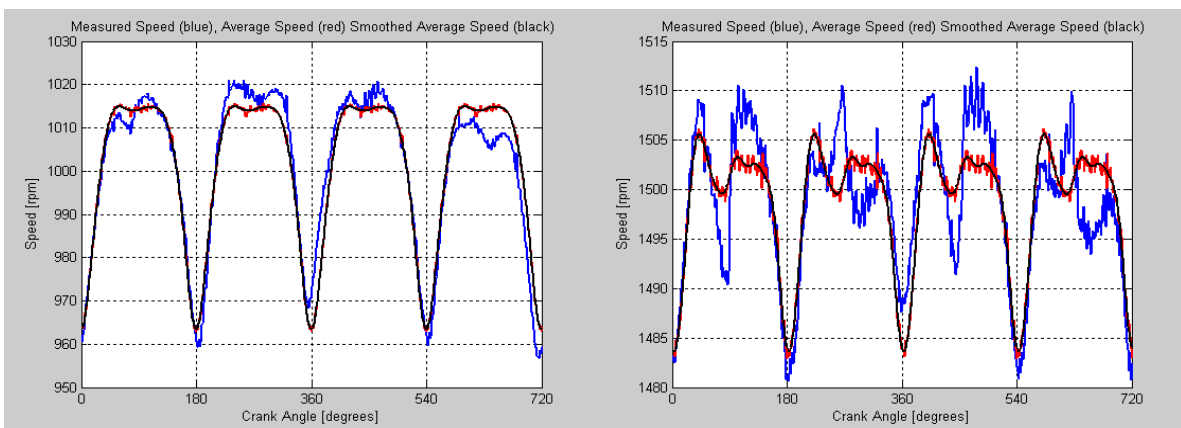


Figure 3.19 - Engine speed variation idling 1000 rpm (left) and 1500 rpm (right): measured speed (blue), average speed (red), smoothed average speed (black) on ULSD

The engine speed was differentiated to obtain the angular acceleration –
Figure 3.20.

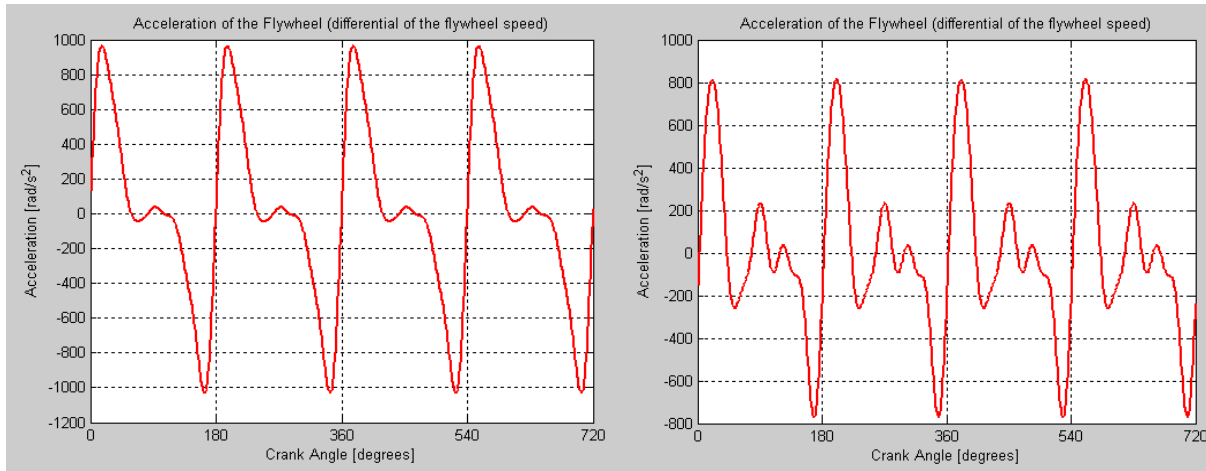


Figure 3.20 - Crankshaft angular acceleration at idling
1000 rpm (left) and 1500 rpm (right)

The angular acceleration was multiplied by the total mass moment of inertia to yield the engine torque, from which the reciprocating inertia torque was subtracted to evaluate the gas pressure torque – Figure 3.21.

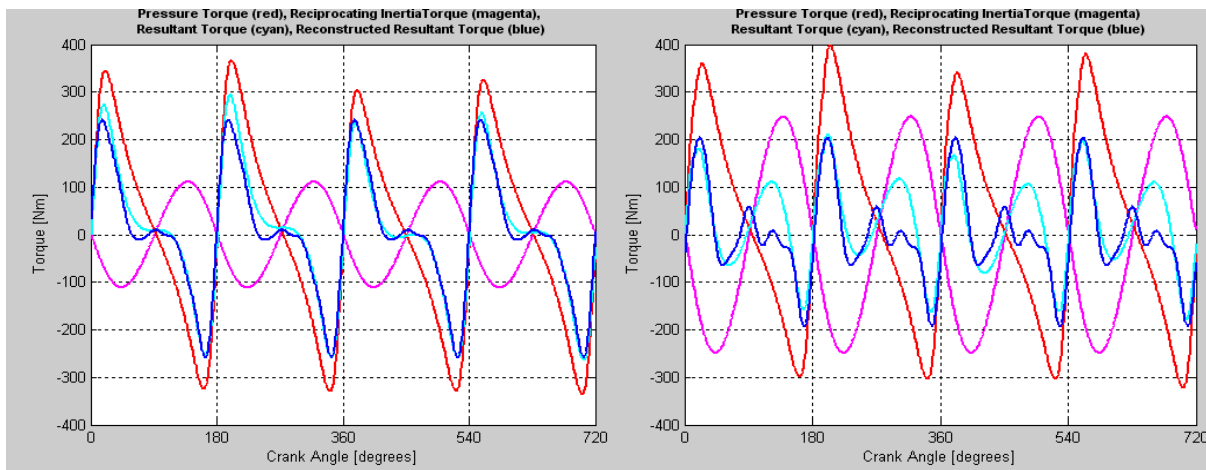


Figure 3.21 - Torques acting on the crankshaft when idling 1000 rpm (left) and 1500 rpm (right): gas pressure torque (red), inertia torque (magenta), resultant torque (cyan), reconstructed torque (blue)

Even though the resultant torque and the reconstructed torque do not overlap over the entire 720 CAD interval, their coincidence was fairly good around the area of interest at TDC.

From the gas pressure torque the cylinder pressure were computed –

Figure 3.22.

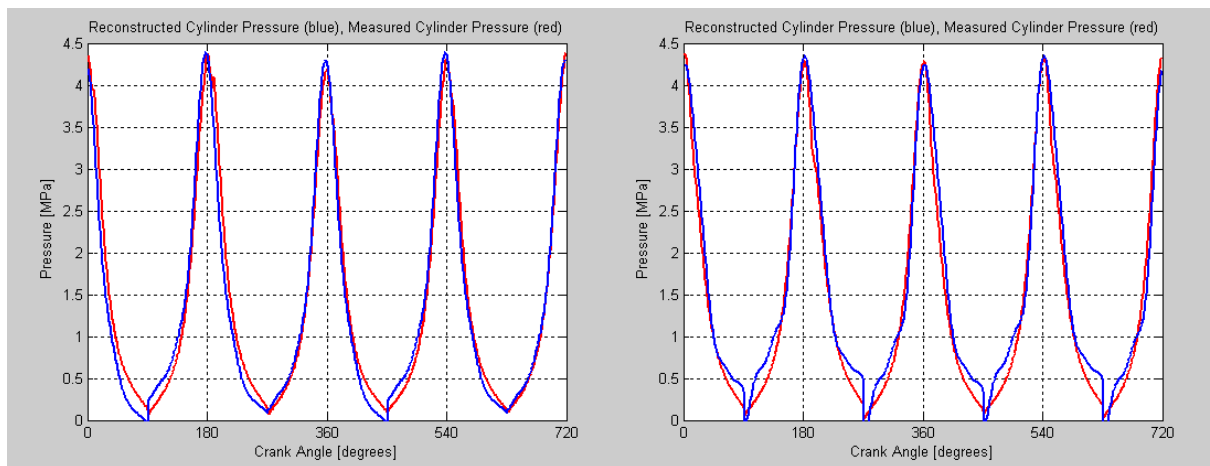


Figure 3.22 - Reconstructed cylinder pressure (blue) and measured cylinder pressure (red) when idling 1000 rpm (left) and 1500 rpm

In conclusion, the results show that the Direct Recognition Technique can be successfully used in estimating the peak cylinder pressure in single and multiple cylinder engines. Combustion parameters such as:

- value and location of peak pressure with respect to TDC
- start of combustion (or ignition delay)
- rate of cylinder pressure rise

can be used to determine the fuel type.

The measured instantaneous crankshaft speed can be used to estimate the peak cylinder pressure and its location with respect to TDC.

Both Direct Recognition and Model-Based Recognition methods determine fairly well the peak cylinder pressure and its location with respect to the TDC, which are an indicative of the ignition properties of the fuel. The Model-Based Recognition Technique yields slightly better estimates, while the Direct Recognition Method is less computationally intensive.

CHAPTER 3

FUEL IDENTIFICATION METHODS

3.1 Methodology

The purpose is to develop a method to estimate at least one of the main combustion characteristics: peak cylinder pressure, rate of pressure rise or ignition delay. That is easily achieved when in-cylinder pressure sensors are used and the pressure trace is readily obtained.

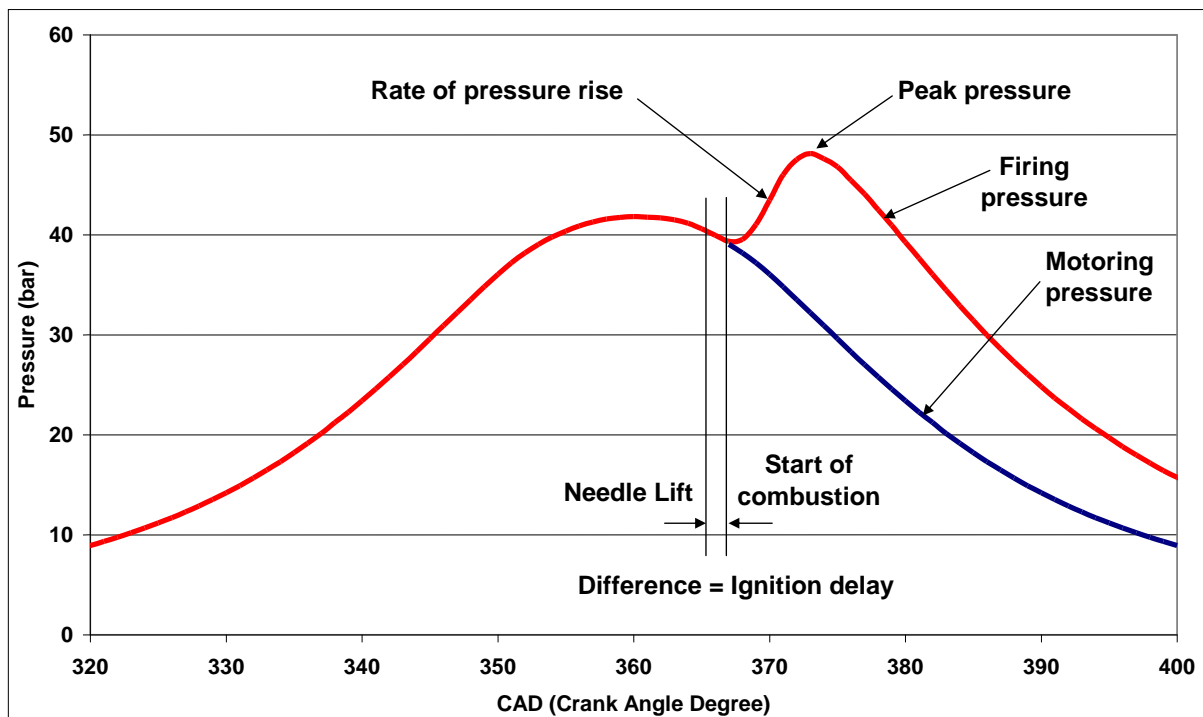


Figure 3.1 - Typical in-cylinder pressure trace

The start of combustion is defined as the point where the firing pressure curve separates from the motoring (cranking) pressure curve – Figure 3.1. The needle lift is measured separately with a position sensor.

The difference between the two signals represents the ignition delay. Estimation of ignition delay means, in fact, estimation of start of combustion. Thus, ideally, the measurement of the pressures in each cylinder will provide the required information for electronic controls.

For that purpose engineers usually use a pressure transducer whose price ranges from 1,800 to 2,500 US dollars, including cables and signal amplifier, and that happens for each cylinder under study. If an engine has four cylinders for example, then four such transducers are required – Figure 3.2. This is a very expensive solution.

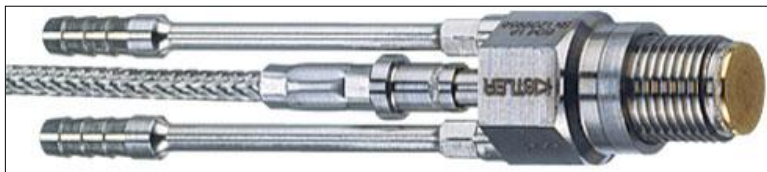
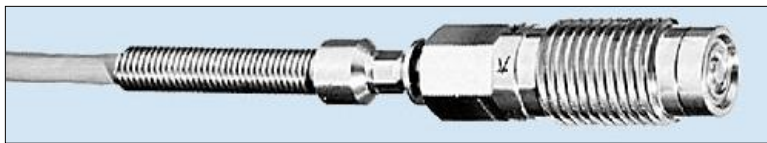


Figure 3.2 - Pressure sensors: regular and cooled, for high temperatures operating conditions

Moreover, special sleeves must be machined into the cylinder head in order to install these pressure sensors – Figure 3.3.

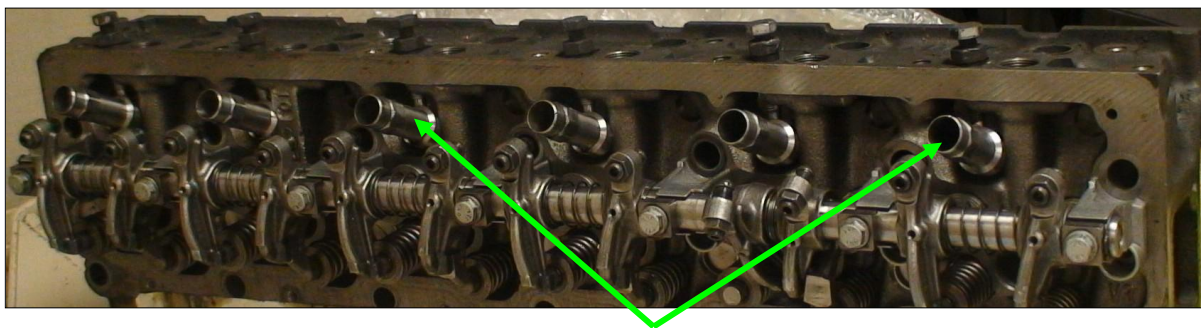


Figure 3.3 - Customized cylinder head with sleeves for pressure transducers (7.2 l Mercedes engine)

Proper handling and maintenance are among other issues. Obviously the solution offered by the use of pressure transducers is not feasible for series engines as far as it concerns price and reliability.

Fortunately there are other estimating methods of the pressure trace that do not require a pressure sensor. One of them is to use the engine speed signal which is measured by a speed sensor present on any vehicle. This methodology is robust since the instantaneous crankshaft speed (not the average rpm) fluctuates due to the in-cylinder pressure variations transmitted through the crank-slider mechanism and is directly expressed by the flywheel gear tooth spacing variations.

If the estimated pressure trace is satisfactory, then the cost of its evaluation is reduced drastically by eliminating the need of pressure sensors. The measurement of speed variation of the crankshaft is simple, inexpensive and is already available on modern engines – Figure 3.4. That is why the possibility of using crankshaft speed measurement to estimate engine torque and cylinder

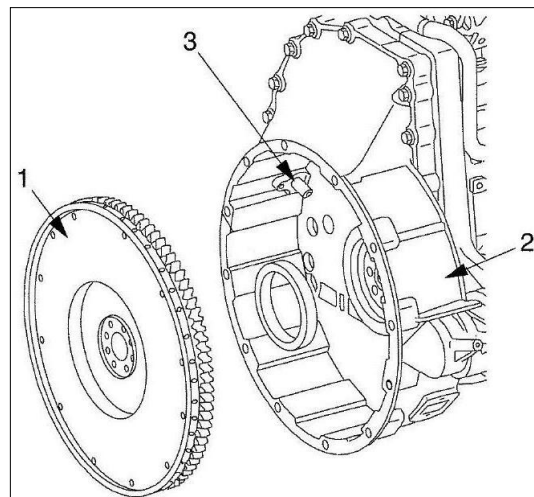


Figure 3.4 - Mercedes engine:

- 1. flywheel, 2. housing
- 3. crankshaft speed sensor

pressure variation, mainly peak cylinder pressure and its location with respect to TDC, looks very attractive. In order to achieve that, reliable correlations must be established between cylinder pressure variation and crankshaft speed variation. The estimated parameter (peak pressure, start of combustion, rate of pressure rise or its derivative) is then correlated to the cetane number to recognize the fuel type and finally, the engine controls are switched so that the engine operates safely and optimally on the identified fuel.

3.2 Dynamic model of the crankshaft

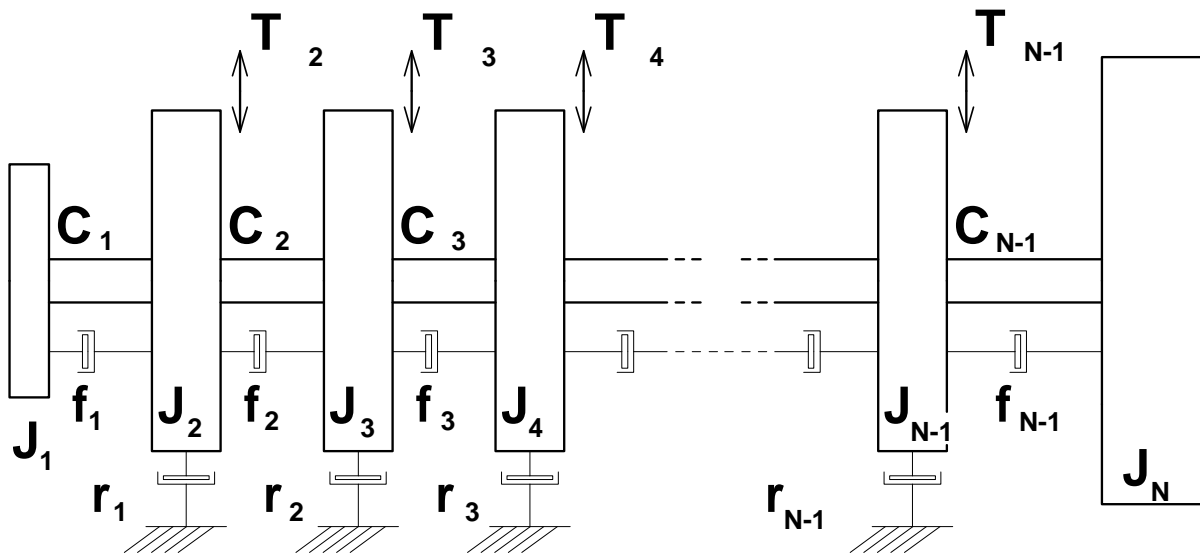


Figure 3.5 - Dynamic model of the crankshaft

In figure 3.5 a lumped mass dynamic model of the crankshaft has been represented using the following notations [24]:

J_1 = Mass moment of inertia of the pulley and auxiliaries at the front end

$J_2, J_3 \dots J_{N-1}$ = Mass moment of inertia the crank-slider mechanism

J_N = Mass moment of inertia of the flywheel

$C_1, C_2 \dots C_{N-1}$ = Crankshaft stiffness coefficients for each elastic element

$r_1, r_2 \dots r_{N-1}$ = Absolute damping coefficients

$f_1, f_2 \dots f_{N-1}$ = Relative damping coefficients

Excitation torques $T_2, T_3 \dots T_{N-1}$ represent the individual cylinder torques acting on the crankshaft.

3.3 Direct simulation method. Computation of motion for the 1st mass using transfer matrices

One way to determine the angular motion of the crankshaft is to use the transfer matrices of the lumped masses and mass-less elastic elements of the dynamic model of the crankshaft.

According to D.Taraza [24] the transfer matrices of masses and mass-less elastic elements are multiplied according to the crankshaft dynamic model to obtain:

$$Z_{N_k}^R = P_{N_k} \times E_{(N-1)_k} \times P_{(N-1)_k} \times \dots \times E_{1_k} \times P_{1_k} \times Z_{1_k}^L = H_k \times Z_{1_k}^L \quad (1)$$

The boundary conditions reveal that at both ends of the crankshaft the excitation torques are 0 (zero). The state vectors become:

$$Z_{1_k} = \begin{bmatrix} \theta^{\text{Re}} \\ 0 \\ \theta^{\text{Im}} \\ 0 \\ 1 \end{bmatrix}_{1k} \quad \text{and} \quad Z_{N_k} = \begin{bmatrix} \theta^{\text{Re}} \\ 0 \\ \theta^{\text{Im}} \\ 0 \\ 1 \end{bmatrix}_{Nk} \quad (2)$$

therefore only columns one, three and five will subsist in the H_k matrix:

$$H_k = \begin{bmatrix} h_{11_k} & 0 & h_{13_k} & 0 & h_{15_k} \\ h_{21_k} & 0 & h_{23_k} & 0 & h_{25_k} \\ h_{31_k} & 0 & h_{33_k} & 0 & h_{35_k} \\ h_{41_k} & 0 & h_{43_k} & 0 & h_{45_k} \\ 0 & 0 & 0 & 0 & 1 \end{bmatrix} \quad (3)$$

Cylinder excitations are in accordance with D. Taraza [24]:

$$M_i = M_{0_i} + \sum_{k=1}^N [A_{k_{p_i}} \cos k(\omega t + \varphi_i) + (B_{k_{p_i}} + B_{k_r}) \sin k(\omega t + \varphi_i)] \quad (4)$$

For an arbitrary harmonic component “k” the following relation is true:

$$M_{k_i} = (M_k^{\text{Re}})_i \cos k\omega t + j(M_k^{\text{Im}})_i \sin k\omega t \quad (5)$$

thus real and imaginary parts to be introduced in the point matrices are:

$$(M_k^{\text{Re}})_i = A_{k_{p_i}} \cos k\varphi_i - (B_{k_{p_i}} + B_{k_r}) \sin k\varphi_i \quad (6)$$

$$(M_k^{\text{Im}})_i = -A_{k_{p_i}} \sin k\varphi_i - (B_{k_{p_i}} + B_{k_r}) \cos k\varphi_i \quad (7)$$

The system has four equations with four unknowns: θ_{1k}^{Re} , θ_{1k}^{Im} , θ_{Nk}^{Re} , θ_{Nk}^{Im} .

The situation is similar for any intermediary mass i : θ_{1k}^{Re} , θ_{1k}^{Im} , θ_{ik}^{Re} , θ_{ik}^{Im} , therefore all four unknowns can be determined. For example, the components of the first mass deflections are:

$$\theta_{1k}^{\text{Re}} = \frac{-h_{25}h_{43}+h_{45}h_{23}}{h_{21}h_{43}-h_{23}h_{41}} \quad \text{and} \quad \theta_{1k}^{\text{Im}} = \frac{-h_{45}h_{21}+h_{25}h_{41}}{h_{21}h_{43}-h_{23}h_{41}} \quad (8)$$

By superposition the variation in time of the first mass angular deflection is obtained:

$$\theta_1 = \sum_{k=1}^M (\theta_{1k}^{\text{Re}} \cos k\omega t - \theta_{1k}^{\text{Im}} \sin k\omega t) \quad (9)$$

and furthermore the variation in time of the first mass angular speed according to D. Taraza [24]:

$$\dot{\theta}_1 = \omega_1 = k\omega \sum_{k=1}^M [-\theta_{1k}^{\text{Im}} \cos(k\omega t) - \theta_{1k}^{\text{Re}} \sin(k\omega t)] \quad (10)$$

The motion of each mass i is determined if the excitations (engine torques) are known for each cylinder i . In other words, if the in-cylinder pressure is known, the angular speed can be determined.

This direct calculation is used to validate the parameters of the dynamic model to assure the required accuracy when the calculation is reversed to determine the gas pressure torque from the measured crankshaft speed.

3.4 Single cylinder engine model validation

The direct simulation method used to determine the crankshaft speed from the cylinder pressure can be applied to single and multi-cylinder engines. Due to the complexity of the problem, the development of the technique has been implemented first on a single cylinder engine, the 0.7 L Deutz engine. The notations for the connecting elements, used in subchapters 3.2 and 3.3 are utilized to build the dynamic model of the crankshaft – Figure 3.6.

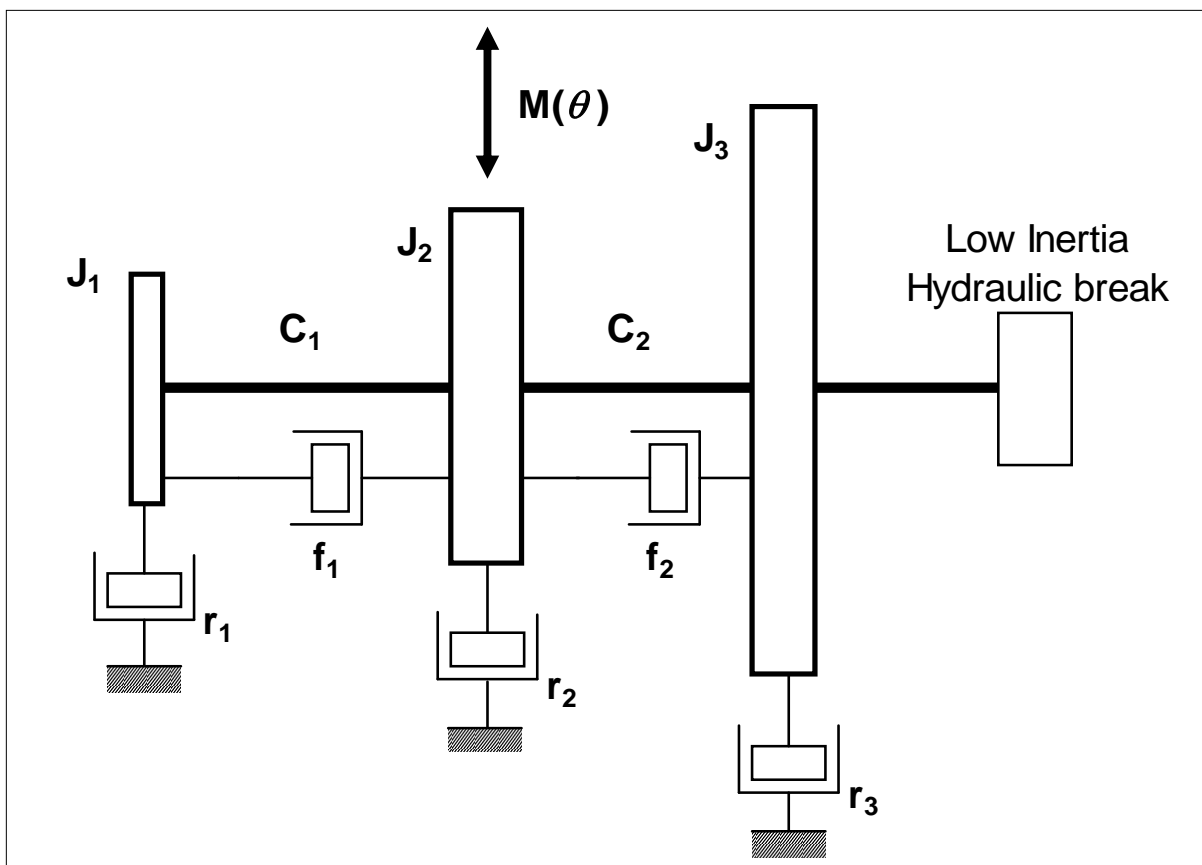


Figure 3.6 - Lumped mass dynamic model of the single cylinder engine

The point and field transfer matrices are determined by the mass moments of inertia, by the absolute damping coefficients as a consequence of the friction between the piston and the liner, by the stiffness coefficients of the elastic elements of the crankshaft and by the relative damping coefficients as a result of the oil film being squeeze in the main bearings as stated by D. Taraza [24].

The question is how to determine these parameters. The absolute and relative damping coefficients can be adopted. The mass moments of inertia and the stiffness coefficients must be precisely determined though. To achieve that a spare 0.7 l Deutz engine was dismantled and the separate rotating parts such as crankshaft, camshaft, flywheel, balancing shaft, oil pump gear, connecting rods were drawn using CAD software, as represented in Table 3.1.

By individually weighing the parts, their masses were determined. After drawing the parts, their volumes could be computed using the software. An alternate method would be to submerge the parts in liquid in a tank and measure the difference in liquid heights. Having the mass and the volume for each part, the individual densities were then calculated. Finally, after inserting the density as a value, the mass moment of inertia of each rotating part was automatically computed using the software.

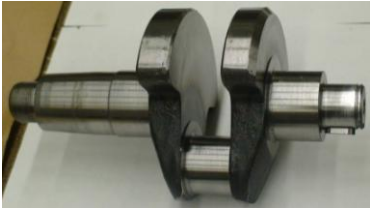
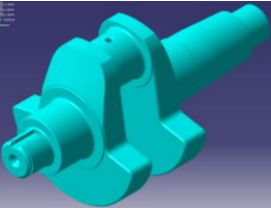





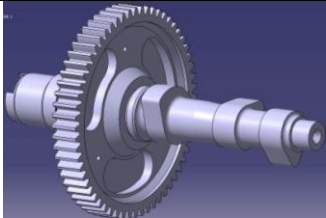
Part name	Actual part	Designed part	Mass (kg)	Mass moment of inertia (kg*m ²)
Crankshaft			5.415	0.006740
Flywheel			23.45	0.227400
				
Camshaft			1.91	0.001874

Table 3.1 - Deutz single cylinder engine parts and their mass characteristics


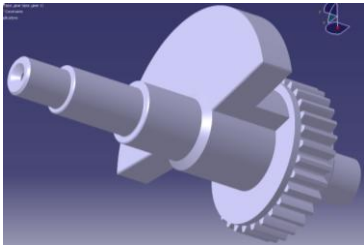



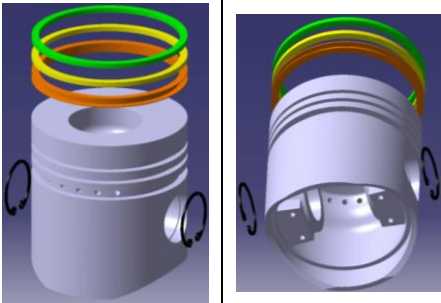
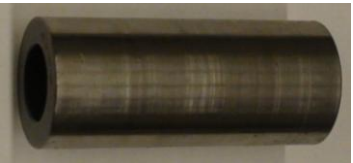

Part name	Actual part	Designed part	Mass (kg)	Mass moment of inertia (kg*m ²)
Balancing shaft			1.705	0.000904
Connecting rod			0.5	-
Piston assembly			0.52	-
Piston bolt			0.21	-

Table 3.1 (continued) - Deutz single cylinder engine parts and their mass characteristics







Part name	Actual part	Designed part	Mass (kg)	Mass moment of inertia (kg*m ²)
Pulley			0.445	0.000898
Crankshaft gear			0.285	0.000162
Oil pump gear			0.14	0.000172
Total moving engine parts			34.58	0.24481

Table 3.1 (continued) - Deutz single cylinder engine parts and their mass characteristics

The mass in translation is:

$$m_{tr} = m_{group_piston} + 0.275 * m_{connecting_rod} = 0.73 + 0.275 * 0.5 = 0.8675 \text{ kg}$$

The individual mass of the connecting rod in rotation is:

$$m_{cr} = 0.725 * m_{connecting_rod} = 0.725 * 0.5 \text{ kg} = 0.3625 \text{ kg}$$

The corresponding summation is:

$$m_{tr}/2 + m_{cr} = 0.8675 \text{ kg} / 2 + 0.3625 \text{ kg} = 0.79625 \text{ kg}$$

The crankshaft radius is:

$$r = \text{stroke} / 2 = 0.082 \text{ m} / 2 = 0.041 \text{ m}$$

The total mass moment of inertia is:

$$J_{total} = J_{crankshaft} + 4 * (m_{tr} / 2 + m_{cr}) * r^2 + J_{flywheel} + J_{camshaft} * (1/2)^2 + \\ + 2^2 * J_{balancing_shaft} + J_{pulley} + J_{gear1} + J_{gear_oil}$$

$$J_{total} = 0.006740 + 4 * 0.79625 * 0.041^2 + 0.227400 + 0.001874 / 4 + \\ + 4 * 0.000904 + 0.000898 + 0.000162 + 0.000172$$

$$J_{total} = 0.006740 + 0.005353985 + 0.227400 + 0.0004685 + \\ + 0.003616 + 0.000898 + 0.000162 + 0.000172$$

$$J_{total} = 0.244810485 \text{ kg} * \text{m}^2$$

Using the same software, the stiffness coefficients were evaluated by FEA (Finite Element Analysis) while applying a known torque and reading the corresponding angular deformation - Figure 3.8. The torque divided by the deformation yielded the stiffness of each elastic element.

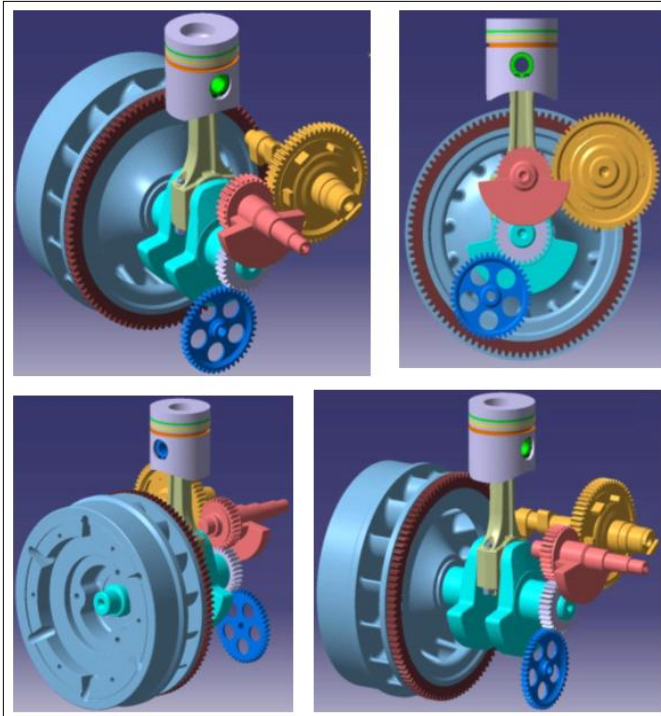


Figure 3.7 - 3D drawing of the single cylinder engine (Catia V5)

Once the field and point matrices were determined, the computational procedure presented in subchapter 3.3 was followed and the angular speed variation was estimated from the in-cylinder pressure.

ULSD and S-25 (Synthetic fuel S-8 having cetane number 25) were tested at 1500 rpm

and 4 Nm torque (2.9 bar IMEP). Both cases show good coincidence between simulation and measured data – Figure 3.9.

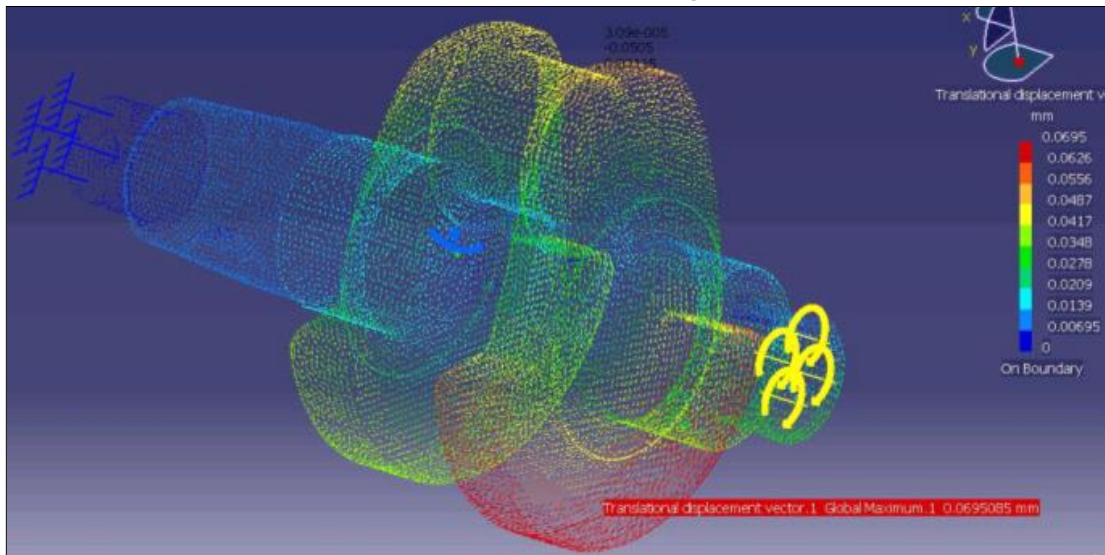


Figure 3.8 - FEM computation of the shaft stiffness (Catia V5)

The Matlab code for the computation of the crankshaft speed from the in-cylinder pressure is presented in the Appendix.

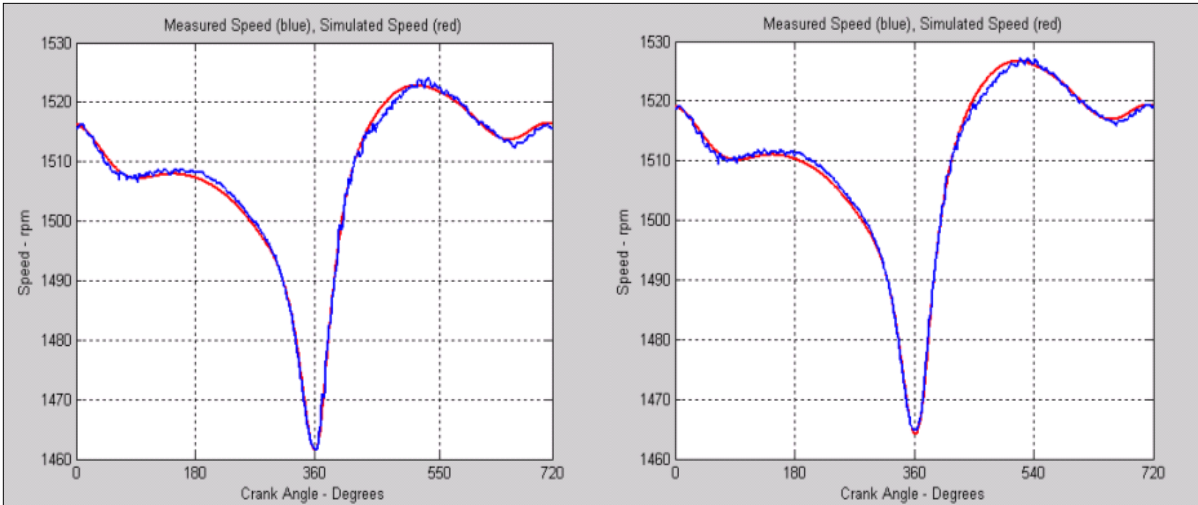


Figure 3.9 - Single-cylinder engine model validation: left (ULSD), right (S-8); measured speed (blue), simulated speed (red); the operating point is 1500 rpm and 4 Nm torque / 2.9 bar IMEP

The direct method of calculation of the crankshaft speed from the in-cylinder pressure has been used to validate the parameters of the dynamic model in order to ensure the required accuracy for a reversed computation of the in-cylinder pressure from the crankshaft speed.

This reversed estimation, as the name suggests, uses the same transfer matrices but in a reverse order, and is called the transfer matrices reversed approach.

3.5 Model-based recognition (transfer matrices reversed) method on a single cylinder engine

This approach is accurate but it requires a very precise dynamic model of the power-train. Mass moments of inertia of the engine moving parts, shafts stiffnesses, absolute and relative damping coefficients and detailed engine construction data are necessary. Instantaneous crankshaft speed can be measured using a shaft encoder at the front of the engine (pulley side) or at the back of the engine (flywheel side). The second option is preferred in order to minimize distortions caused by torsional vibrations. From the measured crankshaft speed the gas pressure torque is calculated. The gas pressure torque is used to determine the cylinder pressure.

As compared to the transfer matrices direct approach where the crankshaft speed was computed from the in-cylinder pressure, in the transfer matrices reversed approach the input data is now the instantaneous engine speed, preferably at the flywheel where the measured signal is less affected by noise and vibrations. The output is the engine torque from which the in-cylinder pressure is computed.

In this case the terms of the matrix $H_k (h_{ij_k})$ are functions of the unknown values of the harmonic components of the engine torque.

Using the notations in Figure 3.5 and the dynamic model in Figure 3.6 the transfer matrices of masses and mass-less elastic elements according to the crankshaft are multiplied to obtain:

$$Z_{1_k} = P_{1_k} \times F_{1_k} \times P_{2_k} \times F_{2_k} \times P_{3_k} \times Z_{3_k} , \quad (14) \quad \text{where:}$$

$$P_{3_k} = \begin{bmatrix} 1 & 0 & 0 & 0 & 0 \\ -J_3(k\omega)^2 & 1 & -r_3(k\omega) & 0 & 0 \\ 0 & 0 & 1 & 0 & 0 \\ r_3(k\omega) & 0 & -J_3(k\omega)^2 & 1 & 0 \\ 0 & 0 & 0 & 0 & 1 \end{bmatrix} = \begin{bmatrix} P_{3_k}^* & 0 \\ 0 & 1 \end{bmatrix} \quad (15) \quad \text{and}$$

$$F_{2_k} = \begin{bmatrix} 1 & \frac{C_2}{C_2^2 + (f_2 k\omega)^2} & 0 & \frac{f_2(k\omega)}{C_2^2 + (f_2 k\omega)^2} & 0 \\ 0 & 1 & 0 & 0 & 0 \\ 0 & \frac{-f_2(k\omega)}{C_2^2 + (f_2 k\omega)^2} & 1 & \frac{C_2}{C_2^2 + (f_2 k\omega)^2} & 0 \\ 0 & 0 & 0 & 1 & 0 \\ 0 & 0 & 0 & 0 & 1 \end{bmatrix} = \begin{bmatrix} F_{2_k}^* & 0 \\ 0 & 1 \end{bmatrix} \quad (16) \quad \text{and}$$

$$P_{2_k} = \begin{bmatrix} 1 & 0 & 0 & 0 & 0 \\ -J_2(k\omega)^2 & 1 & -r_2(k\omega) & 0 & -A_{kp} \cos k\varphi_i + (B_{kp} + B_{ktr}) \sin k\varphi_i \\ 0 & 0 & 1 & 0 & 0 \\ r_2(k\omega) & 0 & -J_2(k\omega)^2 & 1 & A_{kp} \sin k\varphi_i + (B_{kp} + B_{ktr}) \cos k\varphi_i \\ 0 & 0 & 0 & 0 & 1 \end{bmatrix} \quad (17)$$

$$\text{or } P_{2_k} = \begin{bmatrix} 0 \\ P_{2_k}^* & -T_k^{\text{Re}} \\ 0 \\ -T_k^{\text{Im}} \\ 0 & 1 \end{bmatrix}, \quad \text{with the notation } \begin{bmatrix} 0 \\ -T_k^{\text{Re}} \\ 0 \\ -T_k^{\text{Im}} \end{bmatrix} = T_{2k}$$

It is true that:

$$F_{1_k} = \begin{bmatrix} 1 & \frac{C_1}{C_1^2 + (f_1 k \omega)^2} & 0 & \frac{f_1(k\omega)}{C_1^2 + (f_1 k \omega)^2} & 0 \\ 0 & 1 & 0 & 0 & 0 \\ 0 & \frac{-f_1(k\omega)}{C_1^2 + (f_1 k \omega)^2} & 1 & \frac{C_1}{C_1^2 + (f_1 k \omega)^2} & 0 \\ 0 & 0 & 0 & 1 & 0 \\ 0 & 0 & 0 & 0 & 1 \end{bmatrix} = \begin{bmatrix} F_{1_k}^* & 0 \\ 0 & 1 \end{bmatrix} \quad (18)$$

and

$$P_{1_k} = \begin{bmatrix} 1 & 0 & 0 & 0 & 0 \\ -J_1(k\omega)^2 & 1 & -r_1(k\omega) & 0 & 0 \\ 0 & 0 & 1 & 0 & 0 \\ r_1(k\omega) & 0 & -J_1(k\omega)^2 & 1 & 0 \\ 0 & 0 & 0 & 0 & 1 \end{bmatrix} = \begin{bmatrix} P_{1_k}^* & 0 \\ 0 & 1 \end{bmatrix} \quad (19)$$

The multiplication in steps in the initial matrix equation is the following:

$$F_{2_k} \times P_{3_k} = \begin{bmatrix} F_{2_k}^* P_{3_k}^* & 0 \\ 0 & 1 \end{bmatrix}$$

$$P_{2_k} \times (F_{2_k} \times P_{3_k}) = \begin{bmatrix} P_{2_k}^* & T_{2k} \\ 0 & 1 \end{bmatrix} \times \begin{bmatrix} F_{2_k}^* P_{3_k}^* & 0 \\ 0 & 1 \end{bmatrix} = \begin{bmatrix} P_{2_k}^* F_{2_k}^* P_{3_k}^* & T_{2k} \\ 0 & 1 \end{bmatrix}$$

$$F_{1_k} \times (P_{2_k} \times F_{2_k} \times P_{3_k}) = \begin{bmatrix} F_{1_k}^* & 0 \\ 0 & 1 \end{bmatrix} \times \begin{bmatrix} P_{2_k}^* F_{2_k}^* P_{3_k}^* & T_{2k} \\ 0 & 1 \end{bmatrix} = \begin{bmatrix} F_{1_k}^* P_{2_k}^* F_{2_k}^* P_{3_k}^* & F_{1_k}^* T_{2k} \\ 0 & 1 \end{bmatrix}$$

$$P_{1_k} \times (F_{1_k} \times P_{2_k} \times F_{2_k} \times P_{3_k}) = \begin{bmatrix} P_{1_k}^* & 0 \\ 0 & 1 \end{bmatrix} \times \begin{bmatrix} F_{1_k}^* P_{2_k}^* F_{2_k}^* P_{3_k}^* & F_{1_k}^* T_{2k} \\ 0 & 1 \end{bmatrix} = \begin{bmatrix} P_{1_k}^* F_{1_k}^* P_{2_k}^* F_{2_k}^* P_{3_k}^* & P_{1_k}^* F_{1_k}^* T_{2k} \\ 0 & 1 \end{bmatrix}$$

or in a simpler form:

$$P_{1_k} \times (F_{1_k} \times P_{2_k} \times F_{2_k} \times P_{3_k}) = \begin{bmatrix} H_k & P_{1_k}^* F_{1_k}^* T_{2k} \\ 0 & 1 \end{bmatrix} \quad (20)$$

For a single cylinder engine mass # 3 represents the flywheel (F). The indices 'F' is used instead of '3' and the initial system of equations becomes:

$$\begin{bmatrix} \theta^{\text{Re}} \\ 0 \\ \theta^{\text{Im}} \\ 0 \\ 1 \end{bmatrix}_{1k} = \begin{bmatrix} H_k & P_{1_k}^* F_{1_k}^* T_{2k} \\ 0 & 1 \end{bmatrix} \times \begin{bmatrix} \theta^{\text{Re}} \\ 0 \\ \theta^{\text{Im}} \\ 0 \\ 1 \end{bmatrix}_{F_k} \quad (21)$$

where the H_k matrix is a function of engine physical parameters only. The

$P_{1_k}^* F_{1_k}^* T_{2k}$ term also includes the influence of the engine torque.

$$F_{1_k}^* \times T_{2k} = \begin{bmatrix} 1 & \frac{C_1}{C_1^2 + (f_1 k \omega)^2} & 0 & \frac{f_1(k\omega)}{C_1^2 + (f_1 k \omega)^2} \\ 0 & 1 & 0 & 0 \\ 0 & \frac{-f_1(k\omega)}{C_1^2 + (f_1 k \omega)^2} & 1 & \frac{C_1}{C_1^2 + (f_1 k \omega)^2} \\ 0 & 0 & 0 & 1 \end{bmatrix} \times \begin{bmatrix} 0 \\ -T_k^{\text{Re}} \\ 0 \\ -T_k^{\text{Im}} \end{bmatrix}$$

$$F_{1_k}^* \times T_{2k} = \begin{bmatrix} -T_k^{\text{Re}} \frac{C_1}{C_1^2 + (f_1 k \omega)^2} - T_k^{\text{Im}} \frac{f_1(k\omega)}{C_1^2 + (f_1 k \omega)^2} \\ -T_k^{\text{Re}} \\ T_k^{\text{Re}} \frac{f_1(k\omega)}{C_1^2 + (f_1 k \omega)^2} - T_k^{\text{Im}} \frac{C_1}{C_1^2 + (f_1 k \omega)^2} \\ -T_k^{\text{Im}} \end{bmatrix} \quad (22)$$

Furthermore

$$\begin{aligned}
 P_{1_k}^* F_{1_k}^* T_{2k} &= \begin{bmatrix} 1 & 0 & 0 & 0 \\ -J_1(k\omega)^2 & 1 & -r_1(k\omega) & 0 \\ 0 & 0 & 1 & 0 \\ r_1(k\omega) & 0 & -J_1(k\omega)^2 & 1 \end{bmatrix} \times \begin{bmatrix} -T_k^{\text{Re}} \frac{C_1}{C_1^2 + (f_1 k \omega)^2} - T_k^{\text{Im}} \frac{f_1(k\omega)}{C_1^2 + (f_1 k \omega)^2} \\ -T_k^{\text{Re}} \\ T_k^{\text{Re}} \frac{f_1(k\omega)}{C_1^2 + (f_1 k \omega)^2} - T_k^{\text{Im}} \frac{C_1}{C_1^2 + (f_1 k \omega)^2} \\ -T_k^{\text{Im}} \end{bmatrix} = \\
 &= \begin{bmatrix} -T_k^{\text{Re}} \frac{C_1}{C_1^2 + (f_1 k \omega)^2} - T_k^{\text{Im}} \frac{f_1(k\omega)}{C_1^2 + (f_1 k \omega)^2} \\ -J_1(k\omega)^2 \left[-T_k^{\text{Re}} \frac{C_1}{C_1^2 + (f_1 k \omega)^2} - T_k^{\text{Im}} \frac{f_1(k\omega)}{C_1^2 + (f_1 k \omega)^2} \right] - T_k^{\text{Re}} - r_1(k\omega) \left[T_k^{\text{Re}} \frac{f_1(k\omega)}{C_1^2 + (f_1 k \omega)^2} - T_k^{\text{Im}} \frac{C_1}{C_1^2 + (f_1 k \omega)^2} \right] \\ T_k^{\text{Re}} \frac{f_1(k\omega)}{C_1^2 + (f_1 k \omega)^2} - T_k^{\text{Im}} \frac{C_1}{C_1^2 + (f_1 k \omega)^2} \\ r_1(k\omega) \left[-T_k^{\text{Re}} \frac{C_1}{C_1^2 + (f_1 k \omega)^2} - T_k^{\text{Im}} \frac{f_1(k\omega)}{C_1^2 + (f_1 k \omega)^2} \right] - J_1(k\omega)^2 \left[T_k^{\text{Re}} \frac{f_1(k\omega)}{C_1^2 + (f_1 k \omega)^2} - T_k^{\text{Im}} \frac{C_1}{C_1^2 + (f_1 k \omega)^2} \right] - T_k^{\text{Im}} \end{bmatrix} \quad (23)
 \end{aligned}$$

and the system of equations (21) becomes:

$$\begin{bmatrix} \theta^{\text{Re}} \\ 0 \\ \theta^{\text{Im}} \\ 0 \\ 1 \end{bmatrix}_{1k} = \begin{bmatrix} h_{11} & h_{12} & h_{13} & h_{14} & h_{15} \\ h_{21} & h_{22} & h_{23} & h_{24} & h_{25} \\ h_{31} & h_{32} & h_{33} & h_{34} & h_{35} \\ h_{41} & h_{42} & h_{43} & h_{44} & h_{45} \\ 0 & & & & 1 \end{bmatrix} \times \begin{bmatrix} \theta^{\text{Re}} \\ 0 \\ \theta^{\text{Im}} \\ 0 \\ 1 \end{bmatrix}_{F_k} \quad (24). \text{ The coefficients } h_{15}, h_{25}, h_{35} \text{ and } h_{45} \text{ are:}$$

$$h_{15} = -T_k^{\text{Re}} \frac{C_1}{C_1^2 + (f_1 k \omega)^2} - T_k^{\text{Im}} \frac{f_1(k\omega)}{C_1^2 + (f_1 k \omega)^2}$$

$$h_{25} = -J_1(k\omega)^2 \left[-T_k^{\text{Re}} \frac{C_1}{C_1^2 + (f_1 k \omega)^2} - T_k^{\text{Im}} \frac{f_1(k\omega)}{C_1^2 + (f_1 k \omega)^2} \right] - T_k^{\text{Re}} - r_1(k\omega) \left[T_k^{\text{Re}} \frac{f_1(k\omega)}{C_1^2 + (f_1 k \omega)^2} - T_k^{\text{Im}} \frac{C_1}{C_1^2 + (f_1 k \omega)^2} \right]$$

$$h_{35} = T_k^{\text{Re}} \frac{f_1(k\omega)}{C_1^2 + (f_1 k \omega)^2} - T_k^{\text{Im}} \frac{C_1}{C_1^2 + (f_1 k \omega)^2}$$

$$h_{45} = r_1(k\omega) \left[-T_k^{\text{Re}} \frac{C_1}{C_1^2 + (f_1 k \omega)^2} - T_k^{\text{Im}} \frac{f_1(k\omega)}{C_1^2 + (f_1 k \omega)^2} \right] - J_1(k\omega)^2 \left[T_k^{\text{Re}} \frac{f_1(k\omega)}{C_1^2 + (f_1 k \omega)^2} - T_k^{\text{Im}} \frac{C_1}{C_1^2 + (f_1 k \omega)^2} \right] - T_k^{\text{Im}}$$

The terms h_{25} and h_{45} are regrouped and expressed as:

$$h_{25} = T_k^{\text{Re}} \left[\frac{J_1 C_1 (k\omega)^2}{C_1^2 + (f_1 k\omega)^2} - 1 - r_1(k\omega) \frac{f_1(k\omega)}{C_1^2 + (f_1 k\omega)^2} \right] + T_k^{\text{Im}} \left[J_1 \frac{(k\omega)^2 f_1(k\omega)}{C_1^2 + (f_1 k\omega)^2} + r_1(k\omega) \frac{C_1}{C_1^2 + (f_1 k\omega)^2} \right]$$

$$h_{45} = T_k^{\text{Re}} \left[-r_1(k\omega) \frac{C_1}{C_1^2 + (f_1 k\omega)^2} - J_1 \frac{(k\omega)^2 f_1(k\omega)}{C_1^2 + (f_1 k\omega)^2} \right] + T_k^{\text{Im}} \left[-r_1(k\omega) \frac{f_1(k\omega)}{C_1^2 + (f_1 k\omega)^2} + J_1 \frac{(k\omega)^2 C_1}{C_1^2 + (f_1 k\omega)^2} - 1 \right]$$

By using the following convenient notations:

$$\psi = \frac{J_1 C_1 (k\omega)^2}{C_1^2 + (f_1 k\omega)^2} - 1 - r_1(k\omega) \frac{f_1(k\omega)}{C_1^2 + (f_1 k\omega)^2}$$

$$\phi = J_1 \frac{(k\omega)^2 f_1(k\omega)}{C_1^2 + (f_1 k\omega)^2} - r_1(k\omega) \frac{C_1}{C_1^2 + (f_1 k\omega)^2}$$

and equations (2) and (4) of the system of equations (24):

$$0 = h_{21} \theta_{F_k}^{\text{Re}} + h_{23} \theta_{F_k}^{\text{Im}} + h_{25}$$

$$0 = h_{41} \theta_{F_k}^{\text{Re}} + h_{43} \theta_{F_k}^{\text{Im}} + h_{45}$$

the following expressions are obtained:

$$-(h_{21} \theta_{F_k}^{\text{Re}} + h_{23} \theta_{F_k}^{\text{Im}}) = h_{25} = T_k^{\text{Re}} \psi + T_k^{\text{Im}} \phi$$

$$-(h_{41} \theta_{F_k}^{\text{Re}} + h_{43} \theta_{F_k}^{\text{Im}}) = h_{45} = -T_k^{\text{Re}} \phi + T_k^{\text{Im}} \psi \quad \text{from which the expressions}$$

of the real and imaginary parts of the engine torque are derived as a function of the deflections (or the speed) at the flywheel :

$$T_k^{\text{Re}} = \frac{-(h_{21} \theta_{F_k}^{\text{Re}} + h_{23} \theta_{F_k}^{\text{Im}}) \psi + (h_{41} \theta_{F_k}^{\text{Re}} + h_{43} \theta_{F_k}^{\text{Im}}) \phi}{\psi^2 + \phi^2} \quad (25) \quad \text{and}$$

$$T_k^{\text{Im}} = \frac{-(h_{41}\theta_{F_k}^{\text{Re}} + h_{43}\theta_{F_k}^{\text{Im}})\psi - (h_{41}\theta_{F_k}^{\text{Re}} + h_{43}\theta_{F_k}^{\text{Im}})\phi}{\psi^2 + \phi^2} \quad (26)$$

The harmonic component of order “k” of the engine torque is:

$$T_k = (T_k^{\text{Re}})\cos k\omega t + j(T_k^{\text{Im}})\sin k\omega t \quad (27)$$

and the total engine torque is [24]:

$$T = T_0 + \sum_{k=1}^N [A_{k_p} \cos k(\omega t + \varphi) + (B_{k_p} + B_{k_r}) \sin k(\omega t + \varphi)] \quad (28)$$

The simulation results show that for the operating condition of 1500 rpm, 4 Nm torque / 2.9 bar IMEP the single cylinder engine Deutz 0.7 l the engine torque can be evaluated from the measured flywheel speed both when ULSD and S-8 are used - Figure 3.10.

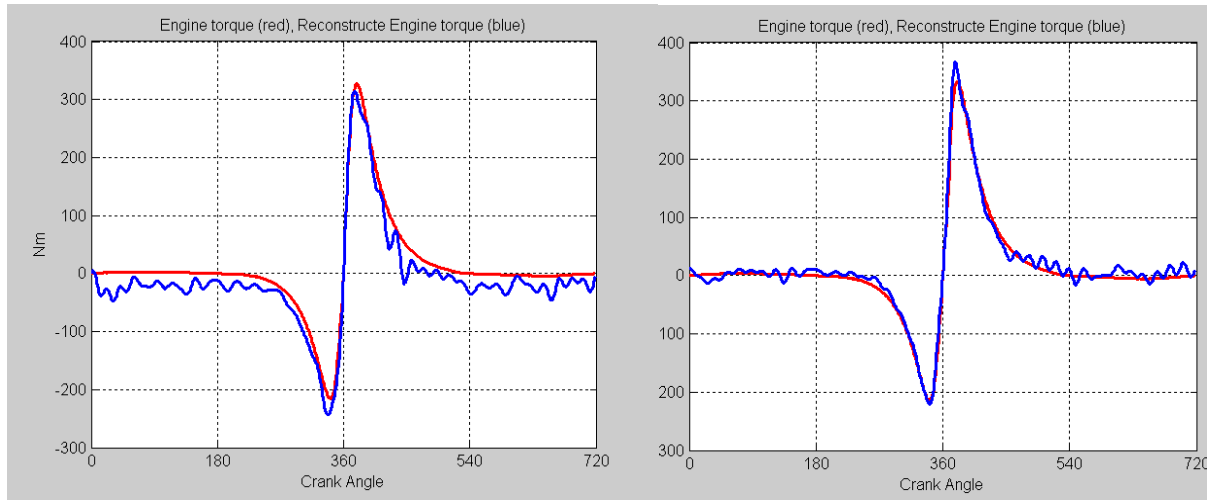


Figure 3.10 - Gas pressure torque reconstruction by reverse calculation at 1500 rpm, 4 Nm torque: left (ULSD), right (S-8), engine torque (red), reconstructed engine torque (blue)

It is to be noticed that the gas pressure torque T_p at TDC is = 0 (zero).

The in-cylinder pressure p is related to the gas pressure torque T_p by:

$$p = p_c + T_p \cos \beta / (A_p R \sin(\theta + \beta)) \quad (29)$$

where

p = in-cylinder pressure

p_c = carter pressure

T_p = gas pressure torque

A_p = piston area

R = crank radius

L = length of connecting rod

θ = crank angle

β = angle between the connecting rod and the cylinder axis,

$$\beta = \arcsin\left(\frac{R}{L} \sin \theta\right)$$

At TDC, where θ and β are 0 (zero), $\sin(\theta + \beta)$ also equals 0 (zero) hence the second term of the summation in (29) represents a division of 0 (zero) to 0 (zero) which, mathematically, is undefined.

To avoid the division by zero, the pressure around TDC is calculated

as:

$$P_{j+1} = \frac{M_{j+1} - M_j}{\text{trig}(\theta_{j+1}) - \text{trig}(\theta_j)} \frac{1}{A_p R}$$

and the results are displayed in figure 3.11.

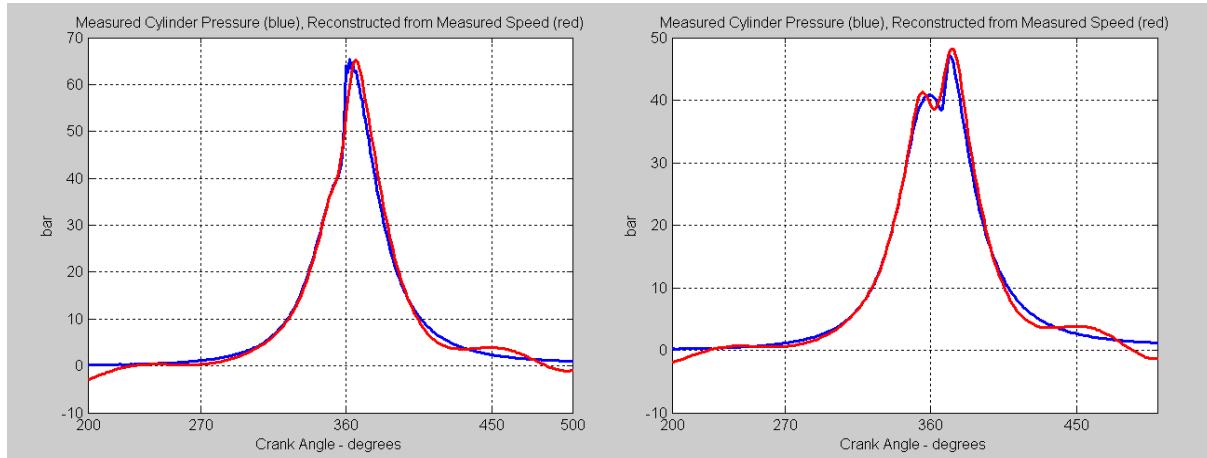


Figure 3.11 - Cylinder pressure reconstruction by reverse calculation at 1500 rpm, 4 Nm torque: left (ULSD), right (S-8); measured cylinder pressure (Blue), reconstructed pressure from measured speed (Red)

In conclusion, the model based method applied on a single-cylinder engine is fairly accurate because it reconstructs the pressure trace from which different combustion parameters can be evaluated. On the other hand, the technique is computationally intensive and it is hard to imagine that it could be used in real time (on-board) applications to identify the fuel. For this reason a more direct method has been developed and it is presented in the next chapter.

3.6 Direct Recognition Method on a single-cylinder engine

In order to find a technique less computational than the Model-Based Recognition Method, the Direct Recognition Method is considered as an alternative. The procedure assumes that the crankshaft is a rigid body and consists of the following steps:

1) the measured speed is smoothed by a Fast Fourier Transformation and expressed as a Fourier series

2) the speed is then differentiated to obtain the crankshaft angular acceleration

3) the angular acceleration is multiplied by the total mass moment of inertia to yield the engine torque

4) the reciprocating inertia torque is subtracted from the engine torque and the gas pressure torque is obtained

5) the gas pressure torque is used in the same way to obtain the cylinder pressure.

For the single cylinder engine, the 0.7 L Deutz, the engine torque is obtained from the measured flywheel speed for the same operating conditions: 1500 rpm, 4 Nm torque IMEP = 2.9 bar - Figure 3.12.

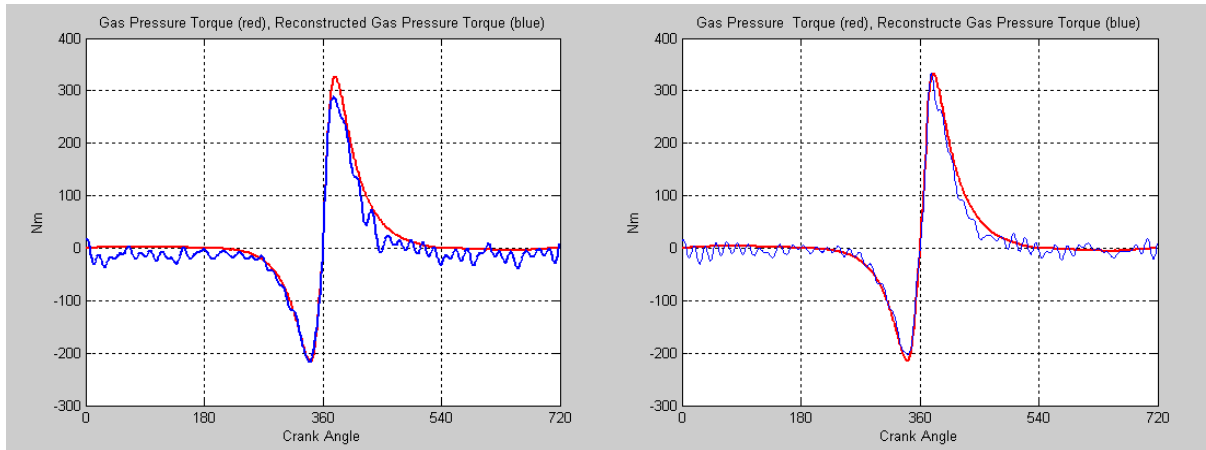


Figure 3.12 - Gas pressure torque reconstruction by direct recognition method: left (ULSD), right (S-8); engine torque (red), reconstructed engine torque (blue)

From the gas pressure torque the cylinder pressure is calculated –

Figure 3.13.

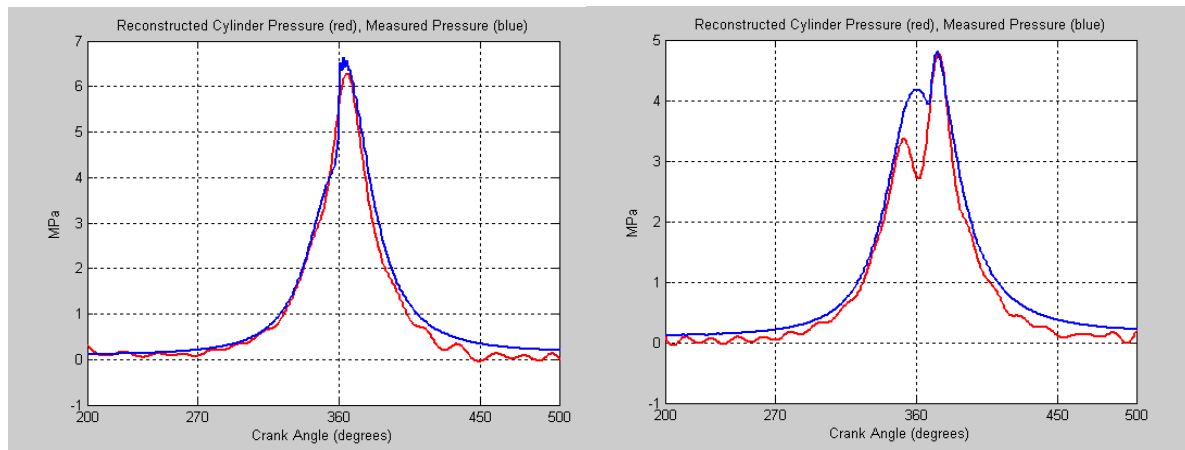


Figure 3.13 - Cylinder pressure reconstruction by direct recognition method: left (ULSD), right (S-8) reconstructed cylinder pressure (red), measured pressure (blue)

In conclusion, because of the rigid body assumption, the estimation of pressure trace using Direct Recognition Method is less accurate than the estimation of pressure trace using Model-Based Recognition Method – compare Figures 3.11 and 3.13.

Nonetheless, on a single-cylinder engine, both Direct Recognition Method and Model-Based Recognition Method determine fairly well the peak cylinder pressure and its location with respect to the TDC. The Model-Based Recognition Technique yields slightly better estimates, while the Direct Recognition Technique is less computationally intensive.

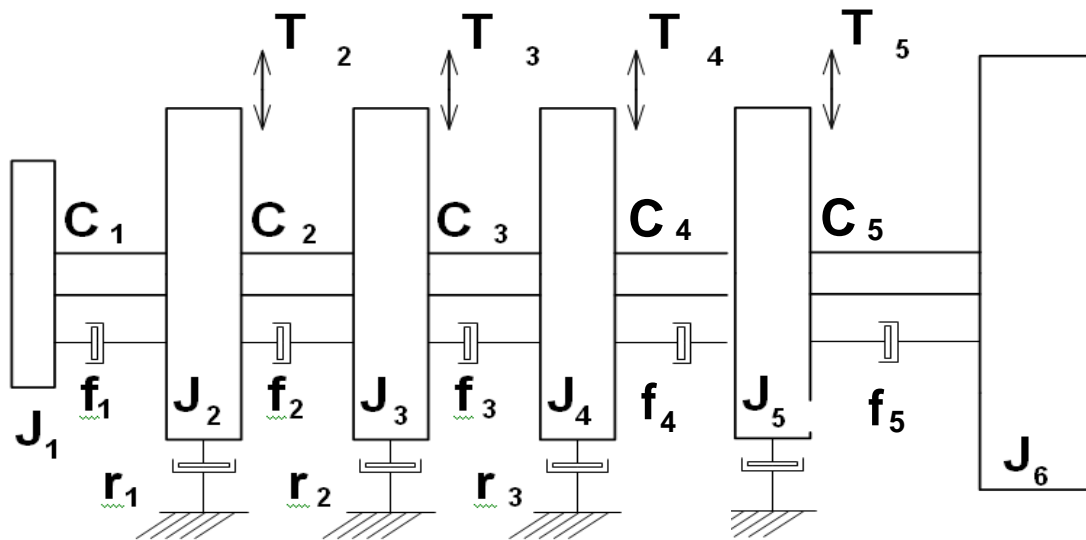


Figure 3.14a - Lumped mass dynamic model of a four-cylinder engine

If the Model-Based Recognition Technique is applied on a multi-cylinder engine, e.g. on a four-cylinder engine – Figure 3.14, then expression (14) in subchapter 3.5, representing the multiplication of

transfer matrices of masses and mass-less elastic elements according to the crankshaft model, becomes as follows:

$$Z_{1_k} = P_{1_k} \times F_{1_k} \times P_{2_k} \times F_{2_k} \times P_{3_k} \times F_{3_k} \times P_{4_k} \times F_{4_k} \times P_{5_k} \times F_{5_k} \times P_{6_k} \times Z_{6_k} \quad (30)$$

Considering that all four cylinder torques are equal $T_{2k} = T_{3k} = T_{4k} = T_{5k} = T_k$,

then the multiplication in steps – see expression (20), is the following:

$$F_{5_k} \times P_{6_k} = \begin{bmatrix} F_{5_k}^* P_{6_k}^* & 0 \\ 0 & 1 \end{bmatrix}$$

$$P_{5_k} \times (F_{5_k} \times P_{6_k}) = \begin{bmatrix} P_{5_k}^* & T_k \\ 0 & 1 \end{bmatrix} \times \begin{bmatrix} F_{5_k}^* P_{6_k}^* & 0 \\ 0 & 1 \end{bmatrix} = \begin{bmatrix} P_{5_k}^* F_{5_k}^* P_{6_k}^* & T_k \\ 0 & 1 \end{bmatrix}$$

$$F_{4_k} \times (P_{5_k} \times F_{5_k} \times P_{6_k}) = \begin{bmatrix} F_{4_k}^* & 0 \\ 0 & 1 \end{bmatrix} \times \begin{bmatrix} P_{5_k}^* F_{5_k}^* P_{6_k}^* & T_k \\ 0 & 1 \end{bmatrix} = \begin{bmatrix} F_{4_k}^* P_{5_k}^* F_{5_k}^* P_{6_k}^* & F_{4_k}^* T_k \\ 0 & 1 \end{bmatrix}$$

$$\begin{aligned} P_{4_k} \times (F_{4_k} \times P_{5_k} \times F_{5_k} \times P_{6_k}) &= \begin{bmatrix} P_{4_k}^* & T_k \\ 0 & 1 \end{bmatrix} \times \begin{bmatrix} F_{4_k}^* P_{5_k}^* F_{5_k}^* P_{6_k}^* & F_{4_k}^* T_k \\ 0 & 1 \end{bmatrix} \\ &= \begin{bmatrix} P_{4_k}^* F_{4_k}^* P_{5_k}^* F_{5_k}^* P_{6_k}^* & (P_{4_k}^* F_{4_k}^* + 1)T_k \\ 0 & 1 \end{bmatrix} \end{aligned}$$

$$\begin{aligned} F_{3_k} \times (P_{4_k} \times F_{4_k} \times P_{5_k} \times F_{5_k} \times P_{6_k}) &= \begin{bmatrix} F_{3_k}^* & 0 \\ 0 & 1 \end{bmatrix} \times \begin{bmatrix} P_{4_k}^* F_{4_k}^* P_{5_k}^* F_{5_k}^* P_{6_k}^* & (P_{4_k}^* F_{4_k}^* + 1)T_k \\ 0 & 1 \end{bmatrix} = \\ &= \begin{bmatrix} F_{3_k}^* P_{4_k}^* F_{4_k}^* P_{5_k}^* F_{5_k}^* P_{6_k}^* & F_{3_k}^* (P_{4_k}^* F_{4_k}^* + 1)T_k \\ 0 & 1 \end{bmatrix} \end{aligned}$$

⋮

The final multiplication in expression (30) becomes as follows:

$$P_{1_k} \times (F_{1_k} \times P_{2_k} \times F_{2_k} \times P_{3_k} \times F_{3_k} \times P_{4_k} \times F_{4_k} \times P_{5_k} \times F_{5_k} \times P_{6_k}) =$$

$$= \begin{bmatrix} P_{1_k}^* F_{1_k}^* P_{2_k}^* F_{2_k}^* P_{3_k}^* F_{3_k}^* P_{4_k}^* F_{4_k}^* P_{5_k}^* F_{5_k}^* P_{6_k}^* & (P_{1_k}^* F_{1_k}^* P_{2_k}^* F_{2_k}^* P_{3_k}^* F_{3_k}^* P_{4_k}^* F_{4_k}^* + P_{1_k}^* F_{1_k}^* P_{2_k}^* F_{2_k}^* P_{3_k}^* F_{3_k}^* + P_{1_k}^* F_{1_k}^* P_{2_k}^* F_{2_k}^* + P_{1_k}^* F_{1_k}^*) T_k \\ 0 & 1 \end{bmatrix}$$

or in a simpler form:

$$P_{1_k} \times (F_{1_k} \times P_{2_k} \times F_{2_k} \times P_{3_k} \times F_{3_k} \times P_{4_k} \times F_{4_k} \times P_{5_k} \times F_{5_k} \times P_{6_k}) = \quad (31)$$

$$= \begin{bmatrix} H_k & (P_{1_k}^* F_{1_k}^* P_{2_k}^* F_{2_k}^* P_{3_k}^* F_{3_k}^* P_{4_k}^* F_{4_k}^* + P_{1_k}^* F_{1_k}^* P_{2_k}^* F_{2_k}^* P_{3_k}^* F_{3_k}^* + P_{1_k}^* F_{1_k}^* P_{2_k}^* F_{2_k}^* + P_{1_k}^* F_{1_k}^*) T_k \\ 0 & 1 \end{bmatrix}$$

If we continue the computation pattern presented in subchapter 3.5 we will eventually derive an expression of the engine torque from the crankshaft speed, similar to formula (28).

However, because expression (31) already involves a very large number of computations (matrices multiplications), the final formula for the engine torque for a four cylinder engine will be even more computationally expensive therefore it is less likely that this method can be used in real time (on-board) applications.

Because of that reason, for multi-cylinder engines, it is preferred to use the direct method in the same manner as it was applied on single-cylinder engines. The procedure and the results are presented in the next subchapter.

3.7 Direct Recognition Method on a four-cylinder engine

The Direct Recognition Technique yields good results on a single-cylinder engine – see subchapter 3.6. Nonetheless, it can also be applied on multiple-cylinder engines. In a multi-cylinder engine there are small differences in the operation of the cylinders even under steady state operation conditions. Due to the increased length of the crankshaft, torsional vibrations disturb the variation of the crankshaft speed.

The less disturbed speed is that of the flywheel where the measurement has to be performed.

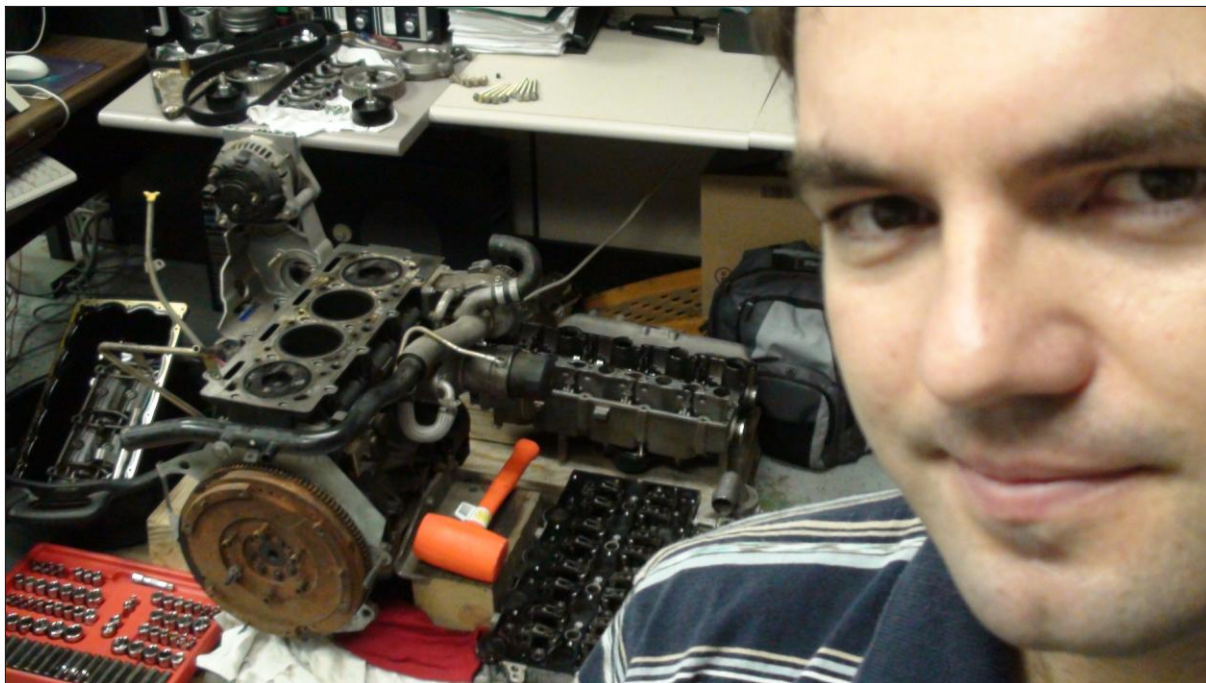


Figure 3.14b - VM Motori 2.5 L engine dismantled
in order to draw its moving parts

All these disturbances require that average values for the cylinder pressure and the crankshaft speed variations should be first determined.

Similarly to the single-cylinder engine case, in order to proceed with our calculations, the value of the total mass moment of inertia of the parts in rotation had to be known.

The total mass moment of inertia of the parts in rotation has been determined by dismantling a spare four-cylinder 2.8 l VM Motori engine (figure 3.14) and drawing the corresponding 3D parts - figures 3.15–3.17.

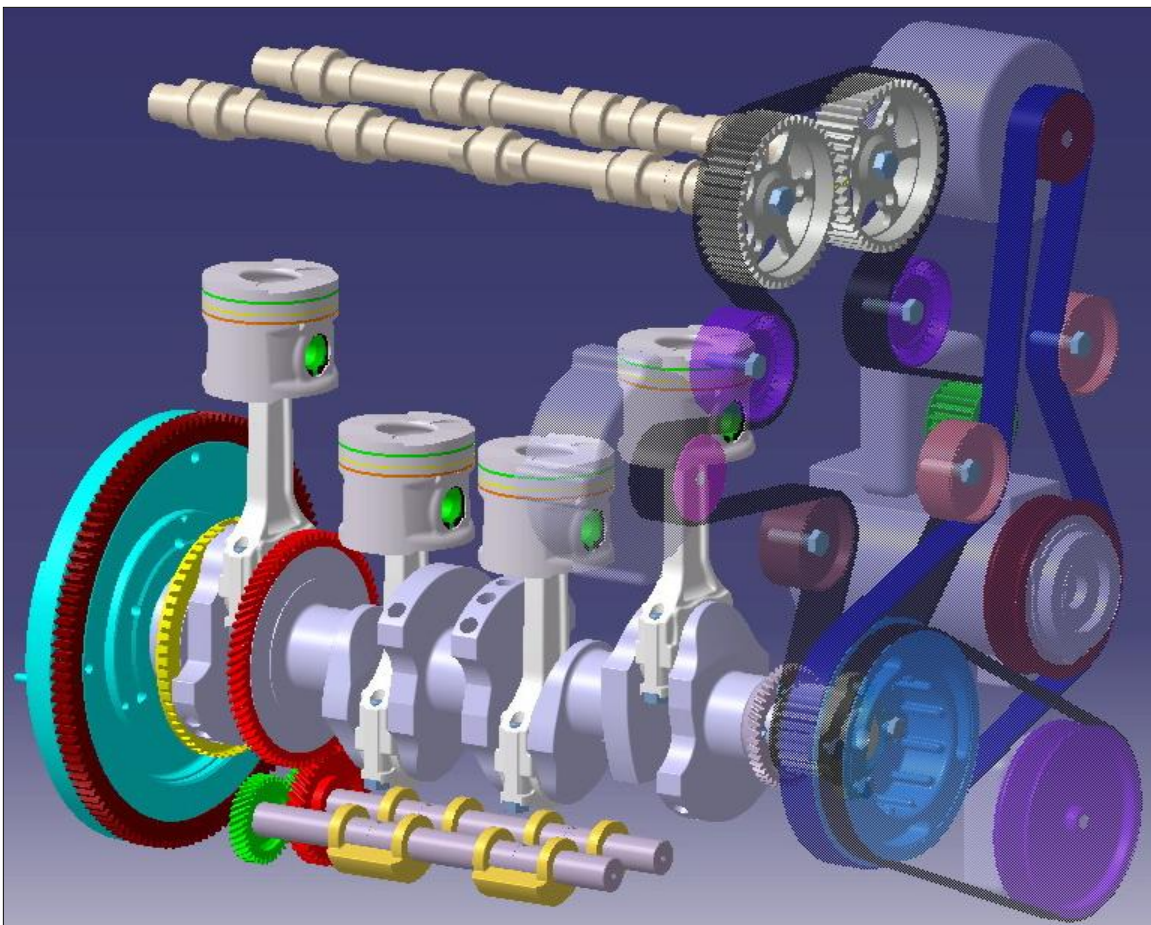


Figure 3.15 - VM Motori 2.5 L engine: drawing of the moving parts

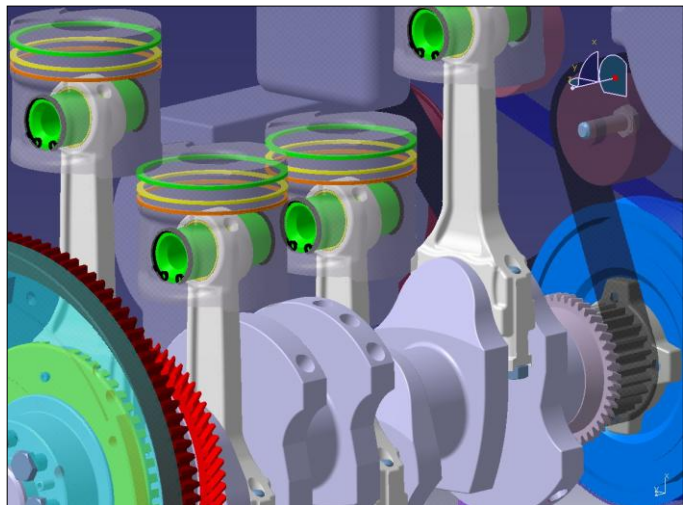
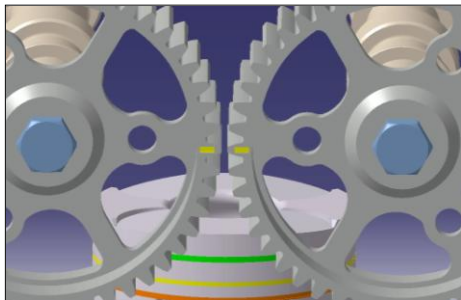
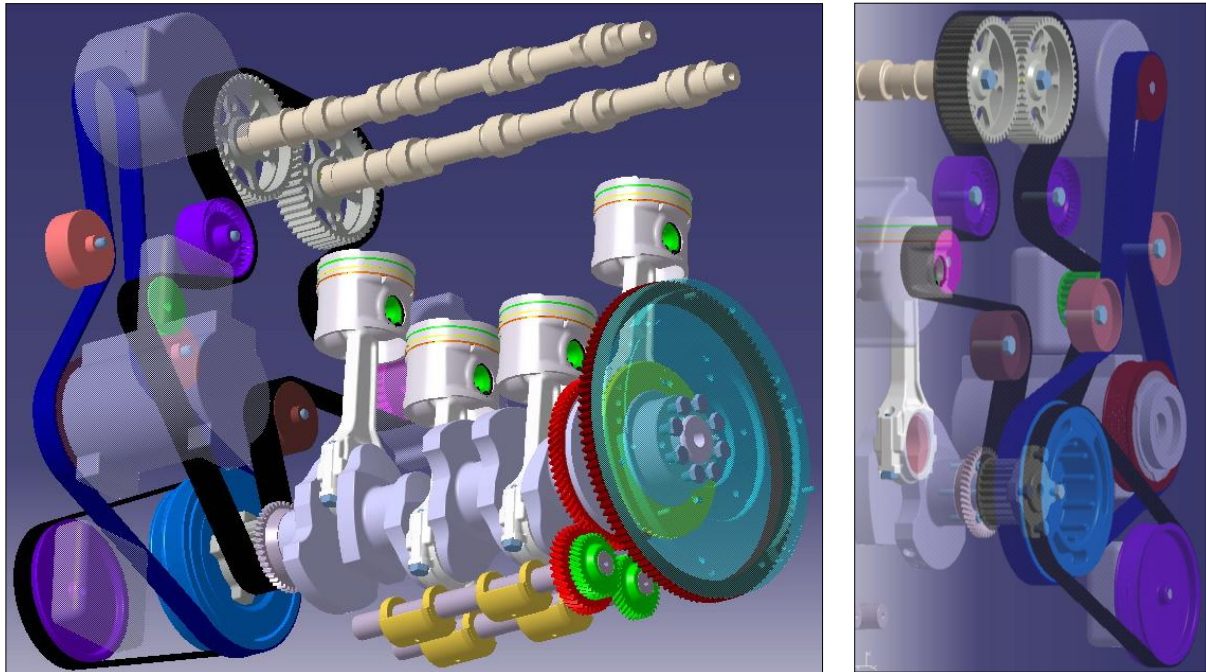
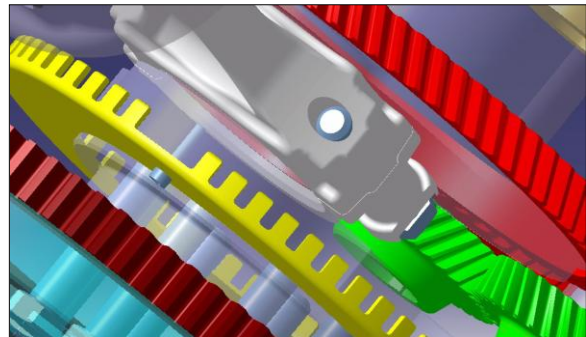
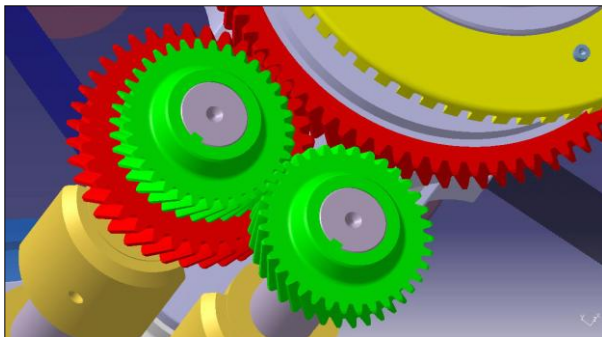


Figure 3.16 - VM Motori engine: drawings of the moving parts



By following the procedure described in chapter 3.4 the mass moment of inertia of the VM Motori engine was determined – see Table 3.2.


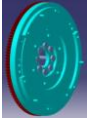

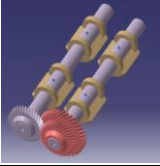
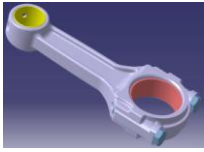
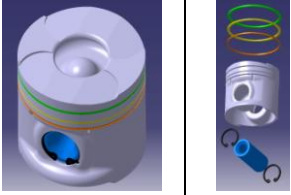


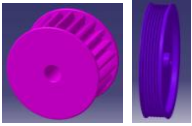
Part name	Designed part	Mass (kg)	Mass moment of inertia around the principal axis of the part (kg*m ²)
Crankshaft		21.65	0.0397
Flywheel		14.36	0.1882
Camshafts assembly		2 * 3.543 = 7.086	2 * 0.002169 = 0.004338
Balancing shafts assembly		2.464 + 2.061 = 4.4525	0.008704 + 0.005241 = 0.013945
Connecting rod assembly (4 pieces)		4 * 0.374 = 1.496	-
Piston assembly, including piston bolt (4 pieces)		4 * 0.811 = 3.244	-
Pulley		4.663	0.01984
Crankshaft gear		0.87	0.00557164
5 auxiliary components, wheels		5 * 0.081 = 0.405	5 * 0.00031181 = 0.00155905
Total moving engine parts (see calculations on the next page)		58.225	0.317372822

Table 3.2 - VM Motori 2.5 L four cylinder engine parts and their masses characteristics

The individual mass in translation is:

$$m_{tr} = m_{group_piston} + 0.275 * m_{connecting_rod} = 0.811 + 0.275 * 0.374 = 0.914 \text{ kg}$$

The individual mass of the connecting rod in rotation is:

$$m_{cr} = 0.725 * m_{connecting_rod} = 0.725 * 0.374 \text{ kg} = 0.271 \text{ kg}$$

The summation is:

$$m_{tr}/2 + m_{cr} = 0.914 \text{ kg} / 2 + 0.271 \text{ kg} = 0.457 \text{ kg} + 0.271 \text{ kg} = 0.728 \text{ kg}$$

The crankshaft radius is:

$$r = \text{stroke} / 2 = 0.088 \text{ m} / 2 = 0.044 \text{ m}$$

The total mass moment of inertia of the engine moving parts is:

$$J_{total} = J_{crankshaft} + 4 * (m_{tr} / 2 + m_{cr}) * r^2 + J_{flywheel} + J_{camshafts} * (1/2)^2 + \\ + 2^2 * J_{balancing_shafts} + J_{pulley} + J_{gear} + J_{wheels}$$

$$J_{total} = 0.0397 + 4 * 0.728 * 0.044^2 + 0.1882 + 0.004338 / 4 + \\ + 4 * 0.013945 + 0.01984 + 0.00557164 + 0.00155905$$

$$J_{total} = 0.0397 + 0.005637632 + 0.1882 + 0.0010845 + 0.05578 + 0.01984 \\ + 0.00557164 + 0.00155905$$

$$J_{total} = 0.317372822 \text{ kg} * \text{m}^2$$

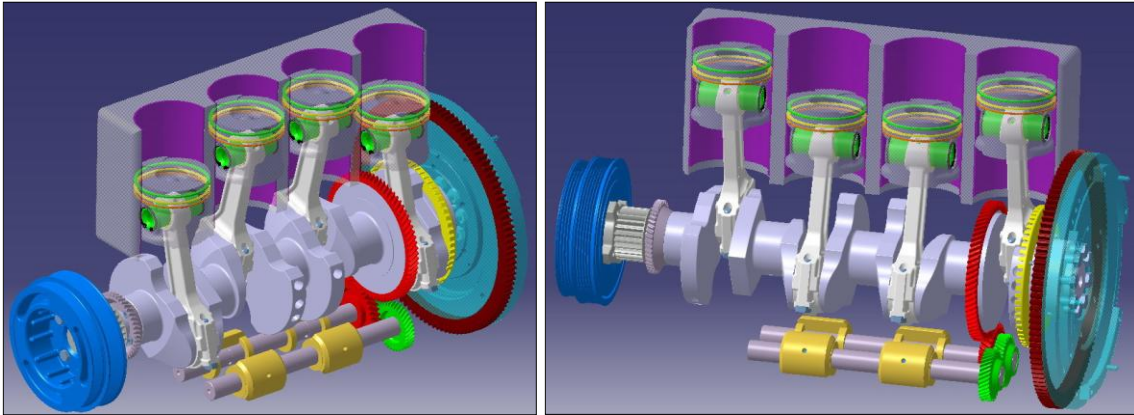


Figure 3.17 - VM Motori 2.5 L engine in motion

Then the average values of the cylinder pressure and of the crankshaft speed variations were calculated – figures 3.18 and 3.19.

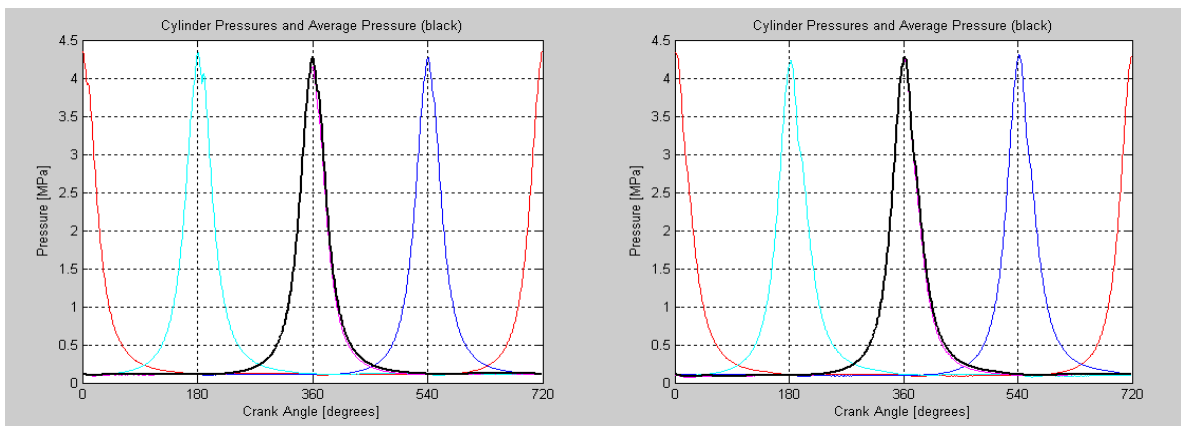


Figure 3.18 - Four cylinder pressures and average cylinder pressure variation (black curve) when idling at 1000 rpm (left) and 1500 rpm (right) on ULSD

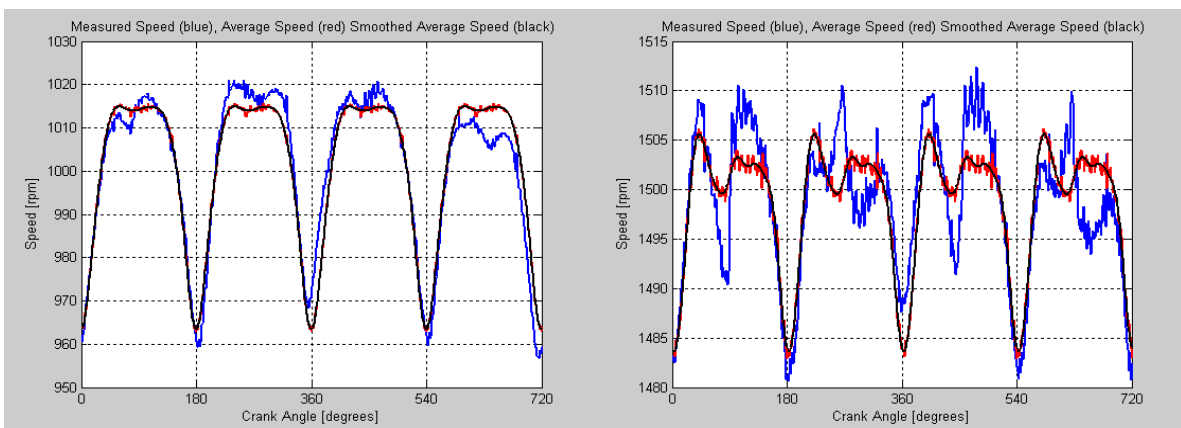


Figure 3.19 - Engine speed variation idling 1000 rpm (left) and 1500 rpm (right): measured speed (blue), average speed (red), smoothed average speed (black) on ULSD

The engine speed was differentiated to obtain the angular acceleration –
Figure 3.20.

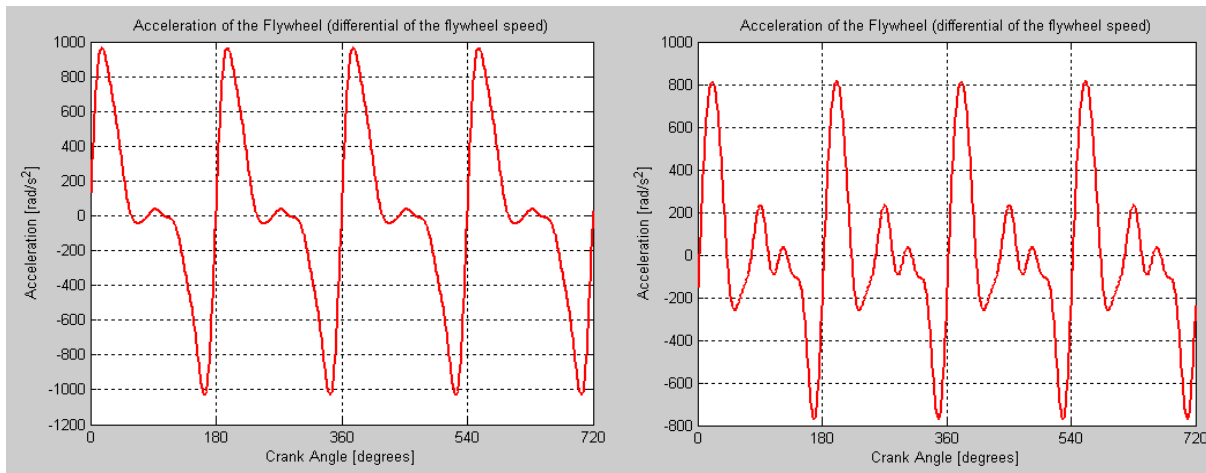


Figure 3.20 - Crankshaft angular acceleration at idling
1000 rpm (left) and 1500 rpm (right)

The angular acceleration was multiplied by the total mass moment of inertia to yield the engine torque, from which the reciprocating inertia torque was subtracted to evaluate the gas pressure torque – Figure 3.21.

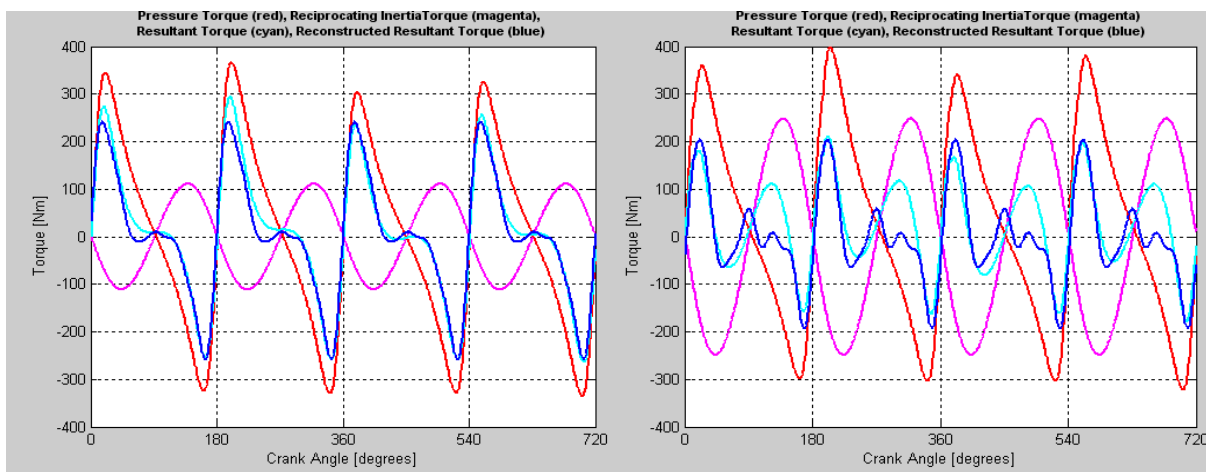


Figure 3.21 - Torques acting on the crankshaft when idling 1000 rpm (left) and 1500 rpm (right): gas pressure torque (red), inertia torque (magenta), resultant torque (cyan), reconstructed torque (blue)

Even though the resultant torque and the reconstructed torque do not overlap over the entire 720 CAD interval, their coincidence was fairly good around the area of interest at TDC.

From the gas pressure torque the cylinder pressure were computed –

Figure 3.22.

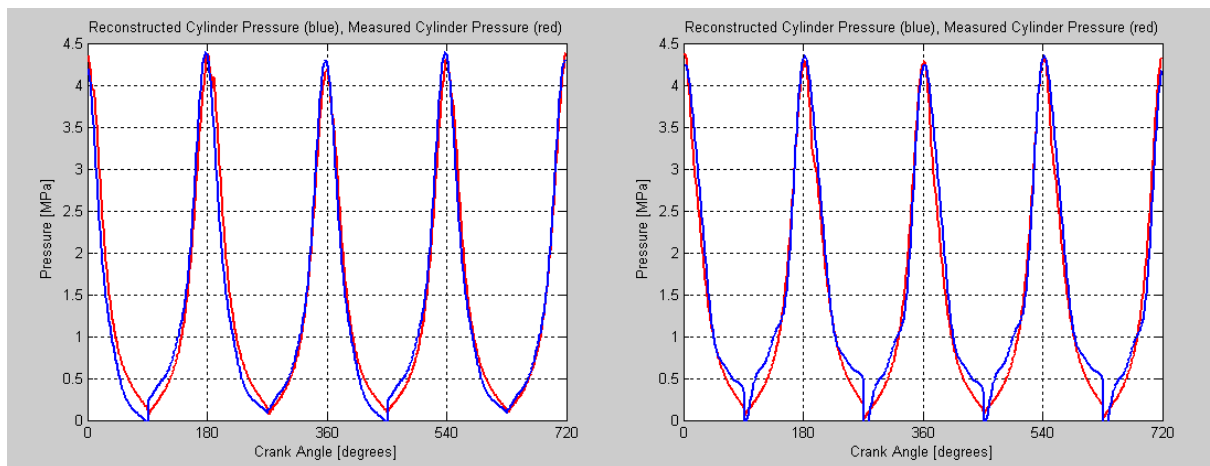


Figure 3.22 - Reconstructed cylinder pressure (blue) and measured cylinder pressure (red) when idling 1000 rpm (left) and 1500 rpm

In conclusion, the results show that the Direct Recognition Technique can be successfully used in estimating the peak cylinder pressure in single and multiple cylinder engines. Combustion parameters such as:

- value and location of peak pressure with respect to TDC
- start of combustion (or ignition delay)
- rate of cylinder pressure rise

can be used to determine the fuel type.

The measured instantaneous crankshaft speed can be used to estimate the peak cylinder pressure and its location with respect to TDC.

Both Direct Recognition and Model-Based Recognition methods determine fairly well the peak cylinder pressure and its location with respect to the TDC, which are an indicative of the ignition properties of the fuel. The Model-Based Recognition Technique yields slightly better estimates, while the Direct Recognition Method is less computationally intensive.

3.8 Estimation of Start of Combustion (Ignition Delay)

3.8.1. Introduction

An original method to determine the fuel type is to estimate the start of combustion from the engine speed. At the beginning of Chapter 3 the start of combustion was defined as being the point where the firing pressure curve separates from the motoring (cranking) pressure curve – Figure 3.1. The needle lift is measured separately with a position sensor. The difference between the two signals represents the ignition delay. Estimation of ignition delay means, in fact, estimation of start of combustion and of the cetane number.

The ignition delay is strongly correlated to the cetane number of a fuel: the higher the cetane number, the shorter the ignition delay. Also, the higher the cetane number, the higher the tendency of that fuel to auto-ignite. More information about the cetane number of a fuel has been provided in sub-chapter 2.2.2.

The influence of the cetane number on the combustion process is probably best depicted in Figure 3.23 where the rates of heat release at 1500 rpm / 360 Nm (7.5 bar IMEP) have been represented for the four tested fuels: ULSD, JP-8, S-8 and bio-diesel B100. Even though the

behavior of these fuels is dissimilar in the later stages of combustion, in the beginning they perform as follows: S-8, having the highest cetane number, 56, ignites first; it is followed by ULSD, then by B20 closely and finally by JP-8 with the lowest cetane number, 43.

Perhaps it should be also discussed how the ignition delay influences the pressure curve. The longer the ignition delay is, the more fuel vaporizes and better mixture is prepared. Consequently, the burning will take place later but faster, in a predominant pre-mixed type with high peak pressures and rates of pressure rise. As long as the crank-slider mechanism is not being stressed beyond the admissible limits, the pre-mixed combustion, generated by a longer ignition delay, is beneficial to the engine because it burns the fuel efficiently, generating maximum power, low CO and HC but high NO_x emissions.

On the other hand, if the ignition delay is short, there is less time for proper mixing and fuel starts to burn early in a predominant diffusion mode. This means the rate of burning is limited by the rate of fuel diffusion into the surrounding air, generating poor combustion efficiency, high HC, CO and soot levels. Such burning flames, if present, are usually called 'yellow – sooty' flames therefore, generally, this is not desired. An example of such two fuels, S-8 with short ignition delay and diffusion combustion and ULSD

with long ignition delay and pre-mixed combustion, has been presented in Figure 2.34, sub-chapter 2.3.3.

If at a certain operating point, the start of injection is kept constant then, for different fuels, different starts of combustion or ignition delays are obtained. Also, in a reverse reasoning, for a specific fuel, the start of injection can be adjusted to optimize the engine running for that particular fuel.

In conclusion, the ignition delay or the start of combustion at a certain operating point is specific to each fuel and can be used as a fuel identifying parameter.

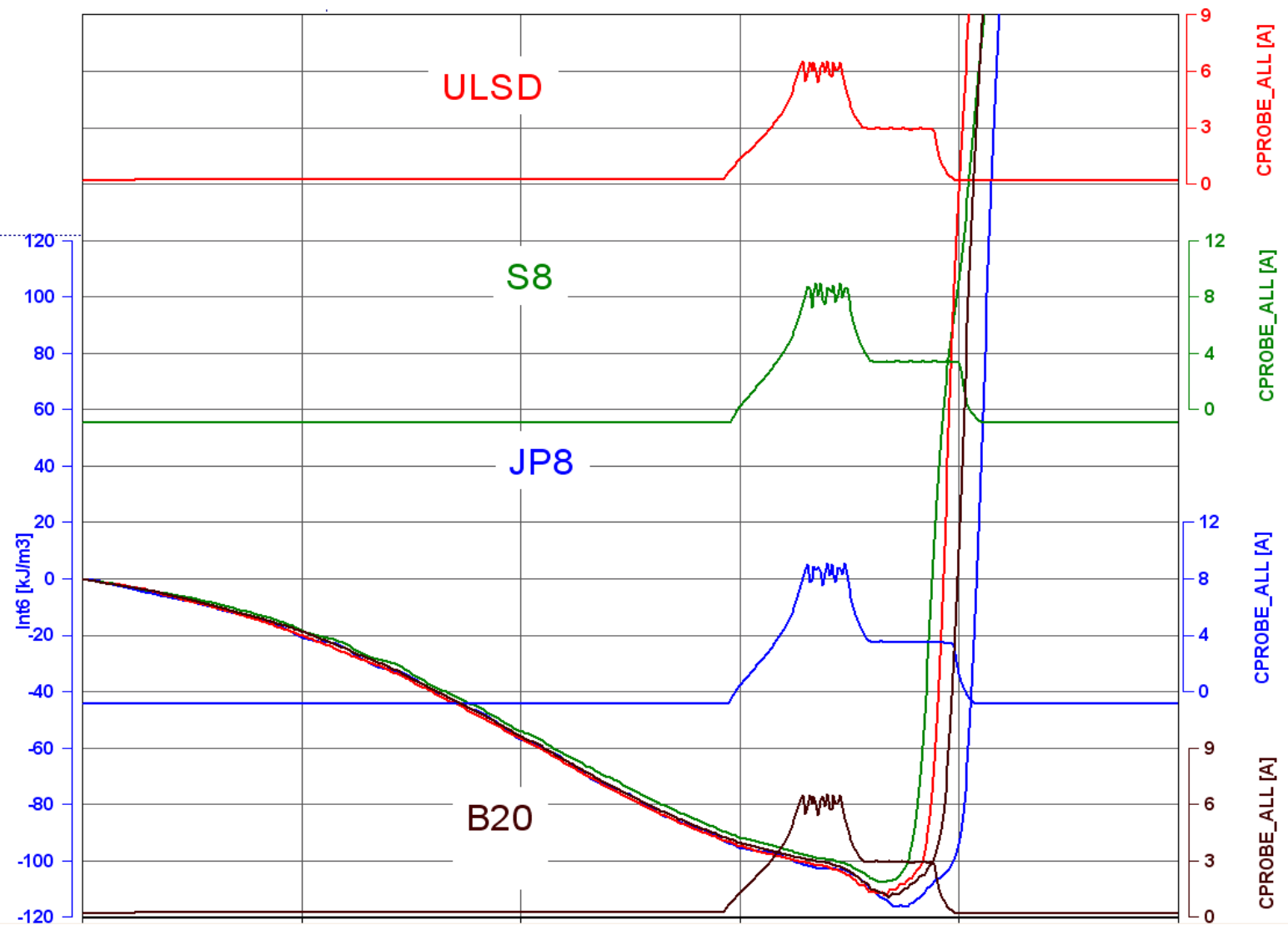


Figure 3.23 – Rates of heat release at cylinder #6 for ULSD, S-8, JP-8 and B-20 at 1500 rpm, 360 Nm / 7.5 bar IMEP (Mercedes 6-cylinder engine)

3.8.2 Representation of measured signal as a Fourier series

The basic idea for fuel identification was to convert first the measured speed signal into frequency domain. In order to achieve that, this periodic signal of period 2π has been subjected to a Fourier series of harmonic components of period 2π , namely sines and cosines.

A periodic function $f(x)$ that is integrable on $[-\pi, \pi]$ can be expressed as a Fourier series [31]:

$$(S_N f)(x) = \frac{a_0}{2} + \sum_{n=1}^N [a_n \cos(nx) + b_n \sin(nx)], \quad N \geq 0 \quad (32)$$

where the harmonic coefficients:

$$a_n = \frac{1}{\pi} \int_{-\pi}^{\pi} f(x) \cos(nx) dx, \quad n \geq 0 \quad (33) \quad \text{and}$$

$$b_n = \frac{1}{\pi} \int_{-\pi}^{\pi} f(x) \sin(nx) dx, \quad n \geq 1 \quad (34)$$

are called the Fourier coefficients of f .

The expression $S_N f$ in (32) is a sum of trigonometric polynomials that approximate the function f . This approximation improves as N tends to infinity.

Among the important functions used in Fourier series are odd and even functions. They satisfy particular symmetry relations. A real-valued function of a real variable $f(x)$ is even if the following equation holds for all x in the domain of f [31]:

$$f(x) = f(-x).$$

Geometrically, the graph face of an even function is symmetric with respect to the y -axis, meaning that its graph remains unchanged after reflection about the y -axis.

A real-valued function of a real variable $f(x)$ is odd if the following equation holds for all x in the domain of f :

$$-f(x) = f(-x)$$

The graph of an odd function has rotational symmetry with respect to the origin, meaning that its graph remains unchanged after rotation of 180 degrees about the origin.

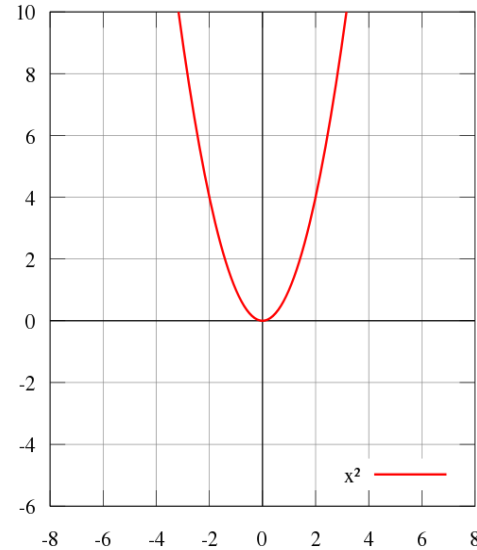


Figure 3.24 - Example of an even function: $f(x) = x^2$

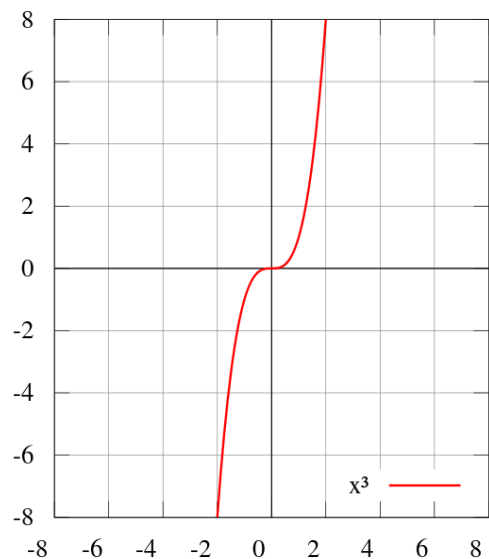


Figure 3.25 - Example of an odd function: $f(x) = x^3$

Some of the properties of odd and even functions are as follows:

- the sum of two even functions is even, and any constant multiple of an even function is even
- the sum of two odd functions is odd, and any constant multiple of an odd function is odd
- the sum of an even and odd function is neither even nor odd, unless one of the functions is equal to zero over the given domain
- the product of two even functions is an even function
- the product of two odd functions is an even function
- the product of an even function and an odd function is an odd function.

As a consequence of the latest property mentioned above, it results that, if f is a 2π -periodic odd function, then $a_n = 0$ (see formula 33 in this subchapter) for all n because the integral of an odd function over the interval $[-\pi, \pi]$ is 0 (zero). It means that the corresponding Fourier series (see formula 32) contains only sine terms in its summation.

Similarly, if f is a 2π -periodic even function, then $b_n = 0$ (see formula 34) for all n because the integral of an odd function over the interval $[-\pi, \pi]$ is 0 (zero). It means that the corresponding Fourier series contains only cosine terms in its summation.

In conclusion:

- if f is a 2π -periodic odd (symmetrical) function then its corresponding Fourier series contains only sine terms in its summation
- if f is a 2π -periodic even (anti-symmetrical) function then its corresponding Fourier series contains only cosine terms in its summation.

3.8.3 Estimation of Start of Combustion (Ignition Delay) on a single-cylinder engine

A way to correlate speed measurement variation with gas pressure torque is to consider separately the components of the engine torque which are the reciprocating inertia torque and the gas pressure torque. The gas pressure torque consists of the motoring torque and the combustion torque, as presented in figures 3.26 and 3.27 for the 0.7 L Deutz engine.

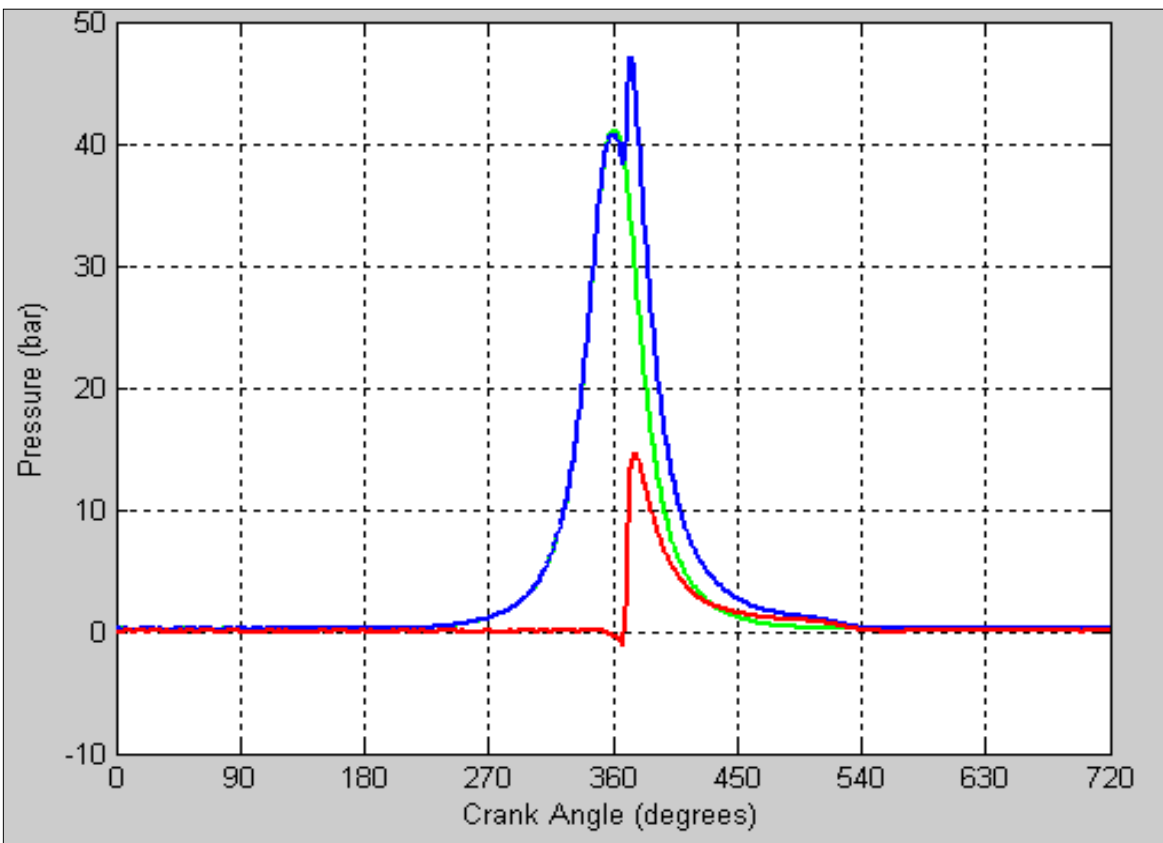


Figure 3.26 - 0.7 L Deutz engine running on ULSD:
Cylinder pressures at 1500 rpm and 4 Nm torque / 2.9 bar IMEP -
motoring (green), combustion (red), total (blue)

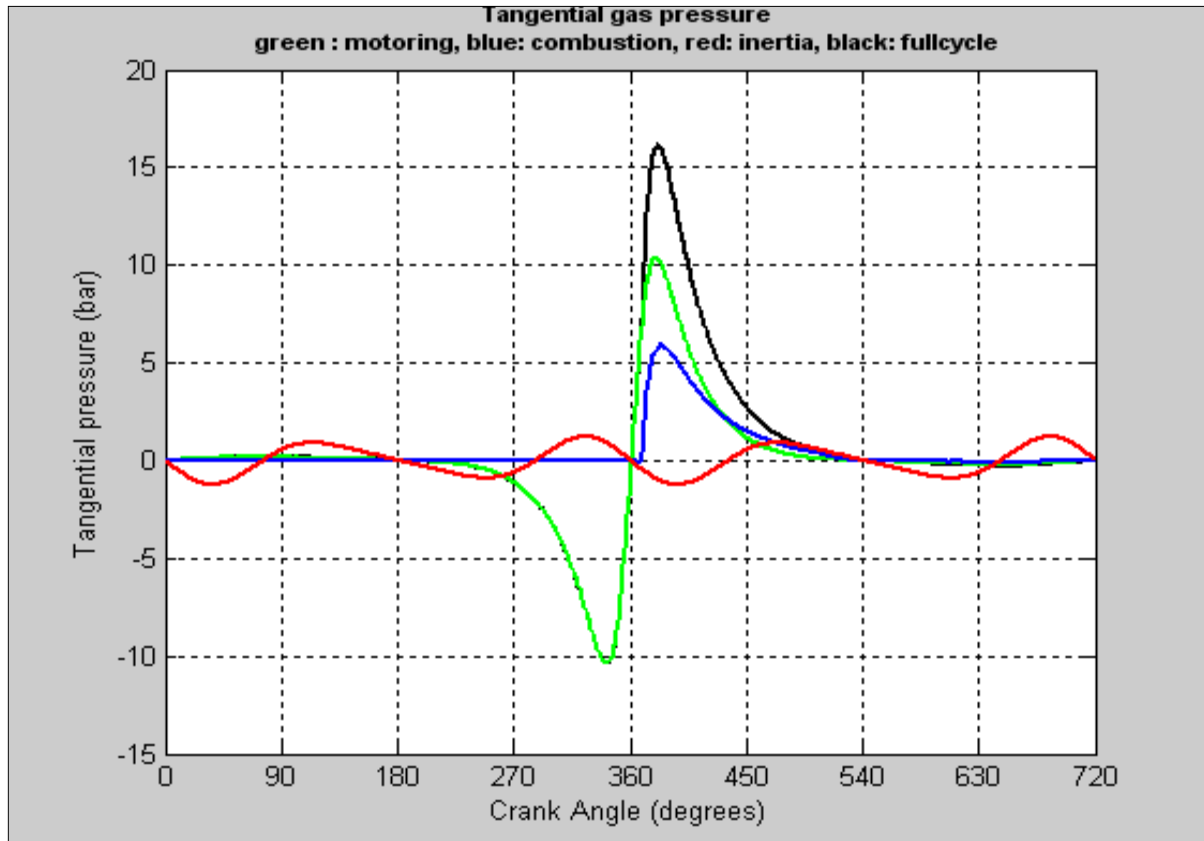


Figure 3.27 - 0.7 L Deutz engine running on ULSD:

Tangential gas pressures at 1500 rpm and 4 Nm torque/2.9 bar IMEP:
motoring (green), combustion (blue), inertia (red), total (black)

The inertia torque and the motoring torque are odd (symmetrical) functions over the four stroke cycle of the engine [24]. By following the conclusions of subchapter 3.8.2, it results that both Fourier series of the inertia torque and of the motoring torque consist of only $\sin(k\theta)$ terms. The combustion torque, being neither an odd nor an even function, is described by a Fourier series containing both sine and cosine terms.

The harmonic components of the reciprocating inertia torque are known and only the first 6 terms are important [24]. They depend on the

translating mass of the crank slider mechanism, the crank radius and the crankshaft speed.

The harmonic components of the motoring torque can be determined as a function of engine speed by running the engine without firing and stored then in look-up tables. The estimated engine torque is obtained from the measured crankshaft speed as presented in subchapter 3.5 or subchapter 3.6. The following equation is true [24]:

$$\text{Combustion torque} = \text{Engine torque} - \text{Inertia torque} - \text{Motoring torque} \quad (33)$$

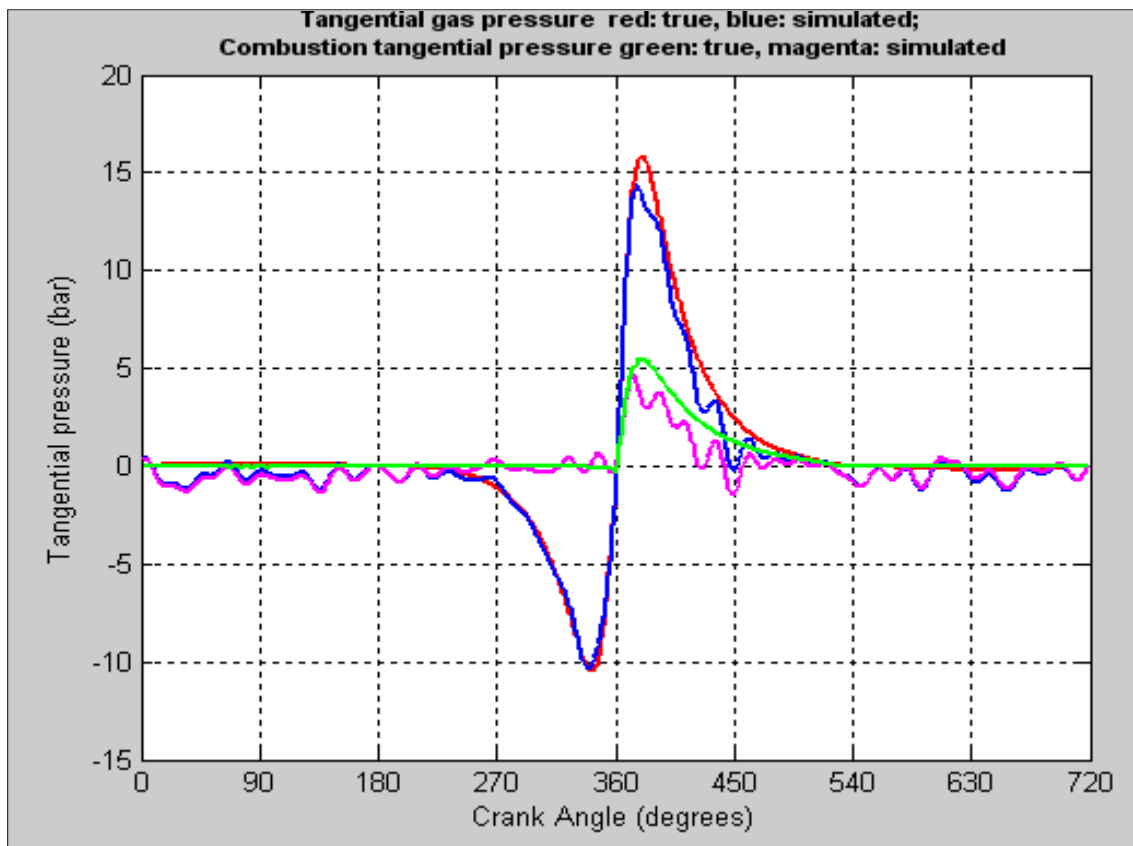


Figure 3.28 - 0.7 L Deutz engine on ULSD: Tangential gas pressure at 1500 rpm and 4 Nm torque / 2.9 bar IMEP: total (red), simulated (blue), combustion (green), combustion simulated (magenta)

The combustion torque can be computed because the terms in the right hand side of equation (34) are all known. Because of the sharp rise of the combustion torque, the start of combustion could be determined.

For the single-cylinder engine, there are two such examples: first is ULSD represented in figure 3.28. If the area around TDC in figure 3.28 is zoomed in, then figure 3.29 is obtained, where one can observe that the SOC (Start Of Combustion) is at 360 CAD (TDC).

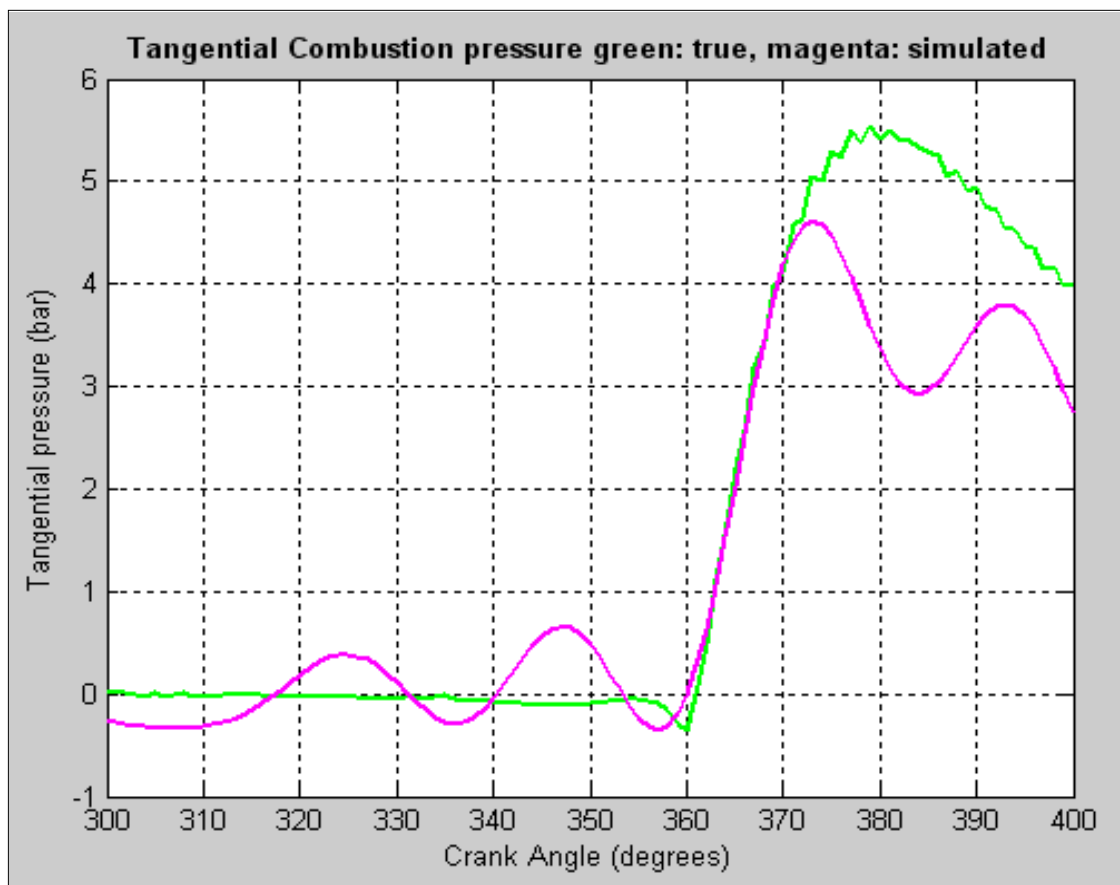


Figure 3.29 - 0.7 L Deutz engine on ULSD:
Tangential combustion pressure at 1500 rpm and 4 Nm torque /
2.9 bar IMEP: total (green), simulated (magenta); SOC is at TDC

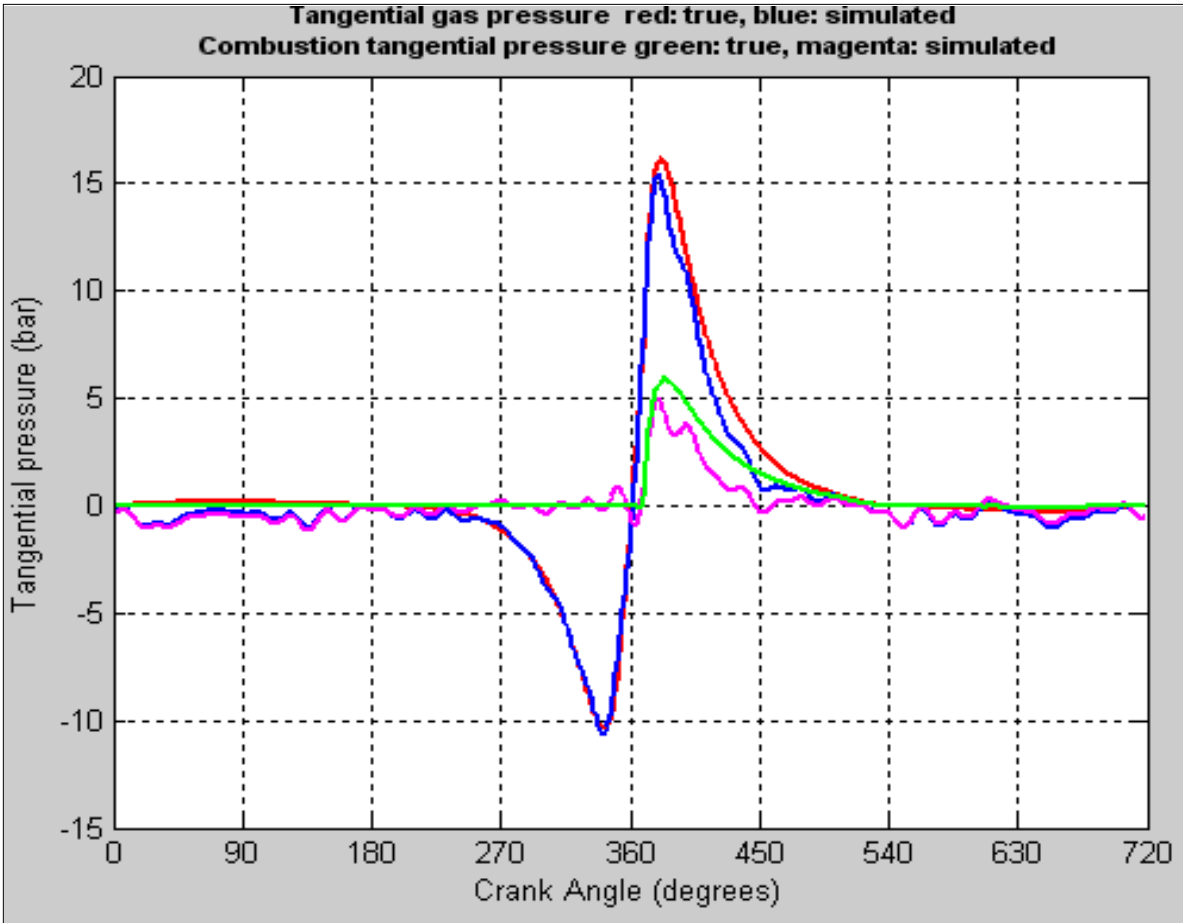


Figure 3.30 - 0.7 L Deutz engine on S-8: Tangential gas pressure at 1500 rpm and 4 Nm torque / 2.9 bar IMEP: total (red), simulated (blue), combustion (green), combustion simulated (magenta)

The second example is for S-8, represented in figure 3.30.

If the area around TDC in figure 3.30 is zoomed in, then figure 3.31 is obtained, where one can observe that the SOC (Start Of Combustion) is at 7 CAD after TDC.

The Matlab code for the computation of the start of combustion is presented in the Appendix.

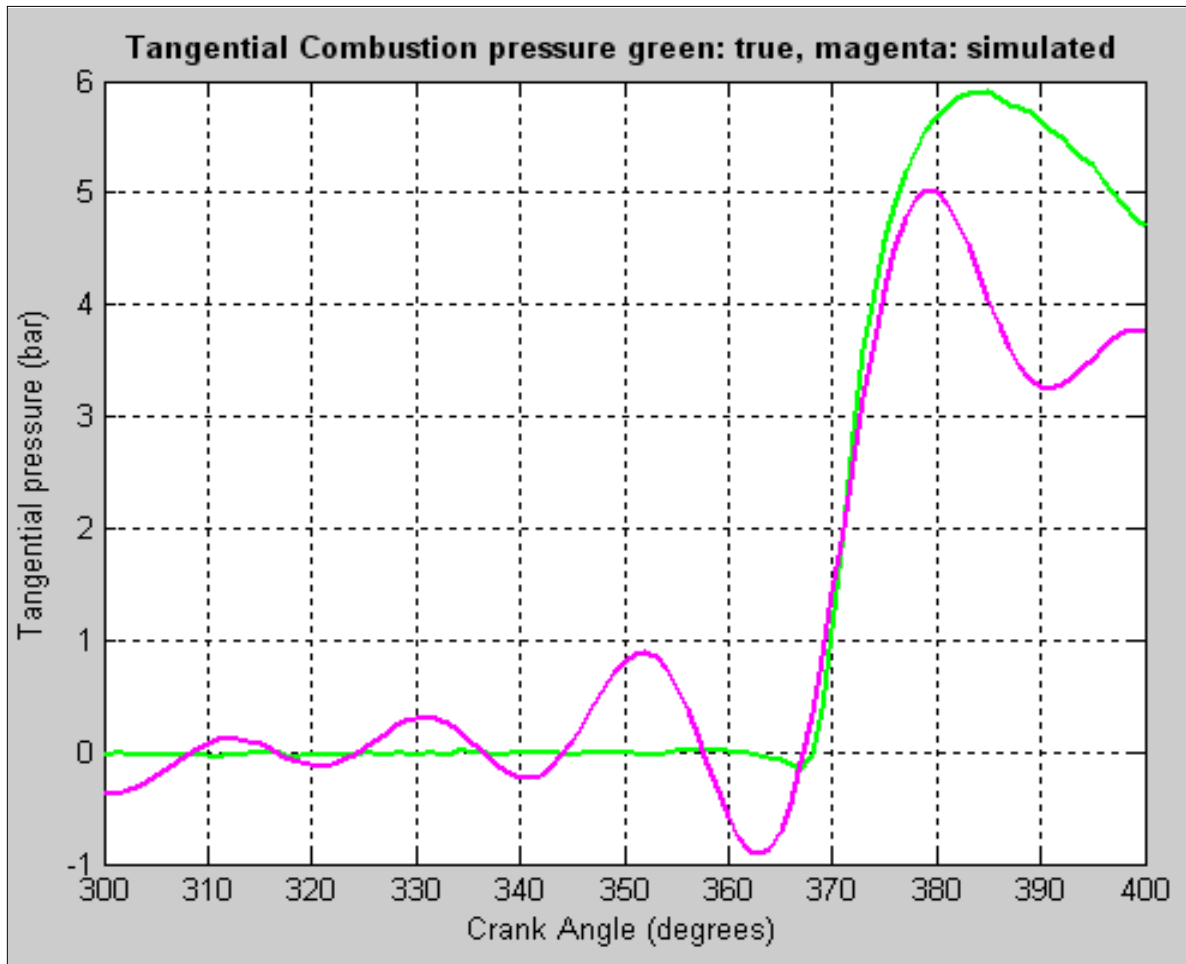


Figure 3.31 - 0.7 L Deutz engine on S-8:

Tangential combustion pressure for S-8 at 1500 rpm and 4 Nm torque / 2.9 bar IMEP: total (green), simulated (magenta);

Start Of Combustion is at 7 CAD after TDC

Since the start of combustion technique yielded promising results on a single cylinder engine, its application on multi-cylinder engines is investigated in the next chapter.

3.8.4 Estimation of Start of Combustion (Ignition Delay) on a multi-cylinder engine

In a multi-cylinder engine there are small differences in the operation of the cylinders even under steady state operation conditions but torsional vibrations disturb the variation of the engine speed due to the increased length of the crankshaft. The measurement is performed where it is less disturbed, which is at the flywheel. In addition, only a very accurate dynamic model of the power-train assures successful reversed calculation. But the dynamic model of this engine is very complex and a reverse calculation requires a large volume of computation. That is why the estimation of start of combustion approach is preferred.

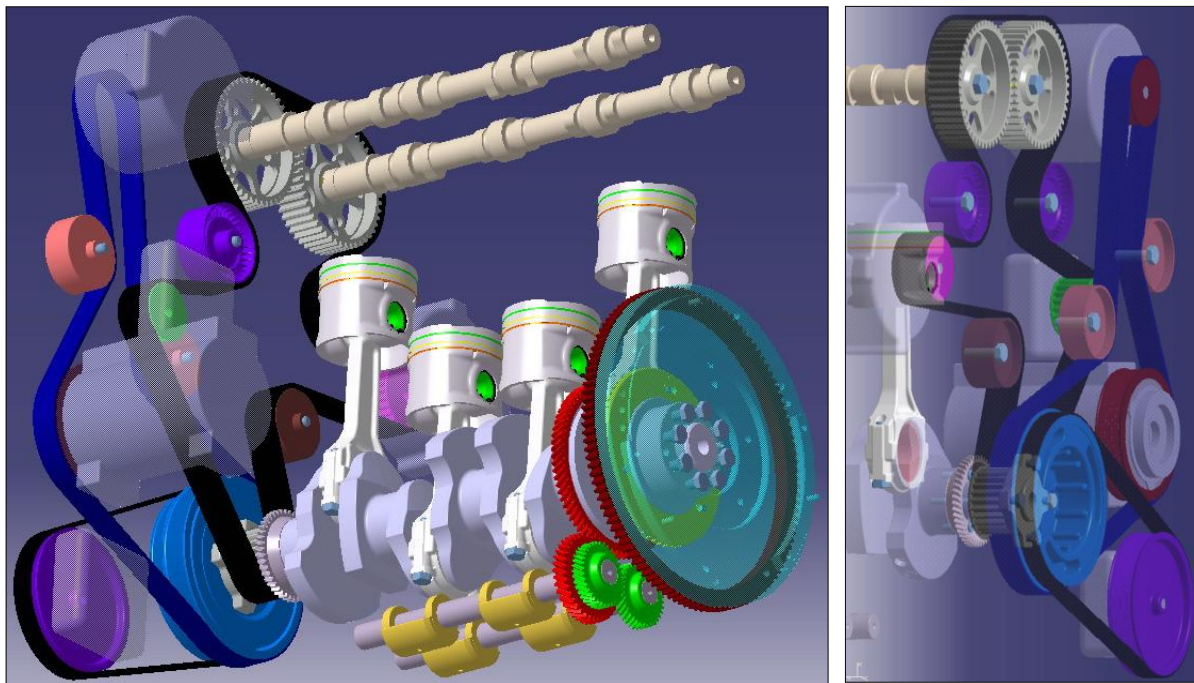


Figure 3.32: 2.5 L VM Motori multi-cylinder engine

The four cylinder pressures are measured then averaged and the contribution of each component is determined. An example of a ULSD run at relatively high speed and low load is illustrated in Figure 3.33.

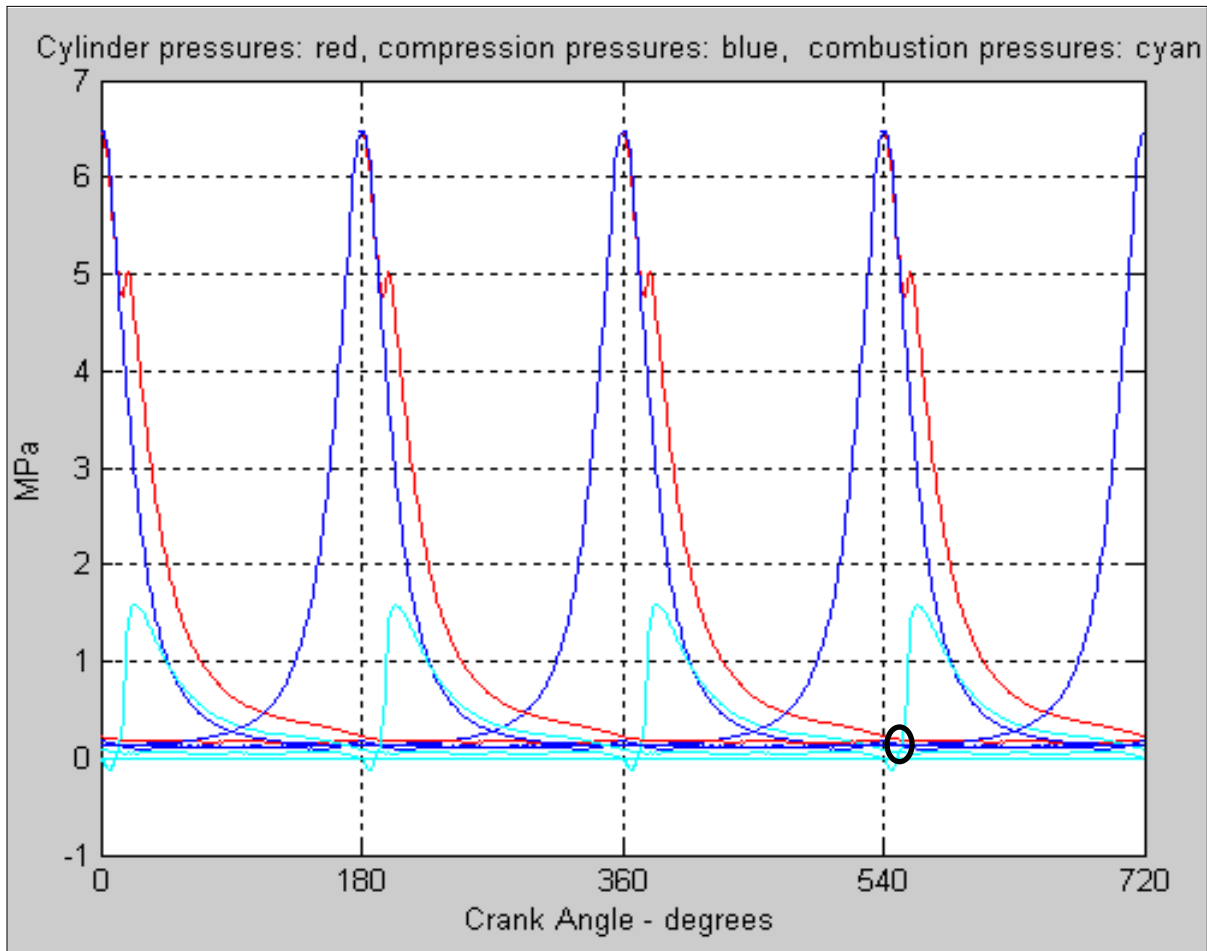


Figure 3.33 - 2.5 L VM Motori 4-cylinder engine on ULSD at 2750rpm / 30 Nm torque: Cylinder pressures and individual contributions - compression (blue), combustion (cyan), total (red)

For cylinder #1 the compression pressure is subtracted from the total pressure. The difference is the combustion tangential gas pressure which defines the start of combustion at 10 CAD after TDC – Fig 3.34.

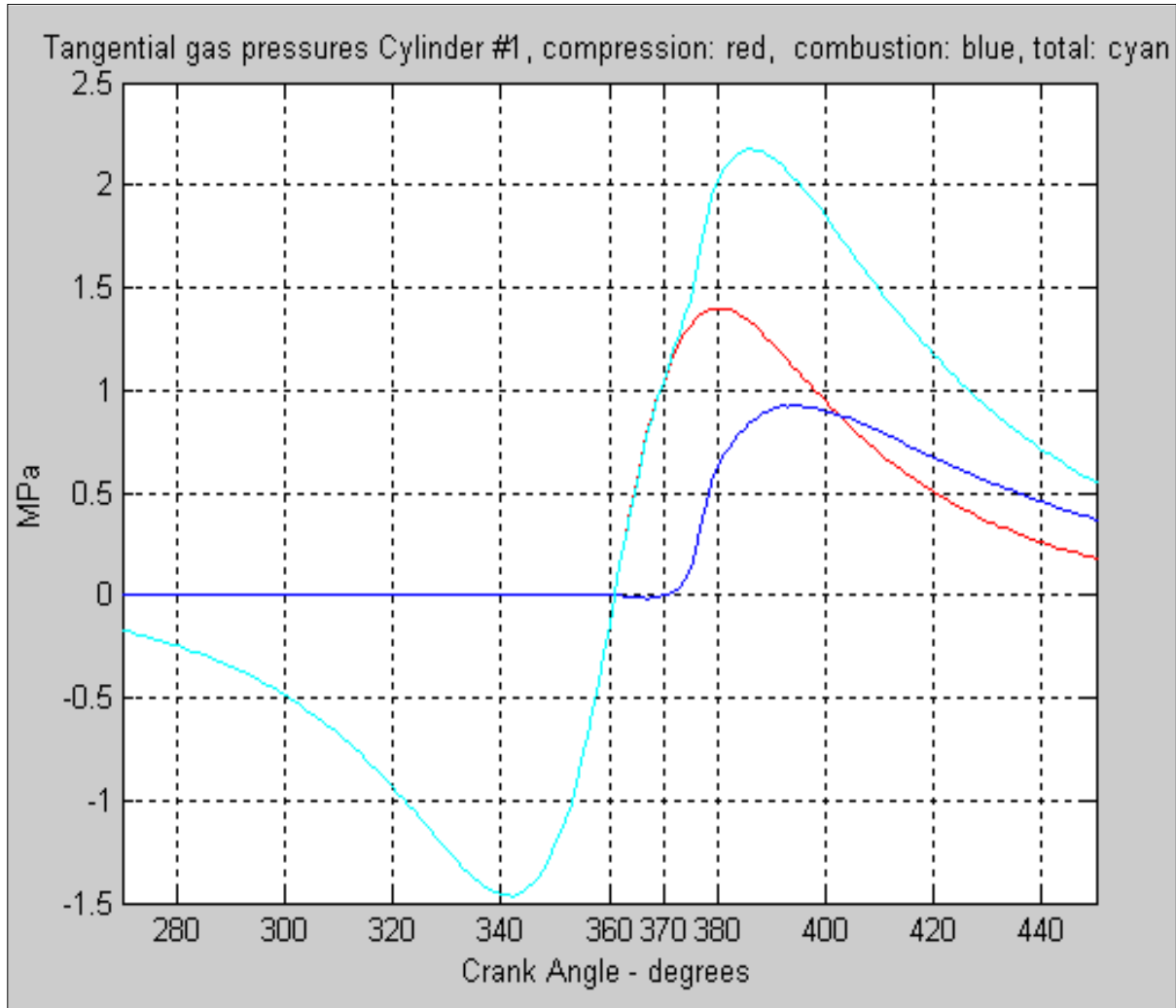


Figure 3.34 - Detail for cylinder #1 of 2.5 L VM Motori engine on ULSD at 2750rpm / 30 Nm torque: Tangential gas pressures - compression (red), combustion (blue), total (cyan); SOC is at 10 CAD after TDC

The inertia tangential pressure for each cylinder group is calculated. By addition, the resultant value is obtained in Figure 3.35.

Similar to the single-cylinder engine case, the components of the engine torque follow the equation (33) and are presented in figure 3.36.

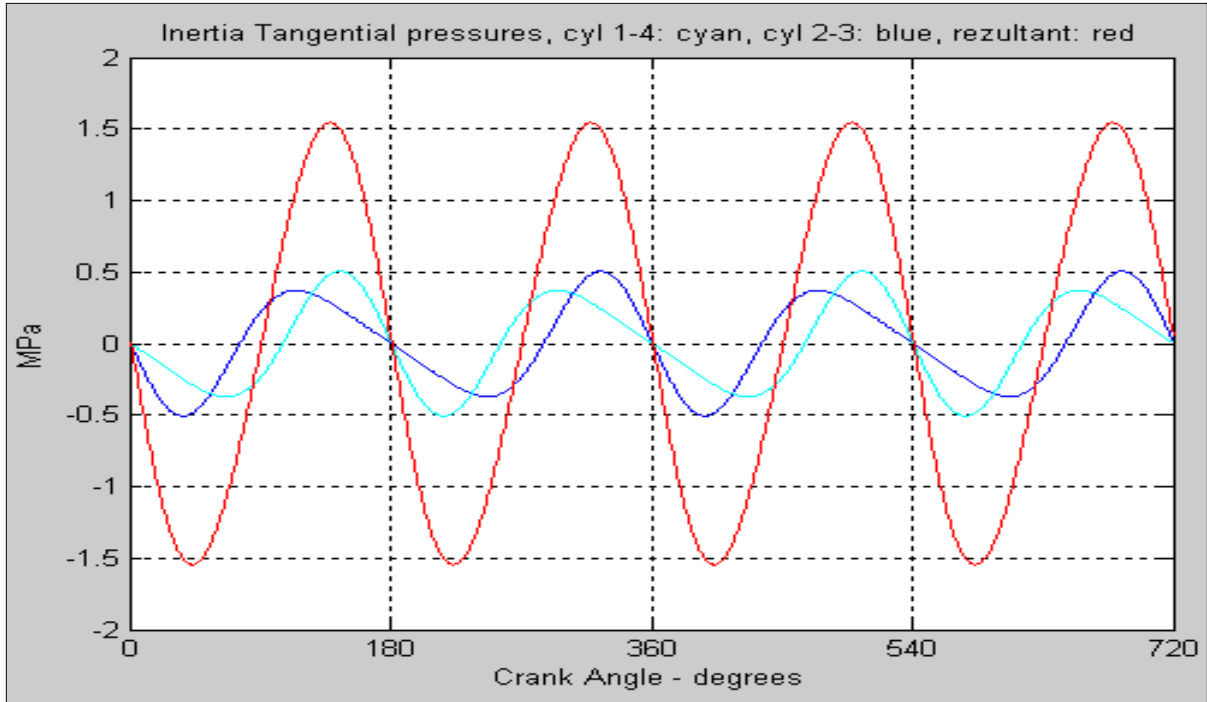


Figure 3.35 - 2.5 L VM Motori 4-cylinder engine on ULSD at 2750rpm / 30 Nm torque: Inertia tangential pressures for each cylinder group: 1-4 (cyan), 2-3 (blue), resultant value (red)

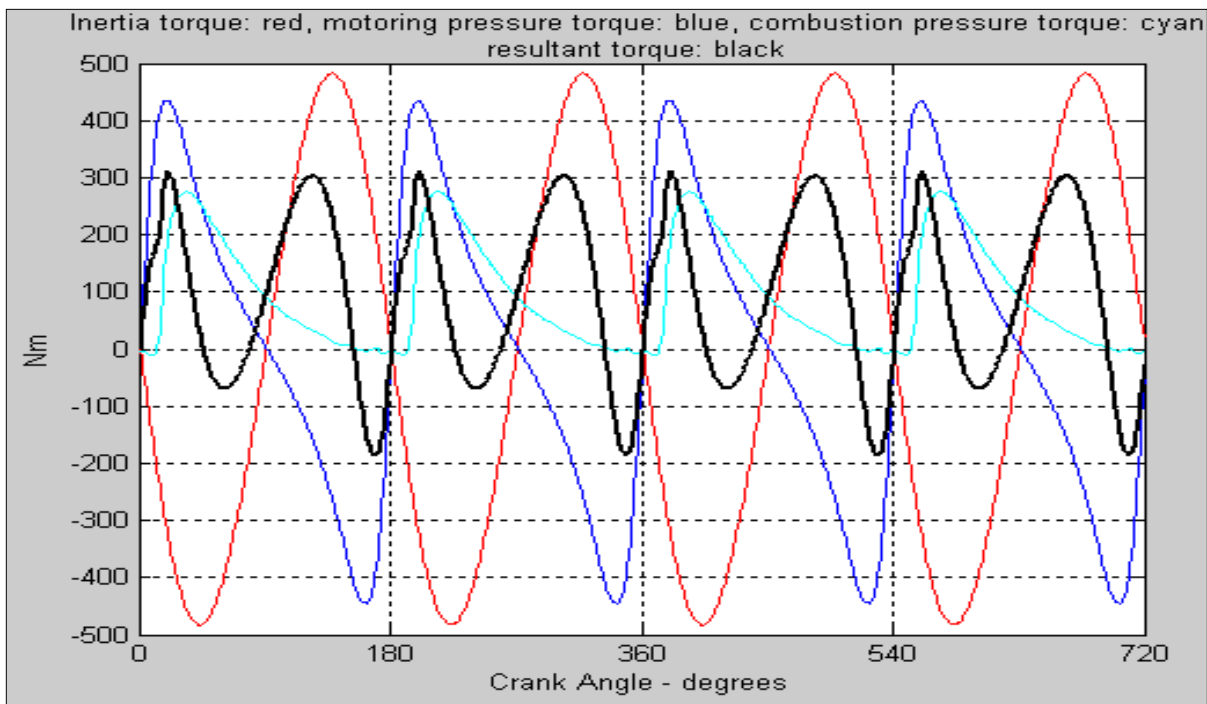


Figure 3.36 - The components of the engine torque for 2.5 L VM Motori 4-cylinder engine on ULSD at 2750rpm / 30 Nm torque: Inertia (red), motoring (blue), combustion (cyan), total (black)

For better uniformity and smoothness, the measured crankshaft speed was first averaged and smoothed - Figure 3.37.

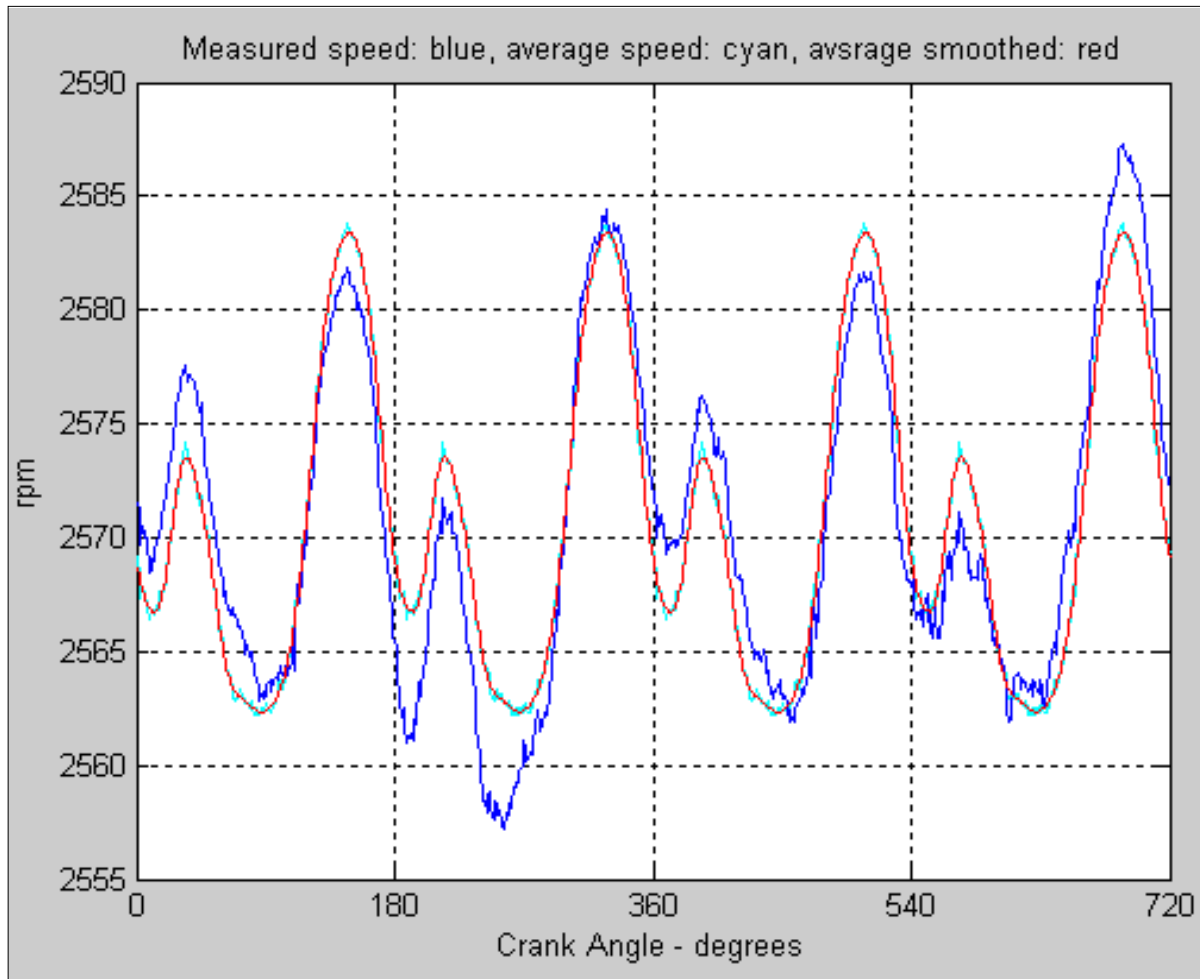


Figure 3.37 - 2.5 L VM Motori 4-cylinder engine on ULSD at 2750rpm / 30 Nm torque: Measured crankshaft speed (blue), averaged crankshaft speed (cyan), smoothed average speed: red

Considering that all four cylinders run uniformly and equally, the resultant engine torque is estimated from the measured crankshaft speed and compared to the actual engine torque – Figure 3.38.

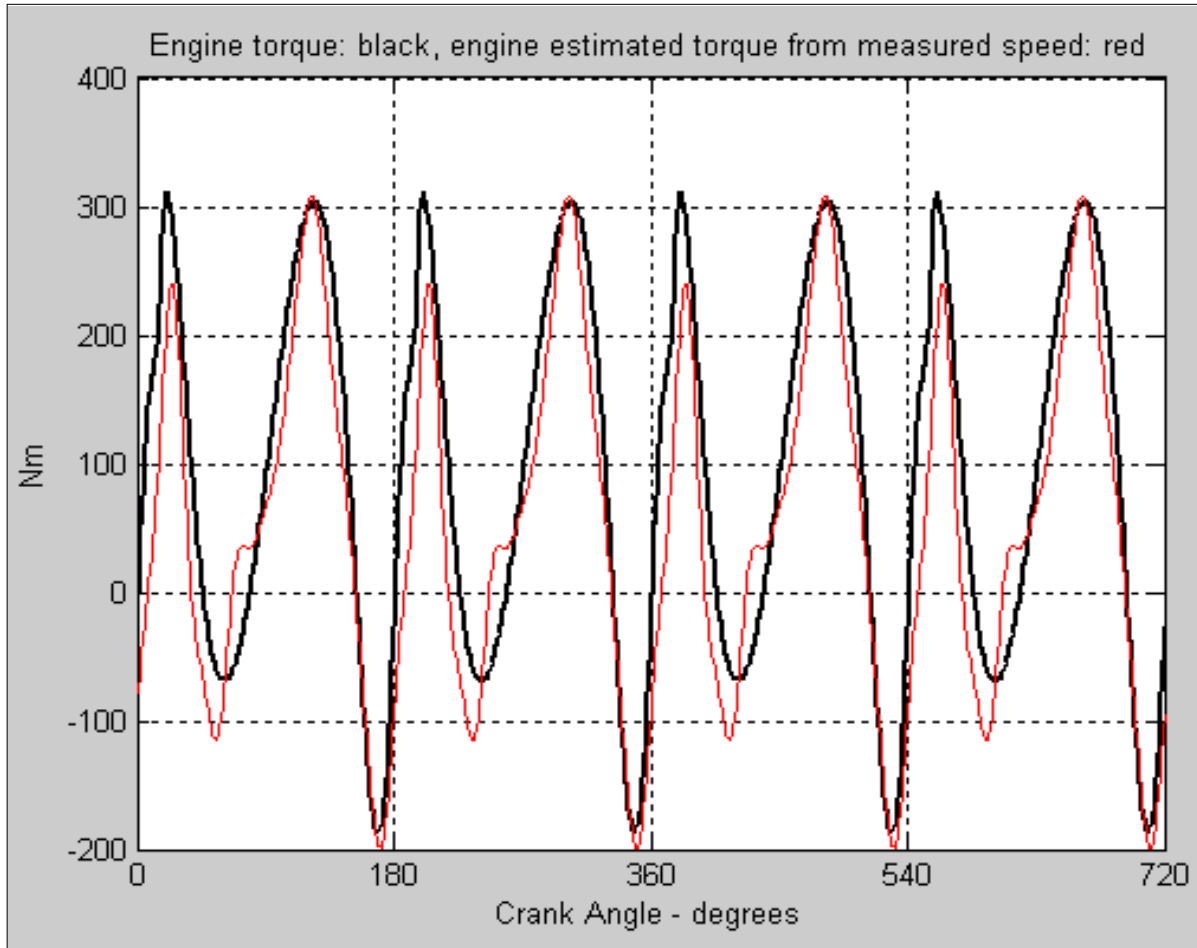


Figure 3.38 - 2.5 L VM Motori 4-cylinder engine on ULSD at 2750rpm / 30 Nm torque: Engine torque from measured cylinder pressure (black) and Engine torque estimated from measured crankshaft speed (red)

By following the engine torques equation (33), the combustion pressure torque is estimated from the engine speed – Figure 3.39.

If the area around TDC in figure 3.39 is zoomed in, then figure 3.40 is obtained, where one can observe that the SOC (Start Of Combustion) is at 10 CAD after TDC.

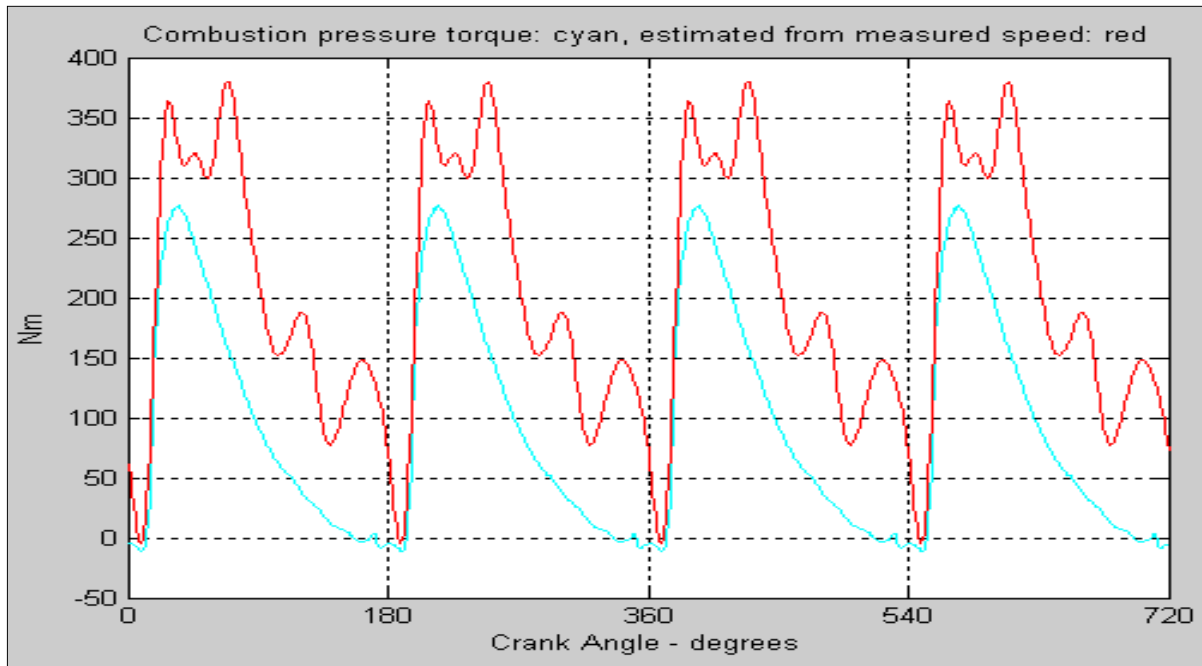


Figure 3.39 - 2.5 L VM Motori 4-cylinder engine on ULSD at 2750rpm / 30 Nm torque - Combustion pressure torque: calculated from pressure (cyan), estimated from speed (red)

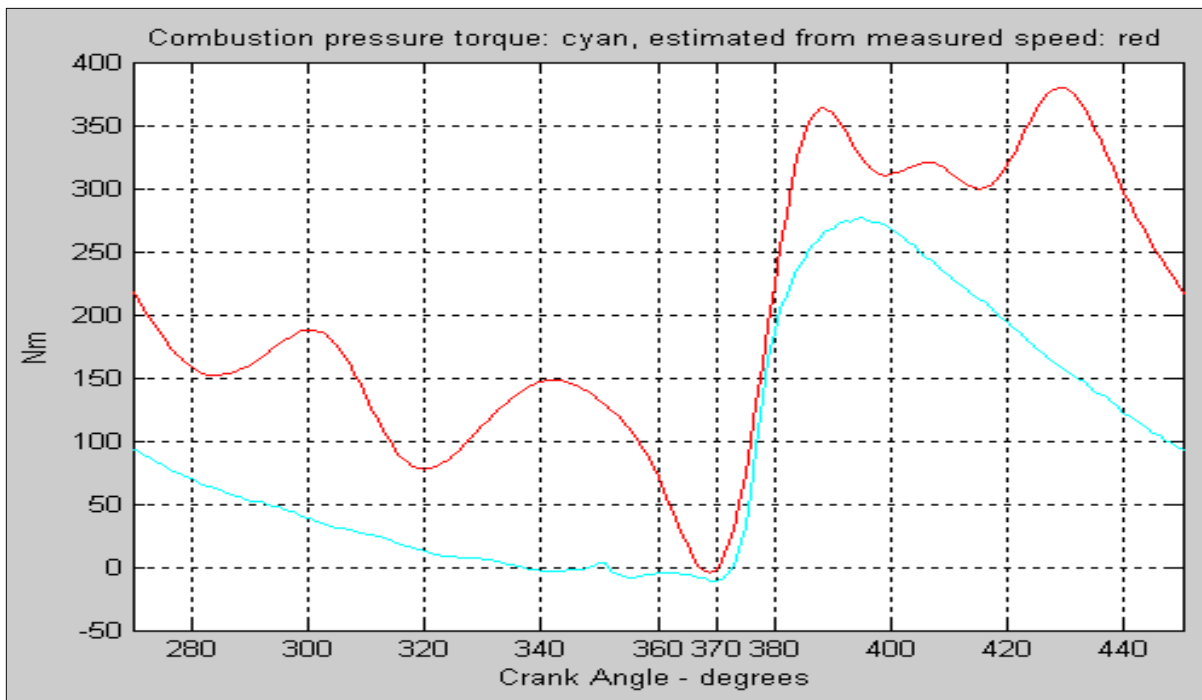


Figure 3.40 - 2.5 L VM Motori 4-cylinder engine on ULSD at 2750rpm / 30 Nm torque - Combustion pressure torque: calculated from pressure (cyan), estimated from speed (red); Start of combustion estimation: 10 CAD after TDC

The procedure can be applied for different fuels, speeds and loads. An example of a JP-8 run at higher load and lower speed – Figure 3.41, where the contribution of each pressure component is determined.

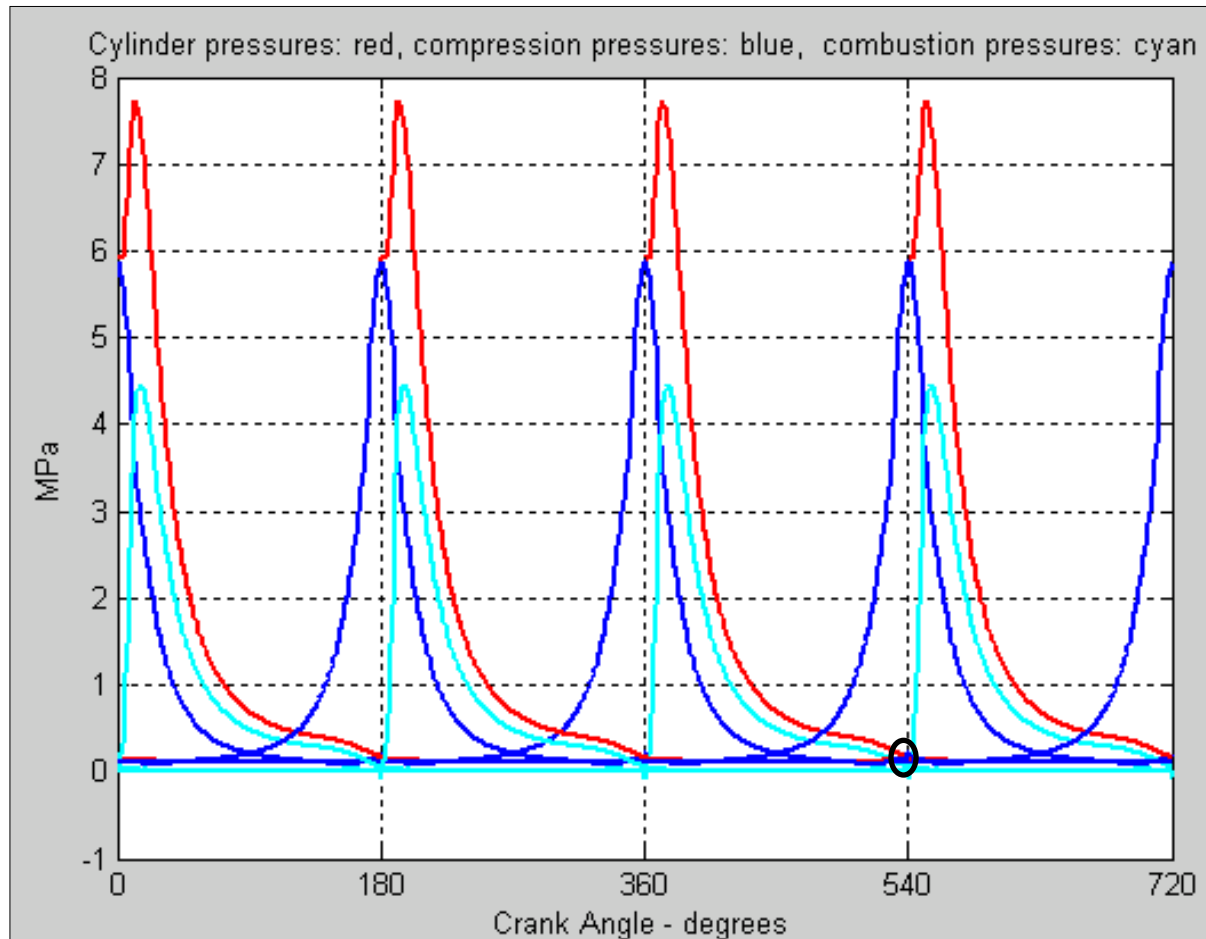


Figure 3.41 - 2.5 L VM Motori 4-cylinder engine on JP-8 at 1300rpm / 150 Nm torque: cylinder pressures and individual contributions - compression (blue), combustion (cyan), total (red)

For cylinder #1 the compression pressure is subtracted from the total pressure. The difference is the combustion tangential gas pressure which defines the start of combustion at 3 CAD after TDC – Fig 3.42.

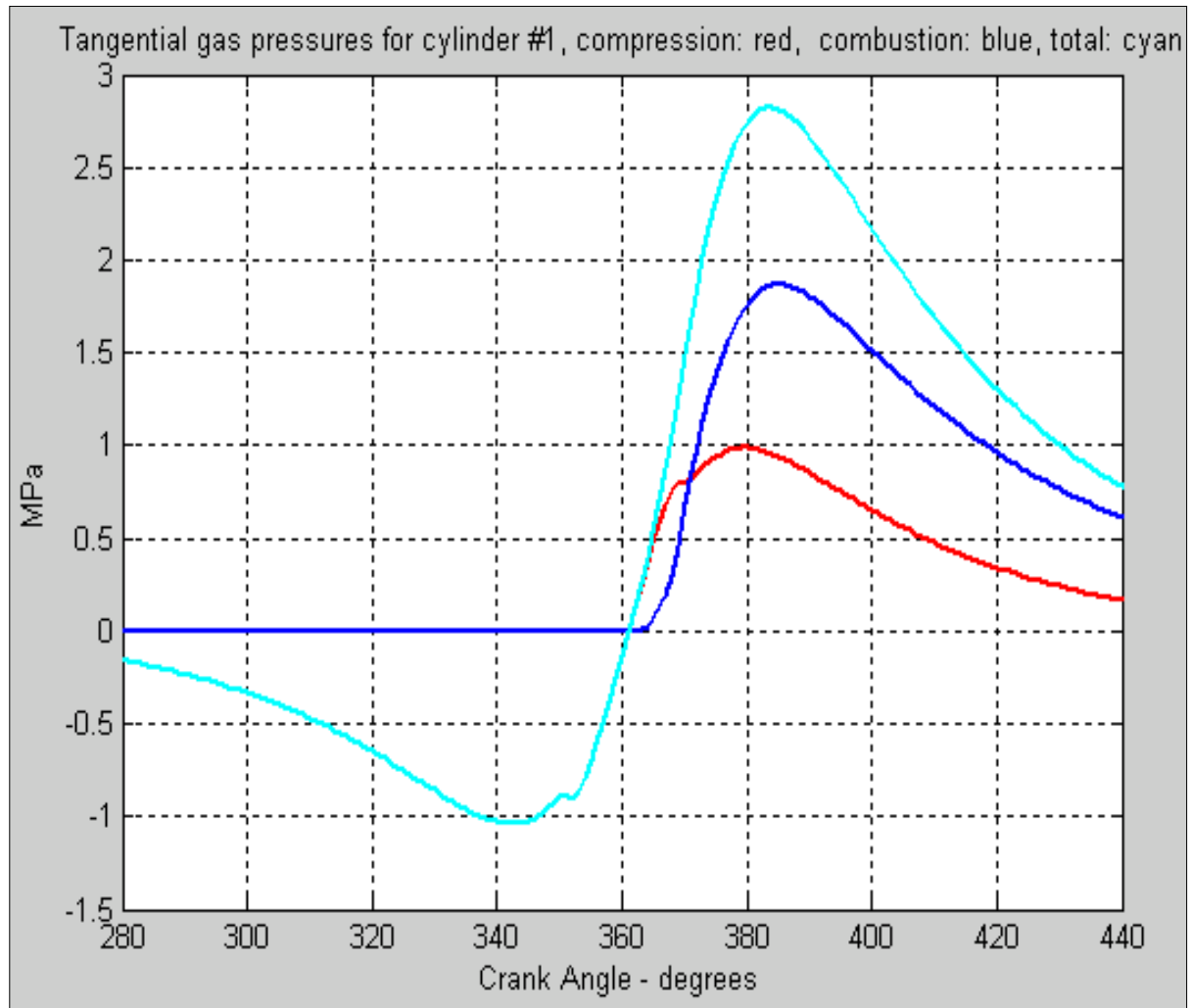


Figure 3.42 - Detail for cylinder #1 of 2.5 L VM Motori engine on JP-8 at 1300rpm / 150 Nm torque: tangential gas pressures - compression (red), combustion (blue), total (cyan); SOC = 3 CAD after TDC

Similarly to the previous high speed - low load case, the inertia tangential pressure for each cylinder group is calculated and, by addition, the resultant value is obtained. For better uniformity and smoothness the measured crankshaft speed was averaged and smoothed - Figure 3.43.

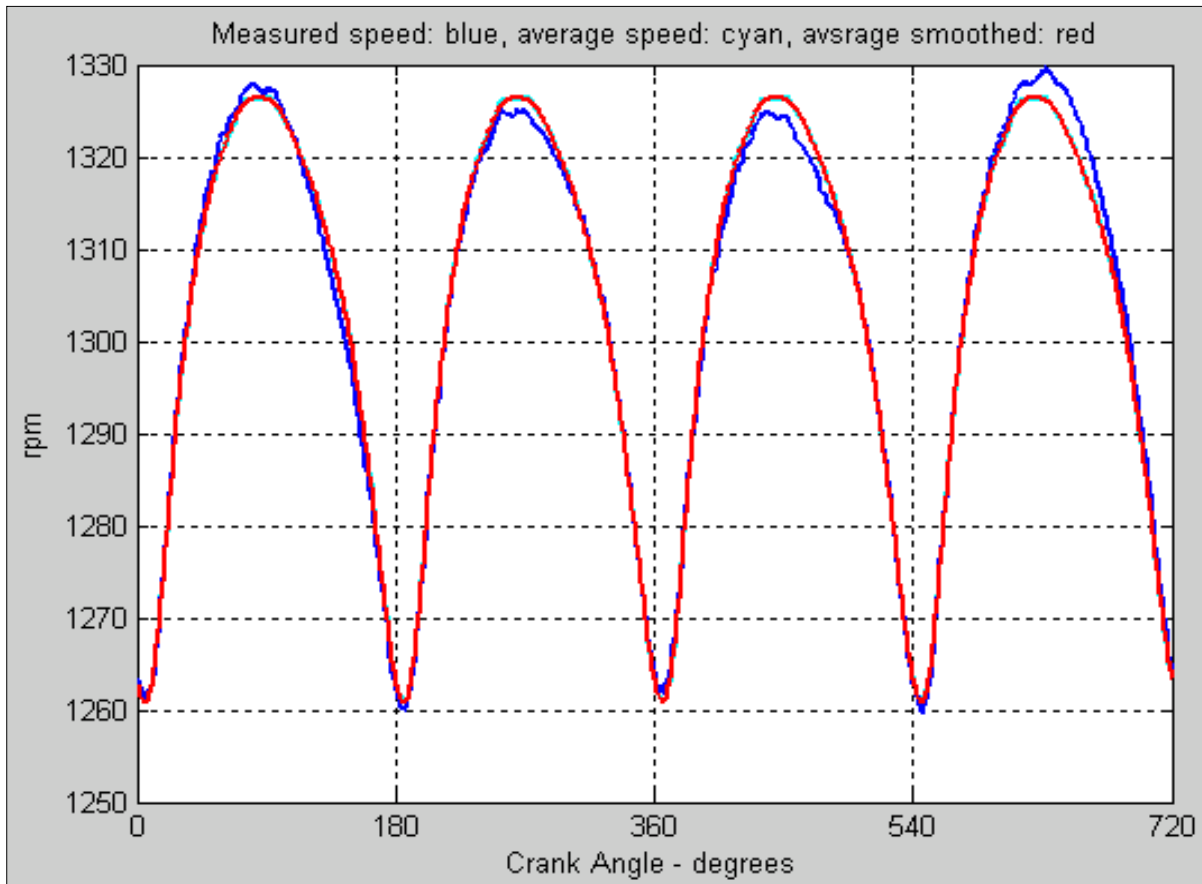


Figure 3.43 - 2.5 L VM Motori 4-cylinder engine on JP-8 at 1300rpm / 150 Nm torque: measured crankshaft speed (blue), averaged crankshaft speed (cyan), smoothed average speed (red)

Considering that all four cylinders run uniformly and equally, the resultant engine torque is estimated from the measured crankshaft speed and compared to the actual engine torque. By following the engine torques equation (33), the combustion pressure torque is estimated from the engine speed – Figure 3.44. If the area around TDC in Figure 3.44 is zoomed in, then Figure 3.45 is obtained, where one can observe that the SOC is at 3 CAD after TDC.

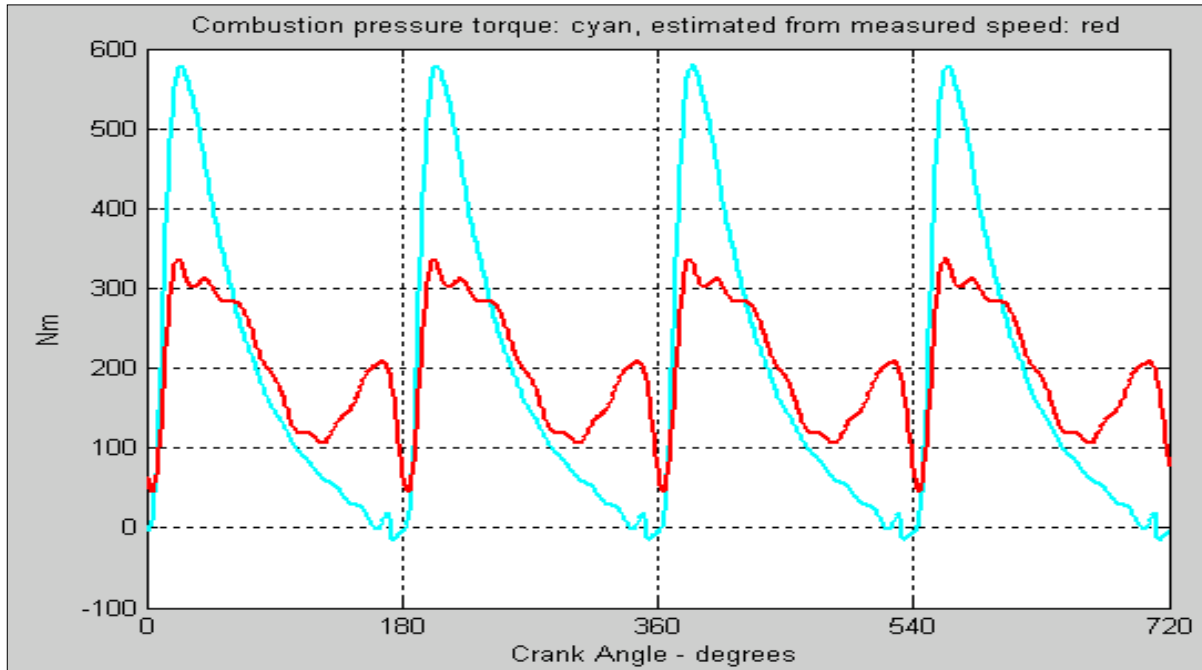


Figure 3.44 - 2.5 L VM Motori 4-cylinder engine on JP-8 at 1300rpm / 150 Nm torque - Combustion pressure torque: calculated from pressure (cyan), estimated from speed (red)

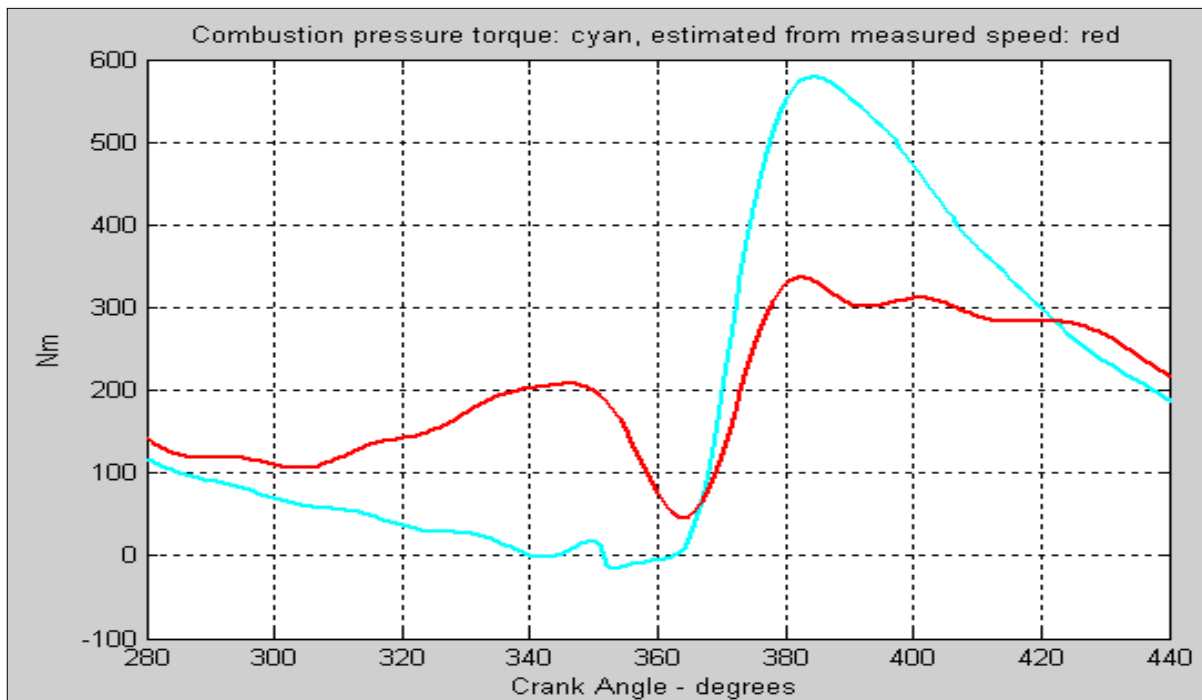


Figure 3.45 - 2.5 L VM Motori 4-cylinder engine on JP-8 at 1300rpm / 150 Nm torque - Combustion pressure torque: calculated from pressure (cyan), estimated from speed (red); Start of combustion estimation: 3 CAD after TDC

By using the measured instantaneous engine speed, the start of ignition approach yields a reasonably accurate value for the start of combustion and, accordingly, for the ignition delay. Once the ignition delay has been estimated, the ECU (Electronic Control Unit) can adjust the injection timing to achieve safe and efficient operation of the engine.

The Matlab code for the computation of the start of combustion for the four cylinder engine is presented in the Appendix.

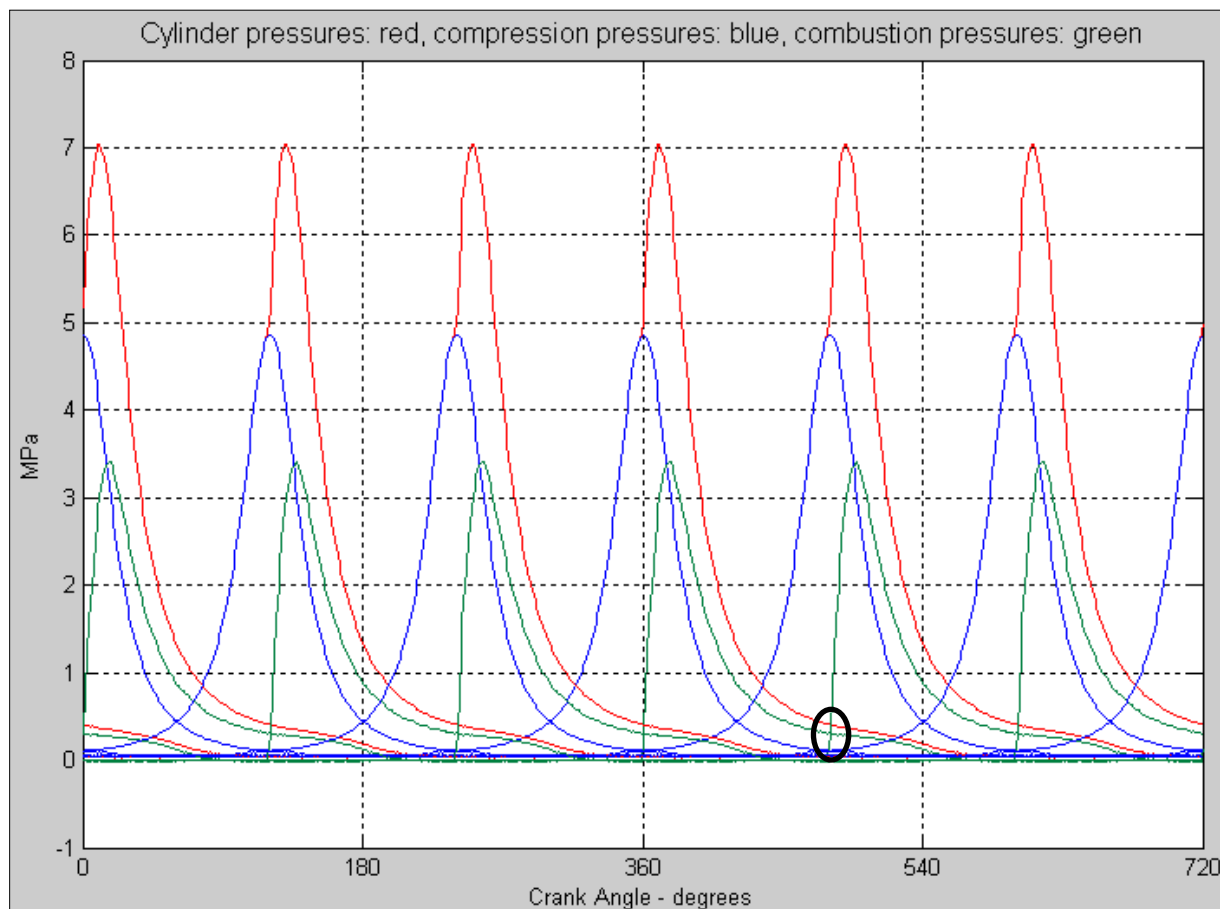


Figure 3.46: Cummins 6-cylinder engine on ULSD at 1360 rpm / 200 Nm torque - Cylinder pressures and individual contributions: compression (blue), combustion (green), total (red). The disturbance (red) of a firing cylinder (green) is higher than in a four-cylinder engine – Fig 3.33, 3.41

In conclusion, the start of ignition approach could be implemented to engines having up to four cylinders were the contribution of three cylinders at the firing TDC of the fourth cylinder is almost zero – Figures 3.33 and 3.41.

Nevertheless this approach is not possible on engines with a larger number of cylinders, e.g. six, due to the disturbance produced by other cylinders when a cylinder is firing. By comparing figures 3.33 and 3.41 with figure 3.46, it can be noticed that, in a six cylinder engine, the disturbance of an adjacent cylinder (red) on a firing cylinder (green) is much higher than in a four-cylinder engine. To avoid the signal interference from adjacent cylinders, a new fuel identification method that does not require physical data about the engine and can be applied to engines having any number of cylinders is being presented in the next subchapter.

3.9 Fuel identification method on a six-cylinder engine

3.9.1 Motivation

One possibility to estimate the fuel type during engine operation is to reconstruct the cylinder pressure variation for the determination of the peak pressure and its location with respect to TDC. Nonetheless, this approach requires a very accurate dynamic model of the power-train and cannot be applied to engines having more than four cylinders where the functionality of one cylinder does not interfere or overlaps with the signal from the adjacent cylinders for at least 180 CAD (= 720 CAD divided by 4 cylinders).

The ANN (Artificial Neural Network) method for fuel identification has two major advantages over the other techniques - Figure 3.47:

1. the network can be trained on any engine
2. there is no restriction on the number of cylinders of the engine.

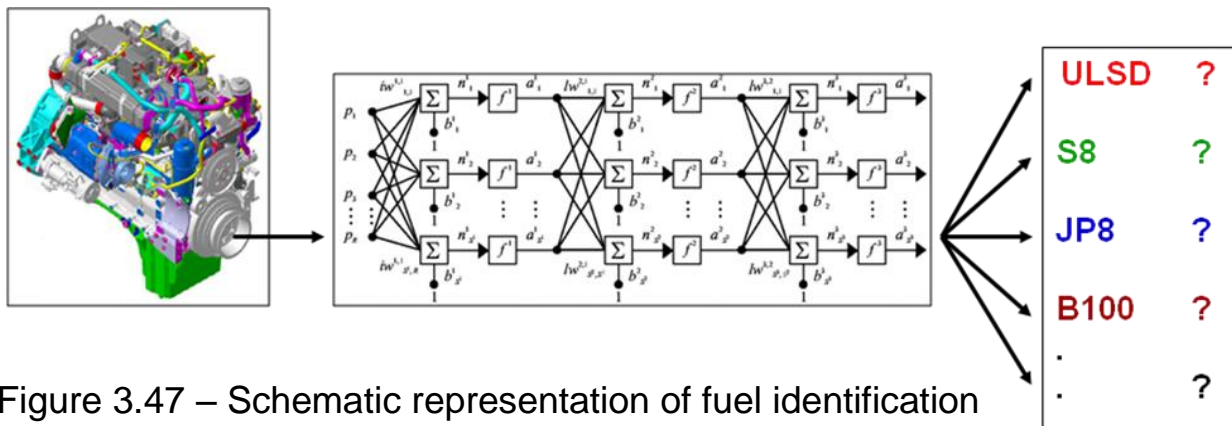


Figure 3.47 – Schematic representation of fuel identification from engine speed using artificial neural network

3.9.2 Artificial neural network functionality and neuron structure

According to Symon Haykin [30], an artificial neural network is a machine designed to model the way in which the brain performs a particular task or function of interest.

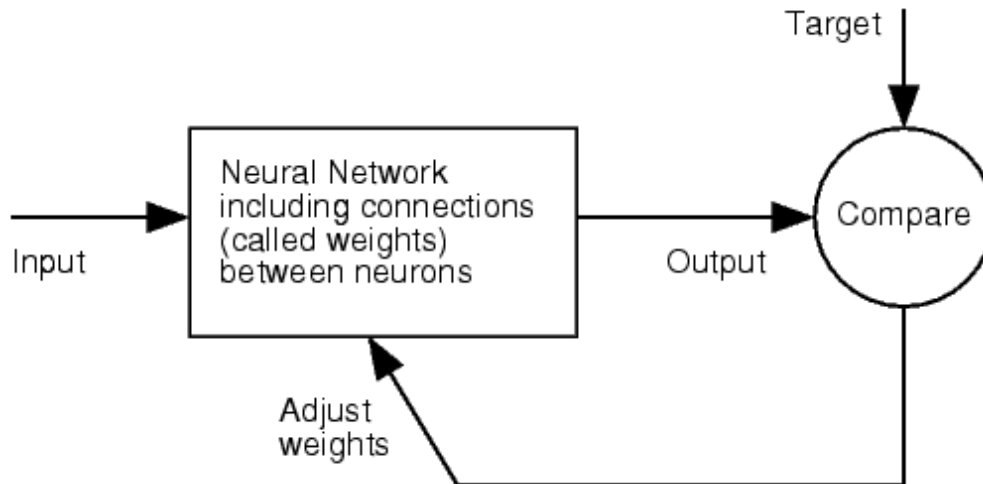


Figure 3.48 – Neural network functional process [31]; see also Figure

By comparing the output to the target and by adjusting the values of the connections between elements, called weights w , a neural network is trained so that a particular input p leads to a desired output a (see Figures 3.48 and 3.49).

Neural networks have been trained to perform complex tasks such as function approximation, classification, pattern recognition in fields like statistics, mechanics, electrical engineering, medical field (e.g. voice recognition, classify a tumor as either benign or malignant based on cell

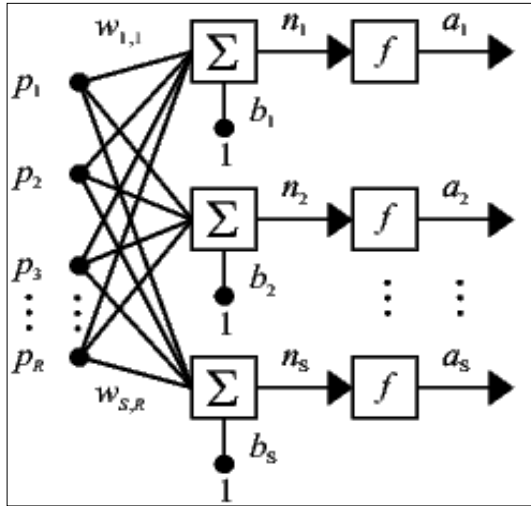


Figure 3.49 – Neural network structure: weights w , biases b , transfer f-ctions f [31]; see Fig 3.42

descriptions) and the list does not stop here.

A neuron with a single scalar input p and no bias appears in Figure 3.50 as

introduced by [31]. When a bias b is added, the neuron in Figure 3.51 is obtained, according to [31].

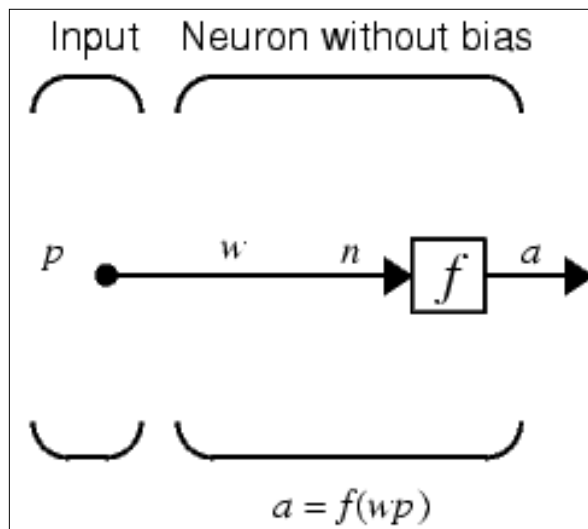


Figure 3.50 – Neuron without bias [31]

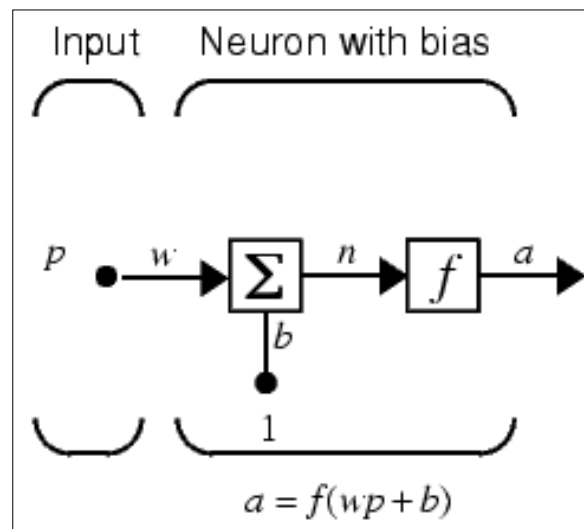


Figure 3.51 – Neuron with a bias [31]

This simple structure is very powerful because the input p can be brought to any desired output a by modifying the multiplier (weight) w , the summation term (bias) b and/or the transfer function f repeatedly during the

training process until the error (performance function) between the output a and the target t becomes satisfactory.

The transfer function f can be any convenient function. Some examples are given in Figure 3.52. A neuron with a hard-limit or sigmoid transfer function is called a perceptron [31].

Transfer Functions

[compet](#)

[hardlim](#)

[hardlims](#)

[logsig](#)

[netinv](#)

[poslin](#)

[purelin](#)

[radbas](#)

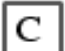



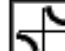





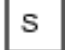
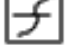
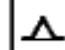
[satlin](#)

[satlins](#)

[softmax](#)

[tansig](#)

[tribas](#)

-  Competitive transfer function
-  Hard limit transfer function
-  Symmetric hard limit transfer function
-  Log-sigmoid transfer function
-  Inverse transfer function
-  Positive linear transfer function
-  Linear transfer function
-  Radial basis transfer function
-  Saturating linear transfer function
-  Symmetric saturating linear transfer function
-  Softmax transfer function
-  Hyperbolic tangent sigmoid transfer function
-  Triangular basis transfer function

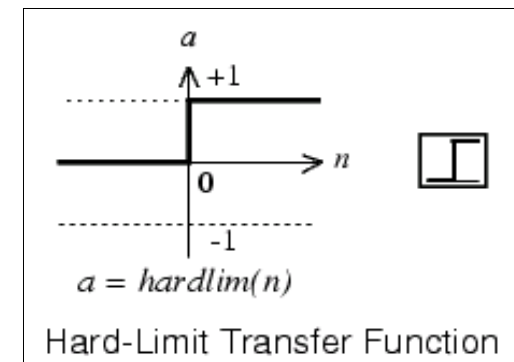
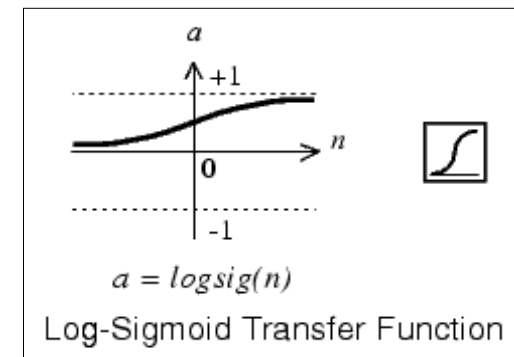
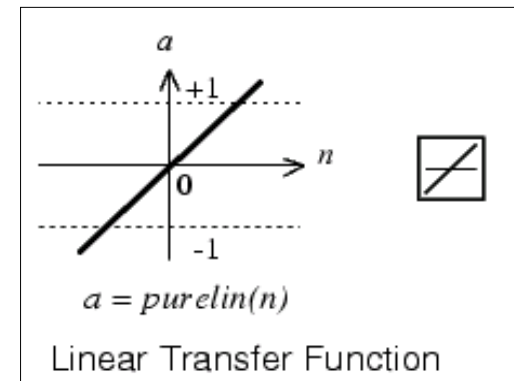


Figure 3.52 – Examples of transfer functions [31]

3.9.3 Layer of neurons and multiple layers of neurons

A layer of neurons represents a positioning of individual neurons as in Figure 3.53 where R is the number of elements in the input vector and S is the number of neurons in the layer.

It can be noticed that R is not necessarily equal to S . According to J, Sandberg [34] the outputs are expressed by:

$$\begin{aligned}
 a_1 &= f\left(\sum_i^R p_i \times w_{i,1} + b_1\right) \\
 &\vdots \\
 a_S &= f\left(\sum_i^R p_i \times w_{i,S} + b_S\right)
 \end{aligned}$$

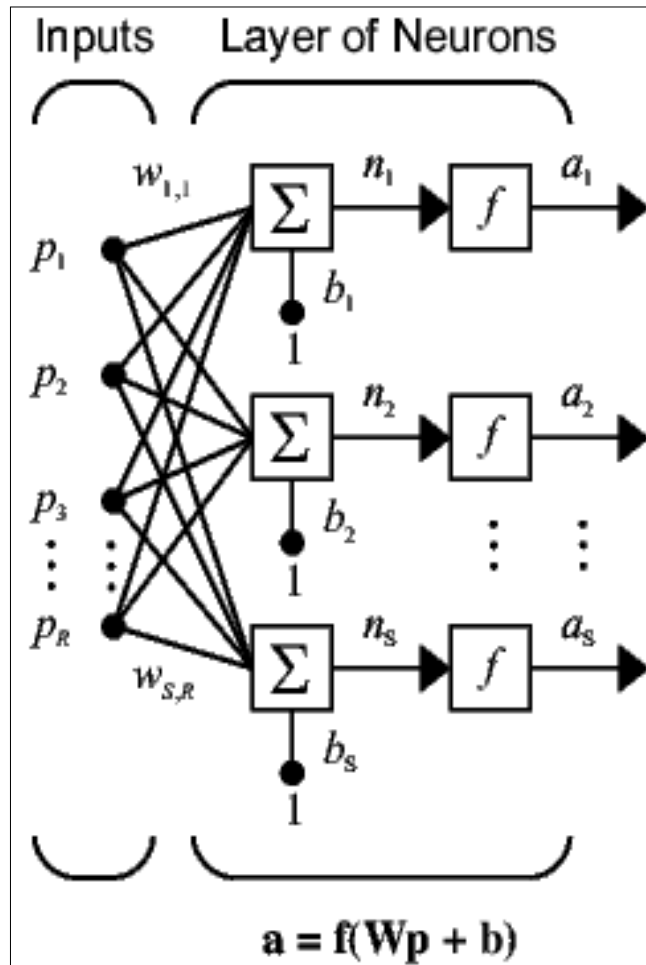


Figure 3.53 – Layer of neurons [31]

therefore the input vector elements enter the network through the weight matrix W defined as:

$$\mathbf{W} = \begin{bmatrix} w_{1,1} & w_{1,2} & \dots & w_{1,R} \\ w_{2,1} & w_{2,2} & \dots & w_{2,R} \\ \vdots & \vdots & \ddots & \vdots \\ w_{S,1} & w_{S,2} & \dots & w_{S,R} \end{bmatrix}$$

When several layers of neurons are combined a more complex structure, called multiple layers of neurons [31], is obtained - Figure 3.54.

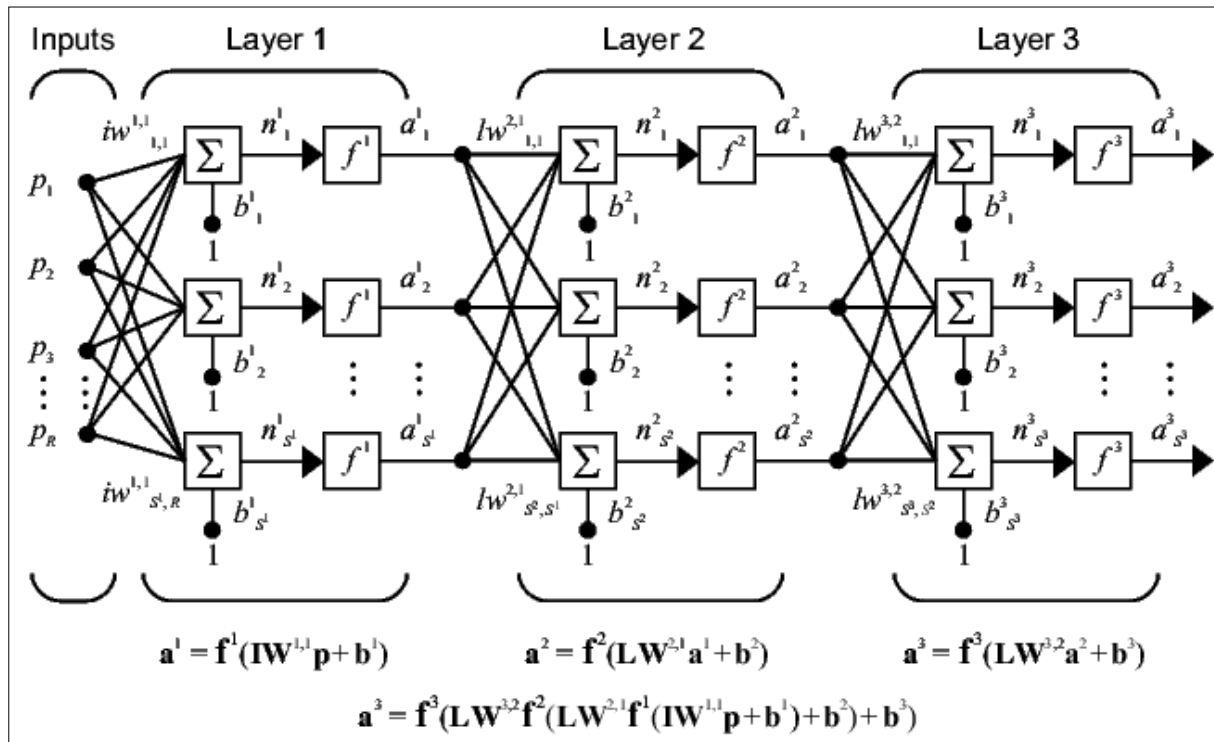


Figure 3.54 – Multiple layers of neurons [31]

ANN are very complex – Figure 3.55, but multiple layers of neurons are very powerful. A network of two layers, where the first layer is sigmoid and the second is linear, can be trained to approximate any function with a finite number of discontinuities arbitrarily well [31]. This kind of two-layer network is extensively used in back-propagation algorithm.

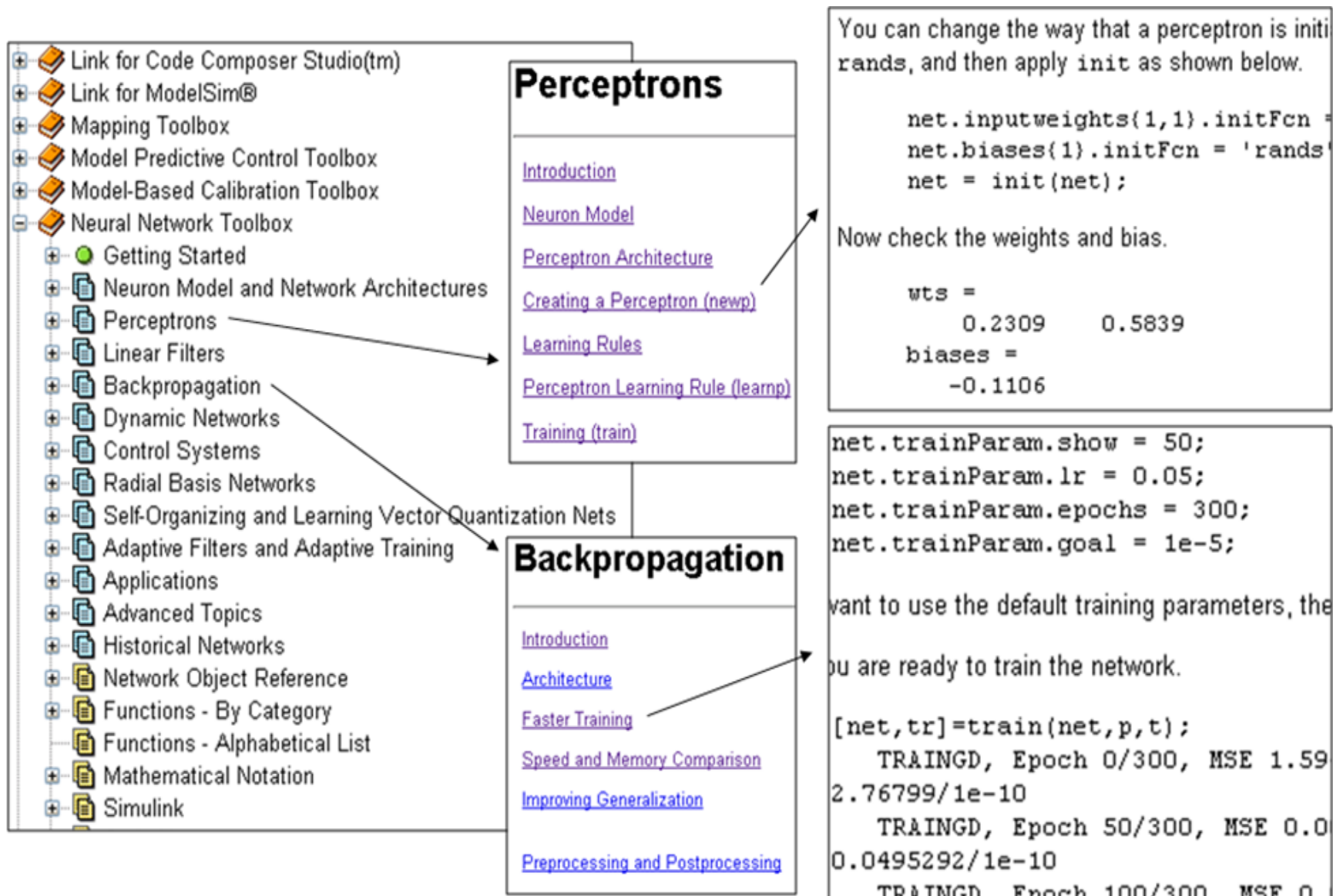


Figure 3.55 – Neural networks types and complexity [31]

3.9.4 Back-propagation algorithm

The algorithm is widely used by the majority of SAE publications, especially in engineering, due to its highly-nonlinear function fitting capabilities. It is based on the error correction rule and it consists of two passes [30] – Figure 3.56:

- 1) a forward pass, in which the weights are fixed; when an input is applied to the node, its effect propagates through the network, producing an output, which now is compared to the target

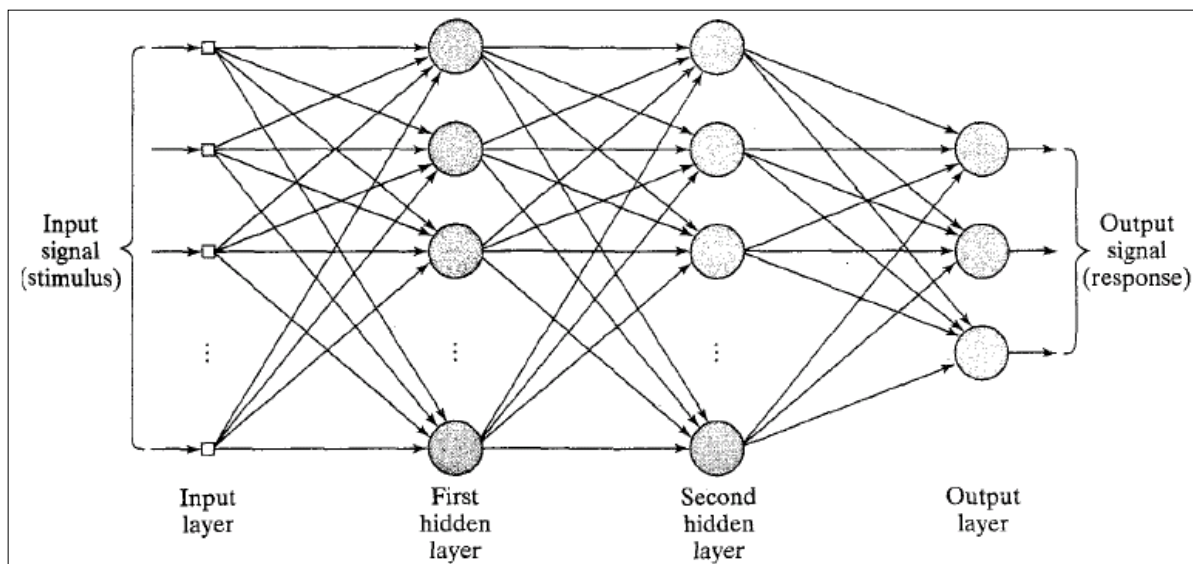
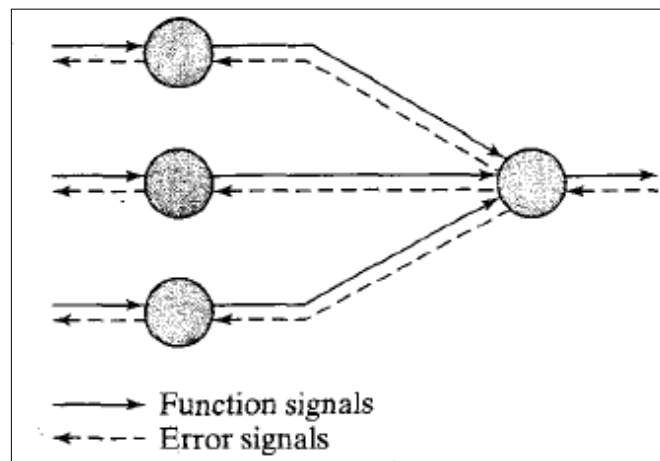


Figure 3.56 –
Network training
back-propagation algorithm:
Function signals
propagates forward while
error propagates
backwards [30]



2) a backward pass, in which the error signal, related to the difference between target and output, propagates backward through the network against the direction of synaptic connections, hence the name (error) back-propagation; the weights are now adjusted so that the new output moves closer to the target.

This iterative process is called learning or training the network.

There are numerous training algorithms in the literature, each of them providing more precision at the cost of more computational time. For our case with high nonlinearity between the input, instantaneous engine speed, and the output, in-cylinder pressure, the preferred one is Levenberg – Marquardt as a compromise between speed and accuracy – Figure 3.57.

Figure 3.57 –
 Network
 training
 algorithms;
 preferred is
 Levenberg –
 Marquardt
 [31]

}	trainb	Batch training with weight and bias learning rules
	trainbfg	BFGS quasi-Newton backpropagation
	trainbfgc	BFGS quasi-Newton backpropagation for use with NN model reference adaptive controller
	trainbr	Bayesian regularization
	trainc	Cyclical order incremental update
	traincgb	Powell-Beale conjugate gradient backpropagation
	traincgf	Fletcher-Powell conjugate gradient backpropagation
	traincgp	Polak-Ribière conjugate gradient backpropagation
	traingd	Gradient descent backpropagation
	traingda	Gradient descent with adaptive learning rule backpropagation
	traingdm	Gradient descent with momentum backpropagation
	traingdx	Gradient descent with momentum and adaptive learning rule backpropagation
	trainlm	Levenberg-Marquardt backpropagation
	trainoss	One step secant backpropagation
	trainr	Random order incremental training with learning functions
trainrp	Resilient backpropagation (Rprop)	
trains	Sequential order incremental training with learning functions	
trainscg	Scaled conjugate gradient backpropagation	

Acronym	Algorithm	
LM	trainlm	Levenberg-Marquardt
BFG	trainbfg	BFGS Quasi-Newton
RP	trainrp	Resilient Backpropagation
SCG	trainscg	Scaled Conjugate Gradient
CGB	traincgb	Conjugate Gradient with Powell/Beale Restarts
CGF	traincgf	Fletcher-Powell Conjugate Gradient
CGP	traincgp	Polak-Ribière Conjugate Gradient
OSS	trainoss	One Step Secant
GDX	traingdx	Variable Learning Rate Backpropagation

Algorithm	Mean Time (s)	Ratio	Min. Time (s)	Max. Time (s)	Std. (s)
LM	18.45	1.00	12.01	30.03	4.27
BFG	27.12	1.47	16.42	47.36	5.95
SCG	36.02	1.95	19.39	52.45	7.78
CGF	37.93	2.06	18.89	50.34	6.12
CGB	39.93	2.16	23.33	55.42	7.50
CGP	44.30	2.40	24.99	71.55	9.89
OSS	48.71	2.64	23.51	80.90	12.33
RP	65.91	3.57	31.83	134.31	34.24
GDX	188.50	10.22	81.59	279.90	66.67

3.9.5 Design of the Artificial Neural Network

To our surprise, the design of a neural network does not follow a strict, well-defined path. The literature provides general rules which are more likely optimization guidelines such as “do not do this” or “avoid that” rather than network creating rules. The design of a neural network is ‘more of an art than a science in the sense that many of the numerous factors involved in the design are the results of one’s personal experience’ according to S. Haykin [30].

The literature does not provide a general ‘recipe’ for how many neurons a layer should contain (3, 8, 20...) or how many layers our network should have (1, 2, 3...) or what transfer function a neuron ought to adopt (linear, hard-limiter, sigmoid) or what performance function one should use (sum of errors, mean error, mean square error) or what configuration is the best (in parallel, in series, combined). One thing must be known for sure though: the scope of that network or what should it do exactly.

Because there were so many variables involved, many network configurations had to be tested. Eventually, the optimal one was identified as having the following characteristics:

Configuration = 3-layer perceptron

Number of neurons = 20 in each layer

Activation function = hyperbolic tangent (sigmoid) function

Training algorithm = Levenberg-Marquardt
back-propagation

Performance function = MSE (Mean Squared Error).

3.9.6 ANN fuel identification on a single-cylinder engine

The tests were performed on the Deutz 0.7 L single-cylinder engine presented in Chapter 2. The tested fuels were synthetic fuel S-8 CN56, ULSD CN46, bio-diesel B-100 CN47 and jet fuel JP-8 Kerosene CN31.

The network input is the instantaneous measured crankshaft speed – Figure 3.58. Nevertheless, in our example at 1400 rpm and 0 Nm torque, the four speed patterns are very similar, a fact that makes the fuel identification process difficult.

In these conditions, the question is what differentiating parameter should be chosen as a network simulated output so that each fuel can be uniquely determined.

An idea would be to select the network output to be the in-cylinder simulated pressure – Figure 3.59. The four pressure patterns for average 100 cycles look fairly different, therefore peak values could be used as a fuel identifying parameter.

On the other hand, instantaneous peak pressure values have cyclic variations that must be compensated for. In Figure 3.60 peak values of measured pressure cyclic variations are represented for all fuels for 200 cycles: 50 cycles of S8, 50 cycles of JP8, 50 cycles of ULSD and 50 cycles of B100.

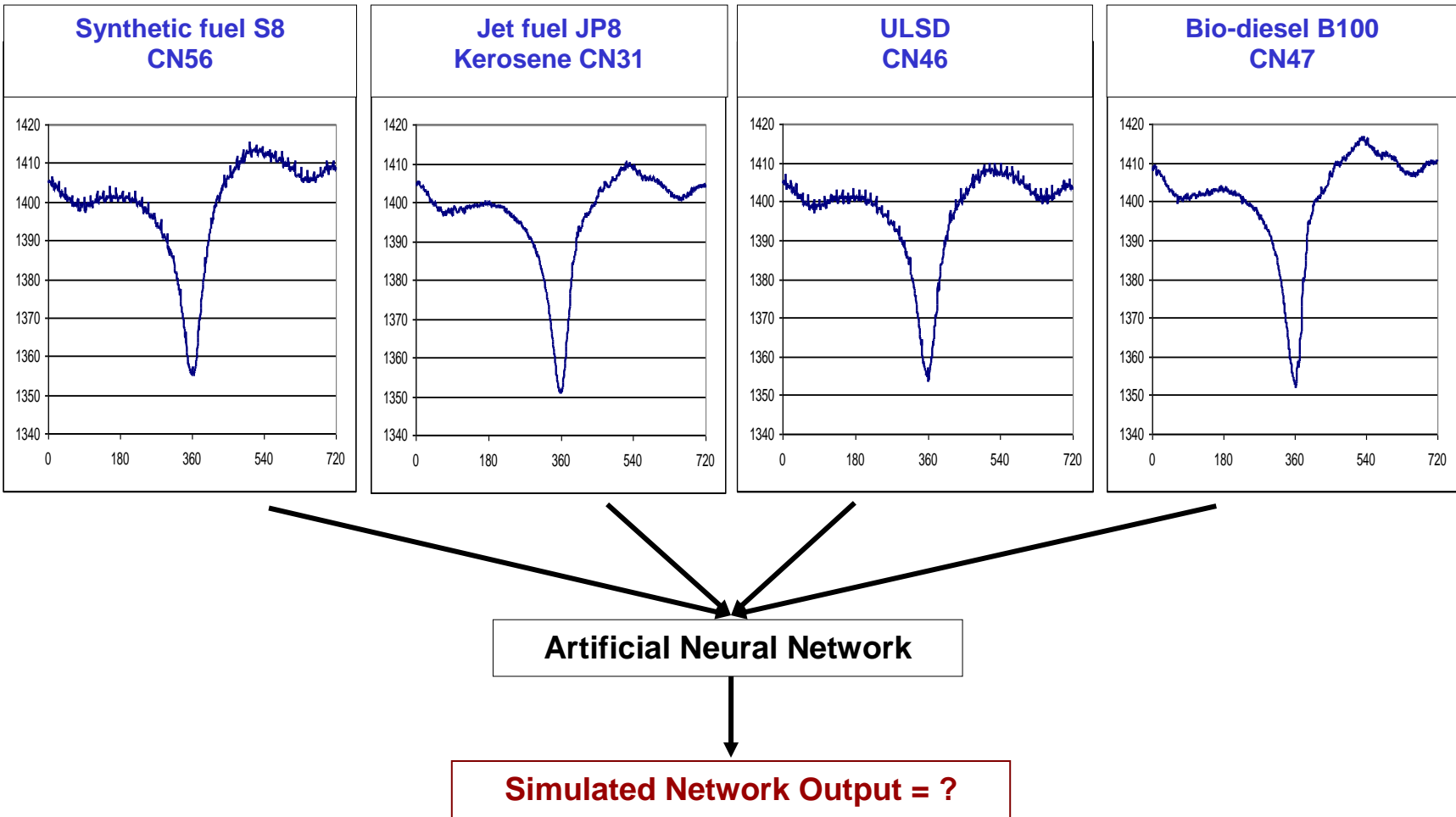
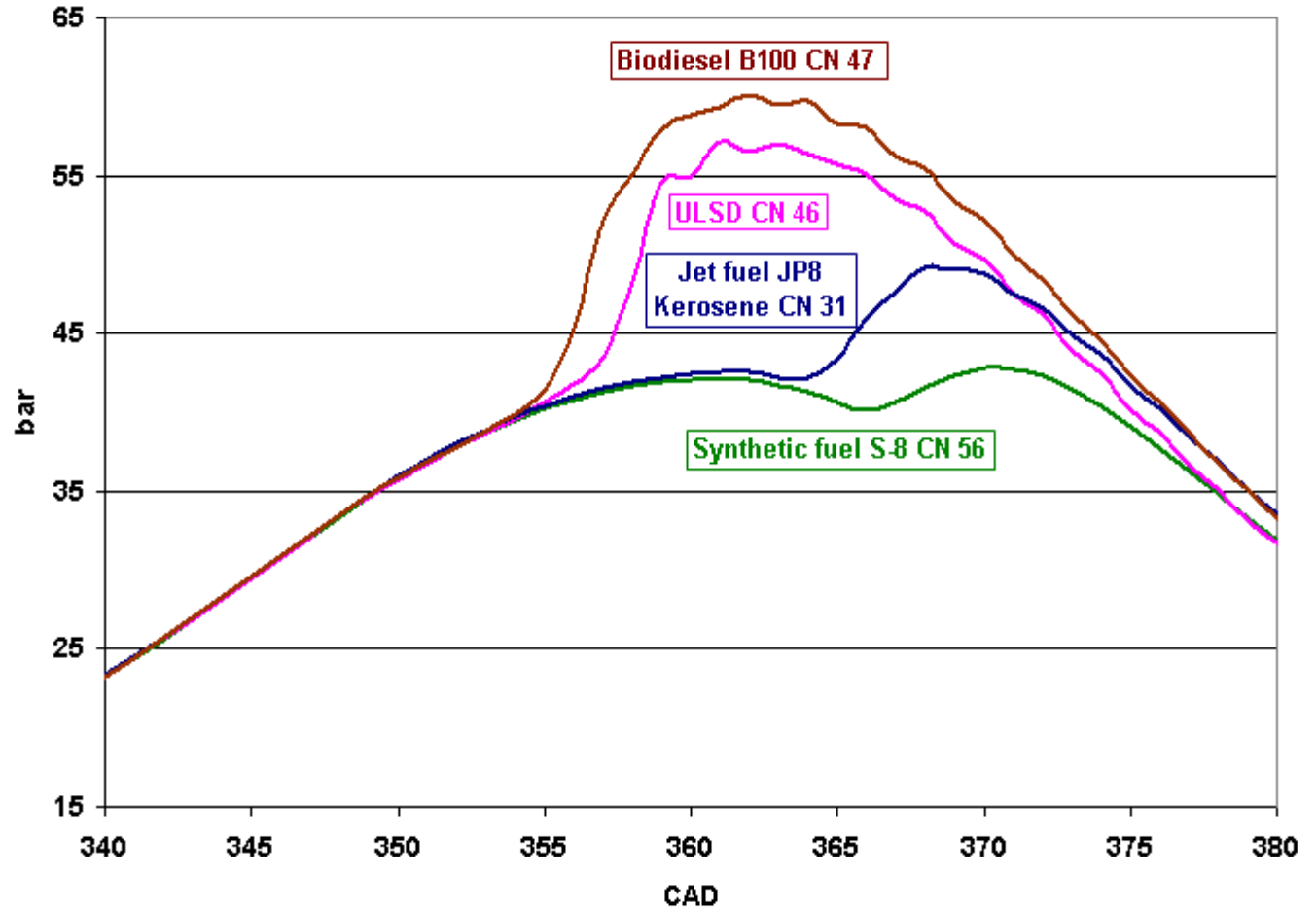


Figure 3.58 – Network input: the instantaneous measured crankshaft speed;
Network output: not set yet

Pressure
traces of all
four fuels
- average of
100 cycles -



- 204 -



Figure 3.59 – Network output selection: in-cylinder pressure

200 cycles:

- 50 cycles of S8 CN 56
- 50 cycles of JP8 CN 31
- 50 cycles of ULSD CN 46
- 50 cycles of B100 CN 47

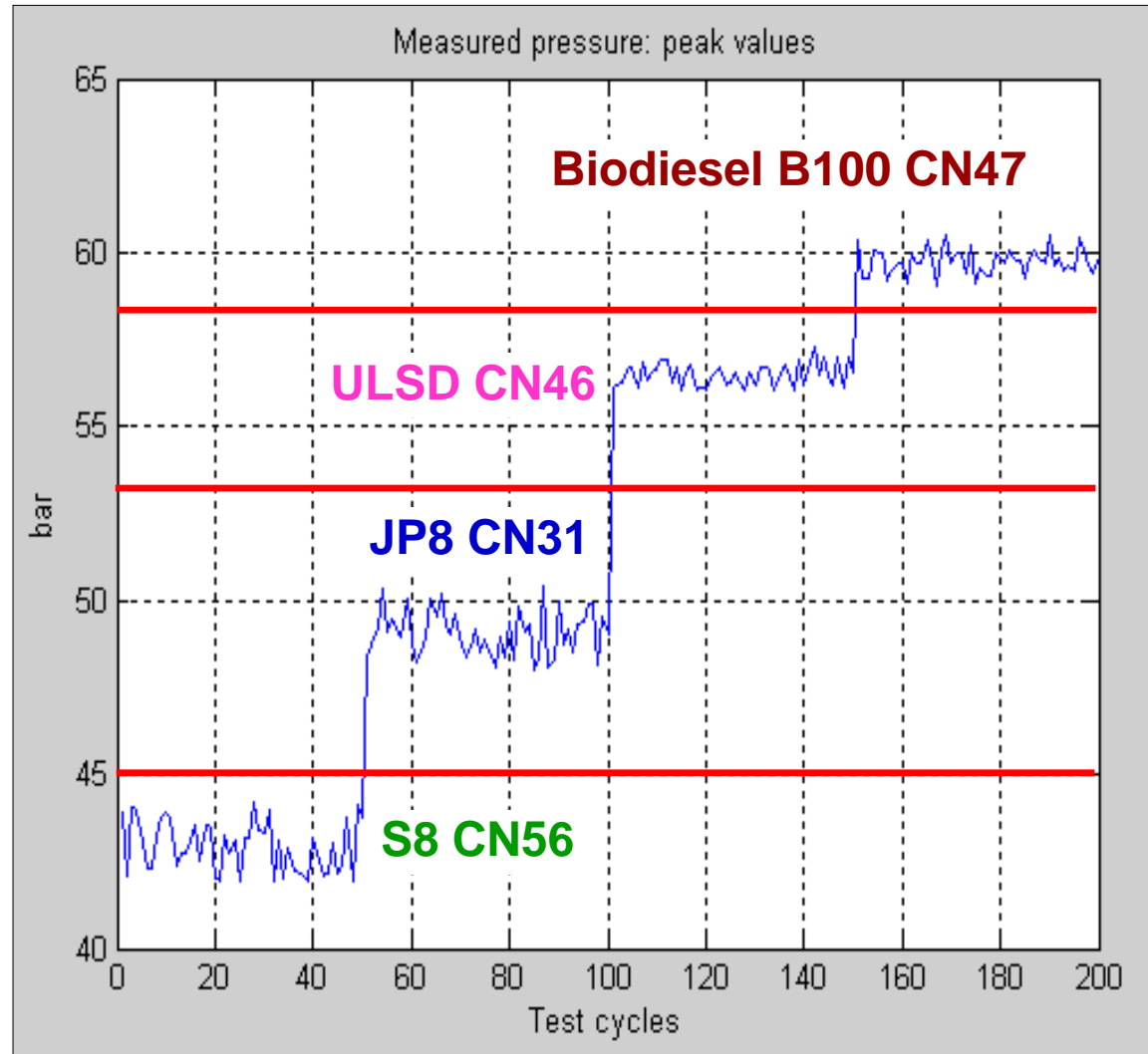


Figure 3.60 – Measured pressure cyclic variations for all fuels: peak values

The range of variation of peak pressures for each fuel is satisfactory because a clear separation between the four fuels is possible by using decision lines, representing a criterion for fuel type identification – horizontal red lines in Figure 3.60.

To put it briefly, if our tool, the trained Artificial Neural Network, is able to render dynamically a similar pattern for the simulated pressures too, using as input the instantaneous crankshaft speed, then the identification of the four fuels is possible.

As it was mentioned in 3.9.2 the network training represents an iterative adjustment of biases and weights to achieve a desired performance. In Figure 3.61 such a process is illustrated. The initial network structure is on the left hand side of the figure. During the training process, its biases and weights are modified in steps until the MSE (Mean Square Error) reaches a pre-set by the user value, e.g. 0.1. In our case the goal was met after seven steps (epochs).

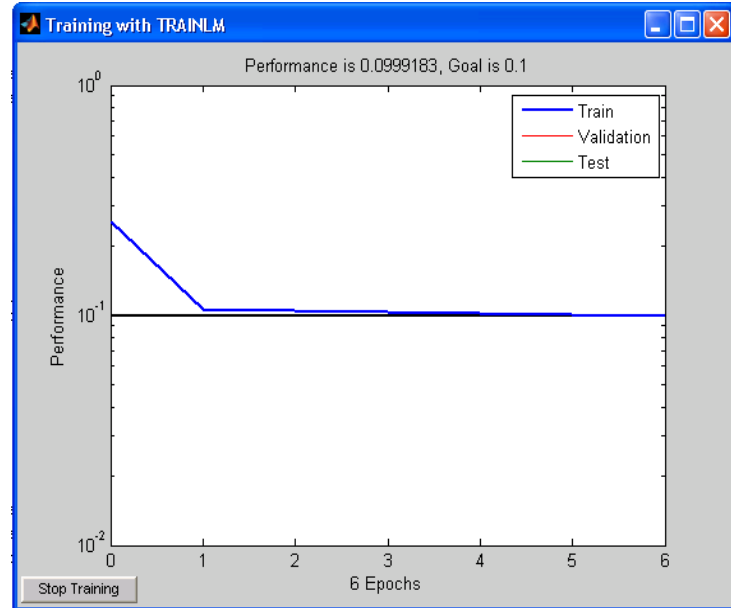
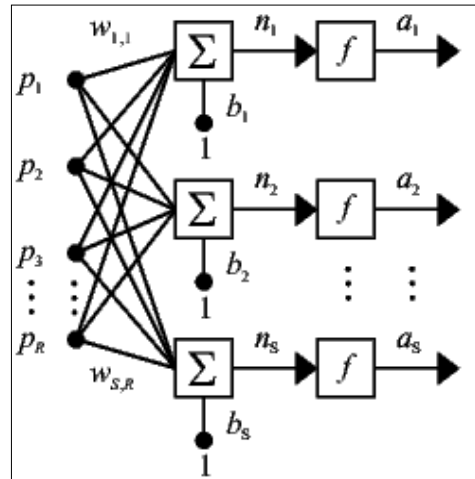
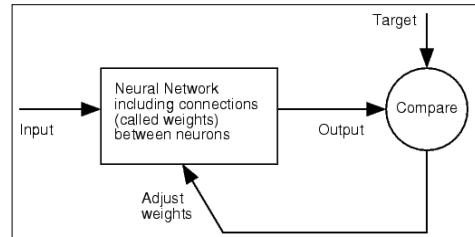
Some might consider that the lower the MSE (error) is, the better that network will perform. That is true only apparently, because a too small desired error, e.g. MSE, leads to a good approximation during training but to a very poor generalization after that, during testing. Instead of learning, the network only copies the example in the training.

```

net =
Neural Network object:
architecture:
  numInputs: 1
  numLayers: 4
  biasConnect: [1; 1; 1; 1]
  inputConnect: [1; 0; 0; 0]
  layerConnect: [4x4 boolean]
  outputConnect: [0 0 0 1]
  targetConnect: [0 0 0 1]

  numOutputs: 1 (read-only)
  numTargets: 1 (read-only)
  numInputDelays: 0 (read-only)
  numLayerDelays: 0 (read-only)
subobject structures:
  inputs: {1x1 cell} of inputs
  layers: {4x1 cell} of layers
  outputs: {1x4 cell} containing 1 output
  targets: {1x4 cell} containing 1 target
  biases: {4x1 cell} containing 4 biases
  inputWeights: {4x1 cell} containing 1 input weight
  layerWeights: {4x4 cell} containing 3 layer weights
functions:
  adaptFcn: 'trainlm'
  gradientFcn: (none)
  initFcn: 'initlay'
  performFcn: 'mse'
  trainFcn: (none)
parameters:
  adaptParam: .epochs, .goal, .max_fail, .mem_reduc,
    .min_grad, .mu, .mu_dec, .mu_inc,
    .mu_max, .show, .time, .lr,
    .max_perf_inc, .lr_inc, .lr_dec, .mc
  gradientParam: (none)
  initParam: (none)
  performParam: (none)
  trainParam: (none)
weight and bias values:
  IW: {4x1 cell} containing 1 input weight matrix
  LW: {4x4 cell} containing 3 layer weight matrices
  b: {4x1 cell} containing 4 bias vectors
other:
  userdata: (user information)

```



TRAINLM-, Epoch 0/1000, MSE 0.255819/0.1, Gradient 1.02704/1e-100
TRAINLM-, Epoch 1/1000, MSE 0.105959/0.1, Gradient 0.0184777/1e-100
TRAINLM-, Epoch 2/1000, MSE 0.105032/0.1, Gradient 0.110819/1e-100
TRAINLM-, Epoch 3/1000, MSE 0.10368/0.1, Gradient 0.275607/1e-100
TRAINLM-, Epoch 4/1000, MSE 0.101516/0.1, Gradient 0.193943/1e-100
TRAINLM-, Epoch 5/1000, MSE 0.100144/0.1, Gradient 0.312705/1e-100
TRAINLM-, Epoch 6/1000, MSE 0.0999183/0.1, Gradient 0.127906/1e-100
TRAINLM, Performance goal met.

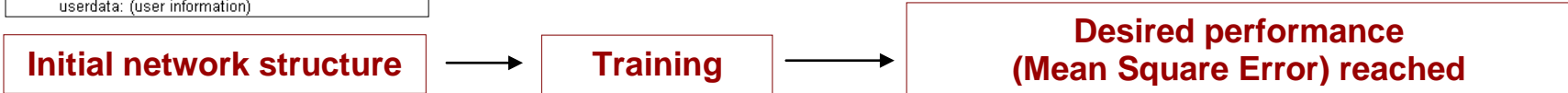


Figure 3.61 – Network training: an iterative adjustment of biases and weights to achieve a desired performance; in our case the goal was met in 7 steps (epochs) [31]

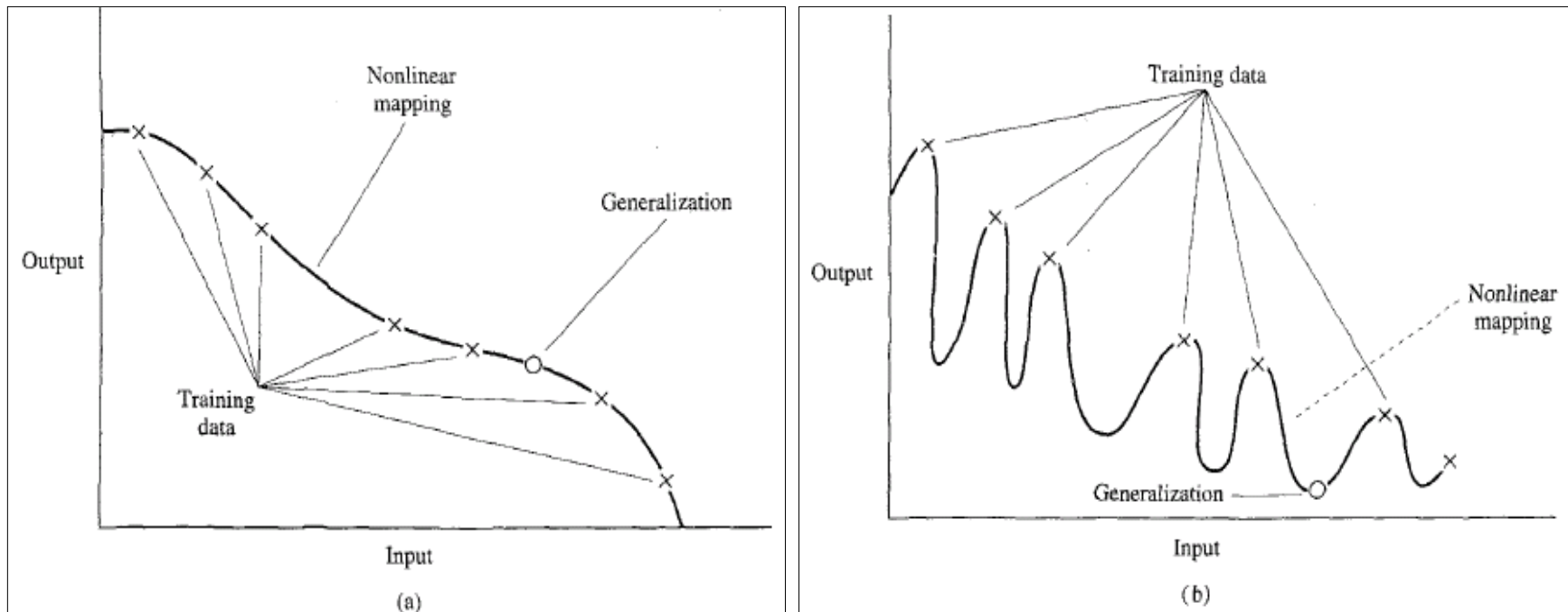


Figure 3.62 – Network over-fitting (overtraining) phenomenon:
 Properly fitted data – good generalization (left);
 overtrained data – poor generalization (right) according to S. Haykin [30]

According to [30], a neural network that is designed to generalize well will produce a correct input-output mapping even when the input is slightly different from the examples used to train the network, as illustrated in Figure 3.62. When, however, a neural network learns too many input-output examples, the network may end up memorizing the training data. It may do so by finding a feature (due to noise, for example), that is present in the training data but not true of the underlying function that is to be modeled. Such a phenomenon is referred to as overfitting or overtraining. When a network is overtrained, it simply loses the ability to generalize between similar input-output patterns.

Once the network was trained, it was tested with input speed cycles never seen before. The results are fairly good: as in the case of measured pressures, the range of variation of simulated peak pressures for each fuel is satisfactory - Figure 3.63. Consequently, a clear separation is possible by drawing decision lines between simulated peak pressures, as a criterion for fuel type identification.

A Matlab dynamic demonstration is also provided in Figure 3.64. Also the Matlab code for the computation of the fuel identification on a single-cylinder engine is presented in the Appendix.

Network testing
with input speed
cycles never
seen before

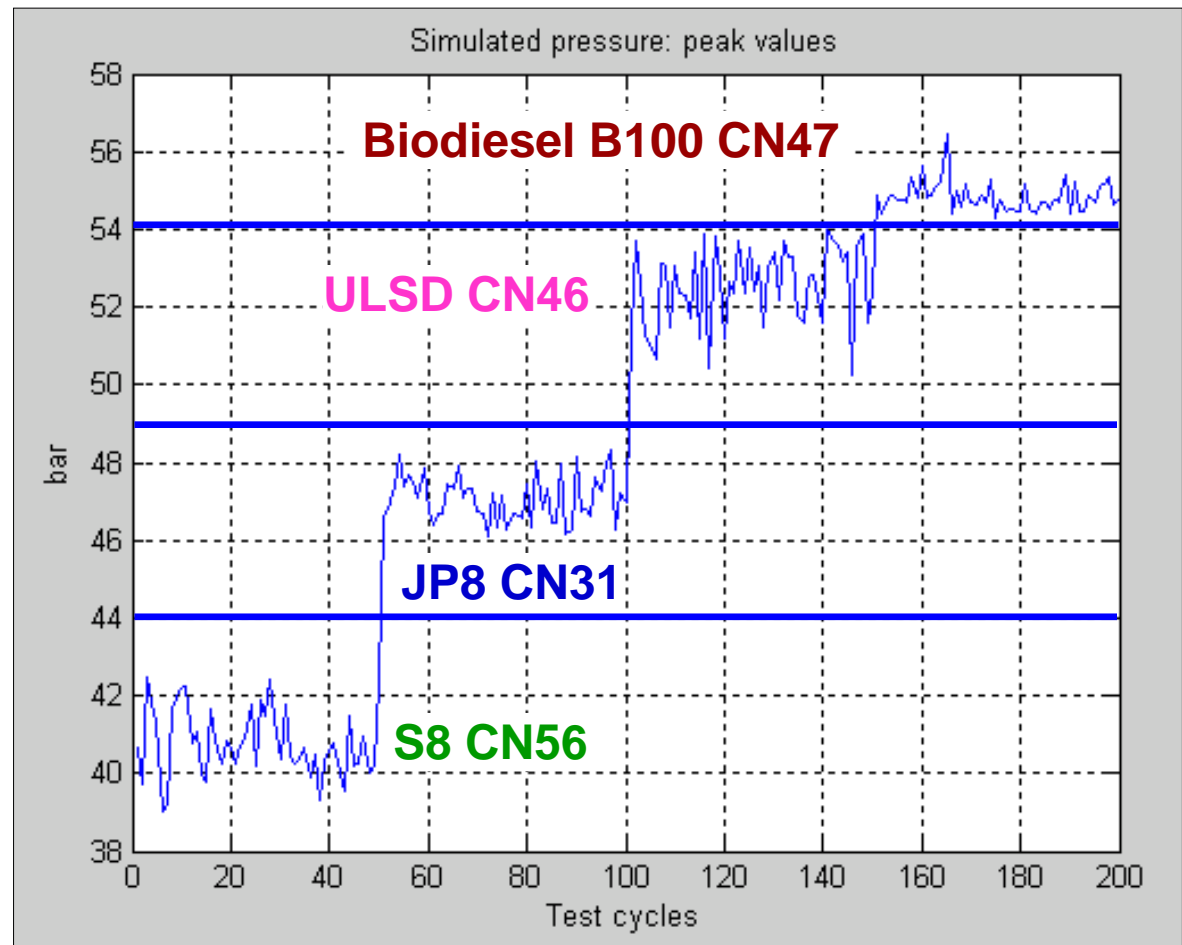


Figure 3.63 – Simulated pressure cyclic variations: peak values

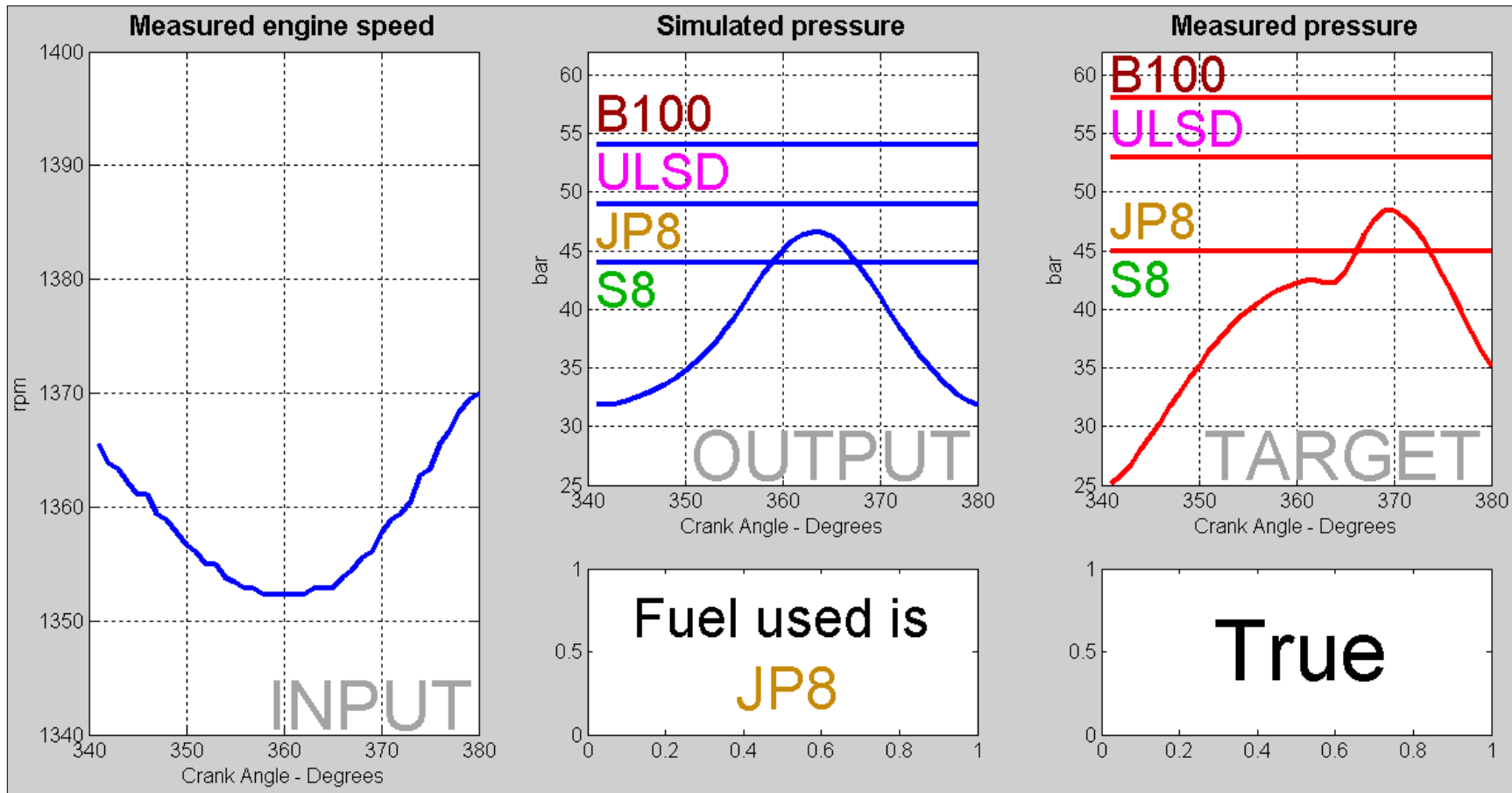


Figure 3.64 – Network testing: validation of simulation and fuel identification;
 blue decision lines between simulated peak pressures determine the fuel type;
 red decision lines between measured peak pressures decide whether it is True / False

3.9.7 ANN fuel identification on a six-cylinder engine

The tests were performed on the Mercedes 7.2 L six-cylinder engine presented in Chapter 2. The tested fuels were: synthetic fuel S8 CN56, ULSD CN46 and Bio-diesel B100 CN47. Jet fuel JP8 Kerosene CN31 could not be tested because the engine did not fire.

The network input is the instantaneous measured crankshaft speed – Figure 3.65. At 1300 rpm / 360Nm torque, the three speed patterns are very similar, a fact that makes the fuel identification process difficult.

The question is what differentiating parameter should be chosen as a network simulated output so that each fuel can be uniquely determined. The idea to select the network output to be the in-cylinder simulated pressure may not work here because their peaks are very close to each other – Figure 3.66. Because cyclic peak pressures fluctuate and their values interfere considerably they cannot be used as a fuel identifying parameter.

However, another parameter such as the rate of pressure rise provides a clear differentiation between the three fuels, thus it can be used as an identifying parameter, representing the network output - Figure 3.67.

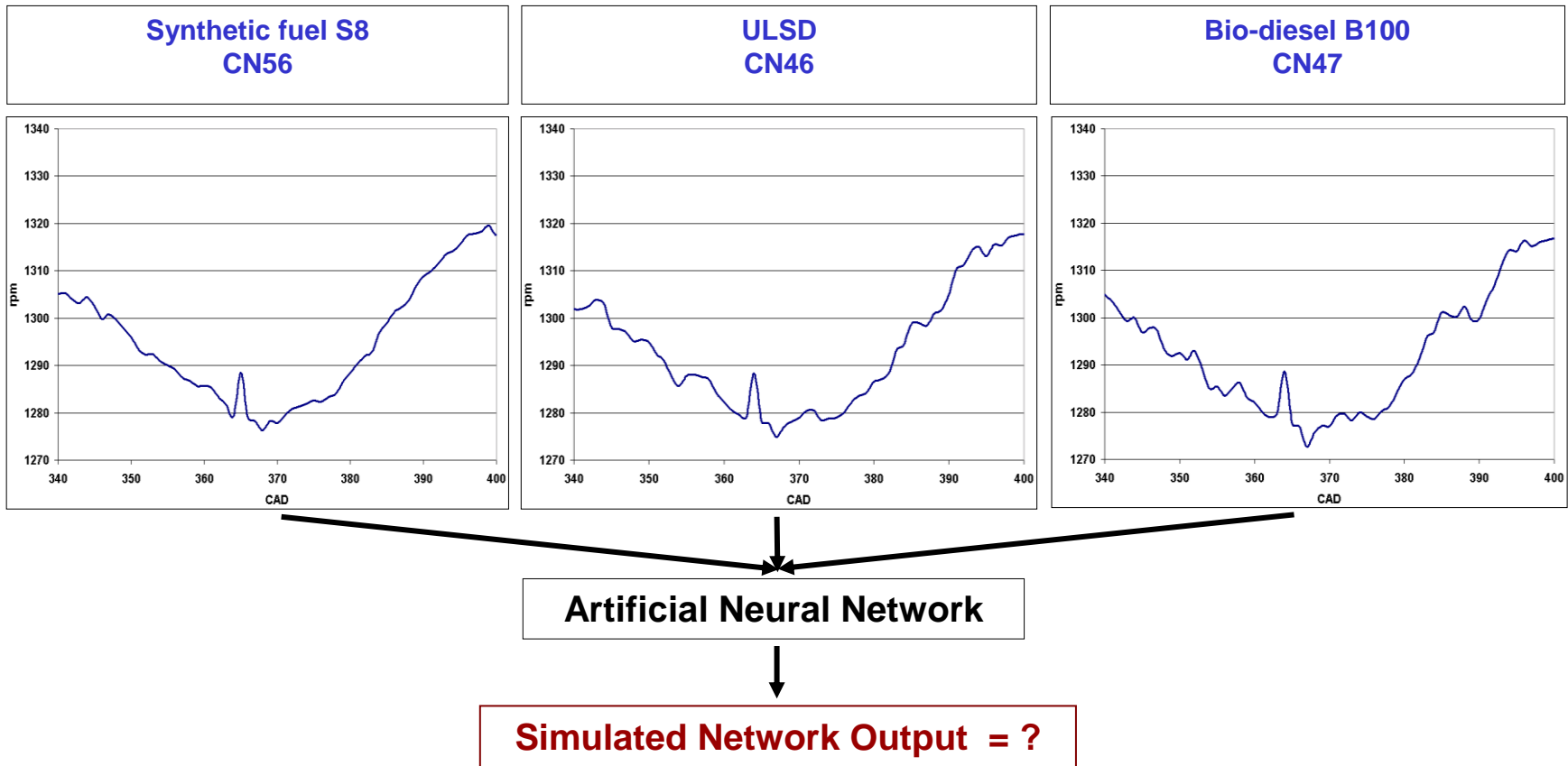


Figure 3.65 – Network input: the instantaneous measured crankshaft speed;
Network output: not set yet

Pressure traces
- average of
100 cycles -

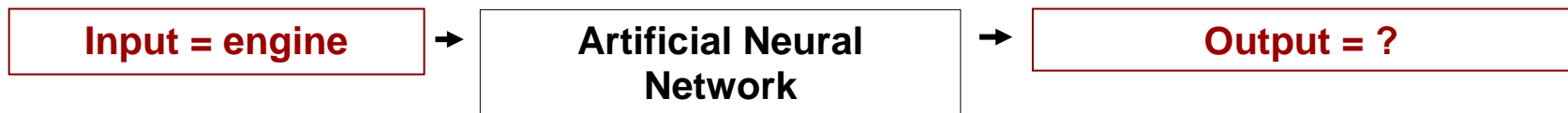
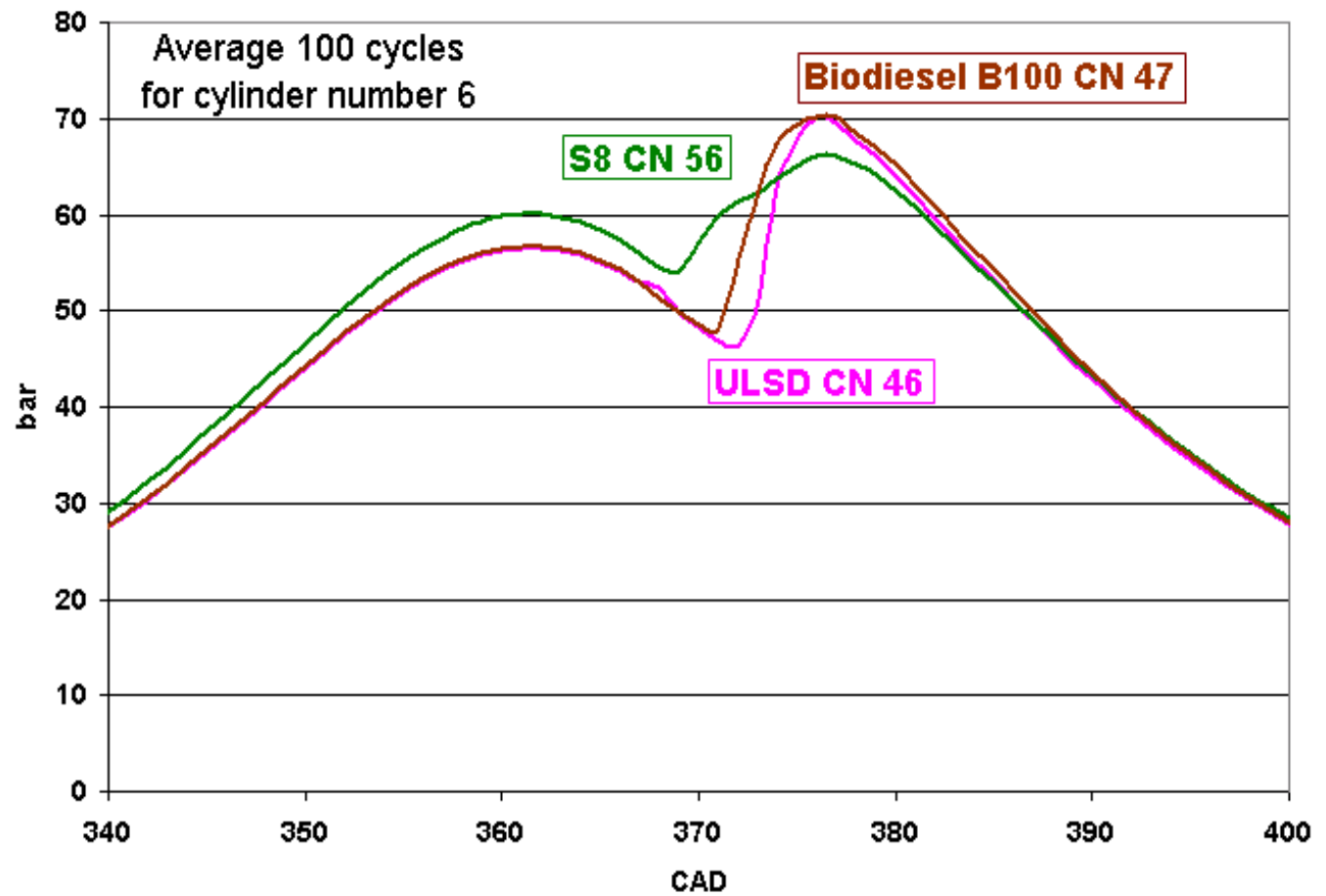
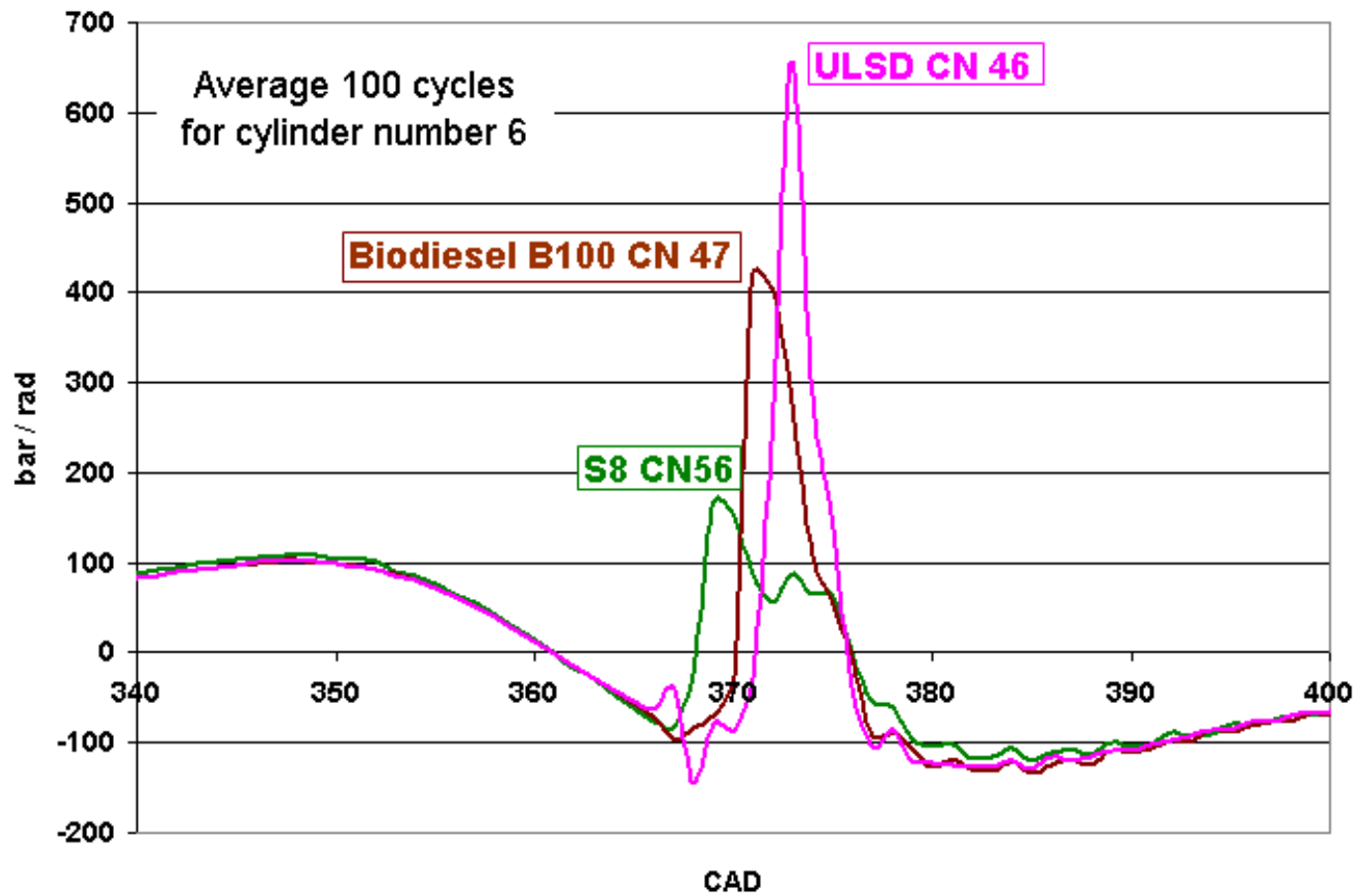


Figure 3.66 – In-cylinder pressures cannot be selected as network output because their peaks are very close to each other

Rates of pressure rise - average of 100 cycles -



- 215 -



Figure 3.67 – Network output selection: rates of pressure rise

Instantaneous peak rates of pressure rise have cyclic variations that must be compensated for. In Figure 3.68 peak values of measured pressure cyclic variations were represented for all fuels for 150 cycles: 50 cycles of S8, 50 cycles of ULSD and 50 cycles of B100.

The range of variation of peaks of rate of measured pressure rise for each fuel is satisfactory because a clear separation between the three fuels is possible by using decision lines, representing a criterion for fuel type identification – horizontal red lines in Figure 3.68.

It means that if the trained Artificial Neural Network is able to provide dynamically a similar pattern for the peaks of the simulated rate of pressure rise too, using as input the instantaneous crankshaft speed, then the identification of the three fuels is possible.

By following the same procedure as described in Figure 3.61 the network training process is illustrated for the six-cylinder case in Figure 3.69.

The initial network structure is on the left hand side of the figure. During the training process, its biases and weights are modified in steps until the MSE (Mean Square Error) reached 0.1, a value pre-set by the user value. In our case the goal was met after two steps (epochs).

150 cycles:

- 50 cycles of S8 CN 56

- 50 cycles of B100 CN 47

- 50 cycles of ULSD CN 46

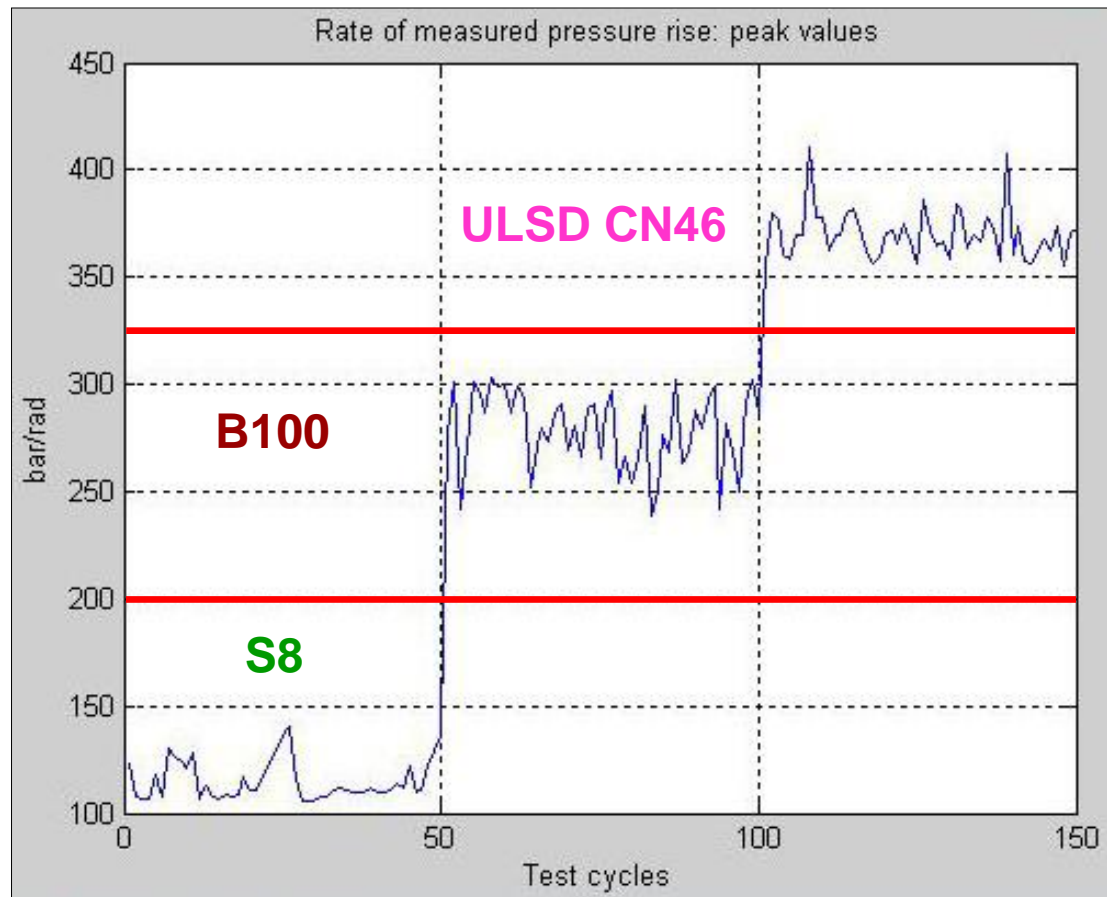


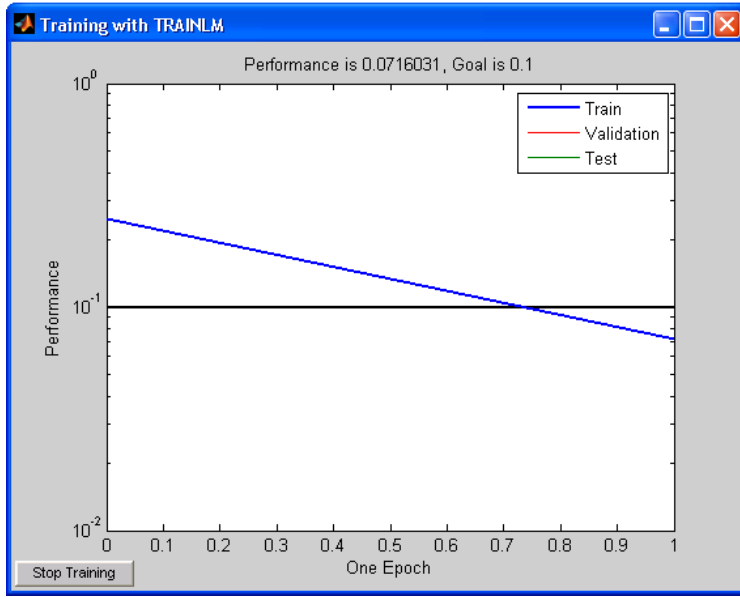
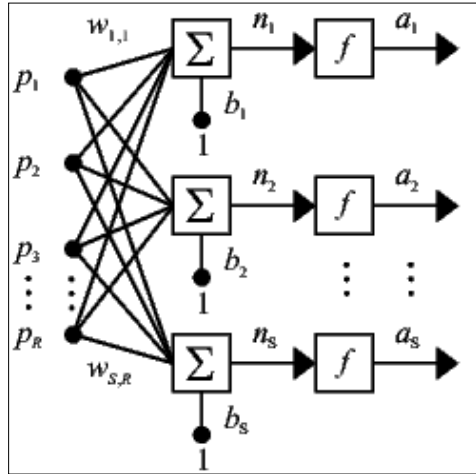
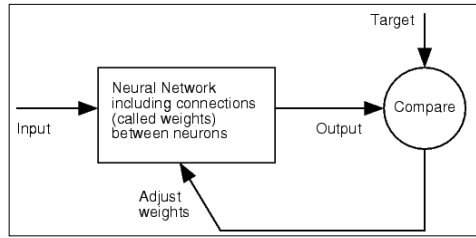
Figure 3.68 – Rate of measured pressure rise: cyclic peak values

```

net =
Neural Network object:
architecture:
  numInputs: 1
  numLayers: 4
  biasConnect: [1; 1; 1; 1]
  inputConnect: [1; 0; 0; 0]
  layerConnect: [4x4 boolean]
  outputConnect: [0 0 0 1]
  targetConnect: [0 0 0 1]

  numOutputs: 1 (read-only)
  numTargets: 1 (read-only)
  numInputDelays: 0 (read-only)
  numLayerDelays: 0 (read-only)
subobject structures:
  inputs: {1x1 cell} of inputs
  layers: {4x1 cell} of layers
  outputs: {1x4 cell} containing 1 output
  targets: {1x4 cell} containing 1 target
  biases: {4x1 cell} containing 4 biases
  inputWeights: {4x1 cell} containing 1 input weight
  layerWeights: {4x4 cell} containing 3 layer weights
functions:
  adaptFcn: 'trainlm'
  gradientFcn: (none)
  initFcn: 'initlay'
  performFcn: 'mse'
  trainFcn: (none)
parameters:
  adaptParam: .epochs, .goal, .max_fail, .mem_reduc,
             .min_grad, .mu, .mu_dec, .mu_inc,
             .mu_max, .show, .time, .lr,
             .max_perf_inc, .lr_inc, .lr_dec, .mc
  gradientParam: (none)
  initParam: (none)
  performParam: (none)
  trainParam: (none)
weight and bias values:
  IW: {4x1 cell} containing 1 input weight matrix
  LW: {4x4 cell} containing 3 layer weight matrices
  b: {4x1 cell} containing 4 bias vectors
other:
  userdata: (user information)

```



```

TRAINLM-, Epoch 0/1000, MSE 0.247142/0.1, Gradient 1.73737/1e-100
TRAINLM-, Epoch 1/1000, MSE 0.0716031/0.1, Gradient 0.111032/1e-100
TRAINLM, Performance goal met.

```

Initial network structure

Training

Desired performance (Mean Square Error) reached

Figure 3.69 – Network training: an iterative adjustment of biases and weights to achieve a desired performance; the goal was met in 2 steps (epochs) [30]

Network testing
with input speed
cycles never
seen before

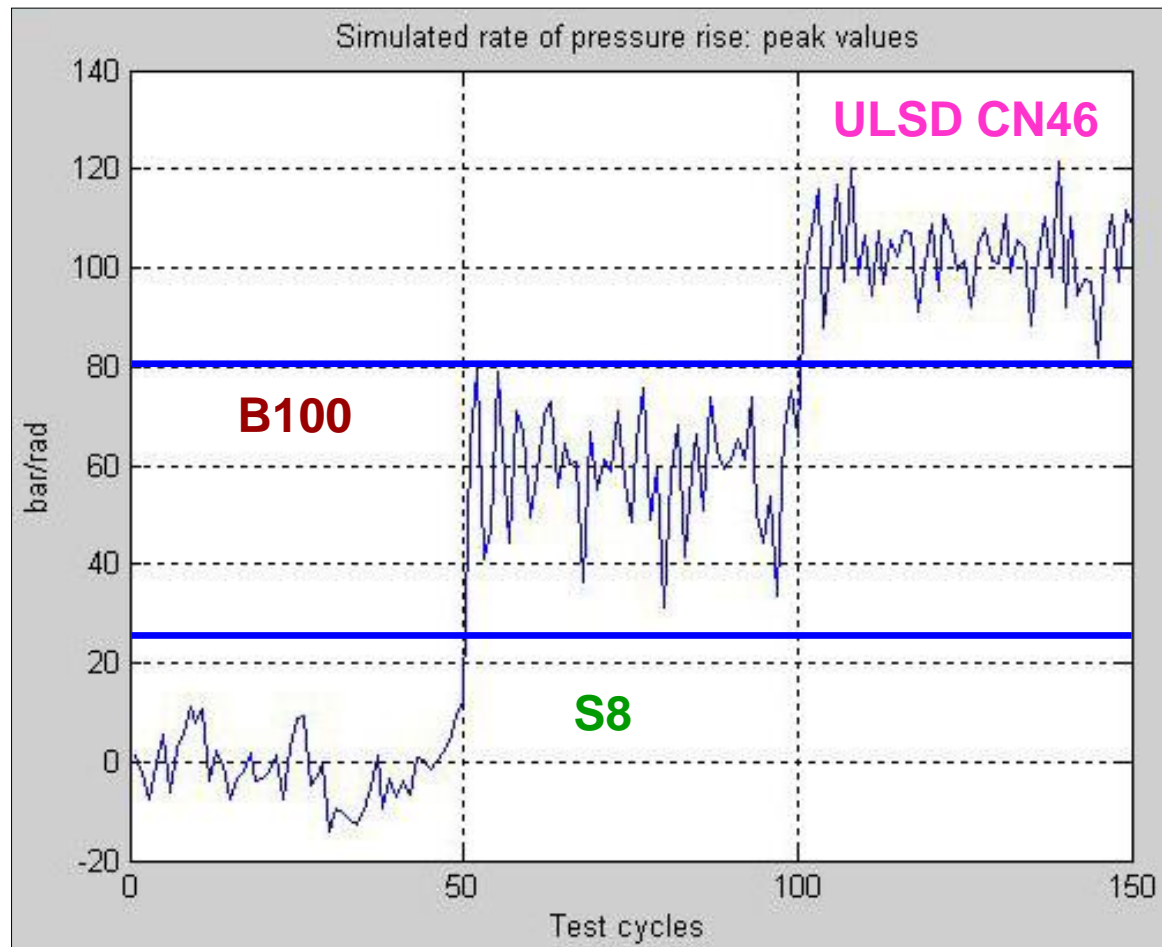


Figure 3.70 – Simulated rate of pressure rise: cyclic peak values

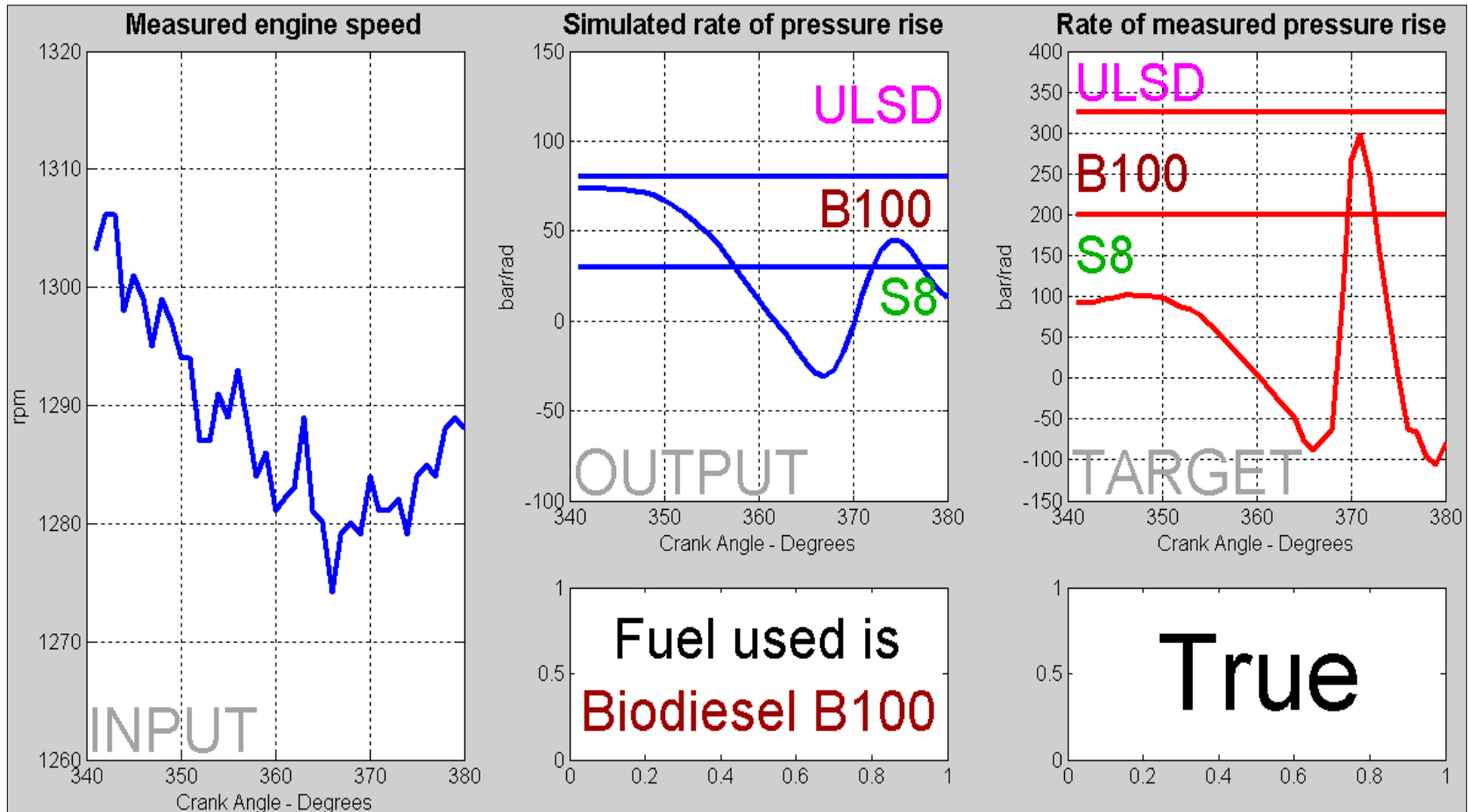


Figure 3.71 – Network testing: validation of simulation and fuel identification

Blue decision lines between peaks of simulated rate of pressure rise determine the fuel type.

Red decision lines between peaks of rate of measured pressure rise decide whether it is True / False

Once the network was trained, it was tested with input speed cycles never seen before. The results are promising: similar to the case of measured pressures, the range of variation of the peaks of simulated rate of pressure rise for each fuel is satisfactory - Figure 3.70. A clear separation is possible by drawing decision lines between simulated peaks of rate of pressure rise, as a criterion for fuel type identification.

A Matlab dynamic demonstration is provided in Figure 3.71. Also the Matlab code for the computation of the fuel identification on a multi-cylinder engine is presented in the Appendix.

In conclusion, for single and multi-cylinder engines the Neural Network Model requires only a shaft encoder or a proximity transducer working with the teeth of the starter gear, ensuring accurately the fuel type recognition. This technique does not require a dynamic model of the crankshaft and can be applied on any engine, regardless of the number of cylinders. It can be utilized in all cases, including those where the previous three methods have failed.

CHAPTER 4

CONCLUSIONS AND FUTURE WORK

4.1. Conclusions

On-board fuel identification is important to ensure engine safe operation, similar power output, fuel economy and emissions levels when different fuels are used.

Real-time detection of physical and chemical properties of the fuel requires the development of identifying techniques based on a simple, non-intrusive sensor. The measured crankshaft speed signal, which is already available on series engine, can be utilized to estimate at least one of the essential combustion parameters such as peak pressure and its location, rate of cylinder pressure rise and start of combustion, which are an indicative of the ignition properties of the fuel.

Four methods have been developed in this research work to identify the fuel type. Their particularities are presented below as follows:

- the **Model-Based Recognition Method** reconstructs the cylinder pressure trace and estimates the fuel identifying combustion parameters in a reasonable manner; it cannot be implemented for real time controls on engines having more than one cylinder, because

of the large amount of computations required in a very short period of time

- the **Direct Recognition Method** can be applied on single and four-cylinder engines; it provides satisfactory results for peak pressure and its location, which are an indicative of the ignition properties of the fuel
- the **Start of Combustion Approach** yields fairly accurate values for the start of combustion / ignition delay; it cannot be applied on engines having more than four cylinders due to the increased disturbance produced by other cylinders when a cylinder is firing
- the **Artificial Neural Network Method** can be applied on any engine, regardless of the number of cylinders, including in those cases where the previous three methods have failed; it is able to identify four fuels (S-8, JP-8 , ULSD, B100) on a single-cylinder engine and three fuels (S-8, ULSD, B100) on a six-cylinder engine; its neural parameters such as input weights, layer weights, biases can be stored in the memory of the ECU of any similar production engine and used as a reliable tool for automatic change of injection control strategy when detecting a different fuel.

In conclusion, the four techniques presented previously demonstrate that the fuels studied in this paper can be identified on-board with high accuracy on single and multi-cylinder engines, using the measured engine speed signal.

4.2. Future work

As a consequence, the proposed research for the future is as follows:

- extend the identification procedure to a larger number of fuels
- improve the identification procedure, including for applications with fuel blends
- improve the neural network model by using several inputs, more layers of neurons and, possibly, several outputs.

APPENDIX

COMPUTATION CODES

Crankshaft speed computation from in-cylinder pressure - Matlab code

```
% Transfer matrices calculation for the single cylinder engine

% Import speed and pressure file data (for ex. Press_1200_81.xls, Excel
format) then create a "pressure" file to be used in our calculations :
for n=1:720 pressure(n)=1e5*(Pres_1500_4Nm_ULSD(n)-1);
    speed(n)=Speed_1500_4Nm_ULSD(n); % measured at the flywheel, for
comparison purposes only
end

%General engine data
D=80e-3;           % Bore [m]
S=82e-3;           % Stroke [m]
R=S/2;            % Crank radius = half of the stroke [m]
LCR=135e-3;        % Length of conrod [m]
MTR=0.898;         % Mass in translation [kg]

%Dynamic system
Ctors=[0 1.6e6 0 1.3e6]; % Torsional stiffnesses
[Nm/rad]
Jp=[0.002 0 0.0013 0 0.263]; % Mass moments of inertia [Nms2]
or kg*m2]
r=[0 0 2 0 0.01]; % Absolute damping coefficients
[N*m*s or kg*m2/s]
f=[0 80 0 80]; % Relative damping coefficients
[N*m*s or kg*m2/s]

%Basic parameters :

crad=pi/180;
lambda=R/LCR; % Ratio between the crank radius and the connecting rod
[non-dimensional]
Ap=pi*D*D/4; % Piston area
[m2]
ki=MTR*R/Ap; % Multiplying coefficient
[kg/m]
kfr=Ap*R; % Multiplying coefficient to obtain the gas pressure
torque from the tangential gas pressure [m3]
KARM=24; % Number of harmonics
smean=0;
for n=1:720 smean=smean+speed(n);
end
smean=smean/720; % Engine speed [rpm]
omg=pi*smean/30; % Angular speed [rad/s]
%-----

% Harmonic analysis of speed :
```

```
% 1) Calculus of harmonic coefficients Ak or ahs(k), Bk or bhs(k) and Ck or
chs(k) for speed
for k=1:KARM ah(k)=0;bh(k)=0;
    for n=1:720 arg=(n-1)*crad;
        ah(k)=ah(k)+speed(n)*cos((k/2)*arg);
        bh(k)=bh(k)+speed(n)*sin((k/2)*arg);
    end
    ahs(k)=ah(k)/360; bhs(k)=bh(k)/360; chs(k)=sqrt(ah(k)^2+bh(k)^2);
    fprintf('k %3.1f Ak=%8.5e Bk=%8.5e Ck=%8.5e\n',k,ahs(k),bhs(k),chs(k));
end
```

```
% 2) Speed curve reconstrucion, veloc = f(teta)
for n=1:720 sve=smean;
    arg=(n-1)*crad;
    for k=1:KARM
sve=sve+ahs(k)*cos((k/2)*arg)+bhs(k)*sin((k/2)*arg);
    end
veloc(n)=sve;
end
```

```
%-----
```

```
% Harmonic analysis of the tangential gas pressure and Gas Pressure Torque :
```

```
% 1) Direct computation of the tangential gas pressure from measured data :
press_carter=20000;
for n=1:720    teta=(n-1)*crad;
                beta=asin(lambda*sin(teta));
                trig(n)=sin(teta+beta)/cos(beta);
                ptg(n)=(pressure(n)-press_carter)*trig(n);
end
```

```
% 2) Indirect computation of the tangential gas pressure from the harmonic
analysis
```

```
    % 2a) Calculus of harmonic coefficients Ak or ahp(k), Bk or bhp(k)
and Ck or chp(k):
```

```
for k=1:KARM    a(k)=0;b(k)=0;
                for n=1:720    arg=(n-1)*crad;
                                a(k)=a(k)+ptg(n)*cos((k/2)*arg);
                                b(k)=b(k)+ptg(n)*sin((k/2)*arg);
                end
    ahp(k)=a(k)/360; bhp(k)=b(k)/360; chp(k)=sqrt(a(k)^2+b(k)^2);
    fprintf('k %3.1f, Ak=%8.5e, Bk=%8.5e, Ck=%8.5e\n', k, ahp(k),bhp(k),chp(k));
end
```

```
    % 2b) Calculus of average tangential gas pressure :
```

```
sve=0;
for n=1:720    sve=sve+ptg(n);
end
pt_avg=sve/720;
```

```
    % 2c) Gas Pressure Torque curve reconstruction, f(CAD):
```

```
for n=1:720    arg=(n-1)*crad;
                sve=pt_avg;
```

```
        for k=1:KARM
sve=sve+ahp(k)*cos(k/2*arg)+bhp(k)*sin(k/2*arg);
        end
ptang(n)=sve; gptorque(n)=kfr*ptang(n); % smoothed PTG by Harmonical Analysis
end

%-----

% Harmonic analysis of the Inertia Torque (rolling moment):

% 1) Calculus of harmonic coefficients :
bi=zeros(1,KARM);
bi(2)=ki*(omg^2)*(lambda/4+lambda^3/16+15*lambda^5/512);
bi(4)=-ki*(omg^2)*(1/2+lambda^4/32+lambda^6/32);
bi(6)=-ki*(omg^2)*(3*lambda/4+9*lambda^3/32+81*lambda^5/512);
bi(8)=-ki*(omg^2)*(lambda^2/4+lambda^4/8+lambda^6/16);
bi(10)=ki*(omg^2)*(5*lambda^3/32+75*lambda^5/512);
bi(12)=ki*(omg^2)*(3*lambda^4/32+3*lambda^6/32);
for k=1:KARM    ai(k)=kfr*bi(k);
                am(k)=kfr*(ahp(k));           % coeff-s corresp to the real
part of the engine torque (cosine)
                bm(k)=kfr*(bhp(k)+bi(k));     % coeff-s corresp to the
imaginary part of the engine torque (sine)
end

% 2) Calculus of the average Inertia Torque :
in_avg=0; % work done by the inertia forces in 1 cycle is 0 (zero) = average
inertia torque * crank radius, so average inertia torque = 0 (zero)

% 3) Tangential Inertia Torque curve reconstruction, f(CAD):
for n=1:720    arg=(n-1)*crad;
                sve=in_avg;
                for k=1:KARM    sve=sve+ai(k)*sin(k/2*arg);
                end
itorque(n)=sve; % smoothed Inertia Torque by Harmonical Analysis
end

%-----

% Total Engine Torque (Gas Pressure Torque + Inertia Torque):

for n=1:720 torque(n)=gptorque(n)+itorque(n);
end

sve=0;
for n=1:720
    sve=sve+torque(n);
end
avgtorque=sve/720; avgtorque

%-----

% Building the transfer matrices
```

```
for k=1:KARM
    mp1=eye(5,5); mp2=eye(5,5); mp3=eye(5,5); mp4=eye(5,5); mp5=eye(5,5);

    % Point matrices : for single cylinder case, there are 3 matrices
    corresp. to 3 masses : pulley, cranks slider mechanism, flywheel
    mp1(2,1)=-Jp(1)*(k/2*omg)^2; mp1(2,3)=-r(1)*(k/2)*omg; mp1(4,1)=-
mp1(2,3); mp1(4,3)=mp1(2,1);
    mp3(2,1)=-Jp(3)*(k/2*omg)^2; mp3(2,3)=-r(3)*(k/2)*omg; mp3(2,5)=-am(k);
mp3(4,1)=-mp3(2,3); mp3(4,3)=mp3(2,1); mp3(4,5)=bm(k);
    mp5(2,1)=-Jp(5)*(k/2*omg)^2; mp5(2,3)=-r(5)*(k/2)*omg; mp5(4,1)=-
mp5(2,3); mp5(4,3)=mp5(2,1);

    % Field matrices : for single cylinder case, there are 2 matrices
    corresp. to the 2 inter-connecting shafts
    mod2=Ctors(2)^2+(f(2)*(k/2)*omg)^2;
    mp2(1,2)=Ctors(2)/mod2; mp2(1,4)=f(2)*(k/2)*omg/mod2; mp2(3,2)=-mp2(1,4);
mp2(3,4)=mp2(1,2);
    mod4=Ctors(4)^2+(f(4)*(k/2)*omg)^2;
    mp4(1,2)=Ctors(4)/mod4; mp4(1,4)=f(4)*(k/2)*omg/mod4; mp4(3,2)=-mp4(1,4);
mp4(3,4)=mp4(1,2);

    % Total transfer matrix = product of all matrices

    mh=mp5*mp4*mp3*mp2*mp1;

    % Real and imaginary components of the angular deflection of the 1st and
    last masses (the calculus for any other mass in between is similar) :

    numi=mh(2,1)*mh(4,3)-mh(2,3)*mh(4,1); % the common numerator
    tlr(k)=(-mh(2,5)*mh(4,3)+mh(4,5)*mh(2,3))/numi; % real component of the
    angular deflection of the 1st mass (pulley)
    tli(k)=(-mh(4,5)*mh(2,1)+mh(2,5)*mh(4,1))/numi; % imaginary component of
    the angular deflection of the 1st mass (pulley)
    tnr(k)=mh(1,1)*tlr(k)+mh(1,3)*tli(k)+mh(1,5); % real component of the
    angular deflection of the last mass (flywheel)
    tni(k)=mh(3,1)*tlr(k)+mh(3,3)*tli(k)+mh(3,5); % imaginary component of
    the angular deflection of the last mass (flywheel)
end

for n=1:720 teta=0; tv=0; tetan=0; tvn=0;
    arg=(n-1)*crad;
    for k=1:KARM
        teta=teta+tlr(k)*cos(arg*k/2)-tli(k)*sin(arg*k/2);
        tv=tv+(-tlr(k)*sin(arg*k/2)-tli(k)*cos(arg*k/2))*(k/2);
        tetan=tetan+tnr(k)*cos(arg*k/2)-tni(k)*sin(arg*k/2);
        tvn=tvn+(-tnr(k)*sin(arg*k/2)-tni(k)*cos(arg*k/2))*(k/2);
    end
theta(n)=teta*180/pi; % simulated deflection at the pulley [hexadecimal
degrees]
speedsim(n)=(1+tv)*smean; % simulated speed at the pulley [rpm]
thetan(n)=tetan*180/pi; % simulated deflection at the flywheel [hexadecimal
degrees]
speedsim1(n)=(1+tvn)*smean; % simulated speed at the flywheel [rpm]
end
```

```
figure(1)
n=1:720;
plot(n,gptorque(n),'r',n,itorque(n),'b',n,torque(n),'k',n,avgtorque,'g'),grid
,xlabel('Crank Angle - Degrees'), ylabel('Torque - Nm'), title('Gas Pressure
Torque (red), Inertia Torque (blue), Total Engine Torque (black)');
```

```
figure(2)
%n=1:720;
plot(n,speed(n),'b',n,veloc(n),'k',n,speedsim1(n),'r',n,speedsim(n),'g'),
grid, xlabel('Crank Angle - Degrees'), ylabel('Speed - rpm'), title('Flywheel
measured speed (blue), Flywheel measured speed - smoothed by harmonics
(black), Flywheel simulated speed from pressure (red), Pulley simulated speed
from pressure (green)');
n=1:720; plot(n,speed(n),'b',n,speedsim1(n),'r'), grid, xlabel('Crank Angle -
Degrees'), ylabel('Speed - rpm'), title('Flywheel measured speed (blue),
Flywheel simulated speed from pressure (red)');
```

```
%figure(3)
%n=1:720; plot(n,thetan(n),'r',n,theta(n),'b'), grid, xlabel('Crank Angle -
Degrees'), ylabel('Deflection - degrees'), title('Simulated deflection at the
flywheel (red), Simulated deflection at the pulley (blue)');
```

In-cylinder pressure computation from crankshaft speed (Matlab code)

```
% Cylinder presure reconstruction
%%%%%%%%%%%%%%%%%%%%%%%%%%%%%%%%%%%%%%%%%%%%%%%%%%%%%%%%%%%%%%%%%%%%%%%%

% import pressure data
%%%%%%%%%%%%%%%%%%%%%%%%%%%%%%%%%%%%%%%%%%%%%%%%%%%%%%%%%%%%%%%%%%%%%%%%
for n=1:720
%pres(n)=Deutz_pres1300(n);
%pres(n)=Pres2000_81(n);
%pres(n)=Pres1200_81(n);
%pres(n)=Pres1500_81(n);
%press(n)=pres_mercedes(n); %From D/recopres
press(n)=Pres_1500_4Nm_ULSD(n); %from D/Single cylinder
speeds(n)=Speed_1500_4Nm_ULSD(n); % from D/Single cylinder
end
srev=0;
% Claculate mean engine speed
for n=1:720
    srev=srev+speeds(n);
    pres(n)=press(n);
    speed(n)=speeds(n);
end
REV=srev/720; % Engine speed

% general engine data
%%%%%%%%%%%%%%%%%%%%%%%%%%%%%%%%%%%%%%%%%%%%%%%%%%%%%%%%%%%%%%%%%%%%%%%%
D= 80e-3; % bore
S= 82e-3; % Stroke
LCR= 135e-3; % length of the connrod
mbl=1.834; % mass of the connrod
MTR= 1.3542; % Translating mass

% Basic engine parameters
%%%%%%%%%%%%%%%%%%%%%%%%%%%%%%%%%%%%%%%%%%%%%%%%%%%%%%%%%%%%%%%%%%%%%%%%
omg=pi*REV/30.0;
omg2=omg^2;
crad=pi/180;
lamb=S/(2*LCR);
csi=0; %???
fp=pi*D*D/4;
ki=MTR*S/(2*fp);
kfr=fp*S/2;
kii=csi*mbl*S/(2*fp); % ???
KARM=160; % number of harmonic components (analysis)
KARMS=24; % number of harmonic components (reconstruction)

% Tangential gas pressure
for n=1:720
    teta=(n-1)*pi/180;
    beta = asin(lamb*sin(teta));
    trig(n)=sin(teta+beta)/cos(beta);
    pt(n)=(pres(n)-0.1)*trig(n); % pt(n) tang. gas pres. from measured speed
end
```

```
% Harmonic analysis
%%%%%%%%%%%%%%%%%%%%%%%%%%%%%%%%%%%%%%%%%%%%%%%%%%%%%%%%%%%%%%%%%%%%%%%%
ah0=0;
for n=1:720
    ah0=ah0+pt(n);
end
pt0=ah0/720;

for k=1:KARM
    ah=0; bh=0;
    av=0; bv=0;
    aw=0; bw=0;
    for n=1:720
        arg=k*(n-1)*crad/2;
        ah=ah+pt(n)*cos(arg); % harmonic components TGP
        bh=bh+pt(n)*sin(arg);
        av=av+speed(n)*cos(arg); % harmonic components speed (rpm)
        bv=bv+speed(n)*sin(arg);
        aw=aw+(pi*speed(n)*cos(arg))/30; % harmonic components angular speed
        bw=bw+(pi*speed(n)*sin(arg))/30;
    end
    ahp(k)=ah/360;
    bhp(k)=bh/360;
    av(k)=av/360;
    bv(k)=bv/360;
    aw(k)=aw/360;
    bw(k)=bw/360;
    chp(k)=sqrt(ahp(k)^2+bhp(k)^2);
    fprintf('k %3.1f Ak= %8.5e Bk= %8.5e\n', k, av(k), bv(k));
end

% curve reconstruction from armonic components
%%%%%%%%%%%%%%%%%%%%%%%%%%%%%%%%%%%%%%%%%%%%%%%%%%%%%%%%%%%%%%%%%%%%%%%%
for n=1:721
    arg=(n-1)*crad;
    ptg=0; recspeed=0; alfa=0; crank=0;
    for k=1:KARM
        ptg=ptg+ahp(k)*cos(k*arg/2)+bhp(k)*sin(k*arg/2); % TGP
        recspeed=recspeed+av(k)*cos(k*arg/2)+bv(k)*sin(k*arg/2); % speed
        (rpm)
        alfa=alfa-2*bw(k)*cos(k*arg/2)/k+2*aw(k)*sin(k*arg/2)/k; % deflection
        %crankacc=crank+
    end
    ptang(n)=ptg+pt0; % TGP including mean value (from Harmonic analys)
    rspeed(n)=recspeed+REV; % speed (rpm)
    ralfa(n)=alfa; % Deflection (radians)
end
% Cylinder presure reconstruction
%%%%%%%%%%%%%%%%%%%%%%%%%%%%%%%%%%%%%%%%%%%%%%%%%%%%%%%%%%%%%%%%%%%%%%%%
for n=2:719
    if abs(trig(n))<2e-2
        prescyl(n)=(pt(n+1)-pt(n-1))/(trig(n+1)-trig(n-1)); % cylinder pressure
        from PTG
        recop(n)=(ptang(n+1)-ptang(n-1))/(trig(n+1)-trig(n-1)); % cylinder
        pressure from Harmonic Analysis.
    end
end
```



```
else prescyl(n)=pt(n)/trig(n); recop(n)=ptang(n)/trig(n);
end
end

%%%%%%%%%%%%%%%%%%%%%%%%%%%%%%%%%%%%%%%%%%%%%%%%%%%%%%%%%%%%%%%%%%%%%%%%
% Transfer Matrices Calculation, Single cylinder engine
%%%%%%%%%%%%%%%%%%%%%%%%%%%%%%%%%%%%%%%%%%%%%%%%%%%%%%%%%%%%%%%%%%%%%%%%

JCYL= 1; % Number of masse in front of cylinder #1
%Dynamic system
%%%%%%%%%%%%%%%%%%%%%%%%%%%%%%%%%%%%%%%%%%%%%%%%%%%%%%%%%%%%%%%%%%%%%%%%
%Ctors=[0 1.608747e5 0 1.3023596e5]; %Stiffness
Ctors=[0 1.608e9 0 2.6e9];
Jp=[0.021185 0 0.07955 0 0.170]; % mass moments of inertia
fr= [0 0 0.02 0 0.01]; % Absolute dampings
ff=[0 12 0 12]; % Relative dampings
Jtot= Jp(1)+Jp(2)+Jp(3)+Jp(4)+Jp(5);

% TANGENTIAL INERTIA PRESSURES
%%%%%%%%%%%%%%%%%%%%%%%%%%%%%%%%%%%%%%%%%%%%%%%%%%%%%%%%%%%%%%%%%%%%%%%%
bi=zeros(KARM);
bi(2)=ki*omg2*(lamb*lamb/4)*lamb/4;
bi(4)=-omg2*ki*(1+(lamb^4)/16)/2;
bi(6)=-ki*omg2*(1+3*lamb*lamb/8)*3*lamb/4;
bi(8)=-omg2*ki*(1+lamb*lamb/2)*lamb*lamb/4;
bi(10)=ki*5*(lamb^3)/32;
bi(12)=3*omg2*ki*(lamb^4)/32;
a0p=0;

% HARMONIC COMPONENTS OF THE CYLINDER TORQUE
%%%%%%%%%%%%%%%%%%%%%%%%%%%%%%%%%%%%%%%%%%%%%%%%%%%%%%%%%%%%%%%%%%%%%%%%
for k=1:KARM

    am(k)=kfr*(ahp(k)*1e5);
    bm(k)=kfr*((bhp(k)*1e5+bi(k)));

end

% Torque VARIATION OVER THE ENGINE CYCLE
%%%%%%%%%%%%%%%%%%%%%%%%%%%%%%%%%%%%%%%%%%%%%%%%%%%%%%%%%%%%%%%%%%%%%%%%
p0=kfr*a0p;
for n=1:720
    arg=(n-1)*pi/180;
    savept=p0;
    savep=0;
    for k=1:KARM
        savept=savept+am(k)*cos(k*arg/2)+bm(k)*sin(k*arg/2); % includes mean
component
        savep=savep+ahp(k)*cos(k*arg/2)+bhp(k)*sin(k*arg/2); % only harmonic
components
    end
    presnew(n)=savept; % Cylinder torque, including mean component
    pcylnew(n)=savep*kfr*1e5; % Gas pressure torque without mean component
end
% presnew(n) Cylinder torque from harmonic analysis of the measured presure +
inertia component
% pcylnew(n) Gas pressure cylinder torque
```

```
% Building the transfer matrices
%%%%%%%%%%%%%%%%%%%%%%%%%%%%%%%%%%%%%%%%%%%%%%%%%%%%%%%%%%%%%%%%%%%%%%%%

for k=1:KARMS;
mp1=zeros(5,5); mp2=zeros(5,5); mp3=zeros(5,5); mp4=zeros(5,5);
mp5=zeros(5,5); ha=zeros(4); hb=zeros(4);
for m=1:5
    for n=1:5
        if m==n
            mp1(n,m)=1; mp2(n,m)=1; mp3(n,m)=1; mp4(n,m)=1; mp5(n,m)=1;
        else
            mp1(n,m)=0; mp2(n,m)=0; mp3(n,m)=0; mp4(n,m)=0; mp5(n,m)=0;
        end
    end
end
end

    mp1(2,1)=-Jp(1)*((k/2)*omg)^2; mp1(2,3)=-fr(1)*((k/2)*omg); mp1(4,1)=-
mp1(2,3); mp1(4,3)=mp1(2,1);
    mp3(2,1)=-Jp(3)*((k/2)*omg)^2; mp3(2,3)=-fr(3)*((k/2)*omg); mp3(4,1)=-
mp3(2,3); mp3(4,3)=mp3(2,1); mp3(2,5)=-am(k); mp3(4,5)=bm(k);
    mp5(2,1)=-Jp(5)*((k/2)*omg)^2; mp5(2,3)=-fr(5)*((k/2)*omg); mp5(4,1)=-
mp5(2,3); mp5(4,3)=mp5(2,1);
    mod2=Ctors(2)^2+(ff(2)*(k/2)*omg)^2; mod4=Ctors(4)^2+(ff(4)*(k/2)*omg)^2;
    mp2(1,2)=Ctors(2)/mod2; mp2(1,4)=ff(2)*(k/2)*omg/mod2; mp2(3,2)=-
mp2(1,4); mp2(3,4)=mp2(1,2);
    mp4(1,2)=Ctors(4)/mod4; mp4(1,4)=ff(4)*(k/2)*omg/mod4; mp4(3,2)=-
mp4(1,4); mp4(3,4)=mp4(1,2);
% DIRECT CALCULATION
    mh=mp5*mp4*mp3*mp2*mp1;
% Deflection first mass
numi=mh(2,1)*mh(4,3)-mh(4,1)*mh(2,3);
t1r(k)=(-mh(2,5)*mh(4,3)+mh(4,5)*mh(2,3))/numi;
t1i(k)=(-mh(2,1)*mh(4,5)+mh(4,1)*mh(2,5))/numi;
% t1r(k)=aw(k);
% t1i(k)=bw(k);
%Deflection flywheel
tnr(k)=t1r(k)*mh(1,1)+t1i(k)*mh(1,3)+mh(1,5);
tni(k)=t1r(k)*mh(3,1)+t1i(k)*mh(3,3)+mh(3,5);
tnc(k)=sqrt(tnr(k)^2+tni(k)^2);

% Reverse Calculation
%%%%%%%%%%%%%%%%%%%%%%%%%%%%%%%%%%%%%%%%%%%%%%%%%%%%%%%%%%%%%%%%%%%%%%%%

% determine terms for reverse calculation
% Harmonic components of deflection at mass #1 from measured speed
reall(k)=(aw(k)/mh(1,3)-bw(k)/mh(3,3)+mh(1,5)/mh(1,3)-
mh(3,5)/mh(3,3))/(mh(1,1)/mh(1,3)-mh(3,1)/mh(3,3));
imag1(k)=(aw(k)/mh(1,1)-bw(k)/mh(3,1)+mh(1,5)/mh(1,1)-
mh(3,5)/mh(3,1))/(mh(1,3)/mh(1,1)-mh(3,3)/mh(3,1));

    ha(1)=-mp4(1,2); hb(1)=-mp4(1,4);
    ha(2)=-1+(Jp(5)*Ctors(4)-fr(5)*ff(4))*((k/2)*omg)^2/mod4;
hb(2)=(k/2)*omg*(Jp(5)*ff(4)*((k/2)*omg)^2+fr(5)*Ctors(4))/mod4;
    ha(3)=-hb(1); hb(3)=ha(1);
    ha(4)=-hb(2); hb(4)=ha(2);
```

```
% torque harmonic components
numit=ha(2)*hb(4)-ha(4)*hb(2);
Tre(k)=(mh(4,1)*t1r(k)+mh(4,3)*t1i(k))*hb(2)-
(mh(2,1)*t1r(k)+mh(2,3)*t1i(k))*hb(4)/numit;
Tim(k)=(mh(2,1)*t1r(k)+mh(2,3)*t1i(k))*ha(4)-
(mh(4,1)*t1r(k)+mh(4,3)*t1i(k))*ha(2)/numit;
Timp(k)=Tim(k)+kfr*bi(k);
% reverse calculation (torque harmonic components from measured speed)
Tqre(k)=(mh(4,1)*reall(k)+mh(4,3)*imag1(k))*hb(2)-
(mh(2,1)*reall(k)+mh(2,3)*imag1(k))*hb(4)/numit;
Tqim(k)=(mh(2,1)*reall(k)+mh(2,3)*imag1(k))*ha(4)-
(mh(4,1)*reall(k)+mh(4,3)*imag1(k))*ha(2)/numit;
Tqimp(k)=Tqim(k)+kfr*bi(k);

% Solution of the system of four equations
%%%%%%%%%%%%%%%%%%%%%%%%%%%%%%%%%%%%%%%%%%%%%%%%%%%%%%%%%%%%%%%%%%%%%%%%
Delh=[mh(1,1) mh(1,3); mh(2,1) mh(2,3); mh(3,1) mh(3,3); mh(4,1) mh(4,3)];
Delha=[ha(1) ha(2) ha(3) ha(4)]; Delhat=Delha';
Delhb=[hb(1) hb(2) hb(3) hb(4)]; Delhbt=Delhb';
tlib=[tnr(k) 0 tni(k) 0]; tlibt=tlib'; % from simulated speed
libt=[aw(k) 0 bw(k) 0]; libtt=libt'; % from measured speed
Delt=[Delh Delhat Delhbt];
numi4=det(Delt);
Deltre=[Delh tlibt Delhbt]; % from simulated speed
Deltim=[Delh Delhat tlibt]; % from simulated speed
Difre=[Delh libtt Delhbt]; % from measured speed
Difrim=[Delh Delhat libtt]; % from measured speed
end
% results:  teta=deflection, tv=speed, tetan=deflection flywheel,
% tvn = speed flywheel
for n=1:720
    arg=(n-1)*crad;
    teta=0; tv=0; tetan=0; tvn=0; tacn=0; torq=0;
for k=1:KARMS
    % From simulated speed
    teta=teta+t1r(k)*cos(k*arg/2)-t1i(k)*sin(k*arg/2);
    tv=tv+(-t1r(k)*sin(k*arg/2)-t1i(k)*cos(k*arg/2))*(k/2);
    tetan=tetan+tnr(k)*cos(k*arg/2)-tni(k)*sin(k*arg/2);
    tvn=tvn+(-tnr(k)*sin(k*arg/2)-tni(k)*cos(k*arg/2))*(k/2);
    tacn=tacn+(-tnr(k)*cos(k*arg/2)+(tni(k))*sin(k*arg/2))*(k/2)^2;
    torq=torq+Tre(k)*cos(k*arg/2)-Tim(k)*sin(k*arg/2);
    % From measured speed
    momt=torq+Tqre(k)*cos(k*arg/2)-Tqim(k)*sin(k*arg/2);
    tetam=teta+reall(k)*cos(k*arg/2)-imag1(k)*sin(k*arg/2);
    accn=tacn+(-reall(k)*cos(k*arg/2)+imag1(k)*sin(k*arg/2))*(k/2)^2;
end
theta(n)=teta; % deflection mass #1, direct calculation
omega(n)=(1+tv)*REV*pi/30; % speed mass #1, direct calculation
thetan(n)=tetan; % deflection flywheel, direct calculation
omegan(n)=(1+tvn)*REV*pi/30; % speed flywheel, direct calculation
acceln(n)=Jtot*tacn*(REV*pi/30)^2; % acceln(n)=tacn*(REV*pi/30)^2; %
acceleration flywheel, direct calculation
maccel(n)=Jtot*accn*(REV*pi/30)^2; % From measured speed
torque(n)=torq; % engine torque from simulated speed (reverse calculation)
mtorq(n)=momt; % engine torque from measured speed
```

```
end

% Harmonic components of the reconstructed torque
%%%%%%%%%%%%%%%%%%%%%%%%%%%%%%%%%%%%%%%%%%%%%%%%%%%%%%%%%%%%%%%%%%%%%%%%
for k=1:KARMS
    % from simulated speed
    ap(k)=(Tre(k)*1e-5)/kfr;
    bp(k)=- (Tim(k)/kfr+bi(k))*1e-5;
    % from measured speed
    apm(k)=(Tqre(k)*1e-5)/kfr;
    bpm(k)=(Tqim(k)/kfr+bi(k))*1e-5;
end
% curve reconstruction
for n=1:721
    arg=(n-1)*crad;
    ptg=0;
    for k=1:KARMS
        ptg=ptg+ap(k)*cos(k*arg/2)+bp(k)*sin(k*arg/2);
        ptgm=ptg+apm(k)*cos(k*arg/2)+bpm(k)*sin(k*arg/2);
    end
    pptang(n)=ptg+pt0; % tangential gas pressure from simulated speed
    (reverse calculation)
    mptang(n)=ptgm+pt0; % TGP from measured speed
end
for n=2:719
    dpt(n)=(pptang(n+1)-pptang(n-1))/2; % differential of tangential gas
    pressure (from simulated speed)
    dspeed(n)=(acceln(n+1)-acceln(n-1))/2; % differential of acceleration
    times the total mass moment of inertia (from simulated speed)
    dprec(n)=(torque(n+1)-torque(n-1))/2; % differential of torque (from
    simulated speed)
    difpt(n)=(mptang(n+1)-mptang(n-1))/2;
    difacc(n)=(maccel(n+1)-maccel(n-1))/2;
    diftrq(n)=(mtorq(n+1)-mtorq(n-1))/2;
end
% Cylinder pressure reconstruction
for n=2:719
    if abs(trig(n))<2e-2
        reccop(n)=(pptang(n+1)-pptang(n-1))/(trig(n+1)-trig(n-1));% reccop(n)
    cylinder pressure from measured speed (reverse calculation)
        repcyl(n)=(mptang(n+1)-mptang(n-1))/(trig(n+1)-trig(n-1));
    else reccop(n)=pptang(n)/trig(n); repcyl(n)=mptang(n)/trig(n);
end

end

% pt=Tangential pressure calculated from presure trace,
% ptang= reconstruction from harmonic components
figure(1) % Tangential gas pressure from measured pres (red), from harmonic
analysis (blue), from reconstruction (cyan)
n=1:720;
plot(n-1, ptang(n), 'r', n-1, pt(n), 'b', n-1, mptang(n), 'c'), grid;
xlabel('Crank Angle - degrees'), ylabel('bar'), title('Tangential gas
pressure; blue-from pressure trace, red-from harmonic analysis, cyan-from
measured speed');
```

```
figure(2) % Measured cylinder pressure, cylinder pressure from tangential gas
presure
% pres= imported pressure trace,
% prescyl=pressure trace reconstructed from tangential pressure
n=2:719;
plot(n-1, pres(n), 'b', n-1, prescyl(n)+0.1, 'r'), grid; xlabel('Crank Angle
- degrees'), ylabel('bar'), title('Cylinder pressure; blue measured, red
harmonic analysis');
% prescyl=pressure trace reconstructed from tangential pressure
% recop=pressure trace reconstructed from harmonic omponents of tangential
pressure
% reccop(n) cylinder pressure from measured speed (reverse calculation)
figure(3) % measured cylinder pressure, from harmonic analysis of PTG, from
reconstructed PTG
n=2:719;
plot(n-1, pres(n), 'b', n-1, (repcyl(n)+0.1), 'r', n-1, reccop(n), 'c'),
grid; xlabel('Crank Angle - degrees'), ylabel('bar'), title('Cylinder
pressure; blue measured, red from harmonic analysis, cyan from measured
speed');
% omega = speed at the front of crankshaft
figure(4) % Speed at mass #1, direct calculation
n=1:720;
plot(n-1, 30*omega(n)/pi, 'r'), grid; xlabel('Crank Angle - degrees'),
ylabel('RPM'), title('Speed mass #1');
% presnew= Torque including inertia
figure(5) % Engine torque (reverse calculation), engine torque torque
n=1:720;
plot(n-1, mptang(n)*kfr*1e5, 'b', n-1, mtorq(n), 'r'), grid; xlabel('Crank
Angle - degrees'), ylabel('Nm'), title('Engine torque (including inertia
torque)- red, Gas pressure Torque - blue');
% omegan= speed at flywheel
figure(6) % speed at the flywheel (direct calculation), measured flywheel
speed
n=1:720;
plot(n-1, 30*omegan(n)/pi, 'r', n-1, rspeed(n), 'b' ), grid; xlabel('Crank
Angle - degrees'), ylabel('RPM'), title('Speed at flywheel');
% acceln= acceleration at flywheel
figure(7)
n=1:720;
plot(n-1, maccel(n)+10, 'r', n-1, mtorq(n), 'b'), grid; xlabel('Crank Angle -
degrees'), ylabel('Nm'), title('Engine torque -blue; Acceleration at
flyweeey multipliyed with total mass moment of inertia - red');
% dpt= differential of tangential pressure
% dspeed= product of flywheel mass moment of inertia and differential of itrs
acceleration
figure(8)
n=2:719;
plot(n-1, difacc(n), 'r', n-1, diftrq(n), 'c'), grid; xlabel('Crank Angle -
degrees'), ylabel('Nm/CA degree'), title('Differential of product Accel. X
Jtotal - red, differential of engine torque from measured speed - cyan');
figure(9)
n=2:719;
plot(n-1, 180*difpt(n)/pi, 'r'), grid, xlabel('Crank Angle - degrees'),
ylabel('bar'), title('Tangential Gas Pressure');
figure(10)
n=1:720;
plot(n-1, thetan(n), 'r', n-1, ralfa(n), 'b'), grid;
```

Ignition delay estimation from crankshaft speed (Matlab code)

```
% Harmonic analysis of measured pressure curves
% import pressure data
% pres= imported data
% Calculation of the tangential gas pressure
%Motoring pressure
for n=1:360
%pres(n)=Motoring_Mercedes(n);
pres(n)=Pres_1500_motoring(n); % from D\Dynamics
%pres(n+361)=Motoring_Mercedes(361-n); % from D\recopres
pres(n+361)=Pres_1500_motoring(361-n); % from D\Dynamics
end
%pres(361)=Motoring_Mercedes(361);
pres(361)=Pres_1500_motoring(361);
%Cycle pressure
for n=1:720
    %press(n)=presss_mercedes1(n); % from D\recopres
    press(n)=Pres_1500_4Nm(n); % from D\Dynamics
    pcomb(n)=press(n)-pres(n);
end
KARM=40;
kfr=pi*(80^2)*0.041/4;
lambda=41/135;
% Tangential gas pressures
for n=1:720
    teta=(n-1)*pi/180;
    beta = asin(lambda*sin(teta));
    trig(n)=sin(teta+beta)/cos(beta);
    pt(n)=(pres(n)-0.1)*trig(n); % Tangential pressure motoring curve
    ptcomb(n)=trig(n)*pcomb(n); % tangential pressure combustion curve
    prestang(n)= trig(n)*(press(n)-0.1); % tangential pressure cylinder
    pressure totque
end

crad=pi/180;
% Harmonic analysis
ah0=0; ahc0=0; ap=0;
for n=1:720
    ah0=ah0+pt(n);
    ahc0=ahc0+ptcomb(n);
    ap=ap+prestang(n);
end
pt0=ah0/720;
ptc0=ahc0/720;
p0=ap/720;
for k=1:KARM
    ah(k)=0; bh(k)=0;
    ahc(k)=0; bhc(k)=0;
    aht(k)=0; bht(k)=0;
    for n=1:720
        arg=k*(n-1)*crad/2;
        ah(k)=ah(k)+pt(n)*cos(arg); % Harmonic coefficients motoring curve
        bh(k)=bh(k)+pt(n)*sin(arg);
        ahc(k)=ahc(k)+ptcomb(n)*cos(arg); % harmonic coefficients combustion
    end
end
curve
```

```
bhc(k)=bhc(k)+ptcomb(n)*sin(arg);
aht(k)=aht(k)+prestang(n)*cos(arg); %harmonic coefficients engine
torque
    bht(k)=bht(k)+prestang(n)*sin(arg);
end
ahp(k)=ah(k)/360; % Harmonic coefficients motoring curve
bhp(k)=bh(k)/360;
chp(k)=sqrt(ahp(k)^2+bhp(k)^2);
ahpc(k)=ahc(k)/360; % harmonic coefficients combustion curve
bhpc(k)=bhc(k)/360;
chpc(k)=sqrt(ahpc(k)^2+bhpc(k)^2);
asum(k)=ahp(k)+ahpc(k); % harmonic coefficients engine torque
motoring+combustion
    bsum(k)=bhp(k)+bhpc(k);
    att(k)=aht(k)/360; % harmonic coefficients engine torque from harmonic
analysis
    btt(k)=bht(k)/360;
    fprintf('k %3.1f Ak= %8.5e Bk= %8.5e\n', k, ahp(k), bhp(k));
end
% curve reconstruction
for n=1:720
    arg=(n-1)*crad;
    ptg=0; ptgc=0;
    for k=1:KARM
        ptg=ptg+ahp(k)*cos(k*arg/2)+bhp(k)*sin(k*arg/2); % tangential
pressure from measured motoring data
        ptgc=ptgc+ahpc(k)*cos(k*arg/2)+bhpc(k)*sin(k*arg/2); %tangential
motoring pressure from harmonic analysis
    end
    ptang(n)=ptg+pt0; % PTG from motoring pressure trace (harmonic analysis)
    ptangc(n)=ptgc+ptc0; % PTG from combustion pressure trace (harmonic
analysis)
end

for n=1:720
    arg=(n-1)*crad;
    save=0; saves=0;
    for k=1:KARM
        save=save+att(k)*cos(k*arg/2)+btt(k)*sin(k*arg/2); % Tangential
pressure form harmonic anlysi of measured data
        saves=saves+asum(k)*cos(k*arg/2)+bsum(k)*sin(k*arg/2); % tangential
pressure from sumation of harmonic coefficients motoring +combustion
    end
    prest(n)=save+p0;
    pressum(n)=saves+pt0+ptc0;
end

for k=1:KARM;
% x(k)=-5.0*exp(-0.17*k);
x(k)=-3.5*exp(-0.17*k);
if k/2 > fix(k/2)
    y(k)=x(k);
else y(k)=abs(x(k));
end
end
```

```
for n=1:720
    arg=(n-1)*crad;
    save=0; save0=0; savel=0;
    for k=1:KARM
        save=save+att(k)*cos(k*arg/2)+(btt(k)-y(k))*sin(k*arg/2);
        save0=save0+y(k)*sin(k*arg/2);
        savel=savel+bhp(k)*sin(k*arg/2);
    end
    prestc(n)=save+pt0+ptc0;    % presumed PTG of the combustion trace
    presmot(n)=save0+pt0+ptc0;
    presmot1(n)=savel+pt0+ptc0;
end

corr=presmot(361); corrl=ptangc(361); corr2=prestc(361); corr3=presmot1(361);
for n=1:720;
    presmot(n)=presmot(n)-corr;
    ptangc(n)=ptangc(n)-corrl;
    prestc(n)=prestc(n)-corr2;
    presmot1(n)=presmot1(n)-corr3;
end
for n=2:719
    if abs(trig(n))<2e-3
        prescyl(n)=(pt(n+1)-pt(n-1))/(trig(n+1)-trig(n-1)); %Reconstructed
        cylinder pressure from measument data
        recop(n)=(ptang(n+1)-ptang(n-1))/(trig(n+1)-trig(n-1)); %reconstructed
        cylinder pressure from harmonic components
        pcomb1(n)=(ptcomb(n+1)-ptcomb(n-1))/(trig(n+1)-trig(n-1)); %Reconstructed
        combustion pressure from measurment data
        repcomb(n)=(ptangc(n+1)-ptangc(n-1))/(trig(n+1)-trig(n-1));
        %Reconstructed combustion pressure from harmonic components
        represt(n)=(prestc(n+1)-prestc(n-1))/(trig(n+1)-trig(n-1)); %
        reconstruction of the presumed combustion pressure trace
        repremot(n)=(presmot(n+1)-presmot(n-1))/(trig(n+1)-trig(n-1));
        %reconstruction of the motoring pressure from model harmonic components
        repremot1(n)=(presmot1(n+1)-presmot1(n-1))/(trig(n+1)-trig(n-1));
        %reconstruction of the motoring pressure from harmonic components
    else prescyl(n)=pt(n)/trig(n); recop(n)=ptang(n)/trig(n);
        pcomb1(n)=ptcomb(n)/trig(n); repcomb(n)=ptangc(n)/trig(n);
        represt(n)=prestc(n)/trig(n); repremot(n)=presmot(n)/trig(n);
        repremot1(n)=presmot1(n)/trig(n);
    end
end
end

figure(1)
n=1:720;
plot(n, ptang(n), 'r', n, pt(n), 'b', n, ptcomb(n), 'c', n, ptangc(n), 'm'),
grid;
figure(2)
n=1:720;
plot(n, kfr*pt(n), 'r'), grid;
figure(3)
k=1:KARM;
plot(k, att(k), 'r', k, btt(k), 'b' , k, ahpc(k), 'black', k, bhpc(k),
'c'),grid;
figure(4)
n=2:719;
```



```
plot(n, pres(n), 'r', n, prescyl(n)+0.1, 'b'), grid;
figure(5)
n=2:719;
plot(n, prescyl(n)+0.1, 'r', n, recop(n)+0.1, 'b'), grid
figure(6)
n=1:720;
plot(n, pres(n), 'r', n, press(n), 'b', n, pcomb(n), 'c'), grid;
figure(7)
n=2:719;
plot(n, pcomb(n)+prescyl(n), 'r', n, press(n), 'b'), grid;
figure(8)
n=300:400;
plot(n, pcomb(n), 'r', n, pcomb1(n), 'b', n, repcomb(n), 'c', n, represt(n),
'black'), grid;
figure(9)
n=2:719;
plot(n, prest(n), 'r', n, pressum(n), 'c', n, prestang(n), 'b'), grid;
figure(10)
n=2:719;
plot(n, pres(n), 'r', n, repremot1(n), 'c', n, repremot(n), 'b'), grid;
figure(11)
k=1:KARM;
plot(k, abs(bhp(k)), 'b', k, bhp(k), 'r', k, y(k), 'black'), grid;
```

Fuel identification on a single-cylinder engine using Artificial Neural Networks (Matlab code)

```
%Sample interval (CAD):

w=340;
v=380;

iptsetpref('ImshowBorder','tight');
set(0,'DefaultFigureMenu','none');
format compact;

% -----
% Fuel identification test for 300 cycles
% -----

s=size(Test(:,1));
no_of_testing_cycles=s(1)/720;
no_of_testing_points=s(1);
pr=(Test(:,1))';
sp=(Test(:,2))';

for i=1:no_of_testing_cycles
    e(2*i-1,:)=pr((i*720-719):(i*720));
    e(2*i,:)=sp((i*720-719):(i*720));
end
Test1=e';

%-----
error=0;

for j=1:no_of_testing_cycles
%j=51;

%Test Pressure
i=(w+1):v;
testpress=Test1(i,2*j-1);
s=size(testpress);
samplesize=s(1);

%-----
%Testspeed
i=(w+1):v;
testspeed1=Test1(i,2*j);
testspeed=Test1(i,2*j);
s=size(testspeed);
samplesize=s(1);

%Test Speed
%figure(7)
%i=1:samplesize;
```

```
%plot(i+w,testspeed(i),'b','linewidth',2), grid, xlabel('Crank Angle -  
Degrees'), ylabel('bar'),  
%title ('Test data: engine speed');
```

```
%-----
```

```
% Network TESTING for a new input (speed):
```

```
B = testpress';  
C = testspeed';  
[b,bs] = mapminmax(B);  
[c,cs] = mapminmax(C);
```

```
a = sim(net,c);
```

```
pressure = mapminmax('reverse',a,bs);
```

```
s=size(pressure);  
samplesize=s(2);
```

```
for i=1:(samplesize-1) pressure(i)=(pressure(i)+pressure(i+1))/2;  
end;
```

```
%Derivative of measured pressure vs derivative of simulated pressure:
```

```
%figure(j)
```

```
pause(0.06);
```

```
i=1:samplesize;  
testnumber(j)=j;  
maxpressure(j)=max(pressure);  
maxpressuremeasured(j)=max(B);
```

```
%Maximize the window and the graphs inside to full-screen  
%set(gcf,'units','normalized','position',[0 0 1 1]);  
%set(gca,'units','normalized','position',[0 0 1 1]);
```

```
%Maximize the window as desired  
set(gcf,'units','normalized','position',[0.003 0.14 0.962 0.823]);  
set(gcf,'DefaultAxesFontSize',12);  
%set(gcf,'DefaultAxesFontWeight','bold');  
%set(gcf,'DefaultTextFontSize',8);
```

```
%subplot(2,3,[1 4])  
subplot('position',[.06 .1 .25 .82]);  
plot(i+w, testspeed1(i),'b', 'linewidth',3), grid,  
xlabel('Crank Angle - Degrees'), ylabel('rpm'),  
xlim([w v]), ylim([1340 1400]),  
text(w+.46*(v-w),1342.5,'INPUT ', 'color',[0.6392 0.6392  
0.6392], 'FontSize',40),  
title('Measured engine speed','FontSize',16,'FontWeight','bold');
```

```
%subplot(2,3,2)
```

```
subplot('position',[.38 .4 .25 .52])

%%%%%%%%plot(i+w, pressure(i), 'b', i+w, B(i), 'r', i+w, i+w+30-
(i+w), 'color', [0.4353 0.4353 1], i+w, i+w+80-(i+w), 'color', [0 0 0.5922], i+w,
i+w+200-(i+w), 'color', [1 0.5098 0.5098], i+w, i+w+325-(i+w), 'color', [0.702 0
0], 'linewidth', 3), grid,
%%%%%%%%plot(i+w, pressure(i), 'b', i+w, B(i), 'r', i+w, i+w+30-
(i+w), 'b', 'linewidth', 3), grid,
%%%%%%%%%UISETCOLOR

plot(i+w, pressure(i), 'b', i+w, i+w+44-(i+w), 'b', i+w, i+w+49-(i+w), 'b', i+w,
i+w+54-(i+w), 'b', 'linewidth', 3)
grid, xlabel('Crank Angle - Degrees'), ylabel('bar'),
xlim([w v]), ylim([25 62]),
text(w+.02*(v-w), 41.6, 'S8', 'color', [0 .7 0], 'FontSize', 30),
text(w+.02*(v-w), 46.6, 'JP8', 'color', [0.7804 0.5412 0.0471], 'FontSize', 30),
text(w+.02*(v-w), 51.7, 'ULSD', 'color', [0.9490 0 0.9490], 'FontSize', 30),
text(w+.02*(v-w), 56.6, 'B100', 'color', [0.6157 0 0], 'FontSize', 30),
text(w+.263*(v-w), 27.4, 'OUTPUT', 'color', [0.6392 0.6392
0.6392], 'FontSize', 40),
title ('Simulated pressure', 'FontSize', 16, 'FontWeight', 'bold');

%subplot(2,3,3)
subplot('position',[.71 .4 .25 .52])

plot(i+w, B(i), 'r', i+w, i+w+45-(i+w), 'r', i+w, i+w+53-(i+w), 'r', i+w,
i+w+58-(i+w), 'r', 'linewidth', 3),
grid, xlabel('Crank Angle - Degrees'), ylabel('bar'),
xlim([w v]), ylim([25 62]),
text(w+.02*(v-w), 42.5, 'S8', 'color', [0 .7 0], 'FontSize', 30),
text(w+.02*(v-w), 47.5, 'JP8', 'color', [0.7804 0.5412 0.0471], 'FontSize', 30),
text(w+.02*(v-w), 55.4, 'ULSD', 'color', [0.9490 0 0.9490], 'FontSize', 30),
text(w+.02*(v-w), 60, 'B100', 'color', [0.6157 0 0], 'FontSize', 30),
text(w+.263*(v-w), 27.4, 'TARGET', 'color', [0.6392 0.6392
0.6392], 'FontSize', 40),
title ('Measured pressure', 'FontSize', 16, 'FontWeight', 'bold');

if maxpressure(j)<44

%subplot(2,3,5)
subplot('position',[.38 .1 .25 .2])
plot(i+w, pressure(i), 'b'), xlim([0 1]), ylim([0 1]),
text(.12, .7, 'Fuel used is', 'color', 'k', 'FontSize', 32),
text(.42, .28, 'S8', 'color', [0 .7 0], 'FontSize', 35);

if maxpressuremeasured(j)<45

%subplot(2,3,6)
subplot('position',[.71 .1 .25 .2])
plot(i+w, pressure(i), 'b'), xlim([0 1]), ylim([0 1]),
text(.33, .5, 'True', 'color', 'k', 'FontSize', 40);

else
```

```
%subplot(2,3,6)
subplot('position',[.71 .1 .25 .2])
plot(i+w, pressure(i),'b'), xlim([0 1]), ylim([0 1]),
text(.33,.5,'False','color','r','FontSize',40);

error=error+1;

        end;

        elseif maxpressure(j)>=44 & maxpressure(j)<49

%subplot(2,3,5)
subplot('position',[.38 .1 .25 .2])
plot(i+w, pressure(i),'b'), xlim([0 1]), ylim([0 1]),
text(.12,.7,'Fuel used is','color','k','FontSize',32),
text(.38,.28,'JP8','color',[0.7804    0.5412    0.0471],'FontSize',35);

        if maxpressuremeasured(j)>=45 & maxpressuremeasured(j)<53

%subplot(2,3,6)
subplot('position',[.71 .1 .25 .2])
plot(i+w, pressure(i),'b'), xlim([0 1]), ylim([0 1]),
text(.29,.5,'True','color','k','FontSize',50);

        else

%subplot(2,3,6)
subplot('position',[.71 .1 .25 .2])
plot(i+w, pressure(i),'b'), xlim([0 1]), ylim([0 1]),
text(.29,.5,'False','color','r','FontSize',50);

error=error+1;

        end;

        elseif maxpressure(j)>=49 & maxpressure(j)<54

%subplot(2,3,5)
subplot('position',[.38 .1 .25 .2])
plot(i+w, pressure(i),'b'), xlim([0 1]), ylim([0 1]),
text(.12,.7,'Fuel used is','color','k','FontSize',32),
text(.31,.28,'ULSD','color',[0.9490    0    0.9490],'FontSize',35);

        if maxpressuremeasured(j)>=53 & maxpressuremeasured(j)<58

%subplot(2,3,6)
subplot('position',[.71 .1 .25 .2])
plot(i+w, pressure(i),'b'), xlim([0 1]), ylim([0 1]),
text(.24,.5,'True','color','k','FontSize',60);

        else
```

```
%subplot(2,3,6)
subplot('position',[.71 .1 .25 .2])
plot(i+w, pressure(i), 'b'), xlim([0 1]), ylim([0 1]),
text(.24,.5, 'False', 'color', 'r', 'FontSize', 60);

error=error+1;

        end;

    else

%subplot(2,3,5)
subplot('position',[.38 .1 .25 .2])
plot(i+w, pressure(i), 'b'), xlim([0 1]), ylim([0 1]),
text(.12,.7, 'Fuel used is', 'color', 'k', 'FontSize', 32),
text(.03,.28, 'Biodiesel B100', 'color', [0.6157 0 0], 'FontSize', 32);

        if maxpressuremeasured(j)>=58

%subplot(2,3,6)
subplot('position',[.71 .1 .25 .2])
plot(i+w, pressure(i), 'b'), xlim([0 1]), ylim([0 1]),
text(.19,.5, 'True', 'color', 'k', 'FontSize', 70);

        else

%subplot(2,3,6)
subplot('position',[.71 .1 .25 .2])
plot(i+w, pressure(i), 'b'), xlim([0 1]), ylim([0 1]),
text(.19,.5, 'False', 'color', 'r', 'FontSize', 70);

error=error+1;

        end;
    end;
%pause(.05);
%close(j);
end;

wacc1 = 100*(1-(error/no_of_testing_cycles));
%fprintf('%3.0f percent accuracy in fuel identification for the first 200
cycles\n', wacc1);
%disp('-----
---');

%-----
%Accuracy test for 100 random cycles
%-----

k=100;

error=0;
```

```
for j=1:k
%j=1;

q1={1}
q = q1(randperm(length(q1)));
l = q{1}(1);

%Test Pressure
i=(w+1):v;
testpress=Test1(i,2*1-1);
s=size(testpress);
samplesize=s(1);

%-----

%Testspeed
i=(w+1):v;
testspeed2=Test1(i,2*1);
testspeed=Test1(i,2*1);
s=size(testspeed);
samplesize=s(1);

%Test Speed
%figure(7)
%i=1:samplesize;
%plot(i+w,testspeed(i),'b','linewidth',2), grid, xlabel('Crank Angle -
Degrees'), ylabel('bar'),
%title ('Test data: engine speed');

%-----
% Network TESTING for a new input (speed):

B = testpress';
C = testspeed';
[b,bs] = mapminmax(B);
[c,cs] = mapminmax(C);

a = sim(net,c);

pressure = mapminmax('reverse',a,bs);

s=size(pressure);
samplesize=s(2);

for i=1:(samplesize-1) pressure(i)=(pressure(i)+pressure(i+1))/2;
end;

%Derivative of measured pressure vs. derivative of simulated pressure :

%figure(j+200)

pause(0.06);
```

```
i=1:samplesize;
testnumber(j)=j;
maxpressure1(j)=max(pressure);
maxpressuremeasured1(j)=max(B);

%Maximize the window and the graphs inside to full-screen
%set(gcf,'units','normalized','position',[0 0 1 1]);
%set(gca,'units','normalized','position',[0 0 1 1]);

%Maximize the window as desired
set(gcf,'units','normalized','position',[0.003 0.14 0.962 0.823]);
set(gcf,'DefaultAxesFontSize',12);
%set(gcf,'DefaultAxesFontWeight','bold');
%set(gcf,'DefaultTextFontSize',8);

%subplot(2,3,[1 4])
subplot('position',[.06 .1 .25 .82]);
plot(i+w, testspeed2(i),'b','linewidth',3), grid,
xlabel('Crank Angle - Degrees'), ylabel('rpm'),
xlim([w v]), ylim([1340 1400]),
text(w+.46*(v-w),1342.5,'INPUT ','color',[0.6392 0.6392
0.6392],'FontSize',40),
title('Measured engine speed','FontSize',16,'FontWeight','bold');

%subplot(2,3,2)
subplot('position',[.38 .4 .25 .52])

%%%%%%%%%plot(i+w, pressure(i),'b', i+w, B(i),'r',i+w, i+w+30-
(i+w),'color',[0.4353 0.4353 1],i+w, i+w+80-(i+w),'color',[0 0 0.5922],i+w,
i+w+200-(i+w),'color',[1 0.5098 0.5098],i+w, i+w+325-(i+w),'color',[0.702 0
0],'linewidth',3), grid,
%%%%%%%%%plot(i+w,pressure(i),'b', i+w,B(i),'r', %i+w,i+w+30-
(i+w),'b','linewidth',3), grid,
%%%%%%%%%UISETCOLOR

plot(i+w, pressure(i),'b',i+w, i+w+44-(i+w),'b',i+w, i+w+49-(i+w),'b', i+w,
i+w+54-(i+w),'b','linewidth',3)
grid, xlabel('Crank Angle - Degrees'), ylabel('bar'),
xlim([w v]), ylim([25 62]),
text(w+.02*(v-w),41.6,'S8','color',[0 .7 0],'FontSize',30),
text(w+.02*(v-w),46.6,'JP8','color',[0.7804 0.5412
0.0471],'FontSize',30),
text(w+.02*(v-w),51.7,'ULSD','color',[0.9490 0
0.9490],'FontSize',30),
text(w+.02*(v-w),56.6,'B100','color',[0.6157 0 0],'FontSize',30),
text(w+.263*(v-w),27.4,'OUTPUT','color',[0.6392 0.6392
0.6392],'FontSize',40),
title ('Simulated pressure','FontSize',16,'FontWeight','bold');

%subplot(2,3,3)
subplot('position',[.71 .4 .25 .52])
```



```
plot(i+w, B(i), 'r', i+w, i+w+45-(i+w), 'r', i+w, i+w+53-(i+w), 'r', i+w,
i+w+58-(i+w), 'r', 'linewidth', 3),
grid, xlabel('Crank Angle - Degrees'), ylabel('bar'),
xlim([w v]), ylim([25 62]),
text(w+.02*(v-w), 42.5, 'S8', 'color', [0 .7 0], 'FontSize', 30),
text(w+.02*(v-w), 47.5, 'JP8', 'color', [0.7804 0.5412
0.0471], 'FontSize', 30),
text(w+.02*(v-w), 55.4, 'ULSD', 'color', [0.9490 0
0.9490], 'FontSize', 30),
text(w+.02*(v-w), 60, 'B100', 'color', [0.6157 0 0], 'FontSize', 30),
text(w+.263*(v-w), 27.4, 'TARGET', 'color', [0.6392 0.6392
0.6392], 'FontSize', 40),
title ('Measured pressure', 'FontSize', 16, 'FontWeight', 'bold');
```

```
if maxpressure1(j)<44
```

```
%subplot(2,3,5)
subplot('position', [.38 .1 .25 .2])
plot(i+w, pressure(i), 'b'), xlim([0 1]), ylim([0 1]),
text(.12, .7, 'Fuel used is', 'color', 'k', 'FontSize', 32),
text(.42, .28, 'S8', 'color', [0 .7 0], 'FontSize', 35);
```

```
if maxpressuremeasured1(j)<45
```

```
%subplot(2,3,6)
subplot('position', [.71 .1 .25 .2])
plot(i+w, pressure(i), 'b'), xlim([0 1]), ylim([0 1]),
text(.33, .5, 'True', 'color', 'k', 'FontSize', 40);
```

```
else
```

```
%subplot(2,3,6)
subplot('position', [.71 .1 .25 .2])
plot(i+w, pressure(i), 'b'), xlim([0 1]), ylim([0 1]),
text(.33, .5, 'False', 'color', 'r', 'FontSize', 40);
```

```
error=error+1;
```

```
end;
```

```
elseif maxpressure1(j)>=44 & maxpressure1(j)<49
```

```
%subplot(2,3,5)
subplot('position', [.38 .1 .25 .2])
plot(i+w, pressure(i), 'b'), xlim([0 1]), ylim([0 1]),
text(.12, .7, 'Fuel used is', 'color', 'k', 'FontSize', 32),
text(.38, .28, 'JP8', 'color', [0.7804 0.5412 0.0471], 'FontSize', 35);
```

```
if maxpressuremeasured1(j)>=45 & maxpressuremeasured1(j)<53
```

```
%subplot(2,3,6)
subplot('position', [.71 .1 .25 .2])
```

```
plot(i+w, pressure(i), 'b'), xlim([0 1]), ylim([0 1]),
text(.29, .5, 'True', 'color', 'k', 'FontSize', 50);

    else

%subplot(2,3,6)
subplot('position', [.71 .1 .25 .2])
plot(i+w, pressure(i), 'b'), xlim([0 1]), ylim([0 1]),
text(.29, .5, 'False', 'color', 'r', 'FontSize', 50);

error=error+1;

    end;

    elseif maxpressure1(j)>=49 & maxpressure1(j)<54

%subplot(2,3,5)
subplot('position', [.38 .1 .25 .2])
plot(i+w, pressure(i), 'b'), xlim([0 1]), ylim([0 1]),
text(.12, .7, 'Fuel used is', 'color', 'k', 'FontSize', 32),
text(.31, .28, 'ULSD', 'color', [0.9490 0 0.9490], 'FontSize', 35);

    if maxpressuremeasured1(j)>=53 & maxpressuremeasured1(j)<58

%subplot(2,3,6)
subplot('position', [.71 .1 .25 .2])
plot(i+w, pressure(i), 'b'), xlim([0 1]), ylim([0 1]),
text(.24, .5, 'True', 'color', 'k', 'FontSize', 60);

    else

%subplot(2,3,6)
subplot('position', [.71 .1 .25 .2])
plot(i+w, pressure(i), 'b'), xlim([0 1]), ylim([0 1]),
text(.24, .5, 'False', 'color', 'r', 'FontSize', 60);

error=error+1;

    end;

    else

%subplot(2,3,5)
subplot('position', [.38 .1 .25 .2])
plot(i+w, pressure(i), 'b'), xlim([0 1]), ylim([0 1]),
text(.12, .7, 'Fuel used is', 'color', 'k', 'FontSize', 32),
text(.03, .28, 'Biodiesel B100', 'color', [0.6157 0 0], 'FontSize', 32);

    if maxpressuremeasured1(j)>=58

%subplot(2,3,6)
subplot('position', [.71 .1 .25 .2])
```

```
plot(i+w, pressure(i), 'b'), xlim([0 1]), ylim([0 1]),
text(.19, .5, 'True', 'color', 'k', 'FontSize', 70);

    else

%subplot(2,3,6)
subplot('position', [.71 .1 .25 .2])
plot(i+w, pressure(i), 'b'), xlim([0 1]), ylim([0 1]),
text(.19, .5, 'False', 'color', 'r', 'FontSize', 70);

error=error+1;

    end;
end;
end;

% Overall accuracy

wacc2 = 100*(1-(error/k));
%disp('-----');
%fprintf('%3.0f percent accuracy in fuel identification for all
cycles\n', (wacc1+wacc2)/2);

%-----

if (wacc1+wacc2)/2>99.999999

figure(j+201)

set(gcf, 'units', 'normalized', 'position', [0.003 0.005 0.963 0.095]);

t=uicontrol('style', 'text', 'string', 'Fuel type identification = 100%');

set(t, 'units', 'normalized', 'position', [0 0 1 1]);

set(t, 'FontSize', 46);

col=get(t, 'foregroundcolor');

for n=1:30
set(t, 'foregroundcolor', 1-col, 'backgroundcolor', col);
col=1-col;
pause(.1);
end;

end;

%-----
%figure(j+202)
%i=1:no_of_testing_cycles;
%plot(i, maxpressuremeasured(i), 'b'), grid, xlabel('Test cycles'),
%ylabel('bar'), title ('Measured pressure: peak values');
```

```
%hold on; plot(i, i+45-i,'k',i, i+53-i,'k',i, i+58-i,'k','linewidth',3);

%-----
%figure(j+203)
%i=1:no_of_testing_cycles;
%plot(i, maxpressure(i),'b'), grid, xlabel('Test cycles'), ylabel('bar'),
%title ('Simulated pressure: peak values');
%hold on; plot(i, i+44-i,'k',i, i+49-i,'k',i, i+54.1-i,'k','linewidth',3);
```

Fuel identification on a multiple-cylinder engine using Artificial Neural Networks (Matlab code)

```
%Sample interval (CAD):

w=340;
v=380;

%Removes the gray border from the figures
iptsetpref('ImshowBorder','tight');

%Removes menu and toolbar from all new figures
set(0,'DefaultFigureMenu','none');

%Makes disp() calls show things without empty lines
format compact;

% -----
% Accuracy new fuel test data: 150 cycles
% -----

% Converting 1 column to 720 CAD interval columns

s=size(Test(:,1));
no_of_testing_cycles=s(1)/720;
no_of_testing_points=s(1);
pr=(Test(:,1))';
sp=(Test(:,2))';

for i=1:no_of_testing_cycles
    e(2*i-1,:)=pr((i*720-719):(i*720));
    e(2*i,:)=sp((i*720-719):(i*720));
end
Test1=e';

%-----

wacc1 = 100;

%-----
%Accuracy test for 100 random cycles
%-----

k=100;

error=0;

for j=1:k
    %j=1;
```

```
q1={1};
q = q1(randperm(length(q1)));
l = q{1}(1);

%Test Pressure
i=(w+1):v;
testpress=Test1(i,2*1-1);
s=size(testpress);
samplesize=s(1);

%-----

%Testspeed
i=(w+1):v;
testspeed2=Test1(i,2*1);
testspeed=Test1(i,2*1);
s=size(testspeed);
samplesize=s(1);

%Test Speed
%figure(7)
%i=1:samplesize;
%plot(i+w,testspeed(i),'b','linewidth',2), grid, xlabel('Crank Angle -
Degrees'), ylabel('bar'),
%title ('Test data: engine speed');

%-----

% Network TESTING for a new input (speed):

B = testpress';
C = testspeed';
[b,bs] = mapminmax(B);
[c,cs] = mapminmax(C);

a = sim(net,c);

pressure = mapminmax('reverse',a,bs);

s=size(pressure);
samplesize=s(2);

for i=1:(samplesize-1) pressure(i)=(pressure(i)+pressure(i+1))/2;
end;

%Rate of measured pressure rise vs. simulated rate of pressure rise:

%figure(j+150)

pause(0.04);

i=1:samplesize;
testnumber(j)=j;
maxpressure1(j)=max(pressure);
```

```
maxpressuremeasured1(j)=max(B);

%Maximize the window and the graphs inside to full-screen
%set(gcf,'units','normalized','position',[0 0 1 1]);
%set(gca,'units','normalized','position',[0 0 1 1]);

%Maximize the window as desired
set(gcf,'units','normalized','position',[0.003 0.14 0.962 0.823]);
set(gcf,'DefaultAxesFontSize',12);

%subplot(2,3,[1 4])
subplot('position',[.06 .1 .25 .82]);
plot(i+w, testspeed2(i),'b','linewidth',3), grid,
xlabel('Crank Angle - Degrees'), ylabel('rpm'),
xlim([w v]), ylim([1260 1320]),
text(w+.005*(v-w),1262.5,'INPUT ','color',[0.6392 0.6392
0.6392],'FontSize',35),
title('Measured engine speed','FontSize',16,'FontWeight','bold');

%subplot(2,3,[2 5])
subplot('position',[.38 .4 .25 .52])

%%%%%%%%%plot(i+w, pressure(i),'b', i+w, B(i),'r',i+w, i+w+30-
(i+w),'color',[0.4353 0.4353 1],i+w, i+w+80-(i+w),'color',[0 0 0.5922],i+w,
i+w+200-(i+w),'color',[1 0.5098 0.5098],i+w, i+w+325-(i+w),'color',[0.702 0
0],'linewidth',3), grid,
%%%%%%%%%plot(i+w,pressure(i),'b', i+w,B(i),'r', %i+w,i+w+30-
(i+w),'b','linewidth',3), grid,
%%%%%%%%%UISETCOLOR

plot(i+w, pressure(i),'b',i+w, i+w+30-(i+w),'b',i+w, i+w+80-
(i+w),'b','linewidth',3), grid,
xlabel('Crank Angle - Degrees'), ylabel('bar/rad'),
xlim([w v]), ylim([-100 150]),
text(w+.82*(v-w),13,'S8','color',[0 .7 0],'FontSize',30),
text(w+.66*(v-w),62,'B100','color',[0.6157 0 0],'FontSize',30),
text(w+.643*(v-w),120,'ULSD','color',[0.9490 0 0.9490],'FontSize',30),
text(w+.01*(v-w),-84,'OUTPUT','color',[0.6392 0.6392
0.6392],'FontSize',35),
title ('Simulated rate of pressure rise','FontSize',16,'FontWeight','bold');

subplot('position',[.71 .4 .25 .52])

plot(i+w, B(i),'r', i+w, i+w+200-(i+w),'r', i+w, i+w+325-
(i+w),'r','linewidth',3),
grid, xlabel('Crank Angle - Degrees'), ylabel('bar/rad'),
xlim([w v]), ylim([-150 400]),
text(w+.02*(v-w),150,'S8','color',[0 .7 0],'FontSize',30),
text(w+.02*(v-w),250,'B100','color',[0.6157 0 0],'FontSize',30),
text(w+.02*(v-w),360,'ULSD','color',[0.9490 0 0.9490],'FontSize',30),
text(w+.01*(v-w),-115,'TARGET','color',[0.6392 0.6392
0.6392],'FontSize',35),
title ('Rate of measured pressure rise','FontSize',16,'FontWeight','bold');
```

```
    if maxpressure1(j)<30

%subplot(2,3,3)
subplot('position',[.38 .1 .25 .2])
plot(i+w, pressure(i),'b'), xlim([0 1]), ylim([0 1]),
text(.12,.7,'Fuel used is','color','k','FontSize',32),
text(.42,.28,'S8','color',[0 .7 0],'FontSize',35);

        if maxpressuremeasured1(j)<200

%subplot(2,3,6)
subplot('position',[.71 .1 .25 .2])
plot(i+w, pressure(i),'b'), xlim([0 1]), ylim([0 1]),
text(.33,.5,'True','color','k','FontSize',40);

                else

%subplot(2,3,6)
subplot('position',[.71 .1 .25 .2])
plot(i+w, pressure(i),'b'), xlim([0 1]), ylim([0 1]),
text(.33,.5,'False','color','r','FontSize',40);

error=error+1;

                end;

        elseif maxpressure1(j)>=30 & maxpressure1(j)<80

%subplot(2,3,3)
subplot('position',[.38 .1 .25 .2])
plot(i+w, pressure(i),'b'), xlim([0 1]), ylim([0 1]),
text(.12,.7,'Fuel used is','color','k','FontSize',32),
text(.03,.28,'Biodiesel B100','color',[0.6157 0 0],'FontSize',32);

                if maxpressuremeasured1(j)>=200 & maxpressuremeasured1(j)<325

%subplot(2,3,6)
subplot('position',[.71 .1 .25 .2])
plot(i+w, pressure(i),'b'), xlim([0 1]), ylim([0 1]),
text(.24,.5,'True','color','k','FontSize',60);

                        else

%subplot(2,3,6)
subplot('position',[.71 .1 .25 .2])
plot(i+w, pressure(i),'b'), xlim([0 1]), ylim([0 1]),
text(.24,.5,'False','color','r','FontSize',60);

error=error+1;
```



```
end;

else

%subplot(2,3,3)
subplot('position',[.38 .1 .25 .2])
plot(i+w, pressure(i), 'b'), xlim([0 1]), ylim([0 1]),
text(.12, .7, 'Fuel used is', 'color', 'k', 'FontSize', 32),
text(.31, .28, 'ULSD', 'color', [0.9490 0 0.9490], 'FontSize', 35);

if maxpressuremeasured1(j)>=325

%subplot(2,3,6)
subplot('position',[.71 .1 .25 .2])
plot(i+w, pressure(i), 'b'), xlim([0 1]), ylim([0 1]),
text(.19, .5, 'True', 'color', 'k', 'FontSize', 70);

else

%subplot(2,3,6)
subplot('position',[.71 .1 .25 .2])
plot(i+w, pressure(i), 'b'), xlim([0 1]), ylim([0 1]),
text(.19, .5, 'False', 'color', 'r', 'FontSize', 70);

error=error+1;

end;
end;
end;

% Overall accuracy

wacc2 = 100*(1-(error/k));
%disp('-----');
fprintf('%3.0f percent accuracy in fuel identification for all
cycles\n', (wacc1+wacc2)/2);

%-----

if (wacc1+wacc2)/2>99.999999

figure(j+151)

set(gcf, 'units', 'normalized', 'position', [0.003 0.005 0.963 0.095]);

t=uicontrol('style', 'text', 'string', 'Fuel type identification = 100%');

set(t, 'units', 'normalized', 'position', [0 0 1 1]);

set(t, 'FontSize', 46);
```

```
col=get(t,'foregroundcolor');

for n=1:30
set(t,'foregroundcolor',1-col,'backgroundcolor',col);
col=1-col;
pause(.1);
end;

end;

%-----

%figure(j+152)

%i=1:no_of_testing_cycles;
%plot(i, maxpressure(i),'b'), grid, xlabel('Test cycles'), ylabel('bar/rad'),
%title ('Simulated rate of pressure rise: peak values');
%hold on; plot(i, i+30-i,'k',i, i+80-i,'k','linewidth',3);

%figure(j+153)

%i=1:no_of_testing_cycles;
%plot(i, maxpressuremeasured(i),'b'), grid, xlabel('Test cycles'),
%ylabel('bar/rad'), title ('Rate of measured pressure rise: peak values');
%hold on; plot(i, i+200-i,'k',i, i+325-i,'k','linewidth',3);
```

REFERENCES

- 1) Jayakumar, C., Nargunde, J., Sinha, A., Bryzik, W., and Henein, N.A., 2012, "Effect of Biodiesel, JP-8 and Ultra Low Sulfur Diesel Fuel on Autoignition, Combustion, Performance and Emissions in a Single Cylinder Diesel Engine", Journal of Engineering for Gas Turbines and Power, 134, 022801
- 2) Jayakumar, C., Nargunde, J., Sinha, A., Bryzik, W., Henein, N.A., and Acharya, K., 2010, "Comparison between Combustion, Performance and Emission Characteristics of JP-8 and Ultra Low Sulfur Diesel Fuel in a Single Cylinder Diesel Engine", SAE Technical Paper 2010-01-1123
- 3) Jayakumar, C., Zheng, Z., Joshi, U.M., Bryzik, W., and Henein, N.A., 2012, "Effect of Inlet Air Temperature on Auto-Ignition of Fuels with Different Cetane Number and Volatility", SAE Technical Paper 2012-01-1317
- 4) McCormick, B., 2005, "Effects Of Biodiesel On Pollutant Emissions", National Renewable Energy Laboratory
- 5) Proc, K., Barnitt, R., Hayes, R., Ratcliff, M., and McCormick, R.L., 2006, "100,000-Mile Evaluation of Transit Buses Operated on Biodiesel Blends (B20)" SAE Paper 2006-01-3253

- 6) Fraer, R., Dinh, H., Proc, K., McCormick, R.L., Battelle, K.C., and Buchholz, B., 2005, "Operating Experience and Teardown Analysis for Engines Operated on Biodiesel Blends (B20)", SAE Paper 2005-01-3641
- 7) Tsolakisa, A., Wyszynskia, M.L., Theinnoia, K., and Megaritisb, A., 2007, "Engine Performance And Emissions Of A Diesel Engine Operating On Diesel-RME (Rapeseed Methyl Ester) Blends With EGR (Exhaust Gas Recirculation)", *ELSEVIER Energy* , 32, pp. 2072–2080
- 8) Hsi-Hsien, Y., Shu-Mei, C., Mei-Yu, L., Chi-Wei, L.J., Wen-Chang, L.U. Yong-Yuan, K.U., 2007, "Effects Of Biodiesel On Emissions Of Regulated Air Pollutants And Polycyclic Aromatic Hydrocarbons Under Engine Durability Testing", *ELSEVIER Atmospheric Environment*, 41, pp 7232–7240
- 9) Eyre, N., et al, 2006, "Previous Comparative Performance Studies", http://www.esru.strath.ac.uk/EandE/Web_sites/0203/biofuels/perf_exsisting.html
- 10) Pugazhivadivu, M., and Jeyachandran, K., 2005, "Investigations On The Performance And Exhaust Emissions Of A Diesel Engine Using Preheated Waste Frying Oil As Fuel", *ELSEVIER Renewable Energy*, 30, pp. 2189–2202

- 11) Kalam, M.A., and Masjuki, H.H., 2005, "Emissions and deposit characteristics of a small diesel engine when operated on preheated crude palm oil", SAE Technical Paper 2005-01-3697
- 12) U.S. Environmental Protection Agency (EPA), 1990, "Clean Air Act Section 211(b)" enacted by Congress; <http://www.epa.gov/air/caa/>
- 13) United States Environmental Protection Agency, 2003, "The Effect of Cetane Number Increase Due to Additives on NOx Emissions from Heavy-Duty Highway Engines", Final Technical Report EPA420-R-03-002
- 14) Ponti, F., and Ravaglioli, V., Serra, G., and Stola, F., 2010, "Instantaneous Engine Speed Measurement and Processing for MFB50 Evaluation", SAE International Journal of Engines, 2, pp. 235-244
- 15) Brand, D., Onder, C.H. and Guzzella, L., 2005, "Estimation of the Instantaneous In-Cylinder Pressure for Control Purposes using Crankshaft Angular Velocity", SAE Technical Paper 2005-01-0228
- 16) Kallenberger, C., Hamedovic, H., Raichle, F., Breuninger, J., Fischer, W., Benninger, K., Nistor, A., Zoubir, A.M., 2009, "Estimation of Cylinder-wise Combustion Features from Engine Speed and Cylinder Pressure", SAE Technical Paper 2008-01-0290

- 17) Taglialatela, F., Cesario, N., Lavorgna, M., Merola, S.S., Vaglieco, B.M., 2009, "Use of Engine Crankshaft Speed for Determination of Cylinder Pressure Parameters" SAE Technical Paper 2009-24-0108
- 18) Guezennec, Y.G., and Gyan, P., "A Novel Approach to Real-Time Estimation of the Individual Cylinder Combustion Pressure for S.I. Engine Control", 1999, SAE Technical Paper 1999-01-0209
- 19) Taraza, D., and Henein, N.A., 1998, "Determination of the Gas-Pressure Torque of a Multicylinder Engine from Measurements of the Crankshaft's Speed Variation", SAE Technical Paper 980164
- 20) Taraza, D., 2001, "Quantifying Relationships Between the Crankshaft's Speed Variation and the Gas Pressure Torque" SAE Technical Paper 2001-01-1007
- 21) Taraza, D., 2001, "Statistical Model and Simulation of Engine Torque and Speed Correlation", SAE Technical Paper 2001-01-3686
- 22) Taraza, D., 2002, "Accuracy Limits of IMEP Determination from Crankshaft Speed Measurements" SAE Technical Paper 2002-01-0331
- 23) Taraza, D., Henein, N.A., Bryzik, W., and Gade, M.J., 2005, "Cylinder Pressure Reconstruction from Crankshaft Speed Measurements in a Four-Stroke Single Cylinder Diesel Engine", Internal Combustion Engine Division

Spring Technical Conference (ICES2005), ASME Paper ICES2005-1023
pp. 387-395

24) Taraza, D., 2001, "Dynamics and Vibrations of Automotive Engines",
Wayne State University, Detroit

25) The encyclopedia Wikipedia website: <http://en.wikipedia.org/wiki/>

26) Medes Group petroleum website: www.mepetroleum.com/jet_fuel.htm

27) Syntroleum material safety data sheet, "S-8 Synthetic Jet Fuel",
[http://www.syntroleum.com/profiles/investor/fullpage.asp?f=1&BzID=2029&
to=cp&Nav=0&LangID=1&s=0&ID=11912](http://www.syntroleum.com/profiles/investor/fullpage.asp?f=1&BzID=2029&to=cp&Nav=0&LangID=1&s=0&ID=11912)

28) 2007, "Petroleum products research department test report",
Southwest Research Institute

29) 2011, "Petroleum products research department test report",
Southwest Research Institute

30) Haykin, S., 2007, "Neural Networks – A Comprehensive Foundation",
McMaster University, Ontario

31) 2006, Matlab Help v. 7.3.0., "Neural Network toolbox"

ABSTRACT

MULTI-FUEL OPERATION OF MODERN ENGINES; ON BOARD FUEL IDENTIFICATION

by

FLORIN MOCANU

August 2012

Advisor: Dr. Dinu Taraza

Major: Mechanical Engineering

Degree: Doctor of Philosophy

Modern engines require enhancement of electronic controls to achieve better fuel economy, high power density and satisfactory emissions levels while operating safely. Commercial and military vehicles should run safely and efficiently on any fuel available on the market or on the battlefield, therefore on-board fuel identification and adaptation of engine controls to the type of fuel becomes extremely important. The use of an inexpensive, nonintrusive sensor is highly desirable. The development of a technique based on the measurement of the instantaneous crankshaft speed and engine dynamics could be a convenient solution. Several such methods have been elaborated at the Center for Automotive Research in the Mechanical Engineering Department at Wayne State University, each of them yielding plausible results regarding on-board fuel identification.

AUTOBIOGRAPHICAL STATEMENT

I was born in 1978, spending my childhood years in Bacau, Romania. The high-school I attended was “Stefan cel Mare” (‘Steven the Great’) in Campulung Moldovenesc, Romania. Out of 144 students I passed the baccalaureate the 1st and also I was admitted the 1st in my automotive specialization at the Military Technical Academy in Bucharest, Romania. I graduated five years later, in 2002, with a Bachelor’s degree. After working for four years in the industry – major and complete engine overhauls, I was accepted, after passing the prerequisite exams, in a graduate program at Wayne State University, Detroit, Michigan / USA in Mechanical Engineering Department. Here, over the course of six years, under Dr. Dinu Taraza and Dr. Naeim Henein’s guidance, I completed several research work projects on single, four and six cylinder engines, with emphasis on power, fuel consumption, emissions and alternative fuels. I obtained my Master diploma in April 2008 and my PhD degree in April 2012. My work so far has been greatly appreciated by the well-known engine company, Cummins, which hired me immediately after graduation. In the future I hope to improve engines power, fuel consumption and emissions, as an ultimate goal of any combustion engine engineer.